

# Investigations into the Product-oriented Glucose Electrooxidation: From Gold Towards High-entropy Alloy Catalysts

Inauguraldissertation  
der Philosophisch-naturwissenschaftlichen Fakultät  
der Universität Bern

vorgelegt von

Nicolas Schlegel

von Zürich ZH

Leiter der Arbeit:  
Professor Dr. Matthias Arenz

Departement für Chemie, Biochemie und Pharmazie



This work is licensed under a Creative Commons  
Attribution-NonCommercial-NoDerivatives 4.0 International License  
(<https://creativecommons.org/licenses/by-nc-nd/4.0>)

# **Investigations into the Product-oriented Glucose Electrooxidation: From Gold Towards High-entropy Alloy Catalysts**

Inauguraldissertation  
der Philosophisch-naturwissenschaftlichen Fakultät  
der Universität Bern

vorgelegt von

Nicolas Schlegel

von Zürich ZH

Leiter der Arbeit:  
Professor Dr. Matthias Arenz  
Departement für Chemie, Biochemie und Pharmazie

Von der Philosophisch-naturwissenschaftlichen Fakultät angenommen.

Bern, 03.07.2023

Der Dekan

Prof. Dr. Herweg

## Abstract

The glucose oxidation reaction (GOR) has gathered increased interest from various fields in the last decades. Besides the more prominent bioelectrocatalytic applications, glucose sensors and direct glucose fuel cells, the product-oriented GOR has more recently gained increased attention, due to the promising application of the oxidation products as smart drop-in chemicals. This thesis is concerned with the electrochemical oxidation of glucose and the identification of operational parameters that promote the efficient formation of glucaric acid. Working in a classical three-electrode RDE setup the influence of forced convection on the product distribution was investigated. The reaction pathway from glucose to glucaric acid was explored by oxidizing glucose as GOR reaction intermediates. To understand the reaction pathway, a high-performance liquid chromatography (HPIC) method was developed which can quantify intermediates and undesired side-products. Combining experimental data using a gold disk electrode and insights gathered from DFT calculations, the selective oxidation of terminal hydroxyl groups has been identified as the most challenging step for forming glucaric acid selectively and efficiently. Additionally, the oxidation of the aldehyde group in glucose is shown to occur fast and selectively.

Overcoming the limitation of the Au-electrode, high-entropy alloys (HEA) have been envisaged as potential catalysts for the GOR. A synthesis approach based on incipient wetness impregnation (IWI) yielding supported single-phase HEA nanoparticles was developed. This facile and reliable method allows for nanoparticle size-control by varying different synthesis parameters. A model system of PtFeCoNiPd was investigated in detail by combining *in-situ* X-ray diffraction (PXRD) and *in-situ* X-ray absorption (XANES). The combination of both analysis techniques enables linking phase transformations and changes in the unit cells to the reduction behavior of the individual constituent elements.

## List of Publications

Publications included in the thesis:

- I. **Nicolas Schlegel**, Gustav K.H. Wiberg, Matthias Arenz, On the electrooxidation of glucose on gold: Towards an electrochemical glucaric acid production as value-added chemical. *Electrochimica Acta* **410**, 140023 (2022). <https://doi.org/10.1016/j.electacta.2022.140023>
  - II. **Nicolas Schlegel**, Alexander Bagger, Jan Rossmeisl, Matthias Arenz, Elucidating the reaction pathway of glucose electrooxidation to its valuable products: the Influence of mass transport and electrode potential on the product distribution, *Submitted*. ChemRxiv: <https://doi.org/10.26434/chemrxiv-2023-5m111>
  - III. **Nicolas Schlegel**, Stefanie Punke, Rebecca Pittkowski, Divyansh Gautam, Ulrik Friis-Jensen, Etienne Berner, Nicola Ramseyer, Kirsten M. Ø. Jensen, Matthias Arenz. Characterization of multimetallic PtFeCoNiPd samples by combined *in-situ* PXRD and XANES during synthesis, *In preparation*.
  - IV. Baiyu Wang<sup>+</sup>, **Nicolas Schlegel**<sup>+</sup>, Olivia Aalling-Frederiksen, Etienne Berner, Damin Zhang, Kirsten M. Ø. Jensen & Matthias Arenz. Elucidating the Steady-State OER Activity of (Ni<sub>1-x</sub>Fe<sub>x</sub>)OOH Binary Nanoparticles in As-prepared and Purified KOH Electrolyte Solutions. *To be submitted, accessible on ChemRxiv*
- <sup>+</sup>These authors contributed equally.

Publications not included in the thesis:

- I. Alinejad S, Quinson J, Wiberg G K H, **Schlegel N**, Zhang D, Li Y, Reichenberger S, Barcikowski S, Arenz M. Electrochemical Reduction of CO<sub>2</sub> on Au Electrocatalysts in a Zero-Gap, Half-Cell Gas Diffusion Electrode Setup: a Systematic Performance Evaluation and Comparison to a H-cell Setup. *ChemElectroChem* **9**, e202200341 (2022). <https://doi.org/10.1002/celec.202200341>
- II. Pittkowski R, Clausen CM, Chen Q, Stoian D, van Beek W, Bucher J, Welten RL, **Schlegel N**, Mathiesen JK, Nielsen TM, Rosenkrant AW, Bøjesen E, Rossmeisl J, Jensen KMØ, Arenz M. High entropy alloy nanoparticle formation at low temperatures. *Submitted*, ChemRxiv: <https://doi.org/10.26434/chemrxiv-2022-khw4t>.

## Table of content

Abstract .....	i
List of Publications.....	ii
List of Abbreviations.....	v
1 Introduction.....	1
1.1 Renewable resources and drop-in chemicals.....	1
1.2 Glucose oxidation reaction (GOR) .....	2
1.3 High-entropy alloys (HEA) .....	6
2 Employed methods and method development .....	8
2.1 Electrochemical measurements in a rotating disk electrode (RDE) setup .....	8
2.2 Product analysis by high-performance ion-chromatography (HPIC) .....	10
2.3 <i>In-situ</i> Raman spectroscopy .....	16
2.4 Characterization of synthesized HEA-NP.....	18
2.4.1 Powder X-ray diffraction (PXRD) .....	18
2.4.2 X-ray absorption near edge spectroscopy (XANES).....	20
2.4.3 Energy dispersive X-ray spectroscopy (EDX) .....	20
2.5 Synthesis of HEA-NP by incipient wetness impregnation (IWI) method.....	21
3 Discussion of appended manuscripts.....	26
3.1 Manuscript I: On the electrooxidation of glucose on gold: Towards an electrochemical glucaric acid production as value-added chemical .....	26
3.1.1 Abstract .....	26
3.1.2 Contribution to the work.....	26
3.1.3 Most relevant findings.....	27
3.2 Manuscript II: Elucidating the reaction pathway of glucose electrooxidation to its valuable products: the Influence of mass transport and electrode potential on the product distribution ....	30
3.2.1 Abstract .....	30
3.2.2 Contribution to the work.....	30
3.2.3 Most relevant findings.....	31
3.3 Manuscript III: Characterization of multimetallic PtFeCoNiPd-HEA samples by <i>in situ</i> PXRD and XANES ( <i>in preparation</i> ).....	34
3.3.1 Abstract .....	34
3.3.2 Contribution to the work.....	34
3.3.3 Most relevant findings.....	35
3.4 Manuscript IV: Elucidating the Steady-State OER Activity of NiFeOOH Binary Nanoparticles in As-prepared and Purified KOH Electrolyte Solutions .....	40
3.4.1 Abstract .....	40
3.4.2 Contribution to the work.....	40
3.4.3 Most relevant findings.....	41
4 Conclusion & Outlook.....	44

## List of Publications

4.1	Conclusion .....	44
4.2	Outlook.....	45
4.2.1	Combining GOR and HEA synthesis.....	45
4.2.2	Development of a flow-cell setup for GOR.....	45
5	Acknowledgement.....	46
6	References.....	47
7	Appended Manuscripts .....	56

## List of Abbreviations

Bcc	Body centred cubic
CAD	Charged aerosol detector
CD	Conductivity detection
CE	Counter electrode
CHEAC	Centre for High-entropy Alloy Catalysis
CO <sub>2</sub> RR	CO <sub>2</sub> reduction reaction
CV	Cyclic voltammogram
DGFC	Direct glucose fuel cell
EDX	Energy dispersive X-ray spectroscopy
ESRF	European Synchrotron Radiation Facility
Fcc	face-centred cubic
FE	Faradaic efficiency
GLA	Glucaric acid
GLU	Gluconic acid
GOR	Glucose oxidation reaction
HEA	High-entropy alloy
HEA-NP	High-entropy alloy nanoparticle
HPIC	High-performance ion chromatography
HPLC	High-performance liquid chromatography
IC	Ion chromatography
IWI	Incipient wetness impregnation
LC	Liquid chromatography
LDH	Layered double hydroxide
MS	Mass spectrometry
NMR	Nuclear magnetic resonance
NP	Nanoparticles
OER	Oxygen evolution reaction



## List of Abbreviations

ORR	Oxygen reduction reaction
PAD	Pulsed amperometric detection
PDF	Pair distribution function
PGM	Platinum group metals
PTFE	Polytetrafluoroethylene (Teflon)
PXRD	Powder x-ray diffraction
RDE	Rotating disk electrode
RE	Reference electrode
RHE	Reversible hydrogen electrode
TEM	Transmission electron microscope
WE	Working electrode
XANES	X-ray absorption near edge structure

# 1 Introduction

## 1.1 Renewable resources and drop-in chemicals

Fossil resources are currently the primary global source of fuels, chemical feedstock<sup>1</sup>, and “energy production”<sup>2</sup>. One major consequence of the heavy reliance on fossil resources is the net-increase of carbon species, mainly CO<sub>2</sub>, in the atmosphere. These compounds act as greenhouse gases leading to climatic changes<sup>3</sup> and resulting consequences observed over the last decades<sup>4</sup>. To combat the climate crisis society faces today, the dependence on fossil resources must be reduced. In other words, the anthropogenic carbon cycle must be closed. In the context of fuels and energy production, electricity and hydrogen from renewable sources<sup>5,6</sup> offer promising alternatives to the conventional, fossil fuel, and carbon-based solutions used today. However, other than energy storage and electricity production, commodity chemicals and chemical feedstock can never be completely decarbonized. A possible way of addressing this challenge is to replace fossil resources with alternative, renewable carbon sources, for example carbon from the biosphere. These renewable resources are defined as agricultural or forestry products used not as food products but instead as chemical feedstock or to produce electricity or fuels<sup>7</sup>.

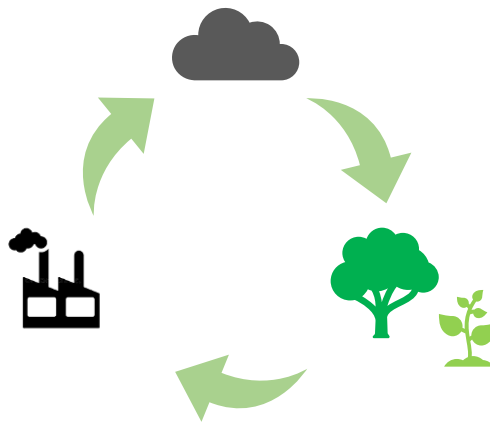


**Figure 1.1.1:** Schematic illustration of a closed anthropogenic carbon cycle relying on biosphere-sourced carbon.

Sustainable sourcing of renewable resources can help in closing the anthropogenic carbon cycle, schematically illustrated in **Figure 1.1.1**, and decreases the emission of greenhouse gases. This is however only one of many approaches in combatting the dependence on fossil sources and will not be able to solve the problems on its own. In terms of chemical feedstocks, molecules like cellulose and hemicellulose can be derivatized into a plethora of drop-in chemicals, such as ethanol, ethylene, and acetone. Those small organic molecules can directly replace their fossil-sourced counterparts in the chemical synthesis<sup>8</sup> while preserving the conventional synthesis pathways towards more complex

## Introduction

molecules. In addition, when using molecules like the previously mentioned cellulose, their structural complexity can be utilized to circumvent synthesis steps as certain desirable structures can already be present in the cellulose molecule. Compounds employed in this way are called smart drop-in chemicals (**Figure 1.1.2**).

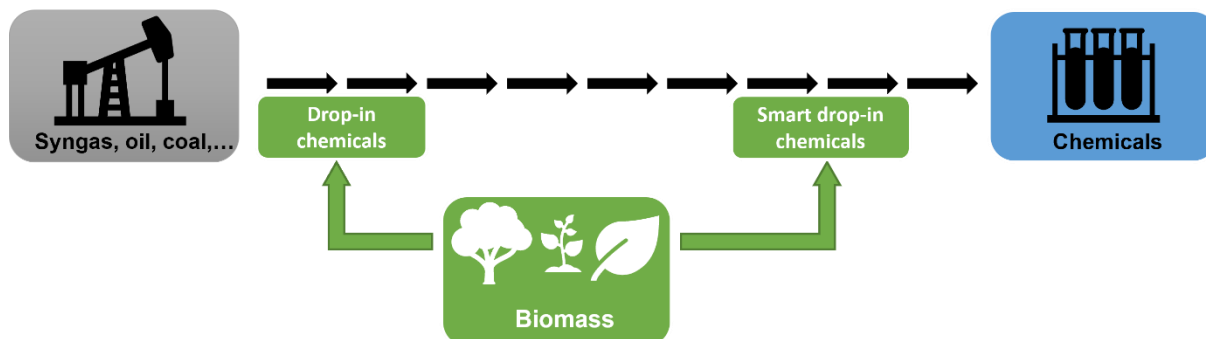


**Figure 1.1.2:** Illustration of the application of drop-in and smart drop-in chemicals derived from biomass.

## 1.2 Glucose oxidation reaction (GOR)

An abundant and currently cheap renewable resource is glucose. It can be sourced from cellulose, the most abundant biopolymer<sup>9</sup>. Since glucose is a relatively large molecule it can be derivatized into a wide range of different compounds through oxidation. Fully oxidizing glucose results in the formation of CO<sub>2</sub><sup>10</sup> making available the most chemical energy stored in the glucose molecule. However, CO<sub>2</sub> is not an interesting molecule in terms of synthesis since the structural complexity of glucose is lost during the oxidation. Other products resulting from the dissociation of glucose C<sub>6</sub>-chain during oxidation are small organic molecules, e.g., formic acid, glycolic acid, tartaric acid, and glycoaldehyde<sup>11,12</sup>. Some of these chemicals can directly be used in the chemical industry<sup>13</sup>. Glucose can also be oxidized keeping its carbon spine intact, forming the three sugar acids gluconic acid, glucuronic acid, and glucaric acid<sup>14–16</sup> (**Figure 1.2.2**). Gluconic acid is already used in the food and pharmaceutical sector<sup>17</sup> and glucuronic acid has detoxifying and anti-inflammatory effects<sup>18</sup>. Most importantly however, glucaric acid has been labelled as a building block chemical by the U.S. Department of Energy<sup>19</sup> which has led to an immediate rise in research interest. It is currently used as a chelating agent but has the prospect of becoming a precursor to various chemicals, such as Nylon<sup>20,21</sup>, in the future. Historically, glucose is oxidized to glucaric acid in hot, concentrated nitric acid<sup>22,23</sup>. However, these processes were never commercialized due to the harsh conditions, problems in temperature control, and toxic side products. Catalytic approaches to glucose oxidation promise improved efficiencies and product selectivity. Various heterogenous approaches have been pursued. The use of 2,2,6,6-tetramethylpiperidin-1-oxyl (TEMPO) results in high yields of glucaric acid<sup>24,25</sup>.

## Introduction

However, the drawback of toxic side-products remains. In recent years, molecular oxygen has been used as a non-toxic oxidation agent. Employing Pt-based catalysts at mild conditions (pH 8-11, up to 80 °C) a yield of 55 % was reached in the conversion of glucose to glucaric acid<sup>26</sup>. At increased pressures and more optimized conditions, Lee et al. reported yields of up to 74 % on commercially available Pt/C catalysts<sup>12</sup>. Under similar conditions, Au-based catalyst can oxidize glucose only to gluconic acid<sup>27-29</sup>. Operating in reaction mixtures at increased pH was found to increase oxidation rates. However, the formation of side products involving the dissociation of the C-C chain in glucose also increased<sup>12</sup>. Importantly, the degradation of glucose in alkaline solution occurs also in the absence of a catalyst<sup>30</sup>. Working in these conditions therefore requires fast kinetics to ensure selectivity towards the desired products.

Electrocatalytic approaches to glucose oxidation promise equally mild conditions and, additionally, can utilize directly electricity produced from renewable sources. Electrocatalytic glucose oxidation has long been pursued in the field of bioelectrocatalysis<sup>31</sup>. Two applications dominate the bioelectrocatalytic research. First, direct glucose fuel cells (DGFC) employing biomolecules, such as enzymes, seek to be continuous power sources utilizing ambient fuels, e.g., glucose in the bloodstream<sup>32</sup>. These implants can for example power cardiac pacemakers. Hence, the main research interests on from an electrochemical perspective lie on the power density as well as longevity and reliability of the devices. The second application of glucose electrocatalysis is the field of electrochemical glucose sensors. Clark and Lyons developed the first working glucose sensor in the nineteen sixties relying on a combination of glucose oxidase and a Pt-electrode<sup>33</sup>. Nonenzymatic glucose sensors have made significant improvements in the past 20 years. Different metal-based electrodes are being studied extensively. Unsurprisingly, electrodes based on Pt and Au, as well as alloys and composites including the two metals, are among the most prominent<sup>34</sup>. In sensors, the most important properties are the responsivity and sensitivity of the electrode to glucose for accurate assessments of glucose concentration in the blood. The catalysts are additionally optimized to function well under physiological conditions<sup>34</sup>. In both DGFC and the glucose sensors, the oxidation product is of secondary interest. The transfer of insight between these applications and the product-oriented glucose electrooxidation mainly lies in the nature of the electrode material. Hence, Pt and Au also have received the most interest in that regard. As such, in the product-oriented glucose electrooxidation, Vassilyev et al.<sup>35,36</sup> showed that the current response, similar to the previously mentioned catalytic approaches, depends heavily on the electrolyte pH. Specifically, during potentiodynamic measurements on Au and Pt surfaces in glucose containing electrolytes, the strongest current responses were recorded in alkaline conditions. Kokoh et al.<sup>37</sup> conducted one of the first extensive investigations into the product distribution of GOR. The authors showed the nature of the electrode and the applied oxidation potential to be key operational parameters and determined gluconic acid to

## Introduction

be the main oxidation product using a Pt-catalyst. Additional products included glucaric acid, different keto-D-gluconic acid species, and various small carboxylic acids. The authors also expanded their study to the oxidation of D-gluconic acid. Their work on Pt and Pt-Pb electrodes showed the major products to be glucuronic acid or 2-keto-D-gluconic acid, respectively<sup>38</sup>. Importantly, they did not find glucaric acid in substantial amounts. Since then, many more catalyst materials have been tested. Other than Pt, Au-based materials are still among the most thoroughly explored electrodes<sup>39–43</sup>, including studies into different nanostructures. However, non-precious metals have also been investigated<sup>44–48</sup>. Due to the employed alkaline conditions and the ease of synthesis, stable Ni-based materials were the electrodes of choice to circumvent the more noble metal catalysts. Nonetheless, gold remains the most interesting catalyst material due to its good performance in terms of activity and robustness. Recently, Moggia et al. reported the oxidation of glucose to glucaric acid on Au electrodes<sup>49,50</sup>.

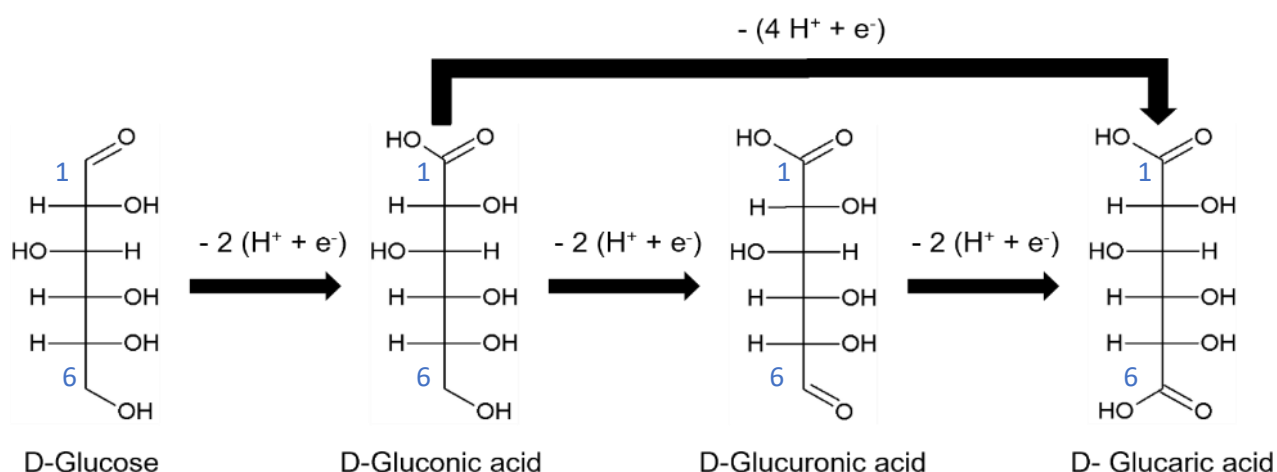
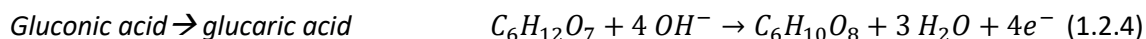
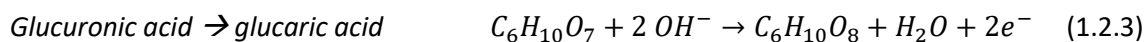
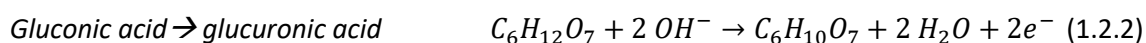
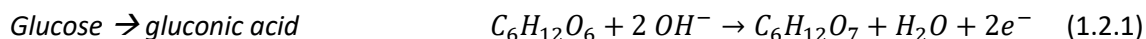


**Figure 1.2.1:** Electrooxidation reaction pathway from glucose to glucaric acid either in three reaction steps, each involving the removal of two proton-electron-pairs, or in two reaction steps, one of which involving the removal of two proton-electron-pairs and of four proton-electron pairs, respectively. The two-step reaction pathway circumvents the formation of glucuronic acid and has been implicitly reported on Au catalysts<sup>49</sup>. The blue indices label the C<sub>1</sub> and C<sub>6</sub> carbons in each compound.

The authors found the applied oxidation potential to be crucial in tuning the product distribution between gluconic and glucaric acid. The oxidation mechanism has also been investigated in detail on Au-surfaces<sup>40,51–53</sup>. These studies are focused on the oxidation of glucose to gluconic acid. The reaction mechanism to form glucaric acid on gold surfaces is still unknown and not fully explored. A likely explanation is that the formation of glucaric acid on Au surfaces is a recent finding. Chemically speaking, on Au surfaces the oxidation of aldehyde groups (C<sub>1</sub> position in glucose) is well understood while the oxidation of hydroxyl groups, preferably terminal at the C<sub>6</sub> position, is unexplored. A further unexplored question is if gluconic acid is oxidized to glucaric acid on Au via two steps additionally

## Introduction

involving glucuronic acid or one step, skipping the formation of glucuronic acid (see **Figure 1.2.2** and **Equation 1.2.1-4**):



The set of reaction equations corresponding to the individual steps to form glucaric acid from glucose is depicted in **Figure 1.2.2**. Importantly, **Equation 1.2.4** is the combination of **Equations 1.2.2 and 1.2.3** reflecting the possibility of omitting glucuronic acid as an intermediate species on the path to glucaric acid. Unfortunately, apart from glucose, the standard Gibbs free energies of formation, and therefore, their corresponding standard potentials cannot be found. In addition to these considerations, kinetic trends and understanding of mass transport influences of glucose oxidation are also lacking as of now. Larew and Johnson<sup>54</sup> studied glucose oxidation in a rotating disk electrode (RDE) setup but did not do any product analysis. Understanding mass transport phenomena and the reaction mechanism to form glucaric acid both appear crucial for future advances in glucose oxidation since any attempts of upscaling depend heavily on these two factors. Additionally, novel catalyst materials are needed to improve the selectivity towards glucaric acid formation. Alloys and other metal composites have been used and have shown promising results<sup>55-58</sup> by improving the catalysts' resiliency towards poisoning and the selectivity towards the GOR<sup>59</sup>.

By working in an RDE-setup on an Au-disk, this thesis investigates the effect of mass transport phenomena on the GOR and its product distribution. Additionally, a possible pathway from glucose to glucaric acid is explored by also oxidizing gluconic and glucuronic acid in said RDE setup.

### 1.3 High-entropy alloys (HEA)

Amongst emerging novel catalyst materials, high entropy alloys have started to gain interest in both theoretical and experimental studies<sup>60,61</sup>. An alloy is considered “high-entropy” when it is comprised of at least five elements in approximately equimolar ratio which are randomly mixed<sup>62</sup>. If five or more elements are combined this way, it is assumed that the mixing entropy offsets the mixing enthalpy of the system. Hence, the formation of a HEA is governed by entropy and not by enthalpy, which is the dominating term in the formation of conventional alloys. The result is a material in which all the elements occupy random positions in the structure. Even though at first believed to form extremely complex crystal structures, HEA solid solutions have been found to form simple crystal lattices, such as face-centered cubing (fcc) or body-centered cubic (bcc), seemingly due to role of the high entropy state<sup>63–66</sup>. However, the developed and investigated HEAs were not intended to be employed in catalysis. Rather, these materials were of interest because of their improved physical and mechanical properties<sup>67</sup>, such as fracture toughness<sup>68</sup>, specific strength<sup>69–71</sup> or resistance to corrosion<sup>72</sup>. HEA as catalysts, due to their random arrangement of elements on the material surface, promise a near infinite number of different possible active sites owing to a nearly continuous distribution of associated adsorption energies<sup>60</sup>. A small fraction of these sites with their supreme properties will facilitate a reaction optimally and as a result determine the catalytic activity of the HEA. Batchelor et al.<sup>60</sup> focused their study on the oxygen reduction reaction but the concept has since been expanded also to the CO<sub>2</sub> reduction reaction (CO<sub>2</sub>RR)<sup>73</sup>. Both theoretical approaches have been validated experimentally<sup>61,74</sup>, showing that HEA-catalysts are promising materials that can be predicted by DFT calculations. Additionally, the hydrogen evolution reaction (HER) has been investigated on HEA catalysts<sup>75</sup> further alluding to the many facets and the potentially wide field of application for HEAs as electrocatalysts. A possible, yet unexplored application of HEA catalysts lies in catalytic reactions involving one, or even multiple, stable intermediates species – such as glucose oxidation. In theory, the continuum of different sites in the HEA can provide optimal sites for the different chemical steps. Meaning that some sites could efficiently catalyze the oxidation of the aldehyde groups while others are optimal for the oxidation of terminal hydroxyl-groups. However, it is also possible to expose sites which could be very efficient at dissociating the glucose molecule resulting in undesired side products.

With the advent of HEA catalysts, the demand for nanosized HEA materials has risen. Before, high entropy alloys were manufactured in bulk, for example by arch-melting<sup>76</sup>. Synthesizing HEA-nanoparticles (NPs) demands different approaches which bring with them new challenges<sup>77–79</sup>. Wet-chemical approaches have been successfully applied to yield a range of HEA with different compositions. Similar to the synthesis of conventional nanostructures, carefully selecting the synthesis

## Introduction

approach and conditions allows tuning of the obtained structures and its resulting properties. In the last three years, the number of possible synthesis approaches has also increased drastically. Physical approaches, such as laser-ablation or sputtering, as well as chemical approaches, including classical solvents and reagents like ethylene glycol or  $\text{NaBH}_4$ , have been reported<sup>80,81</sup>. Especially milder, in some cases even ambient, conditions make those chemical synthesis routes much more accessible. Another synthesis approach worth mentioning is pyrolysis in which metal precursors are dispersed on supports, such as carbon black or aluminum oxide<sup>82</sup>. The resulting, supported NP are promising catalysts due to well-separated particles which ensure high specific surface areas. The formation of HEA-NPs at relatively low temperatures (approx. 350 °C) raises questions about their formation mechanism as conventional HEA syntheses rely on high temperature to achieve high-entropy states. Pittkowski et al. mention a limited atom mobility during precursor reduction and stochastic effects as beneficial for multi-elemental mixtures. They showed that precursor mixtures of five elements reduce into a single phase more readily while bimetallic mixtures tend to form multiple phases during reduction<sup>83</sup>.

Before applying a HEA catalyst to the GOR, the synthesis of said HEA is necessary. Hence, in this thesis a simple, incipient-wetness impregnation (IWI) based synthesis approach to form HEA-NP is presented. The IWI approach was chosen because it also follows the idea of a limited precursor mobility suggested by Pittkowski et al. The HEA formation is discussed based on a combined *in-situ* x-ray diffraction (PXRD) and x-ray absorption near edge structure (XANES) study (see appended manuscript III). It is important to note that, independent of the synthesis route, the characterization of the synthesized HEA-NP is far from trivial, and a standardized characterization assay has not been established so far. In comparison, bulk HEAs can readily be analyzed by standard techniques, such as powder diffraction (PXRD), to investigate the metallic phase(s) and to thereby determine whether a material is a HEA. In the case of nanosized crystallites, standard laboratory techniques and equipment reach their limits. Crystallites of that scale lead to considerable broadening of the interferences in diffraction patterns<sup>84</sup>. A possible solution, that was also pursued as a part of this thesis, is the use of synchrotron radiation which allows a much higher resolution due to larger X-ray beam energies and the analysis with Rietveld refinements of the acquired pattern<sup>85</sup>. When determining the elemental composition of the synthesized HEA-NP, energy dispersive X-ray spectroscopy (EDX) has been found to be an appropriate method. The distribution of elements throughout the sample can be observed including deviations between different sample regions in the case of supported NPs. High-resolution EDX mapping on appropriate instruments enables investigations into the elemental composition of individual particles<sup>82,85</sup>, either confirming or negating the random distribution of the elements throughout the sample.



## 2 Employed methods and method development

In this chapter, the methods, which have been used most prevalently to acquire and analyze data for this thesis, are discussed. Methods and techniques which have been developed or modified specifically for the presented work, and which are not part of the typical repertoire of the Arenz group are presented in more detail. For standard techniques only the type of information gained, and their utilization are described. The theory behind these techniques is not discussed in detail.

### 2.1 Electrochemical measurements in a rotating disk electrode (RDE) setup

This section is concerned with the concept of RDE measurements rather than the specific setup and its preparation used to conduct the experiments. A detailed description of the setup can be found in the appended manuscripts I and II.

Electrochemical measurements were conducted in a conventional three-electrode cell. The employed working electrode was an Au-disk embedded in a Teflon (PTFE) rod. Rotation was controlled by an external control unit. The RDE is a hydrodynamic method involving forced convection. By rotating the disk electrode, the electrolyte is dragged along its surface and then pushed outward. Replenishing of the electrolyte, and the contained reactants, occurs normal to the surface limiting the diffusion layer thickness. Insight about the limiting conditions of the system can be gained by employing the Koutecký–Levich method<sup>86</sup>:

$$\frac{1}{i} = \frac{1}{i_K} + \frac{1}{i_{l,c}} = \frac{1}{i_K} + \frac{1}{0.62 * n * F * A * D^{2/3} * \omega^{1/2} * \nu^{-1/6} * C}$$

Where  $i$  is the measured current [A],  $i_K$  is the kinetically limited current [A], and  $i_{l,c}$  is the steady-state limiting current [A]. Furthermore,  $n$  is the number of transferred electrons,  $F$  is Faraday's constant [C mol<sup>-1</sup>],  $A$  is the electrode surface [cm<sup>2</sup>],  $D$  is the diffusion coefficient [cm<sup>2</sup> s<sup>-1</sup>],  $\omega$  is the angular rotation rate [rad/s],  $\nu$  the kinematic viscosity of the solution [cm<sup>2</sup> s<sup>-1</sup>], and  $C$  is the concentration of the reactant [mol]. By plotting  $1/i$  measured at different rotation speeds at a given potential versus  $\omega^{-1/2}$ , both the kinetically limited current and the average number of transferred electrons can be determined. Therefore, the method allows the deconvolution of the kinetic and mass-transport related contributions to the measured currents. The results of these analyses in the GOR are discussed in appended manuscript I.

For the dedicated glucose oxidation experiments, a three-step potential program<sup>87</sup> (**Fig. 2.1.1**) and constant rotation in an RDE-setup were applied. Such a potential program is necessary to clean the

surface by removing strongly chemisorbed species which would otherwise poison the catalytic surface. Small organic molecules, such as dissociation products in the GOR, have been found to be especially detrimental poisoning species<sup>88</sup>. Subsequent oxidation and reduction of the electrode remove the chemisorbed species restoring the surface.

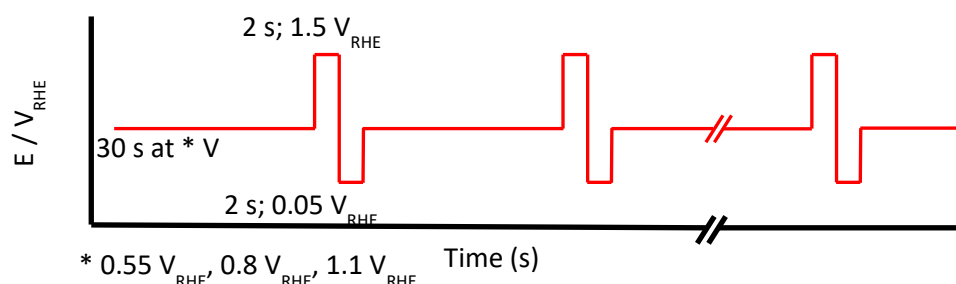


**Figure 2.1.1:** Applied three-step potential program for the GOR experiments. The step at  $1.5 V_{RHE}$  oxidizes the gold surface. The subsequent step at  $0.05 V_{RHE}$  reduces the surface again, and thereby also removes poisoning species. The three-step sequence was applied for 2h.

In appended manuscript IV, in collaboration with Kirsten Jensen's group at the university of Copenhagen, the oxygen evolution reaction (OER) activities of different  $(Ni_xFe_{1-x})OOH$ -samples were investigated in an RDE setup. Mass transport in OER is not a concern of reactant availability at the electrode surface as the electrolyte itself is the reactant. However, the controlled, reproducible forced convection provided by the RDE was used to remove evolved oxygen at the catalyst surface which otherwise would have blocked the surface. Hence, the use of the RDE setup made the individual experiments more reliable compared to measurements in the absence of rotation.

## 2.2 Product analysis by high-performance ion-chromatography (HPIC)

Due to the plethora of possible reaction products in the GOR (**Figure 2.2.1**), product analysis is paramount to understand the occurring reactions and to identify reaction pathways. Among analysis techniques, liquid chromatography (LC) has proven to be a capable method. Even though methods like nuclear magnetic resonance (NMR) spectroscopy<sup>89,90</sup> or mass spectrometry (MS)<sup>91</sup> can be used for product identification, they are employed less because of higher complexity.

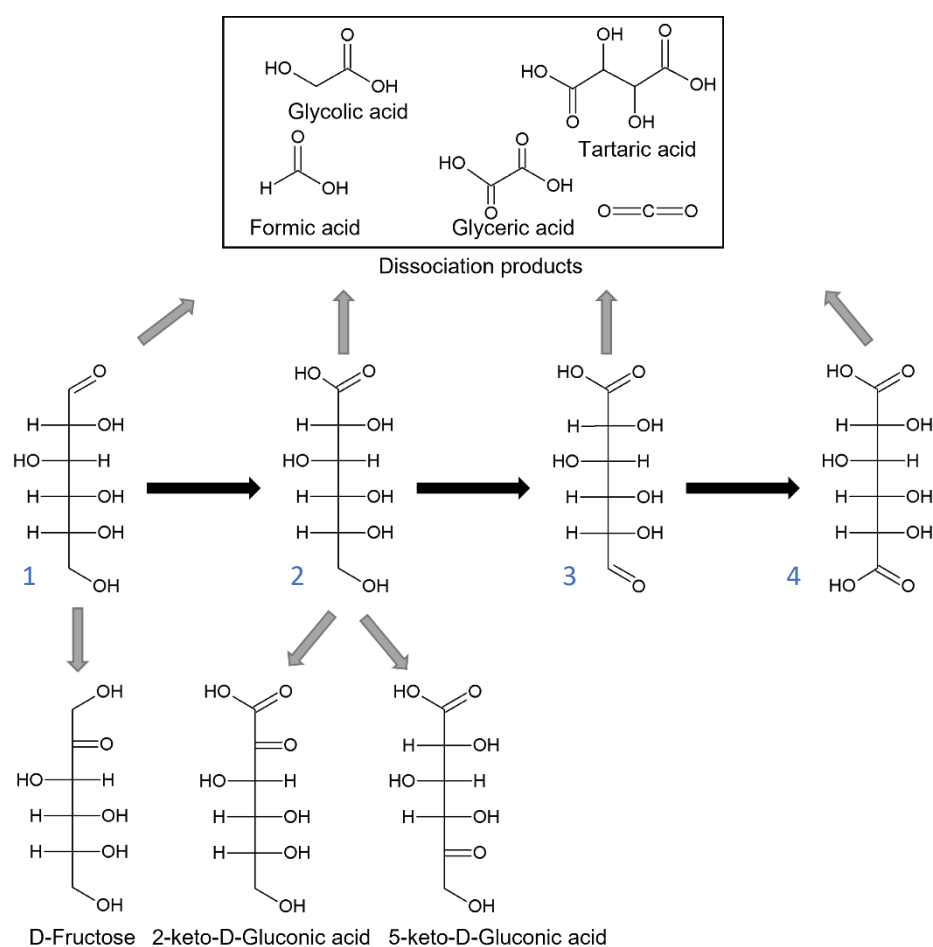


**Figure 2.2.1:** Reaction pathway from glucose (1) to glucaric acid (4) via gluconic acid (2) and glucuronic acid (3). Parts of the dissociation products which were tracked using the chromatographic method are depicted above the saccharic acids. D-fructose is formed through isomerization of glucose. The keto-gluconic acid species are formed through oxidation of non-terminal hydroxyl groups.

NMR lacks the sensitivity to analyze traces of products. MS is tricky to combine with electrochemistry and has fallen out of favor due to interferences of high salt concentrations in the electrolyte which can damage the instrument severely. Improvements introduced to two types of LC methods make them accessible for GOR product analysis. The more common method is high-performance-liquid-

## Employed methods and method development

chromatography (HPLC)<sup>92</sup>. Development of an HPLC method, using an X-Bridge BEH Amide column (Waters) and a charged aerosol detector (CAD), in collaboration with Paola Luciani's group from the DCBP of the University of Bern was tried for this thesis. Insufficient product separation was found due to eluent limitations dictated by the CAD's eluent tolerance. This particular detector does not tolerate any inorganic ions. Unfortunately, according to the manufacturer's specifications, the separation of the sugar acids using the employed column requires the use of sulfuric acid. The second liquid chromatography method is the high-performance-ion-chromatography (HPIC). HPIC was successfully employed for the studies in this thesis by developing a method satisfying the required product separation.

In this section experimental details are provided because HPIC is a technique that is not usually employed in the Arenz group. This chromatography technique requires, most of the time, analytes in ionic form - hence the name ion chromatography. Various detectors can be used for the analysis. One of most common detection method is conductivity detection (CD) which exploits the charged nature of the analytes. The conductivity detector registers deviations in eluent conductivity after separation of the analytes, thereby allowing product quantification. A more specialized detection method is the pulsed amperometric detection (PAD) which is used to quantify organic molecules. The PAD relies on current responses measured on a working electrode to quantify the compounds of interest. Usually a repeating three-step potential program is applied at the working electrode, similar to the program used in the GOR experiments outlined in section 2.1, **Figure 2.1.1**. The measured oxidation currents are then correlated to analyte concentrations. PAD is employed commercially in carbohydrate research where it is used to separate different sugars, such as mixtures of hexoses<sup>93,94</sup>. Separating sugar acids, like gluconic and glucuronic acid, is uncommon and therefore no commercial methods exist but it has been applied previously in glucose oxidation experiments<sup>38,95-98</sup>. For the product analysis in this thesis, both CD and PAD were used on separate chromatographic lines. Since products cannot be identified and quantified directly by the chosen detectors, the instrument must be calibrated for all components that are investigated.

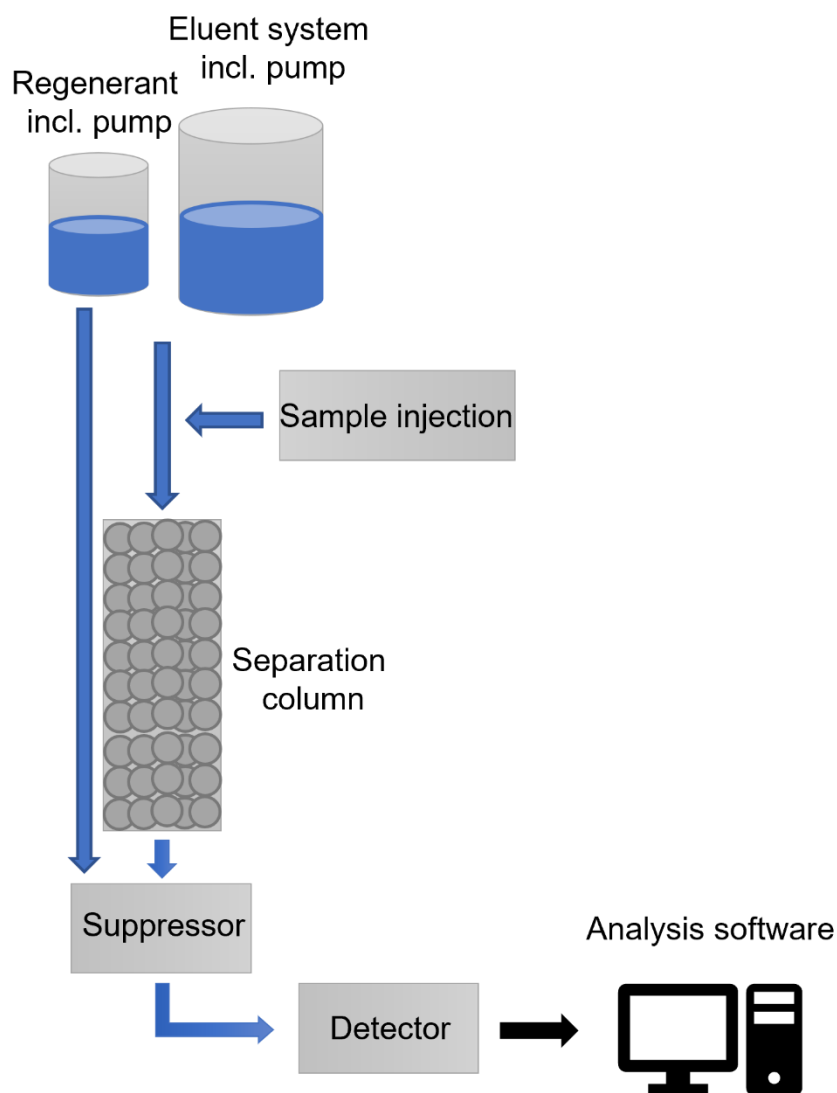


**Fig 2.2.2:** Schematic of a typical HPIC setup illustrating the most important systems in the instrument including the mobile phase (eluent) supply, the sample injection system, the stationary phase (separation column), the suppressor including a regenerant, the detector (CD or PAD), and the analysis system. Importantly, when PAD is chosen for detection a suppressor system is not needed and hence circumvented.

**Fig. 2.2.2** depicts a typical HPIC setup involving the crucial systems required to operate an LC-instrument. The product determination of the studies in this thesis were carried out on a 940 Professional IC Vario I (Metrohm) chromatograph in combination with an 889 IC Sample Center (Methrom). The devices were controlled by the MagIC Net 3.3 software (Methrom). Two separate chromatography lines were run. Both lines were operated in isocratic mode. One line was connected to a CD, the other connected to a PAD. The CD line was used to quantify the organic acids originating from glucose dissociation. Also, glucaric acid was quantified using the CD because it does not produce

## Employed methods and method development

a current response in the PAD (**Table 2.2.1 & Figure 2.2.3 b**)). The CD was operated using a 3 mM NaCO<sub>2</sub> eluent and a Metrosep A Supp 7 – (250/4.0, Metrohm) column heated to 45 °C at 0.7 ml/min. Glucose, gluconic and glucuronic acid were quantified using PAD (**Table 2.2.1 & Figure 2.2.3 a**)). The PAD includes a wall-jet cell equipped with an Au working electrode. The eluent consisted of 0.1 M sodium acetate and 0.11 M sodium hydroxide working with a Metrosep Carb 2 (250/4.0, Metrohm) column which was heated to 30 °C. The flow rate was 0.5 ml/min. Although the applied parameters diverge from the manufacturer's suggestions, it was found that the increased eluent concentration leads to improved retention times. Here, it is important to note that the PAD line is highly sensitive to parameter and setup changes. The continuous oxidation and reduction of the Au working electrode due to the applied repeating three-step potential program seemingly roughens it. This could explain the steady increase of background current which is observed after prolonged periods of use (> 1 month of regular use). Additionally, even though the eluent is stored in a closed container, a fraction of the water evaporates resulting in increased acetate and hydroxide concentrations. Both effects lead to increased current responses during product analysis because the response is a function of both the electrode area and the hydroxide concentration<sup>35</sup>. Thereby, the product concentration is overestimated. This problem can be addressed in multiple ways. First, the working electrode should be cleaned and polished regularly. Second, the eluent should be exchanged after 2 weeks of use. The amplitude of the background current can confirm if the calibrations can still be considered accurate. And third, the instrument should be calibrated regularly with freshly prepared standards. Importantly, the standards must be freshly prepared because also here aging and decomposition of the reference compounds occurs. Adhering to these protocols should minimize the errors in product quantification. Another source of errors is the handling of the samples before product analysis. The spontaneous glucose degradation distorts the product distribution because glucose is converted to product species, which were formed during the GOR experiment and can further degrade into dissociation compounds<sup>30</sup>. Therefore, once an experiment is finished, the collected aliquot is best diluted with ultrapure water (1:10) to reduce the solution's pH and then stored in the fridge until product analysis is performed. Both measures slow down degradation, but do not eliminate it. Hence, timely product analysis is necessary to ensure the accuracy of the product analysis.

Analyte CD	Retention time / min	Analyte PAD	Retention time / min
Gluconic acid	6.3	Glucose	6.65
Glucuronic acid	6.7	Gluconic acid	14.4
Formic acid	8.1	Glucuronic acid	30.2
Glucaric acid	28.1		
Tartaric acid	31		
Glycolic acid	34		

**Table 2.2.1:** Retention times of the oxidation products in the conductivity line (left table) and pulsed amperometry line (right table).

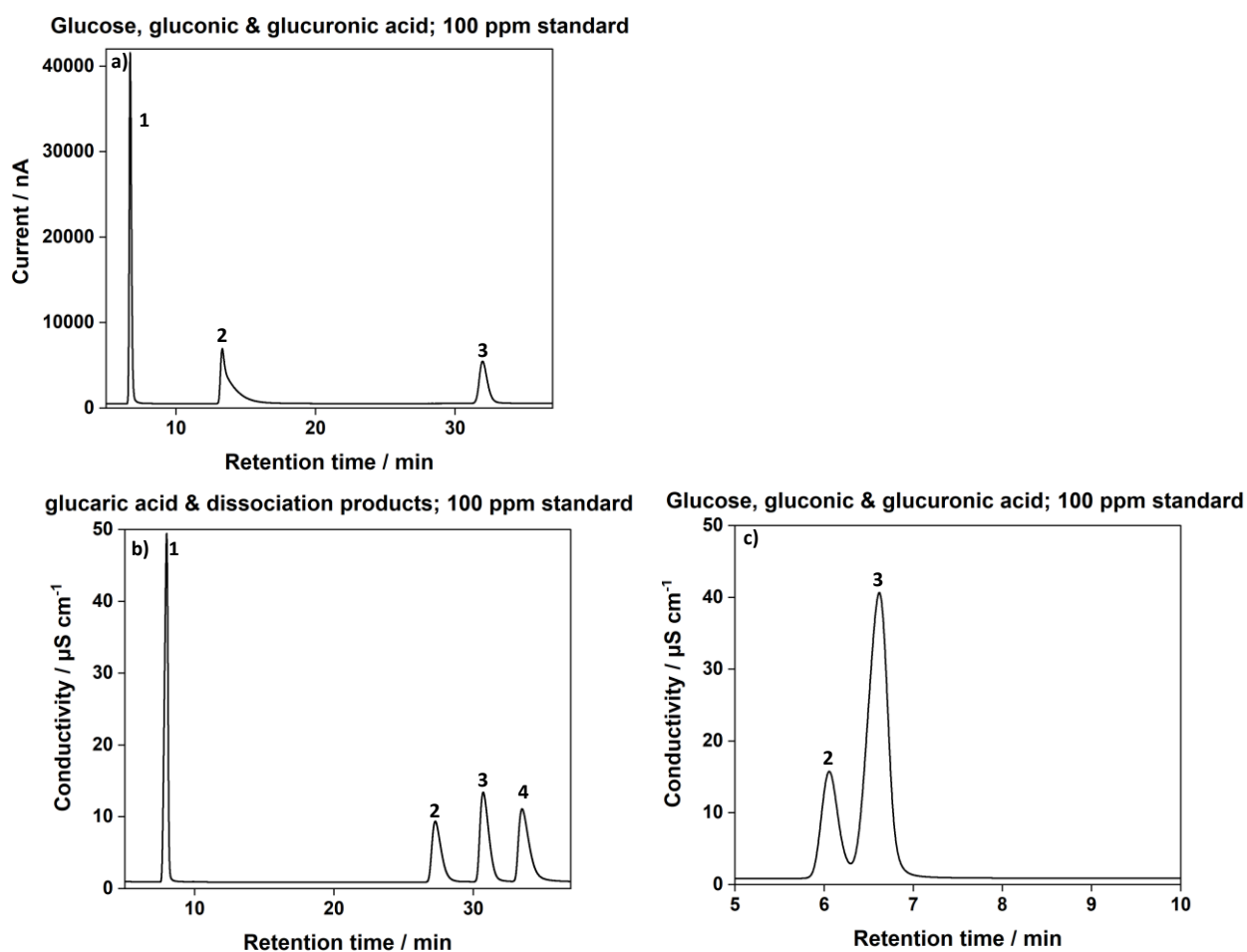


**Figure 2.2.3:** Chromatograms of mixtures of 100 ppm standards in: a) PAD line: glucose (1), gluconic acid (2), and glucuronic acid (3); b) the CD line: formic acid (1), glucaric acid (2), tartaric acid (3), and glycolic acid (4); c) the CD line: gluconic acid (2), and glucuronic acid (3). Glucose is undetectable under the operational conditions in the CD.

In the PAD line the current response to the same analyte concentration is very different (**Figure 2.2.3 a)**). Glucose leads to a much larger peak current response than gluconic acid and glucuronic acid. This

is expected because the species interact differently with the working electrode. The interaction is dictated by the applied current program and the kinetics of the analyte oxidation on the Au electrode. Also, the peak shape varies because the used column that was designed to separate primarily sugars and not sugar acids, such as gluconic and glucuronic. As long as the peak shape is consistent, however, the calibration and subsequent analyses are sufficiently accurate. In the CD line (**Figure 2.2.3 b**), the dissociation products and the glucaric acid are clearly separated, in contrast to gluconic acid and glucuronic acid (**Figure 2.2.3 c**). Especially when the analytes are present at very different concentrations the peak integration becomes inaccurate.

From the product concentrations determined by the IC, the Faradaic efficiencies (FE) towards the individual products can be calculated according to **Equation 2.2.1**:

$$FE_i = \frac{Q_i}{Q_{tot}} * 100 = \frac{ppm_i * Z * V * F}{Q_{tot} * 10^3 * M_i} \quad (2.2.1)$$

$Q_i$  is the partial charge of the compound,  $Q_{tot}$  the total charge transferred during the experiment,  $ppm_i$  the concentration in [g/ml] of compound  $i$  determined by HPIC,  $Z$  the number of electrons involved in the electrode reaction,  $V$  the volume of the electrolyte [l],  $F$  Faraday's constant [C/mol], and  $M_i$  the molar mass [g/mol] of compound  $i$ . Note that FE towards dissociation products cannot be determined because the number of electrons involved in the dissociation,  $Z$ , is not known.

Both analysis methods could be improved further by upgrading the chromatograph with eluent supply systems that enable gradient elution. Thereby, the mobile phase could be changed during a determination resulting in better resolution and shorter retention times. The product analysis could also be expanded in the future to include more GOR products. In the presented method only a fraction of possible dissociation products (**Figure 2.2.1**) is tracked. A more comprehensive list of possible dissociation and isomerization products can be found in the following sources<sup>12,89,99</sup>. Based on the employed columns no apparent reason exists why other organic acids originating from glucose dissociation and isomerization could not be identified. Additionally, keto-gluconic acid species should also be distinguishable. In the presented thesis, however, as gluconic, glucuronic and glucaric acid are of foremost interest, their quantification is most important. The detection of dissociation products serves mainly to validate the accuracy of the product analysis and to exemplary show that dissociation takes place. Hence, the developed method satisfies the required expectation. Lastly, CO<sub>2</sub> as a GOR product would be very tricky to analyze by any technique because it is converted to carbonate species in the alkaline electrolyte. The thereby formed carbonate cannot be distinguished from carbonate originating from the atmosphere.



### 2.3 *In-situ* Raman spectroscopy

Raman spectroscopy exploits inelastic scattering of photons. Light from a monochromatic source interacts with vibrational modes of the illuminated molecules. Thereby, information about structures and adsorbates can be acquired<sup>100</sup>.

*In-situ* Raman spectroscopy measurements during GOR experiments were carried out in a custom-built KEL-F electrochemical cell (**Figure 2.3.1**). A three electrode-setup was used: A flat, polycrystalline Au bead as the working electrode (WE), a coiled Pt wire as the counter electrode (CE), and a leakless Ag|AgCl (eDAQ) reference electrode (RE). A detailed description of cell preparation can be found in manuscript I. The applied potential at the WE was linearly changed over time (linear sweep voltammetry) using a scan rate of 7 mV/s in glucose containing electrolytes. Raman spectra were acquired continuously with acquisition times of one second.

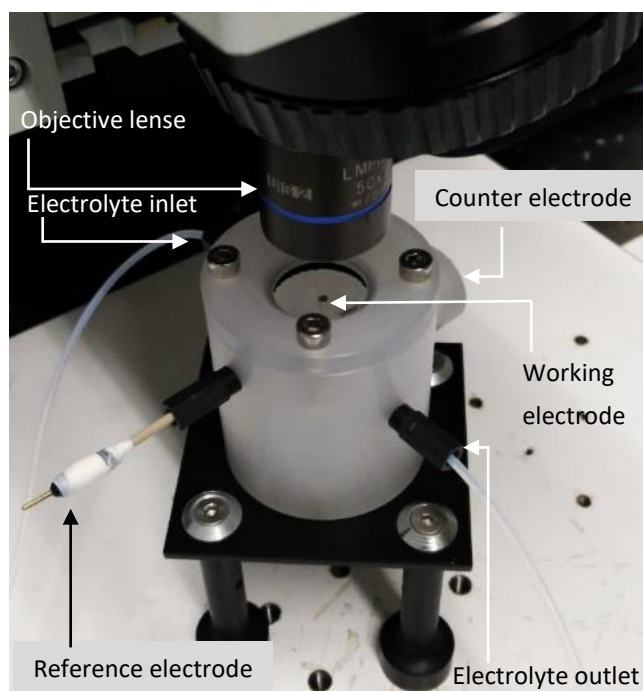


**Figure 2.3.1:** Picture of the assembled Raman cell under the utilized objective lens. Taken from ref<sup>101</sup> with approval of the authors.

Initially it was planned to investigate surface species forming during GOR to possibly determine reaction intermediates and adsorbents before the oxidation of the Au surface. However, this was unsuccessful due to the species' low Raman cross section. On the other hand, the oxidation of the gold surface could be tracked by the intensity of the acquired background signal. To analyze the background signal more quantitatively, in every acquired spectrum a range without any distinguishable Raman peaks was averaged, see **Figure 2.3.2**. These averages could then be plotted as a function of potential

unveiling spectroscopic insight into the oxidation of the Au-bead WE. A more detailed discussion of the analysis is found in the appended manuscript I.

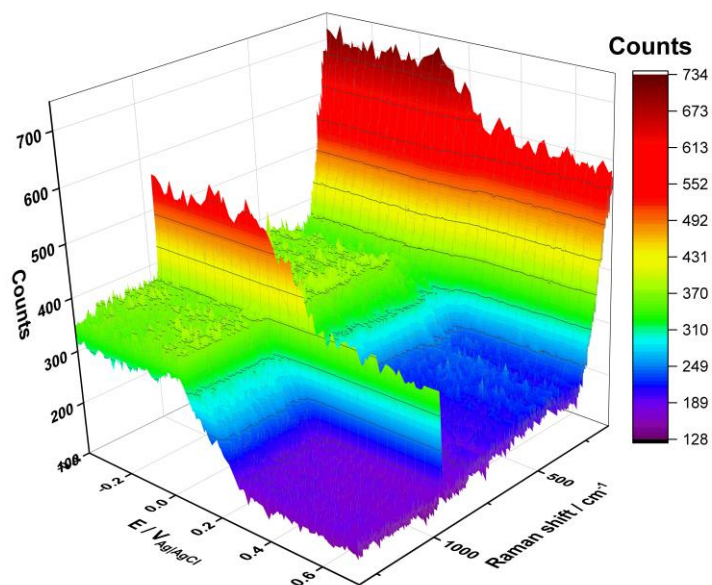


**Figure 2.3.2:** Color map plot of consecutive Raman spectra acquired during a linear sweep voltammogram of the Au bead in 0.1 M NaOH and 0.1 M Na<sub>2</sub>SO<sub>4</sub> electrolyte with a 10 mM glucose concentration. Plotting the intensity versus the WE potential shows the dependence of the background intensity on the electrode potential. In the region between 300 and 1200 cm<sup>-1</sup> the only distinguishable peak is found at 980 cm<sup>-1</sup> corresponding to the symmetric stretching of the sulfate ion<sup>102</sup>.

## 2.4 Characterization of synthesized HEA-NP

Different analysis techniques were employed to characterize synthesized HEA-NP. This section is concerned with the type of information gained from a specific technique. The theory of those techniques will not be discussed in detail.

The definition of the structural composition of a HEA, especially in nanosized structures, is still subject of debate. Therefore, in this thesis it was defined that a synthesized sample is considered a HEA if only one apparent crystal phase is visible in the diffraction pattern (XRD) and the elements are distributed throughout the entire sample determined by energy dispersive X-ray (EDX) analysis.

### 2.4.1 Powder X-ray diffraction (PXRD)

When performing PXRD, the analyzed sample is exposed to X-ray radiation. Part of the radiation reaching the samples is diffracted by the atoms in the sample. In periodic structures, such as crystals, positive interference is possible within periodic planes of the sample. Thereby, the crystal structure can be determined from the specific interferences and the resulting diffraction pattern. The lattice parameters can be obtained from the peak position, while peak broadness gives insight about crystallite size and microstrain within the lattice<sup>103</sup>. Due to the relatively larger wavelength (Cu K $\alpha$  in this thesis) of laboratory X-ray sources their use to perform PXRD to investigate HEA-NP is limited. The presence of distinct crystal phases and their attribution to crystal structures is still possible based on peak symmetry.

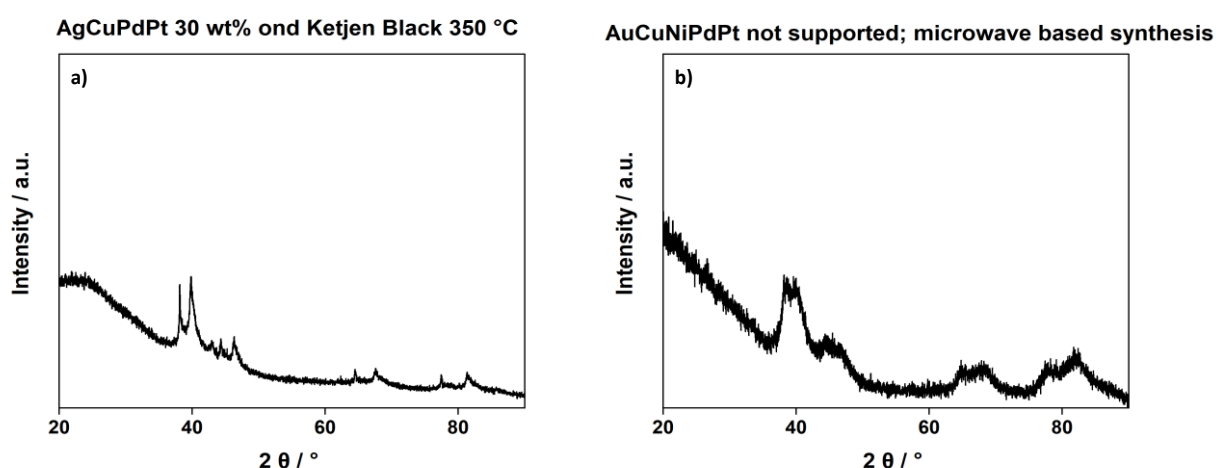


**Figure 2.4.1:** Exemplary diffractograms of multimetallic NP both exhibiting more than a single metallic phase: a) AgCuPdPt 30 wt% on Ketjen Black EC-300 J synthesized via IWI; b) unsupported AuCuNiPdPt-NP synthesized via a microwave approach. In a) too many reflections are observed while in b) the peaks are split indicating the presence of multiple distinct fcc phases. The diffractograms were recorded on a STOE StadiP diffractometer equipped with a Mythen1K detector in Debye-Scherrer geometry.

The diffractograms depicted in **Figure 2.4.1** exemplary show multimetallic samples in which the patterns do not match the pattern of one single space group indicating the presence of multiple phases. In addition to the peak position, the peak width can also be determined in patterns obtained from the in-house STOE StadiP diffractometer. However, the peak broadness is quite deceitful. Additional lattice strain has to be expected in HEA NP<sup>104</sup> not only due to their nanoscopic size but also their high-entropy state. This leads to an additional broadening of the peak resulting in underestimation of the crystallite size for example when applying Scherrer's equation<sup>84</sup>. An additional challenge in the PXRD analysis of the synthesized HEA samples via incipient wetness impregnation approach, outlined in section 2.5, is the presence of the amorphous carbon support. HEA samples synthesized by the IWI approach with a loading below 40 wt% could not be analyzed likely due to the presence of too much amorphous material (**Figure 2.4.2 a**). In this instance, the additional strain, and possibly also smaller crystallites, in HEA-NPs becomes apparent as a Pt/C sample with 30 wt% loading is easily resolved in the in-house PXRD (**Figure 2.4.2 b**).

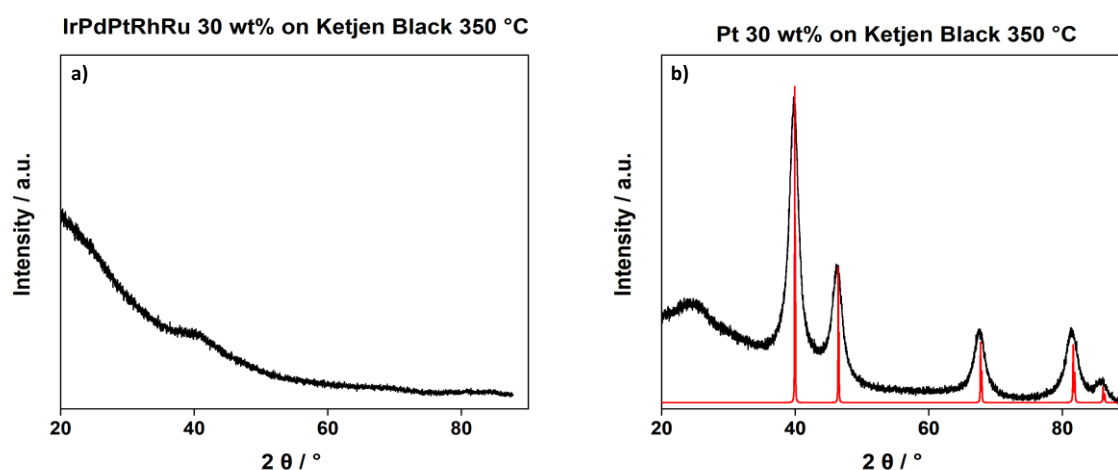


**Figure 2.4.2:** Exemplary diffractograms of samples with 30 wt% metal loading on Ketjen Black: a) a HEA sample containing IrPdPtRhRu; b) a monometallic sample containing only Pt. The red trace in b) corresponds to a Pt-fcc reference<sup>105</sup>. The diffractograms were recorded on a STOE StadiP diffractometer equipped with a Mythen1K detector in Debye-Scherrer geometry.

PXRD data gathered at ESRF (synchrotron X-ray) could be analyzed by the Rietveld refinement method<sup>106</sup>. All sample parameters extracted from refined patterns presented in this thesis were done using GSAS-II.<sup>107</sup> This refinement method fits a calculated profile to the experimentally acquired diffractograms. Many parameters can be fit, including amongst others, lattice parameters, crystallite size, strain, atomic fraction, and phase fraction in multiphase samples. Importantly, reasonable assumptions must be made for the method to return physically feasible refined parameters. Here,

## Employed methods and method development

covariance of certain parameters is an important factor. The refinement is simplified by limiting or not refining certain parameters based on insight about the sample gained from other techniques. For example, *in-situ* XANES and *ex-situ* EDX analysis were used to determine the atomic fraction in the sample for the analysis of the PXRD of the PtFeCoNiPd synthesis (see appended manuscript III).

### **2.4.2 X-ray absorption near edge spectroscopy (XANES)**

XANES exploits the absorption of X-ray photons in the core electrons of a material. The distinct core-electron binding energies of different elements allow the elemental distinction and identification using XANES<sup>108</sup>. Among a plethora of information, the edge structure gives insight into the oxidation state of the investigated elements. Combining XANES and PXRD at ESRF is ideal to investigate the synthesis of HEA-NP. Appended manuscript III utilizes this technique. Importantly, the analysis of the metal oxidation state and the ratio of reduced and oxidized species was used as input in the Rietveld refinements mentioned in section 2.4.1 on PXRD.

### **2.4.3 Energy dispersive X-ray spectroscopy (EDX)**

For this technique, the analyzed sample is exposed to an electron beam. The sample dissipates a portion of the absorbed energy by ejecting core-shell electrons. An electron of a higher energy level fills the hole created by ejection. The difference in energy levels is released in the form of an X-ray photon. Since the energy levels are element specific, EDX analysis can distinguish elements<sup>109</sup>. In the case of HEA analysis, the atomic fraction of elements and the elemental distribution throughout the sample is the most important information to gain from EDX.

## 2.5 Synthesis of HEA-NP by incipient wetness impregnation (IWI) method

To synthesize supported HEA-NP, an incipient wetness impregnation approach was pursued. The goal was to synthesize particles with a single metallic phase of approximately 5 to 7 nm with a loading of 60 weight percent (wt%) on carbon black powder (**Equation 2.5.1**). For NPs of this size, the number of formed crystal phases can still be analyzed adequately by powder diffraction using a laboratory X-ray source, while also being interesting for catalysis applications. Additionally, the high loading ensures that enough scattering material is present and that the amorphous carbon does not dominate the diffraction measurement.

$$wt\% = \frac{m(\text{metals})}{m(\text{metals}+\text{support})} * 100 \quad (2.5.1)$$

Incipient wetness impregnation has the advantage of being a simple and straight-forward synthesis approach. It has been used to synthesize a wide variety of different monometallic and multimetallic nanoparticles on different support materials<sup>110,111</sup>. The metal precursor is dissolved in a specific volume of solvent which is calculated based on the pore volume of the utilized support. Then, the support is impregnated with the precursor solution and subsequently left to rest. Afterwards, the impregnated support is dried in an evacuable muffle oven and finally reduced in a tube furnace under reducing atmosphere. The individual steps are depicted schematically in **Figure 2.5.1**. Depending on the exact synthesis recipe, the individual steps can vary, e.g., various solvents can be used, or the duration of the steps can change. For the synthesis of the HEA-NP the recipe was adjusted to cater to the set goals. First, the precursor salts were dissolved in the solvent which was ultrapure water. Chlorides were the precursors of choice because of their relatively high solubility in water and the availability of platinum group metal (PGM) chlorides. The volume of the solvent was calculated based on the carbon support's pore volume. Ketjen Black EC300-J was preferably employed over Vulcan XC 72R as support owing to its higher specific pore volume. For catalyst loadings larger than 30 wt% the pore volume becomes very small because less support is used in comparison to the amount of metal precursor. Therefore, an increased solvent volume, as compared to the support pore volume, was used. Different solvent volumes were tested to determine the specific volume employed in the different syntheses. It was found experimentally that 210 % of the calculated pore volume is a good starting point. The limiting factors of the solvent volume were the precursor solubility on one hand and the apparent wetness of the support after impregnation on the other hand. In terms of solubility, all the precursor salts have to be dissolved in the solvent without forming any precipitate. The impregnation was deemed successful when all of the support clumped together and was visibly wet. A sample was considered too wet when a support-slurry was formed resulting in recrystallization of precursor salt on the vial walls after drying in the muffle oven. After impregnation, the samples were rested for 24 h in the absence of light to

prevent any possible light-induced metal reduction. Then, the samples were dried in an evacuated (< 100 mbar) oven at 100 °C for another 24 h. Once dry, the samples were transferred into ceramic boats in which they were reduced in a tube furnace. The standard temperature program included a ramp of 100 °C/h to a temperature of 350 °C where the samples were held for an additional hour. Finally, the sample was left in the oven to cool down to approximately 50 °C. While in the tube furnace, the sample was constantly flushed with 2.5 % H<sub>2</sub> in argon. For loadings larger than 40 wt%, the carbon supports were impregnated twice, doubling the solvent volume again (e.g., two times 210 %). Therefore in a first impregnation step only half of the precursor solution was impregnated onto the support. After resting and drying as described above, the second impregnation step with the remaining half of the precursor solution was performed. Subsequently, the sample was again rested, dried, and finally reduced in the tube furnace. Particle size control was achieved by tuning the metal loading and the reduction temperature. Larger particle sizes were reached with higher weight loadings (up to 70 wt%) or increased reduction temperatures (500 °C), see appended manuscript III. The IWI synthesis approach was chosen as a high-entropy state present in the precursor solution could be preserved during drying of the solution. This, in theory, leads to a random distribution of the precursor metal salts on the carbon support. In combination with the limited mobility of the immobilized salts during the reduction, the formation of a high entropy alloy should be encouraged.

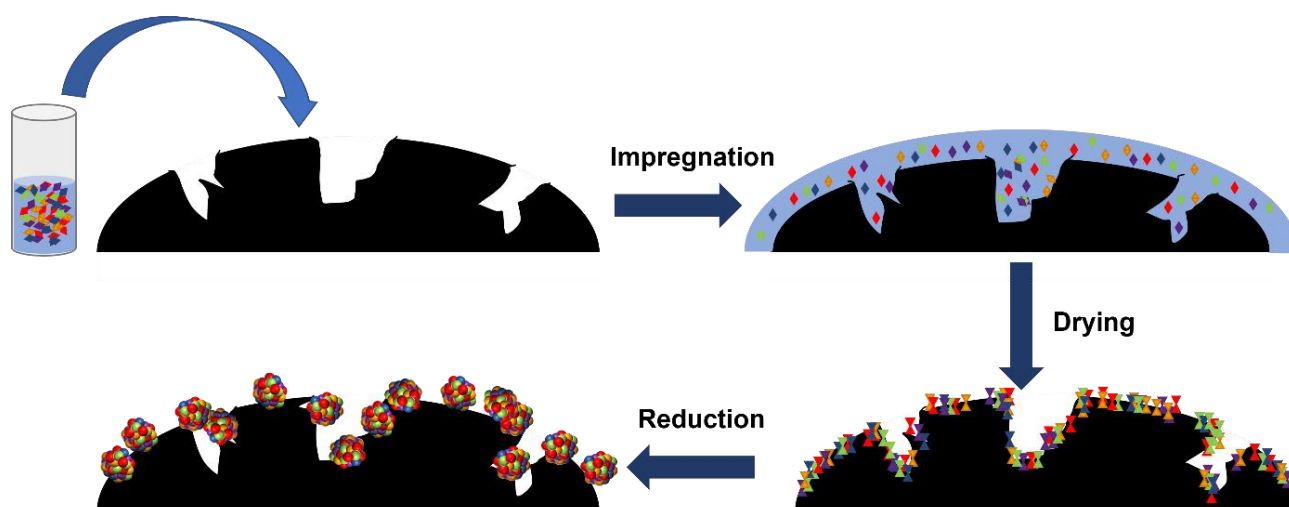


**Figure 2.5.1:** Schematic illustration of the individual synthesis steps to form HEA-NP via an incipient wetness impregnation approach. Each color represents a different element.

In terms of compositions, two HEA systems were successfully synthesized. First, an equimolar PtFeCoNiPd alloy system comprised of precious and non-precious metals intended for the use in the oxygen reduction reaction (ORR) was prepared (**Figure 2.5.2 a**). The formation of this PtFeCoNiPd alloy, as well as a bimetallic PtFe, trimetallic PtFeCo, and quaternary sample PtFeCoNi, was investigated *in-situ* at the ESRF (see appended manuscript III). Second, a PGM system of IrPdPtRhRu was synthesized (**Figure 2.4.2 b**). Collaborators from Jan Rosmeissl's group at the University of Copenhagen

investigated IrPdPtRhRu as a model material by DFT calculation to be potentially used in ORR or HER. In this alloy the elemental fractions can be deviated from equimolar conditions while still resulting in a HEA. Here, the PXRD and EDX analysis for two samples of the mentioned compositions are briefly discussed to outline the process of deduce the success of a synthesis.

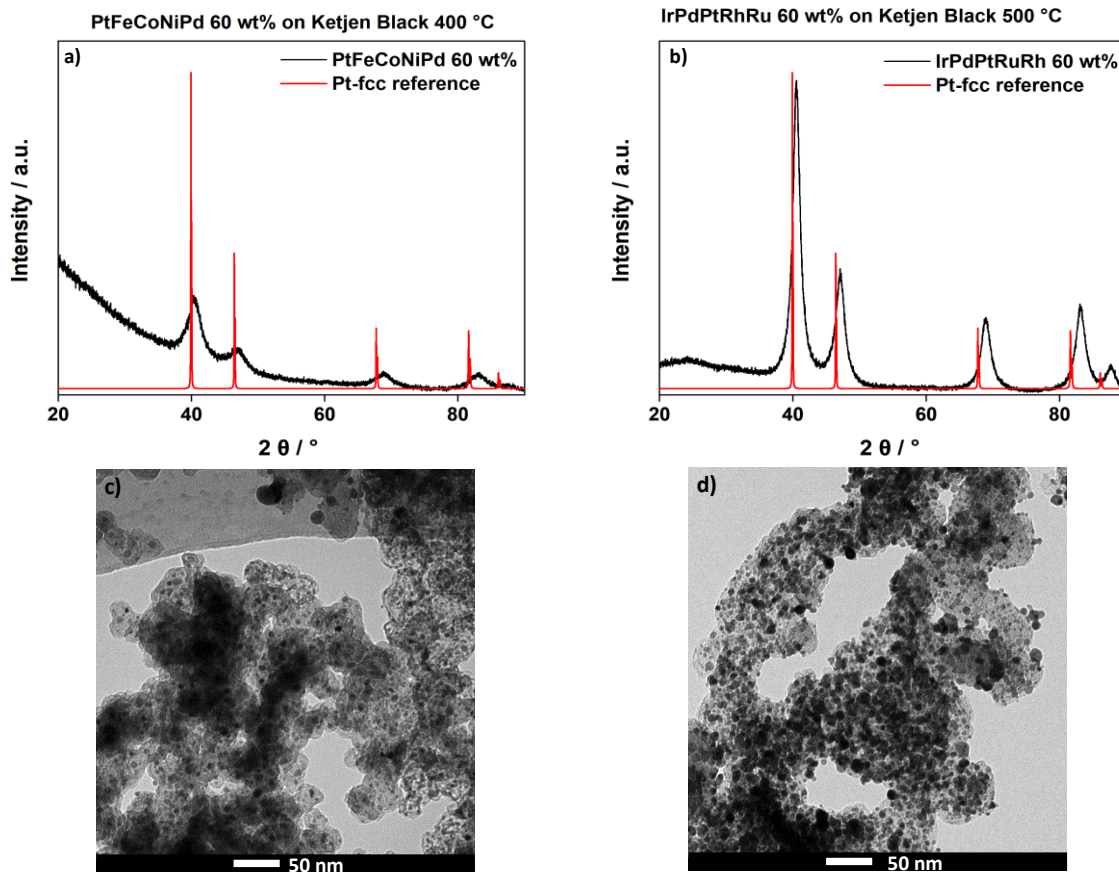


**Figure 2.5.2:** Exemplary diffractograms of the two equimolar single-phase HEA system synthesis via IWI approach: a) PtFeCoNiPd 60wt% on Ketjen Black EC-300 J reduced at 400 °C; b) IrPdPtRhRu 60 wt% on Ketjen Black EC-300 J reduced at 500 °C. The Pt-fcc reference<sup>105</sup> (red line) illustrates the fcc-fingerprint. The diffractograms were recorded on a STOE StadiP diffractometer equipped with a Mythen1K detector in Debye-Scherrer geometry. Exemplary TEM micrographs of sample PtFeCoNiPd 60wt%, c), and IrPdPtRhRu 60 wt%, d), underneath their respective diffractograms. The micrographs were recorded on a Tecnai Spirit microscope using a tungsten filament operated at 80 kV.



Statistic / atomic %	Fe	Co	Ni	Pd	Pt
<b>Max</b>	26.94	25.69	12.37	21.85	20.81
<b>Min</b>	24.12	23.98	10.34	17.01	16.65
<b>Average</b>	<b>25.72</b>	<b>24.83</b>	<b>11.43</b>	<b>19.84</b>	<b>18.18</b>
<b>Standard deviation</b>	0.80	0.60	0.59	1.39	1.25

**Table 2.5.1:** EDX analysis corresponding to the PtFeCoNiPd 60wt% sample showing the average atomic percentages and their standard deviations. The average contains data from 10 spectra recorded on the sample. The EDX analysis was conducted on a Zeiss GeminiSEM 450 operated by SmartbSEM 6.05 software, and an EDS Photodetector Ultim max 65 from Oxford Instruments. Data analysis was conducted by AZTec 5.0 software.

Analysis of the elemental composition by EDX reveals that for the synthesized PtFeCoNiPd 60 wt% sample the elements are not present equimolarly, even though precursors were employed in equimolar ratio. Fe and Co preponderate while Ni is underrepresented. Nonetheless, based on the diffraction pattern shown in **Figure 2.5.2 a)**, a HEA was still formed. And based on the standard deviation of the EDX analysis, it can be concluded that the elements are distributed evenly. Therefore, combining the PXRD and EDX analysis, the synthesis was deemed successful. Also, the elemental ratio in the product can still be tuned by increasing the precursor ratio if deemed necessary.

A similar picture presents itself in the case of the IrPdPtRhRu 60 wt% where the elements are also not present in an equimolar ratio (**Table 2.5.2**). In this case, Ru is overrepresented heavily while Pd is only present at 5 atomic %. Still, because the PXRD shows one apparent phase and since the elements are present throughout the entire sample, the synthesis was deemed successful.

Statistic / atomic %	Ru	Rh	Pd	Ir	Pt
<b>Max</b>	33.49	22.93	6.53	23.61	30.51
<b>Min</b>	21.36	15.83	4.09	19.61	21.26
<b>Average</b>	<b>28.51</b>	<b>20.44</b>	<b>4.99</b>	<b>21.55</b>	<b>24.52</b>
<b>Standard deviation</b>	3.29	1.85	0.65	1.39	2.45

**Table 2.5.2:** EDX analysis corresponding to the IrPdPtRhRu 60wt% sample showing the average atomic percentages and their standard deviations. The average contains data from 10 spectra recorded on the sample. The EDX analysis was conducted on a Zeiss GeminiSEM 450 operated by SmartbSEM 6.05 software, and an EDS Photodetector Ultim max 65 from Oxford Instruments. Data analysis was conducted by AZTec 5.0 software.

Synthesis of Au-containing HEA by IWI were also pursued as prospect catalysts for GOR. Even though there are reports on gold particles formed through a simple IWI approach<sup>112</sup>, the synthesis of a HEA via IWI approach with Au as a constituent element remained unsuccessful in this thesis. The Au was found to reduce during the drying step leading to the formation of large gold crystallites prior to the planned thermal reduction step (**Figure 2.4.3 a**). After the thermal reduction, the Au was still segregated in a solitary phase. In contrast the other metals apparently formed a multi-metallic phase visible as the broad peak at  $40^\circ 2\theta$  (**Figure 2.4.3 b**).

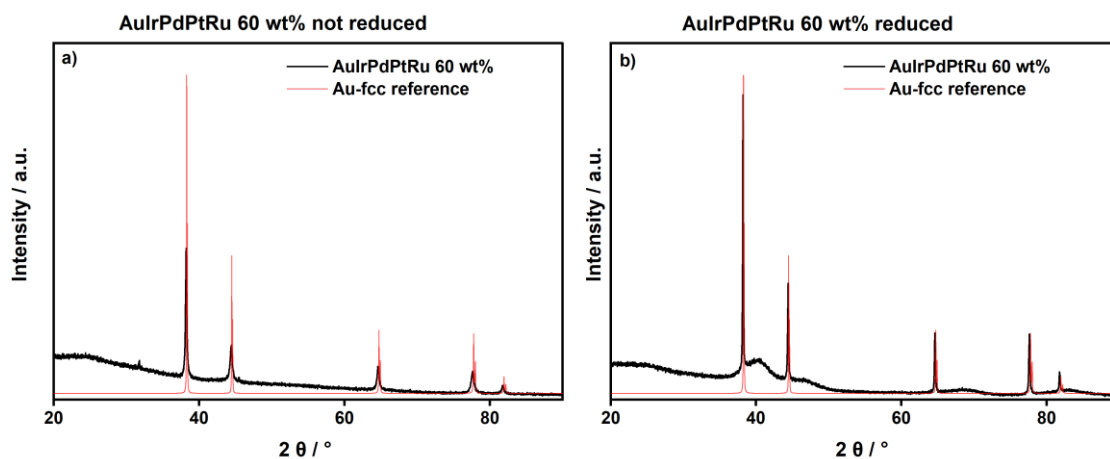


**Figure 2.5.3:** Diffractograms of IWI samples containing the constituent elements Au, Ir, Pd, Pt, and Ru in equimolar amounts with 60 wt% loading on Ketjen Black EC-300 J: a) after the second drying step; b) after the reduction under  $H_2$ -atmosphere. The Au-fcc reference<sup>113</sup> suggests that the Au is segregated forming a solitary phase.

### **3 Discussion of appended manuscripts**

This chapter discusses the manuscripts, that have been published or are in the process of being published in peer reviewed journals, based on work done as part of this PhD thesis. The most relevant findings are highlighted and my contribution to the work is outlined.

#### **3.1 Manuscript I: On the electrooxidation of glucose on gold: Towards an electrochemical glucaric acid production as value-added chemical**

##### **3.1.1 Abstract**

The electrocatalytic oxidation of glucose to value-added chemicals, such as glucaric acid, has gathered increased interest in recent years. Glucose oxidation is a promising process which has the potential to contribute to establishing renewable resources as alternatives to fossil carbon sources. Herein, we present rotating disk electrode (RDE) studies on polycrystalline gold surfaces and subsequent Koutecký-Levich analysis as a benchmark to expand the understanding of reaction kinetics and competition between glucose, reaction intermediates and OH<sup>-</sup> at the catalyst surface. Based on the obtained results it follows that the glucose oxidation reaction (GOR) is predominately mass-transport controlled. Combining electrochemical studies and Raman spectroscopy, it is shown that increasing glucose concentrations lead to a delayed oxidation of the gold catalyst surface, presumably by increased consumption rates of Au-hydroxide species.

##### **3.1.2 Contribution to the work**

For this publication I performed the entire experimental work including the electrochemical measurements and the Raman spectroscopy. The data analysis was done by me with the support of Gustav Wiberg and two developed extensions of his EC4™VIEW software. Matthias Arenz supervised the work. Both Gustav Wiberg and Matthias Arenz amended and edited the manuscript draft I wrote.

### 3.1.3 Most relevant findings

This study focuses on the influence of forced convection on the GOR. Therefore, cyclic voltammograms were recorded with glucose or gluconic acid dissolved in the electrolyte. Varying rotation speeds were applied to gain insight into the kinetics of the respective oxidation reactions.

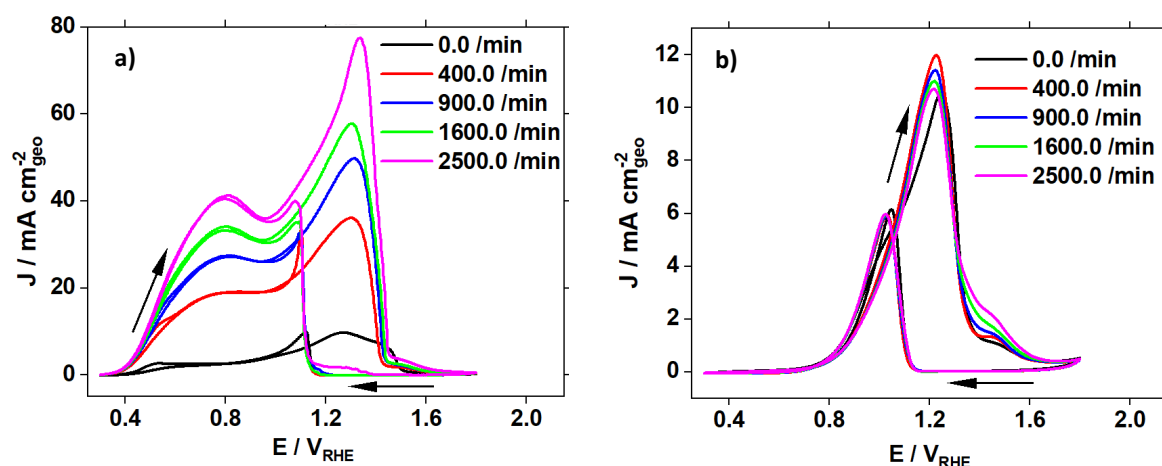


**Figure 3.1.1:** Cyclic voltammograms ( $50 \text{ mVs}^{-1}$ ) on an Au-disk at different rotation speeds recorded in  $0.1 \text{ M NaOH}$  and  $0.1 \text{ NaSO}_4$ : electrolyte containing a)  $50 \text{ mM}$  glucose and b)  $50 \text{ mM}$  gluconic acid. Reprinted with permission of the authors of ref<sup>101</sup>.

Cyclic voltammograms of an Au-disk were recorded in electrolytes containing  $50 \text{ mM}$  of glucose (**Figure 3.1.1 a**) or  $50 \text{ mM}$  of gluconic acid (**Figure 3.1.1 b**). Based on the current response in **Figure 3.1.1 a**) it was concluded that glucose oxidation on gold under the applied conditions is mixed kinetic mass-transport controlled. Therefore, mass transport plays an important role in glucose oxidation. It follows that for the design of future electrochemical setups mass-transport aspects must be taken into account to enable efficient glucose oxidation to high-value products. Forced convection should be applied, e.g., in the form of electrolyte stirring or using a flow cell setup. In contrast, as seen in **Figure 3.1.1 b**), the current response in the presence of gluconic acid does not change systematically with the applied rotation speed. Hence, it was concluded that the oxidation of gluconic acid on gold Au is kinetically limited. This conclusion has several implications for the product-oriented glucose oxidation. First, at mild conditions (oxidation potentials lower than  $0.7 \text{ V}_{\text{RHE}}$ ) the oxidation of glucose can be expected to stop at gluconic acid. Second, if glucaric acid is the target product of the glucose oxidation, the rate-limiting step on an Au electrode will likely be the oxidation of gluconic acid. Catalyst and setup design therefore should be focused on improving the efficiency of gluconic acid oxidation.

The performed RDE studies were analyzed in more detail by applying the Koutecký-Levich method (briefly discussed in section 2.1). Key parameters which can be extracted from this analysis are the number of transferred electrons and the kinetically limited current. The method could only be applied

to the glucose oxidation because only here the current response changed as a function of rotation speed.

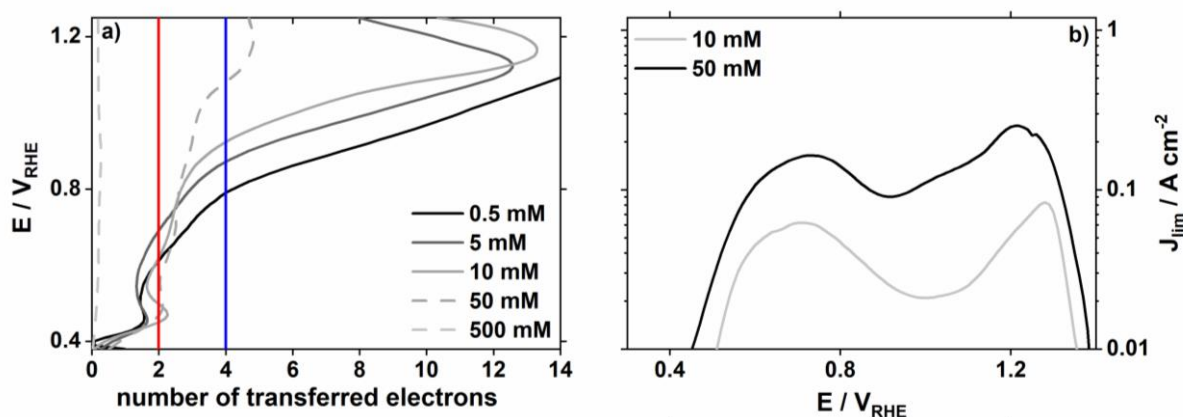


**Figure 3.1.2:** Koutecký-Levich analysis of RDE-measurement on an Au-disc in 0.1 M  $\text{Na}_2\text{SO}_4$  and 0.1 M NaOH in different concentrations of glucose: a) numbers of transferred electrons; b) kinetically limited current. Reprinted with permission of the authors of ref<sup>101</sup>.

The application of the Koutecký-Levich analysis, shown in **Figure 3.1.2**, indicates that the number of electrons transferred during cycling depends on the applied potential as well as the glucose concentration itself. In 0.1 M NaOH at electrode potentials below  $0.8 V_{RHE}$ , the number of transferred electrons lies within the range (1-4  $e^-$ ) where gluconic and glucaric acid are reasonable oxidation products. At electrode potentials larger than  $0.8 V_{RHE}$ , the number of transferred electrons increases drastically, especially at small glucose concentrations. If more than 6  $e^-$  are transferred, the glucose molecule is oxidized further than glucaric acid. An exception is the measurement conducted with a 500 mM glucose concentration where it seems that the number of transferred electrons is not influenced by the applied potential. Hence, the ratio of  $\text{OH}^-$  to glucose molecules is an important factor to consider when optimizing the reaction conditions during GOR: If the  $\text{OH}^-$  concentration far exceeds the glucose concentration, the glucose is oxidized too far. In contrast, if the glucose concentration exceeds the  $\text{OH}^-$  concentration, most molecules are not oxidized at all making the setup inefficient.

In terms of kinetically limited currents (**Figure 3.1.2 b**), the analysis shows that the oxidation of glucose is severely limited by mass-transport. Even at the highest applied rotation speed (pink line in **Figure 3.1.1 a**) the measured currents are still considerably lower than the kinetic limit determined in **Figure 3.1.2 b**). Comparing the kinetically limited currents in 0.1 M NaOH and 10 mM or 50 mM glucose concentration reveals glucose scarcity at the interface determines the kinetically limited current.

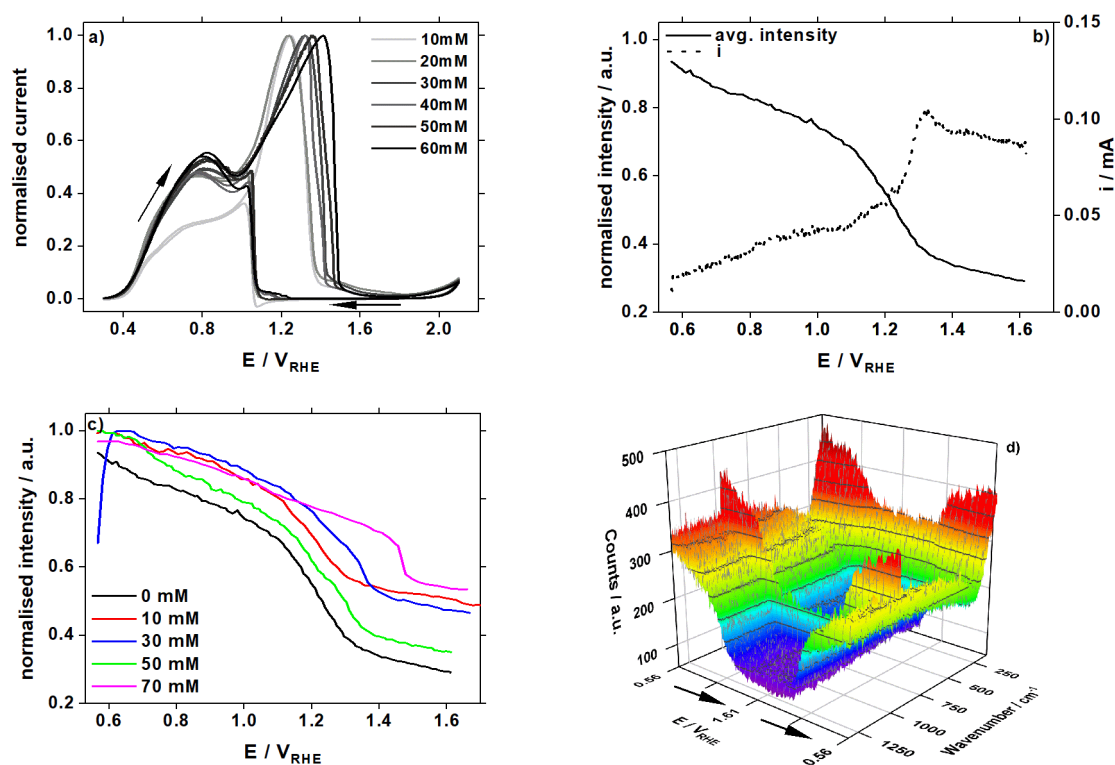


**Figure 3.1.3:** a) 10-60 mM glucose concentration in 0.1 M NaOH and 0.1 M Na<sub>2</sub>SO<sub>4</sub> at 2500 rpm with normalized currents [ $J/J_{max}$ ], arrows indicate the scan direction; b) averaged recorded intensities (400 cm<sup>-1</sup> to 890 cm<sup>-1</sup>) as a function of potential (left y-axis) and corresponding CV recorded on Au-bead (right y-axis); c) comparison of averaged intensities at different glucose concentrations, 0 mM to 70 mM. d) color map of Raman spectra continuously recorded during cyclic voltammetry (7 mV s<sup>-1</sup>) in the absence of glucose. All measurements were recorded at room temperature. Reprinted with permission of the authors of ref<sup>101</sup>.

Cyclic voltammograms recorded in electrolytes with different glucose concentrations show different electrode potentials at which the surface becomes inactive towards glucose oxidation (**Figure 3.1.3a**). Importantly, the deactivation of the electrode coincides with the oxidation of the gold electrode<sup>114</sup>. To test the hypothesis that the presence of glucose shifts the Au oxidation towards higher potential an *in situ* Raman study was conducted. First, a blank experiment on the gold bead electrode in the absence of glucose showed that the intensity of the Raman background indeed coincides with the oxidation of the gold (**Figure 3.1.3b**). During the scan in the negative direction the recorded background intensity increased again upon the reduction of the gold surface (**Figure 3.1.3d**). Then, cyclic voltammograms in different glucose concentrations were recorded. The respective Raman intensities were plotted as a function of the electrode potential (**Figure 3.1.3c**). The plot reveals that the glucose concentration influences the oxidation potential of the gold electrode. A likely explanation is that the GOR consumes

$\text{OH}^-$  adsorbed on the gold. The larger the GOR rate, which is correlated to the glucose concentration, the more  $\text{OH}^-_{\text{ads}}$  is consumed at the electrode, and thereby, the oxidation of gold is delayed.

### **3.2 Manuscript II: Elucidating the reaction pathway of glucose electrooxidation to its valuable products: the Influence of mass transport and electrode potential on the product distribution**

#### **3.2.1 Abstract**

Converting glucose electrochemically to its valuable derivatives, gluconic and glucaric acid, is an increasingly promising process for the utilization of renewable carbon sources. Understanding the reaction pathway to form glucaric acid from glucose is key in performing the process efficiently. In this study, we investigate the influence of rotation and potential on the product distribution in glucose, gluconic acid and glucuronic acid oxidation on a gold disk in an RDE-setup. We find glucose and glucuronic acid to be easily oxidized, while the oxidation of gluconic acid is kinetically limited. Combining DFT calculations and the experimental results, we show that, on gold, the oxidation of aldehyde groups happens readily while the oxidation of hydroxyl groups is challenging and happens almost indiscriminately on all positions in glucose, and its derivatives, molecules.

#### **3.2.2 Contribution to the work**

For this study, I performed all the experimental work and analysis, including the electrochemical measurements as well as the product determination and quantification. Alexander Bagger provided the DFT calculation on the system. The experimental design and methodology were developed in collaboration with all co-authors. I wrote all the parts of the publication concerned with the discussion of and conclusion on the glucose oxidation experiments, while Alexander Bagger contributed the sections concerning the DFT calculations. Jan Rossmeisl and Matthias Arenz supervised the study. Matthias Arenz was additionally involved in manuscript writing and editing.

### 3.2.3 Most relevant findings

This study explores possible reaction pathways from glucose to glucaric acid. Additionally, the influence of the oxidation potential and rotation speed as experimental parameters were investigated. In-tandem with DFT calculation, a possible pathway from glucose to glucaric acid was rationalized.

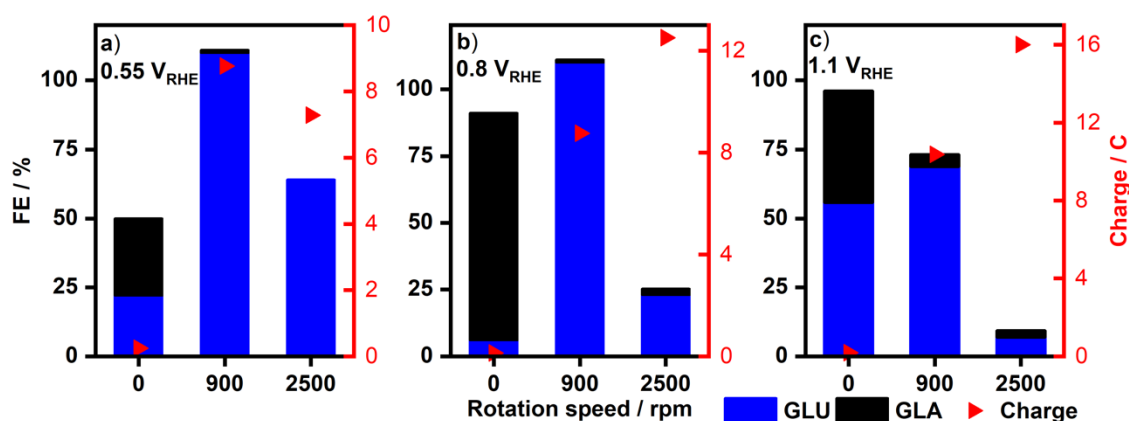


**Figure 3.2.1:** Product distribution in glucose oxidation at different oxidation potentials in 0.1 M NaOH and 0.1 M NaClO<sub>4</sub> with 10 mM glucose after 2h at a) 0.55 V<sub>RHE</sub>, b) 0.8 V<sub>RHE</sub>, and c) 1.1 V<sub>RHE</sub>. Faradaic efficiencies (FE) towards gluconic acid (GLU) and glucaric acid (GLA) depicted in blue and black, respectively. The transferred charge is displayed on the right-hand y-axis of each graph.

When oxidizing glucose under forced convection, gluconic acid (GLU) was found to be the main product. Glucaric acid (GLA) was formed in the absence of rotation. However, the transferred charge in the absence of rotation is much smaller compared to experiments under forced convection (**Figure 3.2.1**). In short, the transferred charge is a function of the rotation speed. Therefore, the reaction rates and the absolute GLA amounts formed in the absence of rotation were only minuscule. This finding has two very different implications for the oxidation of glucose in the absence of rotation: i) The formation rates are too small to be of interest for upscaling (even on a laboratory scale). ii) The product analysis is subject to large uncertainties from the product analysis itself as well as aging processes making the results unreliable. The application of milder oxidation potentials (0.55 V<sub>RHE</sub> and 0.8 V<sub>RHE</sub>) coupled with milder rotation (900 rpm) leads to the most desirable product distribution at substantial reaction rates. Further increasing the oxidation potential and the rotation speed leads to decreased FE towards the desired products and increases the dissociation of the glucose molecule. HPIC confirms the presence of more dissociation products under these conditions. The harsh conditions therefore lead to the oxidation of glucose at undesired positions.

Importantly, independent of the applied oxidation potential and rotation speed, no glucuronic acid was detected.



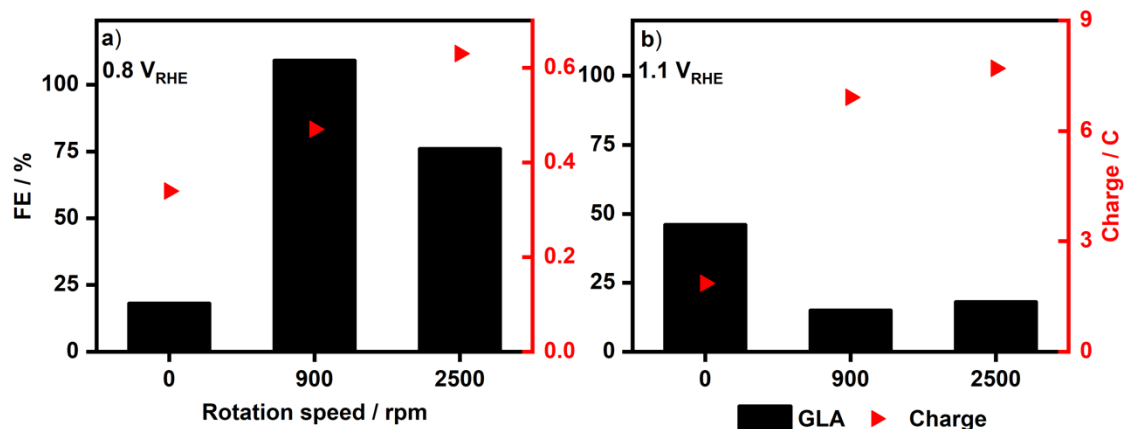


**Figure 3.2.2:** Product distribution and Faradaic efficiencies (FE) towards glucaric acid in gluconic acid oxidation experiments at different oxidation potentials in 0.1 M NaOH and 0.1 M NaClO<sub>4</sub> with 10 mM gluconic acid after 2h at a) 0.8  $V_{RHE}$  and b) 1.1  $V_{RHE}$ . The transferred charge is displayed on the right-hand y-axis of each graph.

The same experiments were repeated with gluconic acid present in the electrolyte. At an oxidation potential of 0.8  $V_{RHE}$  (**Figure 3.2.2 a**) the transferred charge appeared to be less governed by the applied rotation speed. This in contrast to the glucose oxidation experiments (**Figure 3.2.1 a**) discussed above. Nonetheless, it seemed that the product distribution was influenced by the applied rotation rate. A mild rotation (900 rpm) results in the highest FE towards GLA, while only marginal reaction rates were reached. At 1.1  $V_{RHE}$  (**Figure 3.2.2 b**) the rotation speed significantly influences the transferred charge. However, the decreased FE towards GLA implies an increased gluconic acid dissociation.

From these observations, it was concluded that the oxidation of gluconic acid to form glucaric acid is kinetically limited at lower potential while at higher potentials gluconic acid seems oxidizable. However, the oxidation happens indiscriminately on the molecule resulting in a low FE towards GLA which is confirmed by the increased presence of dissociation products. This observation is also in agreement with DFT calculations which indicate that terminal hydroxyl groups are only slightly easier to oxidize than non-terminal groups. Once again, throughout the series of measurements, no glucuronic acid has been detected.

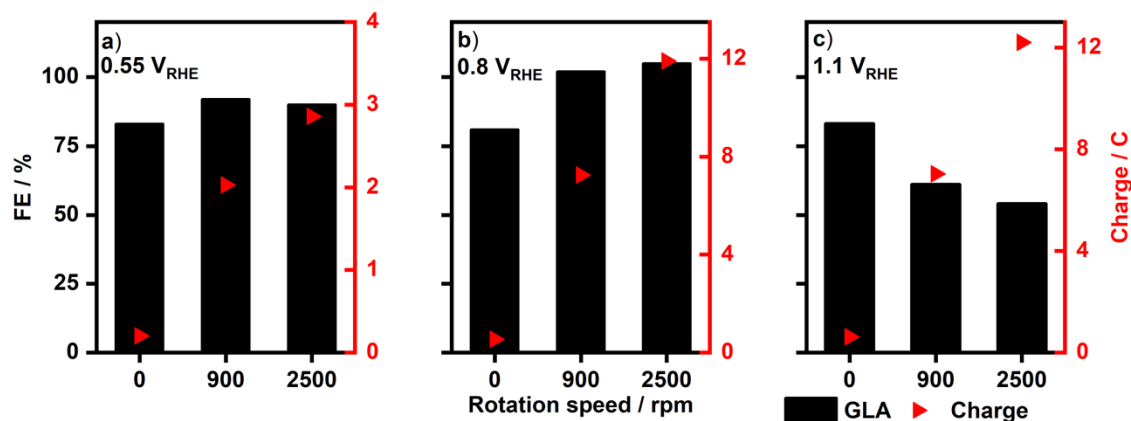


**Figure 3.2.3:** Product distribution and Faradaic efficiencies (FE) towards glucaric acid in glucuronic acid oxidation at different oxidation potentials in 0.1 M NaOH and 0.1 M NaClO<sub>4</sub> with 10 mM glucuronic acid after 2h at a) 0.55  $V_{RHE}$ , b) 0.8  $V_{RHE}$ , and c) 1.1  $V_{RHE}$ . The transferred charge is displayed on the right-hand y-axis of each graph.

The oxidation of glucuronic acid was very similar to the glucose oxidation. In **Figure 3.2.3 a)** and **b)**, high FEs towards GLA are observed. The FE towards GLA decreases at a larger overpotential. Even more so when fast rotation speeds are applied. The increased concentrations of dissociation products confirmed the lower FEs.

Combining the experimental data (**Figure 3.2.1-3.2.3**) and the insights gained from the DFT calculation, it was concluded that the oxidation of the terminal aldehyde groups present in glucose and glucuronic acid occurs selectively on gold surfaces. In contrast, the oxidation of a terminal hydroxyl group is kinetically challenging. However, once the oxidation of the hydroxyl groups occurs, it is not limited to the terminal groups but occurs indiscriminately at all hydroxyl groups in the molecule. For the absence of glucuronic acid two probable explanations were discussed: i) On gold, the bonded oxygen and carbon key intermediates are energetically close. Hence, glucaric acid could be formed through an R-\*C-OH intermediate. Therefore, glucuronic acid would be omitted as possible intermediated. ii) The oxidation occurs via an R-CH<sub>2</sub>-\*O intermediate. Glucuronic acid would be formed but then immediately be oxidized further to glucaric acid as the aldehyde group is swiftly oxidized further. Hypothesis i) seems however more likely as it is hard to imagine that the possibly formed glucuronic acid would be completely converted immediately.

### **3.3 Manuscript III: Characterization of multimetallic PtFeCoNiPd-HEA samples by *in situ* PXRD and XANES (*in preparation*)**

#### **3.3.1 Abstract**

The formation of high-entropy alloy (HEA) nanoparticles at low temperatures (< 350 °C) is not yet fully understood. Investigating the oxidation states of the constituent elements of PtFeCoNiPd samples *in situ* by XANES during the synthesis while simultaneously also tracking the crystal phases by *in situ* PXRD sheds light on the formation of the HEA phase. In this study, we present four different samples with distinct numbers of constituent elements (two, three, four, and five elements) and compare their reduction behavior. We find the precious metals to reduce in a narrow temperature window while the non-precious metals reduce via an intermediate state over the span of a larger temperature range. In all samples, first, the formation of an fcc phase is observed followed by a gradual transformation to a tetragonal phase (P4/mmm) at elevated temperatures.

#### **3.3.2 Contribution to the work**

To this study I contributed the development of the incipient wetness approach-based synthesis that was used to synthesize all investigated samples. Additionally, I recorded and analyzed the PXRD data that was acquired in-house at University of Bern and at BM31 at ESRF in Grenoble. Together with Stefanie Punke we envisioned the approach on how to combine the different analysis techniques to maximize the obtained data. Stefanie Punke additionally analyzed the XANES data using a script developed by Ulrik Friis-Jensen. Divyansh Gautam joined the beamtime experiments and Nicola Ramseyer contributed to the PXRD data analysis. Etienne Berner conducted the EDX characterization of the samples. Rebecca Pittkowski also joined the beamtime and designed the study alongside Kirsten Jensen and Matthias Arenz.

### 3.3.3 Most relevant findings

Samples containing different numbers of elements in equimolar ratios were synthesized by an incipient wetness approach on Ketjen Black EC300J with a metal loading of 60 wt%: PtFe, PtFeCo, PtFeCoNi, and PtFeCoNiPd. At ESRF in Grenoble, the samples were characterized *in situ* during the synthesis using PXRD and XANES. The temperature program for the synthesis consisted of heating to 400 °C at 100 °C h<sup>-1</sup> followed by more rapid heating to 750 °C at 350 °C h<sup>-1</sup>. Then the sample was set to cool down back to ambient temperature. All the while, the sample was kept under a reducing H<sub>2</sub>/Ar atmosphere.

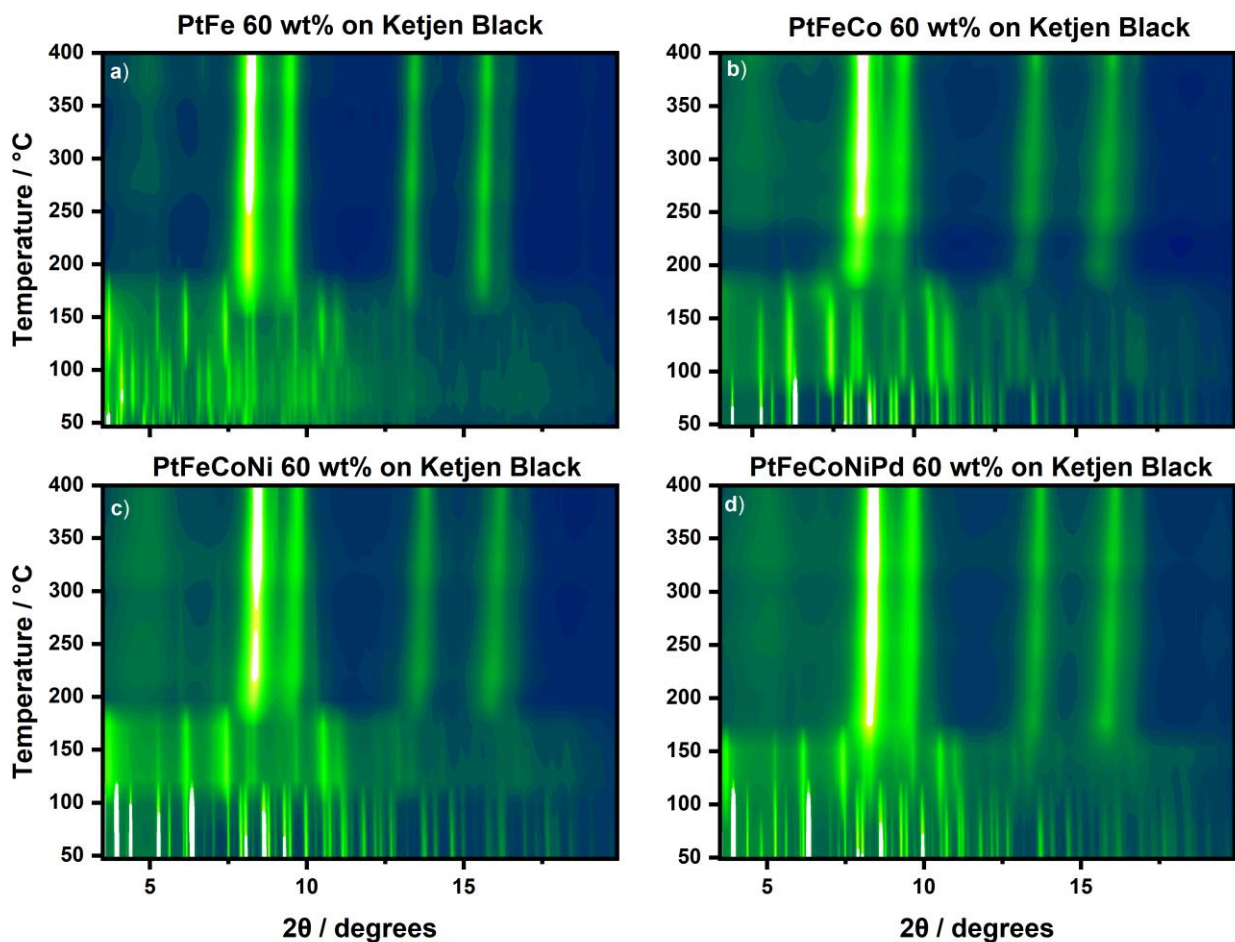


**Figure 3.3.1:** Contour plots of PXRD diffractograms of a) a PtFe, b) a PtFeCo, c) PtFeCoNi, and d) PtFeCoNiPd sample on Ketjen Black EC300-J with a metal loading of 60 wt% recorded during heating to 400 °C. The green regions indicate high intensities while the blue regions indicate low intensities in the diffractograms.

The contour plots in **Figure 3.3.1** show that in all investigated samples from the metal salt precursors a face-centered cubic (fcc) phase forms before 200 °C. In the HEA sample, PtFeCoNiPd (**Figure 3.3.1 d**), this reduction occurs 25 °C earlier than in the other three samples (**Figure 3.3.1 a-c**).

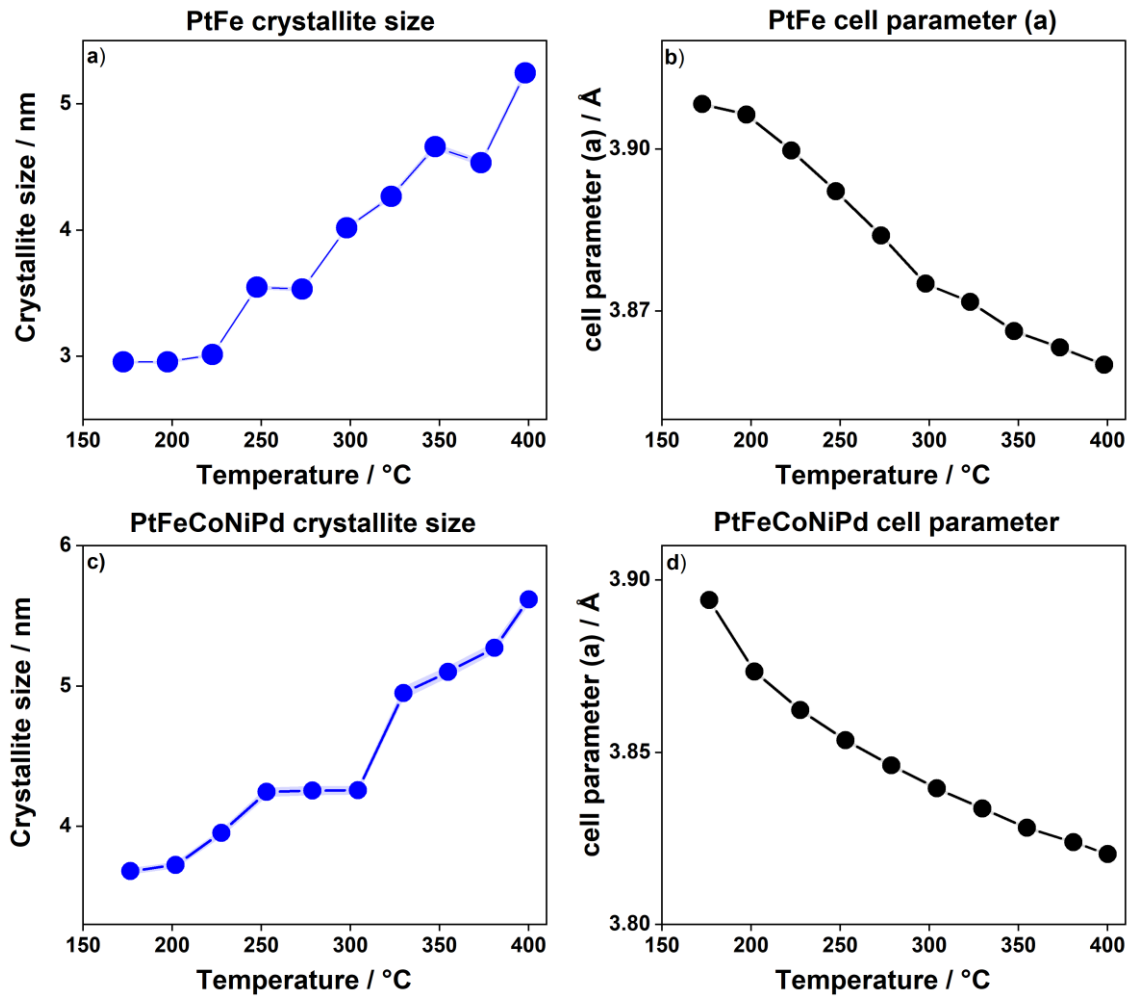


**Figure 3.3.2:** Crystallite size and cell parameter of the formed fcc phase obtained from sequential Rietveld refinements using GSAS-II of PtFe 60 wt%, a) and b), and PtFeCoNiPd 60 wt%, c) and d). Microstrain was kept constant during the sequential refinement.

Sequential Rietveld refinement of the individual diffractograms of the samples PtFe (**Figure 3.3.2a**) and PtFeCoNiPd (**Figure 3.3.2 c**) reveals that the crystallite size of the sample increases during heating. Assuming the crystallite size to correspond to the particle size, it follows that the nanoparticles grow. Simultaneously, the unit cell shrinks as shown in **Figure 3.3.2 b**) and d).

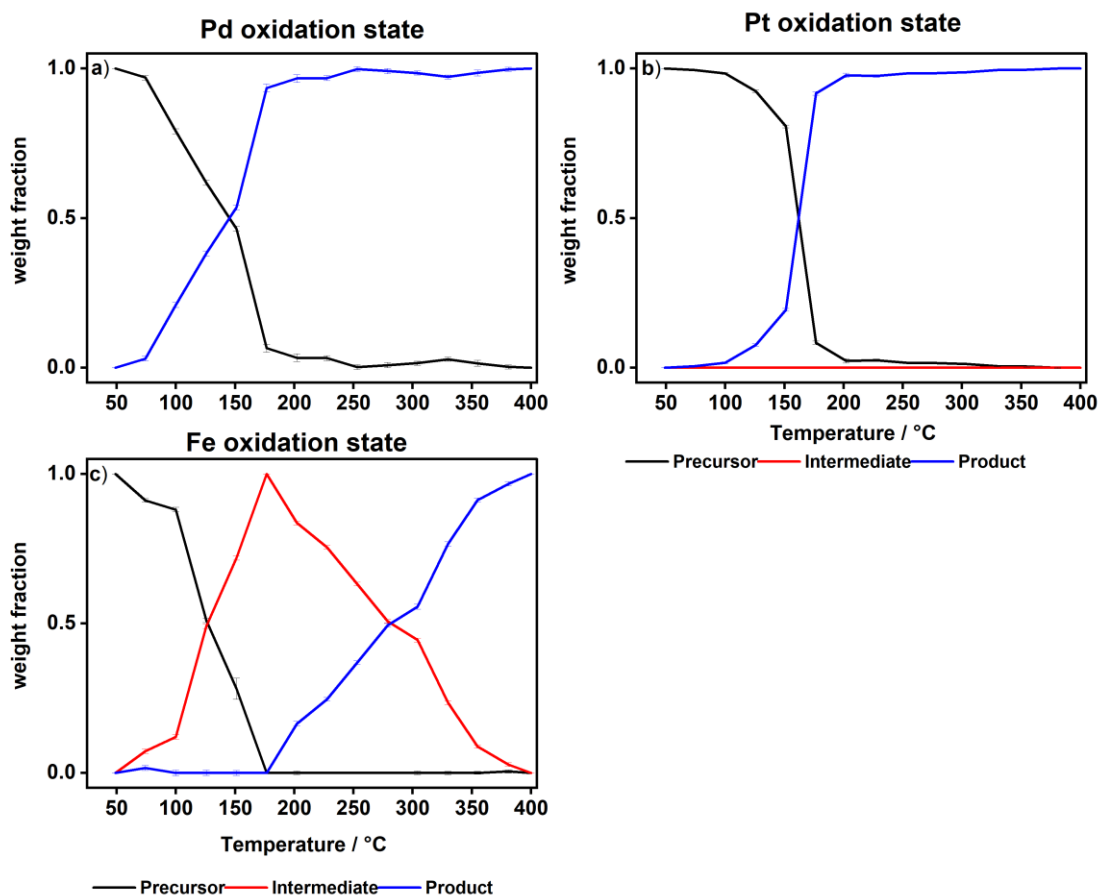


**Figure 3.3.3:** Linear combination analysis (LCA) of XANES spectra recorded during the reduction of a PtFeCoNiPd 60 wt% sample for Pd (a), Pt (b), and Fe (c). Precursors are indicated in black, intermediates in red, and products in blue. The weight fractions determined by the LCA are normalized to the main absorption edge. Note that Pt and Pd do not reduce via an apparent intermediate. The LCA for Co and Ni is missing due to on-going complications with the autoXAS script.

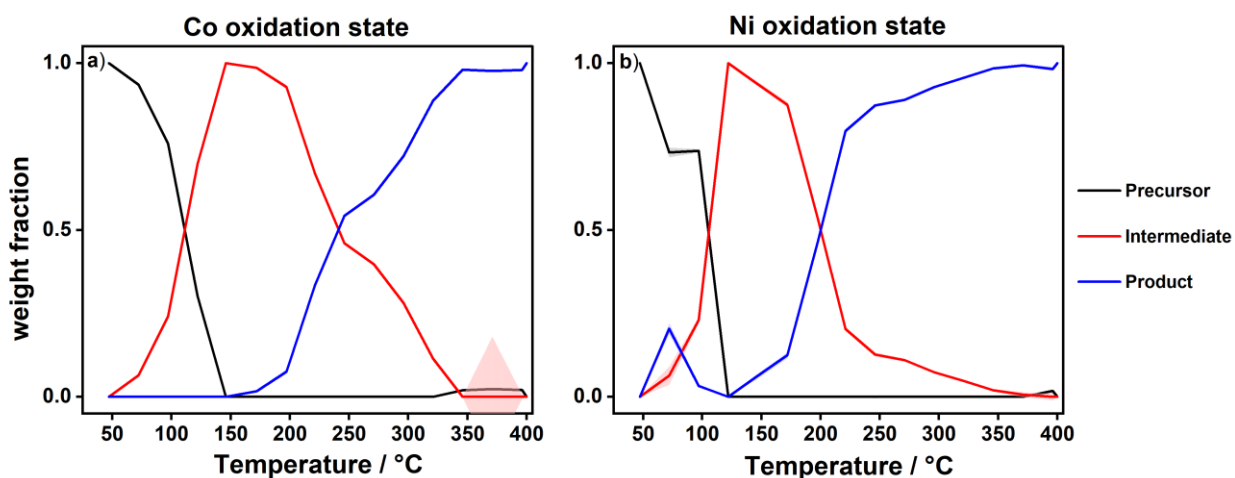


**Figure 3.3.4:** Linear combination analysis (LCA) of XANES spectra recorded during the reduction of a PtFeCoNi 60 wt% sample for Co (a) and Ni (b). Precursors are indicated in black, intermediates in red, and products in blue. The weight fractions determined by the LCA are normalized to the main

absorption edge. We assume the reduction behaviour of these elements to be similar in the PtFeCoNiPd sample. The shaded areas depict the standard deviation of the LCA.

LCA analysis of the XANES spectra recorded during the heat ramp to 400 °C unveils that the metals show different reduction behavior. This is exemplary shown by the LCA of the PtFeCoNiPd sample in **Figure 3.3.3 and 3.3.4**. However, it holds true for all samples. The metals can be broadly separated into two groups, which correspond to their nobility. First, the noble metals, Pd and Pt (**Figure 3.3.3a and b**)), reduce within a narrow temperature window between 100 °C and 200 °C. They rapidly reduce from their precursor to their final state ( $\text{Pd}^{2+} \rightarrow \text{Pd}^0$ ;  $\text{Pt}^{4+} \rightarrow \text{Pt}^0$ ). The second group consists of Fe, Co, Ni. These metals reduce via an intermediate state (e.g.  $\text{Fe}^{3+} \rightarrow \text{Fe}^{2+} \rightarrow \text{Fe}^0$ ). Notably, for Co and Ni no oxidation state was found in the literature that matches the observed intermediate spectra. The onset of reducing from the precursor to intermediate occurs as early as 75 °C. The reducing from the intermediate to the final state slowly occurs up to 300 °C. The reduction temperature window is therefore much broader than in the case of the noble metals. Interestingly, even though the reduction temperatures differ greatly, only one apparent fcc metal phase is formed (**Figure 3.3.1**). The non-precious elements exhibit smaller elemental unit cells than Pd and Pt. Therefore, a continuous incorporation of Fe, Co, and Ni into a Pt- (and Pd-) rich phase can explain the observed shrinking of the unit cell. Exactly how this incorporation occurs has to be investigated further until a conclusive answer can be given.

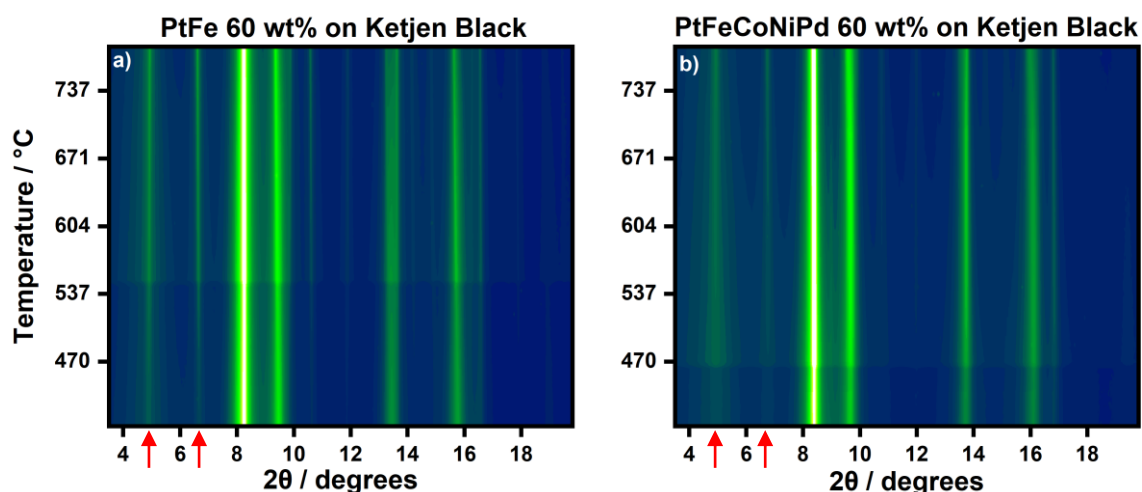


**Figure 3.3.5:** Contour plots of PXRD diffractograms of a) PtFe and a) PtFeCoNiPd samples on Ketjen Black EC300-J with a metal loading of 60 wt% recorded during heating to 750 °C. The green regions indicate high intensities while the blue regions indicate low intensities in the diffractograms. The red arrows in the x-axis indicate the most intense peaks which emerge.

Upon heating the sample to higher temperatures, additional peaks start to emerge in the diffraction patterns. The most intense peaks are indicated by the red arrows in **Figure 3.3.5**. A closer inspection

of the contour plot of sample PtFe (**Figure 3.3.1 a)**) indicates that the transformation already commences at 375 °C. This is not the case for PtFeCoNiPd (**Figure 3.3.1 d)**), and hence, the transformation seems to commence at higher temperatures in the HEA sample. Matching the emerging reflections to reference materials indicates that the peaks correspond a tetragonal phase of space group P4/mmm (**figure 3.3.6**). The crystalline phase transforms from fcc to P4/mmm.

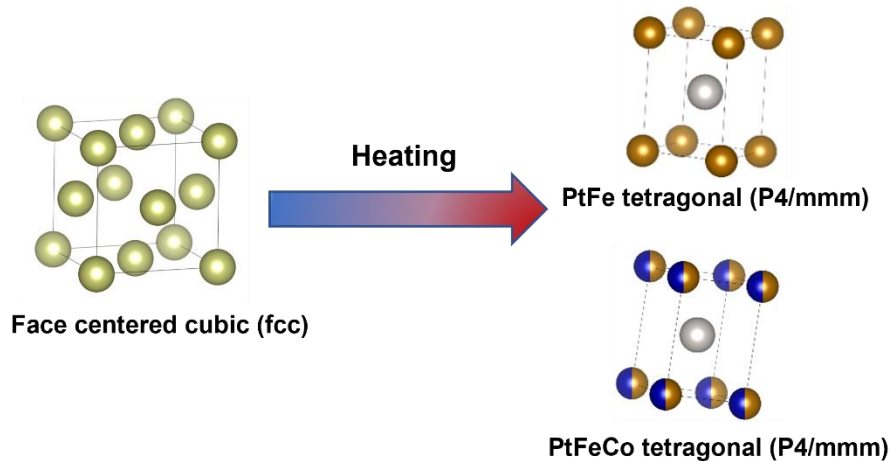


**Figure 3.3.6:** Illustration of the phase transformation occurring from fcc to tetragonal P4/mmm when heating the samples to 750 °C. The PtFe and PtFeCo lattices depicted are from structures available in the open crystallographic database.

However, the diffractograms must be refined further using Rietveld's method. Only then can insight about important parameters be gained. The most interesting parameters to determine are the phase fraction and the atom position within the lattice.



### **3.4 Manuscript IV: Elucidating the Steady-State OER Activity of NiFeOOH Binary Nanoparticles in As-prepared and Purified KOH Electrolyte Solutions**

The work for this manuscript was conducted, as previously alluded to in section 2.1, in collaboration with Kirsten Jensen's group at the University of Copenhagen. This manuscript is not particularly connected to the rest of the presented work in this thesis except that it is from the broad field of electrocatalysis. The results of this work are however discussed for the purpose of knowledge transfer and to deepen the collaboration within the Centre for High-entropy Alloy Catalysis (CHEAC), of which both research groups are a part of.

#### **3.4.1 Abstract**

Replacing critical raw materials employed in water electrolysis applications as electrocatalysts with earth-abundant materials is paramount for the future upscaling of these application to industrial dimensions. In that regard, Ni and Ni-based multimetallic hydroxides, above all NiFe-hydroxides, have shown promising performance towards the oxygen evolution reaction (OER) in alkaline conditions. However, it has been shown that the extraordinary performance of these materials is owed at large to Fe impurities found in commercial KOH from which electrolyte solutions are prepared. The mechanism of action of these impurities is still not fully understood, and therefore, at the heart of on-going discussions. In this study, we investigate the OER activity of different  $(\text{Ni}_{1-x}\text{Fe}_x)\text{OOH}$  samples and find their activities to be influenced differently by the presence of the Fe impurities. From the gathered data, we conclude that the presence of Fe impurities impacts gravely the structure sensitivity of the OER. In the absence of the impurities – in purified electrolyte solutions – the OER appears to be a structure-sensitive reaction while this seems no to be the case in the presence of said impurities.

#### **3.4.2 Contribution to the work**

I instructed and subsequently supervised Baiyu Wang in all questions regarding the experimental performance of electrochemistry including the setup and sample preparation. Additionally, I helped conceptualizing the manuscript and wrote the first draft of the manuscript. Baiyu Wang performed the electrochemical measurements, parts of the structural characterization, and wrote the discussion of these analyses for the manuscript. Olivia Aalling-Frederiksen synthesized and characterized the samples. Kirsten Jensen (structural characterization) and Matthias Arenz (electrochemistry) supervised the work in their fields of expertise, conceptualized the study and edited the paper.

### 3.4.3 Most relevant findings

$(\text{Ni}_{1-x}\text{Fe}_x)\text{OOH}$  and  $(\text{Ni}_{1-x}\text{Co}_x)\text{OOH}$  samples were synthesized from nitrate precursors via a solvothermal approach at varying synthesis times. The main discussion of the study is focused on  $(\text{Ni}_{0.5}\text{Fe}_{0.5})\text{OOH}$  while the other samples serve to verify observed trends. The effect of Fe-impurities present in commercial KOH on OER activity was investigated by comparing activities determined in as-prepared and purified electrolyte solutions.

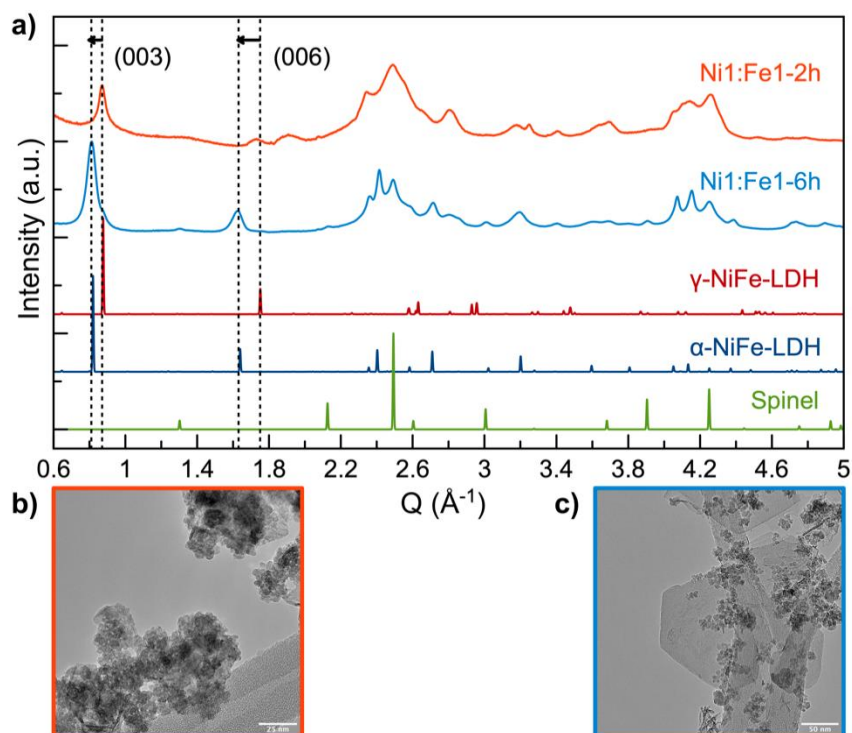


**Figure 3.4.1:** a) PXRD patterns of the same two as-synthesized  $(\text{Ni}_{0.5}\text{Fe}_{0.5})\text{OOH}$  samples collected at the synchrotron DESY, P21.1, with a wavelength of  $0.21 \text{ \AA}$ . PXRD patterns collected with Bruker D8 are in the range  $0.6\text{-}4 \text{ \AA}^{-1}$ . Samples were named by the metal precursor ratio used in synthesis and the synthesis time. b-c) Exemplary TEM images of the two  $(\text{Ni}_{0.5}\text{Fe}_{0.5})\text{OOH}$  samples: (b) Ni1:Fe1-2h and (c) Ni1:Fe1-6h.

Two  $(\text{Ni}_{0.5}\text{Fe}_{0.5})\text{OOH}$  samples with varying synthesis time, hereafter called Ni1:Fe1-2h and Ni1:Fe1-6h, were characterized by PXRD (Figure 3.4.1 a)), TEM (Figure 3.4.1 b) and c)), and pair distribution function (PDF) analysis from total scattering experiments. The termini of the sample names, “2h” and “6h”, correspond to the respective synthesis time – specifically 2 hours and 6 hours. Comparing the samples’ diffraction patterns to references (Figure 3.4.1 a)), the coexistence of a layered double hydroxide phase (LDH) and a spinel phase was confirmed in the two samples. Both structures are visible in the TEM images presented in Figure 3.4.1 b) and c). Based on peak position, after two hours of synthesis time an  $\alpha$ -polymorph LDH was observed, whereas after 6h the samples’ diffraction pattern confirmed a  $\gamma$ -polymorph LDH. Additionally, the synthesis time affected the crystallite size of the

phases as well as the phase ratio of LDH:spinel. This insight is qualitatively observed in the diffraction patterns due to Ni1:Fe1-6h exhibiting sharper peaks than Ni1:Fe1-2h (Scherrer's equation<sup>84</sup> relates full width at half maximum to crystallite size). PDF analysis was used to quantitatively characterize the sample. In the case of sample Ni1:Fe1-2h a LDH:spinel ratio of 70:30 was confirmed, while in the sample Ni1:Fe1-6h the ratio was shifted to 80:20 LDH:spinel. The spherical diameters of the LDH crystallites increased from 19 Å in Ni1:Fe1-2h to 51 Å in Ni1:Fe1-6h and the unit cell parameter "c", which corresponds to the stacking direction of the LDH, increased from 21.79 Å to 22.74 Å with increased synthesis time, respectively. Therefore, the increased synthesis time induces crystallite growth and the transformation of spinel to LDH phase. From the physical characterization it was concluded that, of the two samples, Ni1:Fe1-2h exhibits a larger surface area.

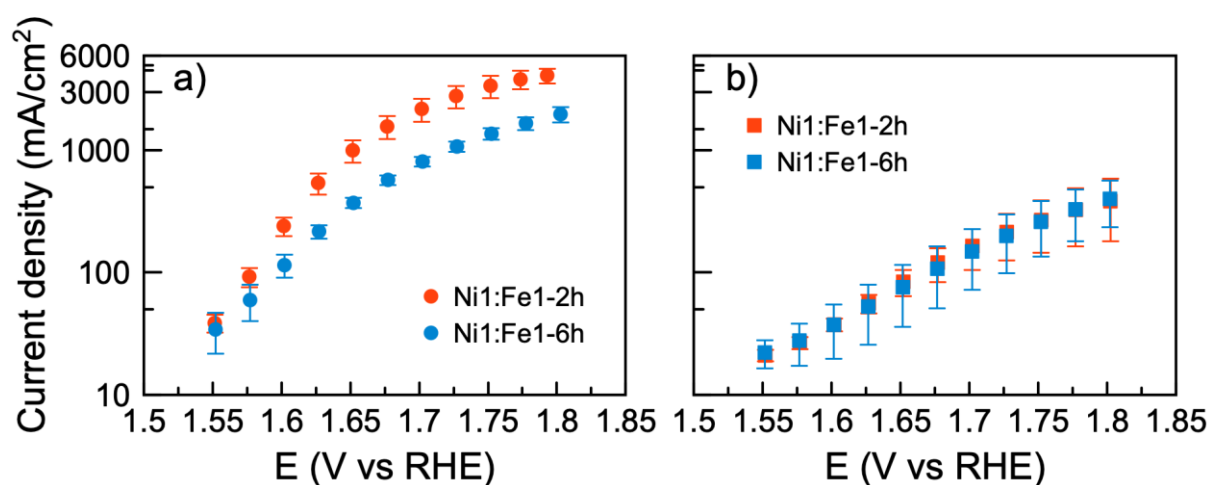


**Figure 3.4.2:** Steady-state OER activities of the two ( $Ni_{0.5}Fe_{0.5}$ )OOH samples in a) as-prepared and b) purified 0.1 M KOH electrolyte measured at 2500 rpm. The activities shown are normalized to the geometric surface area of the RDE tip. The error bars indicate the standard deviation from measuring three different RDE tips.

Thin film electrodes of the two samples were prepared by drop casting catalyst inks onto polished glassy carbon disk electrodes. For both samples, a loading of 50  $\mu\text{g cm}^{-2}$  was targeted. The disk electrodes were tested in an RDE setup. Their respective steady-state OER activities were determined in as-prepared and purified electrolyte by applying a potential step protocol with step width of 25 mV. KOH electrolyte solutions were purified by precipitated bulk Ni(OH)<sub>2</sub> which absorbs the Fe impurities. In as-prepared 0.1 M KOH electrolyte solution (**Figure 3.4.2 a**), sample Ni1:Fe1-2h outperformed sample Ni1:Fe1-6h in terms OER activity and corresponding Tafel-slope (**Table 3.4.1**). Hence, the sample with a larger physical surface area was more active towards the OER.

**Table 3.4.1:** Activities at 1.6  $V_{RHE}$  and calculated Tafel slopes of synthesized samples during the first set of potential steps (2500 rpm).

Sample	As-prepared KOH		Purified KOH	
	Current density @1.6 $V_{RHE}$ (mA/cm <sup>2</sup> )	Tafel slope (mV/dec)	Current density @1.6 $V_{RHE}$ (mA/cm <sup>2</sup> )	Tafel slope (mV/dec)
Ni1:Fe1-2h	241 ± 41.07	63	37 ± 4.58	160
Ni1:Fe1-6h	115 ± 24.69	83	37 ± 17.55	100

In purified KOH electrolyte solution, the OER activities were severely decreased (**Figure 3.4.2 b**), **Table 3.4.1**). This observation is in agreement with reports in the literature. However, the samples now exhibit very similar OER activities, whereas before they were different. Because the samples exhibit features of different sizes, and by extensions different surface areas, we conclude that, in purified electrolyte, the OER is a structure-sensitive reaction. In contrast, the difference in activities measured in as-prepared electrolyte can be explained by the difference in surface area. The same trend is observed in the reference samples presented in the SI. Therefore, the structural features are of less importance as the enhancement effect towards OER activity resulting from Fe-impurities corresponds to the exposed surface area at the interface. To obtain more insights into the interaction between the Fe and the samples *operando* studies including total scattering experiments are necessary where the catalyst structure can be investigated.

## 4 Conclusion & Outlook

### 4.1 Conclusion

In this thesis, the GOR towards glucaric acid was investigated on a Au-disk electrode in a RDE setup. Additionally, a straight-forward and robust synthesis method to achieve HEA of different compositions was developed.

The GOR was investigated with different electrochemical techniques. By oxidizing the reaction intermediate gluconic acid and the closely related glucuronic acid, insight into the kinetics of the individual reaction steps was gained. Cyclic voltammetry experiments showed that glucose oxidation is mixed kinetic mass-transport controlled. Hence, reaction rates, observed as current responses, are influenced substantially by applied forced convection. The same was found for glucuronic acid oxidation. In contrast, gluconic acid oxidation was found to be kinetically limited on the employed gold electrode. A key aspect for the analysis of the GOR was the development of a suitable product analysis technique which unlocked investigations into the influence of experimental parameters on the product selectivity and distribution. The developed HPIC method can quantify the products of interest as well as a portion of the formed dissociation products. The influence of rotation speed and oxidation potential was subsequently studied, and it was found that both parameters influence the product selectivity. Importantly in glucose and glucuronic acid oxidation, milder conditions, both in terms of applied potential and rotation speed, lead to the selective removal of two proton-electron pairs from the aldehyde group resulting in gluconic and glucaric acid, respectively. The oxidation of gluconic acid appears very challenging on a polycrystalline Au-electrode with very low reaction rates. Seemingly the terminal hydroxyl group cannot be oxidized selectively. At larger oxidation potentials, the dissociation of glucose is promoted indicating indiscriminate oxidation along the molecule. The plethora of possible cleavage products due to the many different oxidation sites in the molecules exemplifies the complexity of the GOR. From these results it became apparent that novel catalyst materials must be developed to perform the GOR towards glucaric acid efficiently and selectively.

HEA might be a promising class of materials, also as catalysts in the GOR, due to manifold active sites. To that end, an IWI-method was developed which yielded multi-elemental, one-phase nanoparticles supported on carbon black. Unfortunately, gold could not be incorporated into the alloy via the chosen approach yet. However, a PtFeCoNiPd alloy was synthesized successfully, which might be an interesting ORR catalyst. The IWI-approach allows for the control of particle size by tuning synthesis parameters, i.e., metal loading and reduction temperature. The successful synthesis of the samples enabled the investigation by a combination of *in-situ* XANES and *in-situ* PXRD. This study gave valuable insight into the formation of the crystallographic phases and the transition of an fcc-phase to a

tetragonal phase containing all elements. Interestingly, only a single phase was observed in the PXRD even though from XANES it was apparent that the metals do not reduce at the same reduction temperature.

## **4.2 Outlook**

### **4.2.1 Combining GOR and HEA synthesis**

The most obvious next step is the combination of the two major aspects of this thesis by employing a HEA-catalyst in GOR experiments. First, the successful incorporation of gold into the HEA is necessary. Varying the synthesis parameters, such as changes to the solvent, the metal loading, or the metal precursors, is paramount to preventing the gold from reducing during the drying step. Once successfully incorporating gold into a HEA, the performance and product selectivity would give insights into the catalytic processes taking place under GOR conditions. It will be very interesting to explore the effect of HEA-catalysts in a reaction involving intermediate species such as GOR. For example, it could be investigated if the kinetics of reacting terminal hydroxyl groups, i.e., the limiting step in gluconic acid oxidation, are improved or if dissociation might be favored due to the presence of catalytic sites facilitating these processes. In general, it seems worth to expand the IWI approach for the HEA synthesis by identifying sets of parameters that allow to freely choose the desired elemental composition. This kind of on-demand synthesis resulting in a wide variety of HEA systems for different electrochemical processes would enable the rapid experimental verification of theoretical studies and calculations.

### **4.2.2 Development of a flow-cell setup for GOR**

Since this thesis has shown the importance of mass transport limitations in the GOR, moving away from the batch-reactor employed so far to a flow-cell setup is a logical step. First experiments with the help of Gustav Wiberg and one of his cell designs were successful in circulating the glucose containing electrolyte. Tuning this system and conducting long-term experiments in which all the glucose is converted would not only be of interest in regards of upscaling but could also answer the question about the molecular stability of glucaric acid under prolonged exposure to reaction conditions.

## 5 Acknowledgement

My gratitude goes to Matthias Arenz for giving me the opportunity to pursue this PhD project in his research group. First, for allowing me to choose freely my PhD project and to branch out to what interested me. And second, during my studies, supporting and supervising me - showing interest in my progress and giving invaluable advice. It helped me to grow as a researcher.

I would also like to thank the present and former colleagues of the Arenz group and friends from the Broekmann group. In the lab, on work related things, for showing me without reservation their trade secrets and for answering every question that came to my mind. And during lunch breaks and after work for all the fun times we spent together. Because of you I am going to miss dearly my time in Bern. So, thank you, in no particular order, to Aline, Renan, Pavel, Shima, Etienne, Jia, Gustav, Ilya, Sven, Ivan, Vlad, Maria, Lily, Alain, Rebecca, Francesco, Jan, Damin, Johanna, Divyansh, Reshma, Johanne, Stefanie, Jens and Tim. Special thanks to Johanna for proof-reading my thesis.

Finally, I would like to thank my friends, partner, and family. For the interest you showed in how I spend my time even though it is far detached from real life and for the all the support I have received from you over the years.

## 6 References

1. Levi, P. G. & Cullen, J. M. Mapping Global Flows of Chemicals: From Fossil Fuel Feedstocks to Chemical Products. *Environ. Sci. Technol.* **52**, 1725–1734 (2018).
2. Report - 2022 Edition: Annual benchmarks and Long-term impacts. <https://www.enerdata.net/publications/reports-presentations/world-energy-trends.html>.
3. Global and European Temperatures. <https://www.eea.europa.eu/ims/global-and-european-temperatures>.
4. H.-O. Pörtner, D.C. Roberts, M. Tignor, E.S. Poloczanska, K. Mintenbeck, A. Alegría, M. Craig, S. Langsdorf, S. Löschke, V. Möller, A. Okem, B. R. *IPCC, 2022: Climate Change 2022: Impacts, Adaptation, and Vulnerability. Contribution of Working Group II to the Sixth Assessment Report of the Intergovernmental Panel on Climate Change. Climate Change 2021: The Physical Science Basis.* (2021). doi:10.1017/9781009325844.Front.
5. Renewable Energy Statistics. [https://ec.europa.eu/eurostat/statistics-explained/index.php?title=Renewable\\_energy\\_statistics#:~:text=Renewable energy sources include wind,the renewable part of waste](https://ec.europa.eu/eurostat/statistics-explained/index.php?title=Renewable_energy_statistics#:~:text=Renewable energy sources include wind,the renewable part of waste).
6. Hydrogen - EU. [https://energy.ec.europa.eu/topics/energy-systems-integration/hydrogen\\_en](https://energy.ec.europa.eu/topics/energy-systems-integration/hydrogen_en).
7. Fachagentur Nachwachsende Rohstoffe. <https://www.fnr.de/nachwachsende-rohstoffe/nachwachsende-rohstoffe-im-ueberblick>.
8. Dutta, S. Sustainable Synthesis of Drop-In Chemicals from Biomass via Chemical Catalysis: Scopes, Challenges, and the Way Forward. *Energy & Fuels* (2023) doi:10.1021/acs.energyfuels.2c03891.
9. Klemm, D., Heublein, B., Fink, H. P. & Bohn, A. Cellulose: Fascinating biopolymer and sustainable raw material. *Angew. Chemie - Int. Ed.* **44**, 3358–3393 (2005).
10. Xu, S. & Minteer, S. D. Enzymatic biofuel cell for oxidation of glucose to CO<sub>2</sub>. *ACS Catal.* **2**, 91–94 (2012).
11. Zhang, Z. & Huber, G. W. Catalytic oxidation of carbohydrates into organic acids and furan chemicals. *Chem. Soc. Rev.* **47**, 1351–1390 (2018).
12. Lee, J., Saha, B. & Vlachos, D. G. Pt catalysts for efficient aerobic oxidation of glucose to glucaric acid in water. *Green Chem.* **18**, 3815–3822 (2016).
13. Weissermel, K. & Arpe, H.-J. *Industrial organic chemistry.* (John Wiley & Sons, 2008).



## References

14. Anastassiadis, S. & Morgunov, I. G. Gluconic Acid Production. *Recent Pat. Biotechnol.* **1**, 167–180 (2007).
15. Li, G., Wu, Z., Xu, C. & Hu, Z. Hybrid catalyst cascade for enhanced oxidation of glucose in glucose/air biofuel cell. *Bioelectrochemistry* **143**, 107983 (2022).
16. Solmi, S., Morreale, C., Ospitali, F., Agnoli, S. & Cavani, F. Oxidation of d-Glucose to Glucaric Acid Using Au/C Catalysts. *ChemCatChem* **9**, 2797–2806 (2017).
17. Ramachandran, S., Fontanille, P., Pandey, A. & Larroche, C. Gluconic Acid: Properties, Applications and Microbial Production. *Food Technol. Biotechnol.* **44**, 185–195 (2000).
18. Teng, F. *et al.* Production of D-glucuronic acid from myo-inositol using Escherichia coli whole-cell biocatalyst overexpressing a novel myo-inositol oxygenase from Thermothelomyces thermophile. *Enzyme Microb. Technol.* **127**, 70–74 (2019).
19. Werpy, T. & Petersen, G. Top Value Added Chemicals from Biomass Volume I. *Us Nrel* (2004) doi:10.2172/15008859.
20. Kiely, D. E., Chen, L. & Lin, T. H. Hydroxylated Nylons Based on Unprotected Esterified D-Glucaric Acid by Simple Condensation Reactions. *J. Am. Chem. Soc.* **116**, 571–578 (1994).
21. Van De Vyver, S. & Román-Leshkov, Y. Emerging catalytic processes for the production of adipic acid. *Catal. Sci. Technol.* **3**, 1465–1479 (2013).
22. Mehlretter, C. L. & Rist, C. E. Sugar oxidation, Saccharic and Oxalic Acids by the Nitric Acid Oxidation of Dextrose. *J. Agric. Food Chem.* **1**, 779–783 (1953).
23. Charles L Mehlretter. The United States Patent Office. <https://patents.google.com/patent/US2436659A/en#relatedApplications> (1948).
24. Ibert, M., Marsais, F., Merbouh, N. & Brückner, C. Determination of the side-products formed during the nitroxide-mediated bleach oxidation of glucose to glucaric acid. *Carbohydr. Res.* **337**, 1059–1063 (2002).
25. Thaburet, J. F., Merbouh, N., Ibert, M., Marsais, F. & Queguiner, G. TEMPO-mediated oxidation of maltodextrins and D-glucose: Effect of pH on the selectivity and sequestering ability of the resulting polycarboxylates. *Carbohydr. Res.* **330**, 21–29 (2001).
26. Jin, X. *et al.* Synergistic Effects of Bimetallic PtPd/TiO<sub>2</sub> Nanocatalysts in Oxidation of Glucose to Glucaric Acid: Structure Dependent Activity and Selectivity. *Ind. Eng. Chem. Res.* **55**, 2932–2945 (2016).

## References

27. Cao, Y. *et al.* Base-free oxidation of glucose to gluconic acid using supported gold catalysts. *Catal. Sci. Technol.* **6**, 107–117 (2016).
28. Qi, P. *et al.* Catalysis and Reactivation of Ordered Mesoporous Carbon-Supported Gold Nanoparticles for the Base-Free Oxidation of Glucose to Gluconic Acid. *ACS Catal.* **5**, 2659–2670 (2015).
29. Megías-Sayago, C., Ivanova, S., López-Cartes, C., Centeno, M. A. & Odriozola, J. A. Gold catalysts screening in base-free aerobic oxidation of glucose to gluconic acid. *Catal. Today* **279**, 148–154 (2017).
30. Yun Yang, B. & Montgomery, R. Alkaline degradation of glucose: Effect of initial concentration of reactants. *Carbohydr. Res.* **280**, 27–45 (1996).
31. Yahiro, A. T., Lee, S. M. & Kimble, D. O. Bioelectrochemistry. I. Enzyme utilizing bio-fuel cell studies. *BBA - Spec. Sect. Biophys. Subj.* **88**, 375–383 (1964).
32. Barton, S. C., Gallaway, J. & Atanassov, P. Enzymatic biofuel cells for implantable and microscale devices. *Chem. Rev.* **104**, 4867–4886 (2004).
33. Clark, L. C. & Lyons, C. ELECTRODE SYSTEMS FOR CONTINUOUS MONITORING IN CARDIOVASCULAR SURGERY. *Ann. N. Y. Acad. Sci.* **102**, 29–45 (1962).
34. Hwang, D. W., Lee, S., Seo, M. & Chung, T. D. Recent advances in electrochemical non-enzymatic glucose sensors – A review. *Anal. Chim. Acta* **1033**, 1–34 (2018).
35. Vassilyev, Y. B., Khazova, O. A. & Nikolaeva, N. N. Kinetics and mechanism of glucose electrooxidation on different electrode-catalysts. Part II. Effect of the nature of the electrode and the electrooxidation mechanism. *J. Electroanal. Chem.* **196**, 127–144 (1985).
36. Vassilyev, Y. B., Khazova, O. A. & Nikolaeva, N. N. Kinetics and mechanism of glucose electrooxidation on different electrode-catalysts. Part I. Adsorption and oxidation on platinum. *J. Electroanal. Chem.* **196**, 105–125 (1985).
37. Kokoh, K. B., Leger, J. M., Beden, B., Huser, H. & Lamy, C. 'On line' chromatographic analysis of the products resulting from the electrocatalytic oxidation of D-glucose on pure and adatoms modified Pt and Au electrodes - Par II Alkaline medium. *Electrochim. Acta* **37**, 1909–1918 (1992).
38. Kokoh, K. B. *et al.* Selective oxidation of D-gluconic acid on platinum and lead adatoms modified platinum electrodes in alkaline medium. *Electrochim. Acta* **38**, 1359–1365 (1993).

## References

39. Escalona-Villalpando, R. A. *et al.* Electrodeposition of gold on oxidized and reduced graphite surfaces and its influence on glucose oxidation. *J. Electroanal. Chem.* **816**, 92–98 (2018).
40. Neha, N. *et al.* Revisited Mechanisms for Glucose Electrooxidation at Platinum and Gold Nanoparticles. *Electrocatalysis* **14**, 121–130 (2023).
41. Hebié, S., Napporn, T. W., Morais, C. & Kokoh, K. B. Size-Dependent Electrocatalytic Activity of Free Gold Nanoparticles for the Glucose Oxidation Reaction. *ChemPhysChem* **17**, 1454–1462 (2016).
42. El-Ads, E. H., Galal, A. & Atta, N. F. Electrochemistry of glucose at gold nanoparticles modified graphite/SrPdO<sub>3</sub> electrode - Towards a novel non-enzymatic glucose sensor. *J. Electroanal. Chem.* **749**, 42–52 (2015).
43. Ghosh, S. *et al.* One-pot synthesis of reduced graphene oxide supported gold-based nanomaterials as robust nanocatalysts for glucose electrooxidation. *Electrochim. Acta* **212**, 864–875 (2016).
44. Eshghi, A. & kheirmand, M. Graphene/Ni–Fe layered double hydroxide nano composites as advanced electrode materials for glucose electro oxidation. *Int. J. Hydrogen Energy* **42**, 15064–15072 (2017).
45. Liu, W. J. *et al.* Efficient electrochemical production of glucaric acid and H<sub>2</sub> via glucose electrolysis. *Nat. Commun.* **11**, 265 (2020).
46. Cao, M. *et al.* Nickel-copper oxide nanoflowers for highly efficient glucose electrooxidation. *Int. J. Hydrogen Energy* **46**, 28527–28536 (2021).
47. Yi, Q., Huang, W., Yu, W., Li, L. & Liu, X. Hydrothermal synthesis of titanium-supported nickel nanoflakes for electrochemical oxidation of glucose. *Electroanalysis* **20**, 2016–2022 (2008).
48. Zheng, W. *et al.* CuII-Mediated Ultra-efficient Electrooxidation of Glucose. *ChemElectroChem* **4**, 2788–2792 (2017).
49. Moggia, G., Schalck, J., Daems, N. & Breugelmans, T. Two-steps synthesis of D-glucaric acid via D-gluconic acid by electrocatalytic oxidation of D-glucose on gold electrode: influence of operational parameters. *Electrochim. Acta* **374**, 137852 (2021).
50. Moggia, G., Kenis, T., Daems, N. & Breugelmans, T. Electrochemical Oxidation of d -Glucose in Alkaline Medium : Impact of Oxidation Potential and Chemical Side Reactions on the Selectivity to d -Gluconic and d -Glucaric Acid. *ChemElectroChem* **7**, 1–11 (2019).

## References

51. Pasta, M., La Mantia, F. & Cui, Y. Mechanism of glucose electrochemical oxidation on gold surface. *Electrochim. Acta* **55**, 5561–5568 (2010).
52. Dourado, A. H. B. *et al.* In situ FTIR insights into the electrooxidation mechanism of glucose as a function of the surface facets of Cu<sub>2</sub>O-based electrocatalytic sensors. *J. Catal.* **375**, 95–103 (2019).
53. Ishimoto, T., Hamatake, Y., Kazuno, H., Kishida, T. & Koyama, M. Theoretical study of support effect of Au catalyst for glucose oxidation of alkaline fuel cell anode. *Appl. Surf. Sci.* **324**, 76–81 (2015).
54. A. Larew, L. & Johnson, D. C. Concentration dependence of the mechanism of glucose oxidation at gold electrodes in alkaline media. *J. Electroanal. Chem.* **262**, 167–182 (1989).
55. Wang, J., Cao, X., Wang, X., Yang, S. & Wang, R. Electrochemical oxidation and determination of glucose in alkaline media based on Au (111)-like nanoparticle array on indium tin oxide electrode. *Electrochim. Acta* **138**, 174–186 (2014).
56. Tominaga, M. *et al.* Electrocatalytic oxidation of glucose at gold-silver alloy, silver and gold nanoparticles in an alkaline solution. *J. Electroanal. Chem.* **590**, 37–46 (2006).
57. Habrioux, A. *et al.* Activity of platinum-gold alloys for glucose electrooxidation in biofuel cells. *J. Phys. Chem. B* **111**, 10329–10333 (2007).
58. Neha, N., Kouamé, B. S. R., Rafaïdeen, T., Baranton, S. & Coutanceau, C. Remarkably Efficient Carbon-Supported Nanostructured Platinum-Bismuth Catalysts for the Selective Electrooxidation of Glucose and Methyl-Glucoside. *Electrocatalysis* (2020) doi:10.1007/s12678-020-00586-y.
59. Brouzgou, A. & Tsiakaras, P. Electrocatalysts for Glucose Electrooxidation Reaction: A Review. *Top. Catal.* **58**, 1311–1327 (2015).
60. Batchelor, T. A. A. *et al.* High-Entropy Alloys as a Discovery Platform for Electrocatalysis. *Joule* **3**, 834–845 (2019).
61. Li, S. *et al.* Nanoporous high-entropy alloys with low Pt loadings for high-performance electrochemical oxygen reduction. *J. Catal.* **383**, 164–171 (2020).
62. Yeh, J. Recent progress in high-entropy alloys. *Ann. Chim. Sci. des Mater.* **31**, (2014).
63. Chen, Y. Y., Duval, T., Hung, U. D., Yeh, J. W. & Shih, H. C. Microstructure and electrochemical properties of high entropy alloys-a comparison with type-304 stainless steel. *Corros. Sci.* **47**,

## References

- 2257–2279 (2005).
64. Ranganathan, S. Alloyed pleasures : Multimetallc cocktails. **85**, 10–12 (2003).
  65. Cantor, B., Chang, I. T. H., Knight, P. & Vincent, A. J. B. Microstructural development in equiatomic multicomponent alloys. *Mater. Sci. Eng. A* **375–377**, 213–218 (2004).
  66. Tong, C. *et al.* Microstructure Characterization of Al<sub>x</sub>CoCrCuFeNi High-Entropy Alloy System with Multiprincipal Elements. **36**, (2005).
  67. Miracle, D. B. & Senkov, O. N. A critical review of high entropy alloys and related concepts. *Acta Mater.* **122**, 448–511 (2017).
  68. Gludovatz, B. *et al.* A fracture-resistant high-entropy alloy for cryogenic applications. *Science (80-. )*. **345**, 1153–1158 (2014).
  69. Youssef, K. M., Zaddach, A. J., Niu, C., Irving, D. L. & Koch, C. C. A novel low-density, high-hardness, high-entropy alloy with close-packed single-phase nanocrystalline structures. *Mater. Res. Lett.* **3**, 95–99 (2014).
  70. Stepanov, N. D., Shaysultanov, D. G., Salishchev, G. A. & Tikhonovsky, M. A. Structure and mechanical properties of a light-weight AlNbTiV high entropy alloy. *Mater. Lett.* **142**, 153–155 (2015).
  71. Senkov, O. N., Senkova, S. V., Woodward, C. & Miracle, D. B. Low-density, refractory multiprincipal element alloys of the Cr-Nb-Ti-V-Zr system: Microstructure and phase analysis. *Acta Mater.* **61**, 1545–1557 (2013).
  72. Lee, C. P., Chen, Y. Y., Hsu, C. Y., Yeh, J. W. & Shih, H. C. The Effect of Boron on the Corrosion Resistance of the High Entropy Alloys Al<sub>0.5</sub>CoCrCuFeNiB<sub>x</sub>. *J. Electrochem. Soc.* **154**, C424 (2007).
  73. Pedersen, J. K., Batchelor, T. A. A., Bagger, A. & Rossmeisl, J. High-Entropy Alloys as Catalysts for the CO<sub>2</sub> and CO Reduction Reactions. (2020) doi:10.1021/acscatal.9b04343.
  74. Nellaiappan, S. *et al.* High-Entropy Alloys as Catalysts for the CO<sub>2</sub> and CO Reduction Reactions: Experimental Realization. *ACS Catal.* **10**, 3658–3663 (2020).
  75. Feng, G. *et al.* Sub-2 nm Ultrasmall High-Entropy Alloy Nanoparticles for Extremely Superior Electrocatalytic Hydrogen Evolution. *J. Am. Chem. Soc.* **143**, 17117–17127 (2021).
  76. Yang, T. *et al.* Multicomponent intermetallic nanoparticles and superb mechanical behaviors of complex alloys. *Science (80-. )*. **362**, 933–937 (2018).

## References

77. Fu, M., Ma, X., Zhao, K., Li, X. & Su, D. High-entropy materials for energy-related applications. *ISCIENCE* **24**, 102177 (2021).
78. De Marco, M. L. *et al.* High-Entropy-Alloy Nanocrystal Based Macro- and Mesoporous Materials. *ACS Nano* **16**, 15837–15849 (2022).
79. Haché, M. J. R., Cheng, C. & Zou, Y. Nanostructured high-entropy materials. *J. Mater. Res.* **35**, 1051–1075 (2020).
80. Kusada, K., Mukoyoshi, M., Wu, D. & Kitagawa, H. Chemical Synthesis, Characterization, and Properties of Multi-Element Nanoparticles. *Angew. Chemie - Int. Ed.* **61**, (2022).
81. Zhou, Y., Shen, X., Qian, T., Yan, C. & Lu, J. A review on the rational design and fabrication of nanosized high-entropy materials. *Nano Res.* (2023) doi:10.1007/s12274-023-5419-2.
82. Gao, S. *et al.* Synthesis of high-entropy alloy nanoparticles on supports by the fast moving bed pyrolysis. *Nat. Commun.* **11**, (2020).
83. Pittkowski, R. K. *et al.* High entropy alloy nanoparticle formation at low temperatures. doi:10.26434/chemrxiv-2022-khw4t.
84. Scherrer, P. Bestimmung der Größe und der inneren Struktur von Kolloidteilchen mittels Röntgenstrahlen. *Nachrichten von der Gesellschaft der Wissenschaften zu Göttingen, Math. Klasse* **1918**, 98–100 (1918).
85. Wu, D. *et al.* Platinum-Group-Metal High-Entropy-Alloy Nanoparticles. *J. Am. Chem. Soc.* **142**, 13833–13838 (2020).
86. Bard, A. J., Faulkner, L. R. & White, H. S. *Electrochemical methods: fundamentals and applications.* John Wiley & Sons (2022).
87. Belgsir, E. M. *et al.* Electrosynthesis in aqueous medium: a kinetic study of the electrocatalytic oxidation of oxygenated organic molecules. *Electrochim. Acta* **36**, 1157–1164 (1991).
88. Lamy, C. Electrocatalytic oxidation of organic compounds on noble metals in aqueous solution. *Electrochim. Acta* **29**, 1581–1588 (1984).
89. Armstrong, R. D., Hirayama, J., Knight, D. W. & Hutchings, G. J. Quantitative Determination of Pt- Catalyzed d -Glucose Oxidation Products Using 2D NMR. *ACS Catal.* **9**, 325–335 (2019).
90. Tian, Z. *et al.* Selective photoelectrochemical oxidation of glucose to glucaric acid by single atom Pt decorated defective TiO<sub>2</sub>. *Nat. Commun.* **14**, 1–12 (2023).

## References

91. Karra, S., Wooten, M., Griffith, W. & Gorski, W. Morphology of Gold Nanoparticles and Electrocatalysis of Glucose Oxidation. *Electrochim. Acta* **218**, 8–14 (2016).
92. Galant, A. L., Kaufman, R. C. & Wilson, J. D. Glucose: Detection and analysis. *Food Chem.* **188**, 149–160 (2015).
93. Rocklin, R. D. & Pohl, C. A. Determination Of Carbohydrates By Anion Exchange Chromatography With Pulsed Amperometric Detection. *J. Liq. Chromatogr.* **6**, 1577–1590 (1983).
94. Welch, L. E., Mead, D. A. & Johnson, D. C. A comparison of pulsed amperometric detection and conductivity detection for carbohydrates. *Anal. Chim. Acta* **204**, 323–327 (1988).
95. Parpot, P., Muiuane, V. P., Defontaine, V. & Bettencourt, A. P. Electrocatalytic oxidation of readily available disaccharides in alkaline medium at gold electrode. *Electrochim. Acta* **55**, 3157–3163 (2010).
96. Fabrao, R. M., Brito, J. F. de, da Silva, J. L., Stradiotto, N. R. & Zanoni, M. V. B. Appraisal of photoelectrocatalytic oxidation of glucose and production of high value chemicals on nanotube Ti/TiO<sub>2</sub> electrode. *Electrochim. Acta* **222**, 123–132 (2016).
97. Smith, T. N. *et al.* Modifications in the nitric acid oxidation of d-glucose. *Carbohydr. Res.* **350**, 6–13 (2012).
98. Kokoh, K. B., Léger, J. M., Beden, B. & Lamy, C. 'On line' chromatographic analysis of the products resulting from the electrocatalytic oxidation of d-glucose on Pt, Au and adatoms modified Pt electrodes-Part I. Acid and neutral media. *Electrochim. Acta* **37**, 1333–1342 (1992).
99. Wojcieszak, R., Cuccovia, I. M., Silva, M. A. & Rossi, L. M. Selective oxidation of glucose to glucuronic acid by cesium-promoted gold nanoparticle catalyst. *J. Mol. Catal. A Chem.* **422**, 35–42 (2016).
100. John, N. & George, S. *Raman Spectroscopy. Spectroscopic Methods for Nanomaterials Characterization* vol. 2 (Elsevier Inc., 2017).
101. Schlegel, N., Wiberg, G. K. H. & Arenz, M. On the electrooxidation of glucose on gold: Towards an electrochemical glucaric acid production as value-added chemical. *Electrochim. Acta* **410**, 140023 (2022).
102. Ben Mabrouk, K., Kauffmann, T. H., Aroui, H. & Fontana, M. D. Raman study of cation effect on sulfate vibration modes in solid state and in aqueous solutions. *J. Raman Spectrosc.* **44**,

## References

- 1603–1608 (2013).
103. Dinnebier, R. E. & Billinge, S. J. L. *Powder Diffraction: Theory and Practice*. (Royal Society of Chemistry, 2008).
104. Ye, Y. F., Wang, Q., Lu, J., Liu, C. T. & Yang, Y. High-entropy alloy : challenges and prospects. **19**, (2016).
105. Barth, T. & Lund, G. Die Gitterkonstanten der Platinmetalle, Silber und Gold. *Zeitschrift für Phys. Chemie* **121**, 78–102 (1926).
106. Rietveld, H. A profile refinement method for nuclear and magnetic structures, *Journal of Applied Crystallography. J. Appl. Crystallogr.* **2**, 65–71 (1969).
107. Toby, B. H. & Von Dreele, R. B. GSAS-II: The genesis of a modern open-source all purpose crystallography software package. *J. Appl. Crystallogr.* **46**, 544–549 (2013).
108. Penner-Hahn, J. E. X-ray Absorption Spectroscopy. in *Comprehensive Coordination Chemistry II* vol. 2 159–186 (Elsevier, 2003).
109. Bell, D. C. & Garratt-Reed, A. J. *Energy dispersive X-ray analysis in the electron microscope*. (Garlad Science, 2003).
110. Munnik, P., De Jongh, P. E. & De Jong, K. P. Recent Developments in the Synthesis of Supported Catalysts. *Chem. Rev.* **115**, 6687–6718 (2015).
111. Mehrabadi, B. A. T., Eskandari, S., Khan, U., White, R. D. & Regalbuto, J. R. *A Review of Preparation Methods for Supported Metal Catalysts. Advances in Catalysis* vol. 61 (Elsevier Inc., 2017).
112. Guo, S. *et al.* Efficient base-free direct oxidation of glucose to gluconic acid over TiO<sub>2</sub> - supported gold clusters. *Nanoscale* **11**, 1326–1334 (2019).
113. Owen, E. A. & Yates, E. L. Precision measurements of crystal parameters. *London, Edinburgh, Dublin Philos. Mag. J. Sci.* **15**, 472–488 (1933).
114. Burke, L. D. & Nugent, P. F. The electrochemistry of gold: I. The redox behaviour of the metal in aqueous media. *Gold Bull.* **30**, 43–53 (1997).



## **7 Appended Manuscripts**

In this section, the four manuscripts, including the respective supporting information, discussed as parts of this thesis are appended.

**Manuscript I**

Nicolas Schlegel, Gustav K.H. Wiberg, Matthias Arenz

**On the electrooxidation of glucose on gold: Towards an electrochemical glucaric acid production as value-added chemical**

*Electrochimica Acta* **410**, 140023 (2022)

<https://doi.org/10.1016/j.electacta.2022.140023>



# On the electrooxidation of glucose on gold: Towards an electrochemical glucaric acid production as value-added chemical

Nicolas Schlegel, Gustav K.H. Wiberg, Matthias Arenz\*

Department of Chemistry, Biochemistry and Pharmaceutical Sciences, University of Bern, Freiestrasse 3, 3012 Bern, Switzerland

## ARTICLE INFO

### Keywords:

Glucose oxidation reaction  
Gold electrode  
Glucaric acid  
Gluconic acid  
Value-added chemical production

## ABSTRACT

The electrocatalytic oxidation of glucose to value-added chemicals, such as glucaric acid, has gathered increased interest in recent years. Glucose oxidation is a promising process which has the potential to contribute to establishing renewable resources as alternatives to fossil carbon sources. Herein, we present rotating disk electrode (RDE) studies on polycrystalline gold surfaces and subsequent Koutecký-Levich analysis as a benchmark to expand the understanding of reaction kinetics and competition between glucose, reaction intermediates and  $\text{OH}^-$  at the catalyst surface. Based on the obtained results it follows that the glucose oxidation reaction (GOR) is predominately mass-transport controlled. Combining electrochemical studies and Raman spectroscopy, it is shown that increasing glucose concentrations lead to a delayed oxidation of the gold catalyst surface, presumably by increased consumption rates of Au-hydroxide species.

## 1. Introduction

Gluconic and glucaric acids, both Glucose derivatives, have received increased attention after being labelled top value-added chemicals by the U.S Department of Energy [1]. Gluconic acid finds its main application in the food industry, while also being used in pharmaceutical and hygienic products [2]. Glucaric acid is a precursor of adipic acid, an immensely important commodity chemical, renowned for being a building block for Nylon [3]. In the future, these glucose derivatives could be introduced as an alternative carbon source in the chemical industry, thereby contributing to the development of a closed anthropogenic carbon-cycle and the independence from fossil resources.

Historically, synthesis methods for gluconic and glucaric acid require harsh conditions demanding high temperatures, strong oxidants (NaBr and NaOCl [4,5]) and struggle with product selectivity. Alternatively, an electrochemical conversion approach can promise milder reaction conditions for the oxidation and can potentially make use of peak surplus renewable electricity. Furthermore, when the oxidation is done electrochemically, the product distribution is a function of the applied overpotential. Other key parameters for the product selectivity include the nature of the catalytic electrode and ad-atoms there on as well as the availability of hydroxide ions [6–8]. The most promising catalyst materials to date have been found to be Gold [9–14] and Platinum [15–18], which readily oxidize glucose in alkaline medium.

The electrochemical glucose oxidation typically generates a host of products. For example, Kokoh et al. [15] detected small carboxylic species, formed by breaking C—C bonds in the glucose, showing that gluconic acid is not the final oxidation product. Moggia et al. [19] recently reported that gold is able, in a two-step oxidation, to convert glucose to glucaric acid, with the reaction intermediate being gluconic acid. This makes gold an even more desirable catalyst material.

The general reaction mechanism of the glucose oxidation has been at the heart of a number of investigations [20–24]. A key step in the oxidation mechanism of glucose on gold catalysts is the formation of an OH-ad-atoms species and the availability of  $\text{OH}^-$  at the catalytic interface in general [25]. Hence, alkaline conditions have long been considered optimal. Rotating disk electrode (RDE) studies on polycrystalline gold electrodes by Larew and Johnson [12] found that the surface oxide formation caused deactivation of the gold electrode. To complicate the matter, the deactivation also depended on the glucose concentration. More specifically, with increasing glucose concentration the gold oxidation was shifted to more positive overpotentials. The authors have ascribed this phenomenon to adsorbed glucose molecules blocking the gold surface.

The behaviour of glucose oxidation on metal electrodes has proven to be complex. Oscillatory behaviour has been observed [26–28], similar to other small organic molecules such as methanol [29], ethylene glycol [30] and formic acid [31]. These oscillations suggest temporary surface

\* Corresponding author.

E-mail address: [matthias.arenz@unibe.ch](mailto:matthias.arenz@unibe.ch) (M. Arenz).

<https://doi.org/10.1016/j.electacta.2022.140023>

Received 6 October 2021; Received in revised form 12 January 2022; Accepted 2 February 2022

Available online 5 February 2022

0013-4686/© 2022 The Authors.

Published by Elsevier Ltd.

This is an open access article under the CC BY-NC-ND license

(<http://creativecommons.org/licenses/by-nc-nd/4.0/>).

poisoning either by oxygenated species or glucose residue. Implications arise from this behaviour for the design of more efficient electrocatalysts as they should have a high tolerance for these poisoning species and be able to catalyse more than just one of the reaction steps if glucaric acid is the desired product.

Hence, more insight on these results is still required for the design of an efficient reactor as finding stable electrolysis conditions turns out to be challenging. Potential programs involving three steps have been discussed: First, at low potential, the glucose adsorbs on the catalyst surface. In a second step, the glucose is then oxidized and later, in the third step at very high potentials, the surface is cleaned from all adsorbed species. This stepped program is then repeated for the duration of the operation [32]. Future more elegant solutions are expected to be helpful to increase the catalyst's overall efficiency.

This present work seeks to expand and advance the understanding of the reaction kinetics of the glucose oxidation reaction on gold, especially in the potential region close to the deactivation through gold oxidation. RDE setup using cyclic voltammetry and galvanostatic electrolysis provide the bulk of the experimental data. An RDE approach was chosen as it became obvious that mass transport limitations are reached easily in the glucose oxidation reaction. Operation under mass transport limitations would have meant the loss of valuable insight that influences the design of prospective catalysts and electrolysis setups. With the gathered insight we deem to identify several key aspects for an efficient electrochemical conversion setup.

## 2. Experimental

### 2.1. Chemicals & reagents

Ultra-pure water (MiliQ-systems, 2.7 ppb TOC, 18.2 M $\Omega$ ) was used for all cleaning purposes and to prepare the supporting electrolyte adding sodium hydroxide monohydrate ( $\geq 99.99\%$ , suprapur, Merck) and sodium sulfate ( $\geq 99.0\%$  Sigma Aldrich). D-glucose ( $\geq 99.5\%$ ) and the D-gluconic acid sodium salt ( $\geq 99.0\%$ ) were also obtained from Sigma Aldrich. Argon gas ( $\geq 99.99\%$ , PanGas) was used to purge the electrolyte before experiments and to create slight overpressure in the headspace during operation. The Argon was also used to dry electrode tips and cell parts. Sodium sulfate was added to the electrolyte to yield a final concentration of 0.1 M with the purpose of ensuring sufficient electrolyte conductivity, thereby minimising internal resistances in the electrochemical setup.

### 2.2. Electrochemical setup

A polycrystalline gold-disc (geometric surface area of 0.196 cm<sup>2</sup>) embedded in Teflon served as the working electrode for the RDE studies. The working electrode was polished in an alumina slurry (0.3  $\mu$ m MicroPolish, Buehler) on a polishing cloth (MicroCloth, Buehler) followed by sonicating two times in high-purity water for 3 min each. Then, the Teflon tips were mounted onto a EDI101 rotating disk electrode assembly (Hach-Lange), which was controlled by a CTV101 speed control unit (Radiometer analytical) that was connected to the potentiostat software via plug-in. Furthermore, gold mesh was used as counter electrode. Then the reference electrode, a trapped hydrogen electrode, was produced in-situ by applying  $-8.00$  mA to a dedicated Pt-wire, which was situated in a glass tube.

All RDE experiments were performed in a custom-built one-compartment glass cell (Figure S1). For cleaning, the cell was boiled in 25% HNO<sub>3</sub> followed by boiling twice in ultra-pure water. Between individual experiments the cell was thoroughly rinsed and boiled with ultra-pure water. After filling the electrolyte into the cell, it was purged with Argon gas for 25 min. Potential and electrical current were controlled with an ECI-210 potentiostat using the software EC4 DAQ 4.2, (both Nordic Electrochemistry ApS). Thereafter, the reactant was introduced to the cell, followed by 15 min continued purging with Argon

gas. The galvanostatic experiments were conducted in the same setup, which was treated identically in terms of preparation, by applying absolute integer currents to the working electrode. The resulting geometric current densities (mA cm<sup>-2</sup><sub>geo</sub>) were determined by multiplying the electrode area of 0.196 cm<sup>2</sup> with the applied current.

In order to minimize the potential error due to the iR-drop, before starting the experiments, the solution resistance of the setup was determined by electrochemical impedance spectroscopy (EIS) and subsequently compensated for by following a standardised protocol. First, the working electrode potential was held at 0.3 V<sub>RHE</sub>, in the double layer region of gold. An AC perturbation of 5 kHz and an amplitude of 10 mV was applied in order to measure the effective solution resistance online. An analogue feedback scheme of the potentiostat was applied, and the feedback increased until the control system was almost rendered unstable, as indicated by noise spikes in the frequency analysis of the measured signal. EIS was subsequently performed within a frequency range of 1 kHz to 50 kHz and an amplitude of 10 mV. From this measurement the apparent solution resistance was determined to be less than 3  $\Omega$ .

### 2.3. Raman spectroscopy

The Raman spectroscopy experiments were conducted with a Lab-RAM HR800 confocal Raman microscope (Horiba Jobin Yvon) and a custom-built polychlorotrifluoroethylene Kel-F cell (Figure S2) used previously [33]. The excitation laser wavelength was 633 nm, typically operating with a power of 17 mW. A 10x magnification long-working-distance objective (10.5 mm) was used to focus the laser onto the sample and to collect the scattered light in a backscattering geometry. The collection time of the Raman spectra was typically 1 second. The WE, a polycrystalline gold bead electrode was aligned parallel to the quartz-window (EMATAG AG). A coiled Pt-wire was used as counter electrode, a leakless micro Ag/AgCl (ET069-1, eDAQ) reference electrode was used, and the potential was controlled using an ECI-100 potentiostat (Nordic Electrochemistry ApS). Working electrode and electrolyte were treated identically as in the RDE experiments, the only alteration was that the Ar purging took place in an external bubbler from which the electrolyte then was pumped into the electrochemical cell.

## 3. Results and discussion

We start the discussion of the results with the cyclic voltammograms (CV) of a polycrystalline gold disc-electrode in the base electrolyte, i.e., the 0.1 M NaOH + 0.1 M Na<sub>2</sub>SO<sub>4</sub> aqueous electrolyte without glucose, see Fig. 2a. The CVs serve as reference for the interaction of Au with the base electrolyte, knowledge that is important for the discussion of the reaction pathway of the glucose oxidation. In the positive going scan, between 0.3 and 1.2 V<sub>RHE</sub> the typical double layer region of Au is

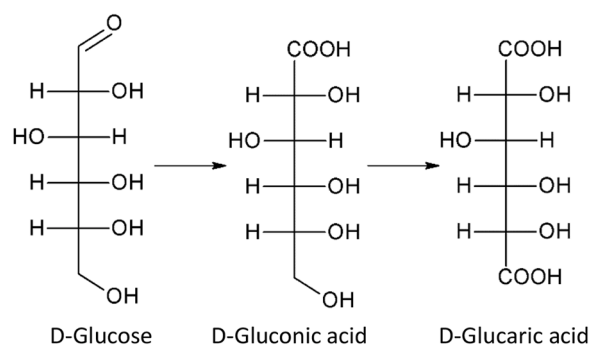
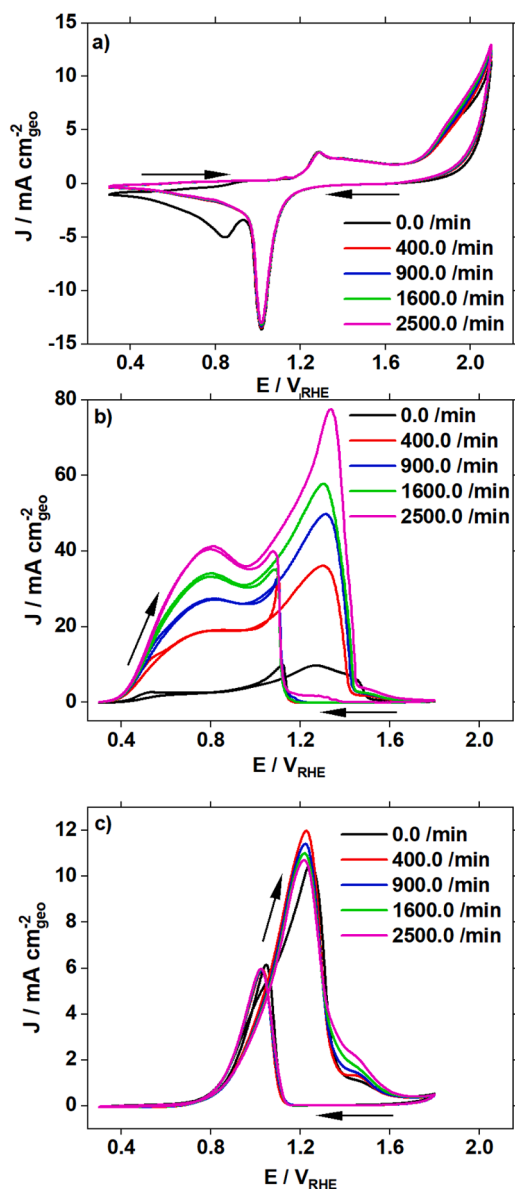


Fig. 1. Proposed two step oxidation from glucose to glucaric acid via gluconic acid.



**Fig. 2.** Cyclic voltammograms recorded with a scan rate of  $50 \text{ mV s}^{-1}$  on a polycrystalline Au-RDE in  $0.1 \text{ M NaOH}$  and  $0.1 \text{ M Na}_2\text{SO}_4$ ; a) without glucose; b)  $50 \text{ mM}$  glucose; c)  $50 \text{ mM}$  gluconic acid. All measurements were recorded at room temperature. The arrows indicate the scan direction.

observed followed by a distinct peak after ca.  $1.25 V_{\text{RHE}}$ , which can be attributed to the formation of gold hydroxide-species [34]. At potentials  $> 1.8 V_{\text{RHE}}$  overlap of oxygen evolution (OER) and gold oxide ( $\text{AuO}_2$ ) formation is observed. Reversing the scan direction, the oxidized Au-electrode reduces to metallic gold at ca.  $1.1 V_{\text{RHE}}$  after which once more the double layer region is observed. The hysteresis between the formation and reduction of gold points towards an irreversible and rather sluggish process. In the absence of glucose (see Fig. 2a) different rotation rates do not significantly influence the features of the voltammograms. Only slight deviations in current density are seen in the potential region of the OER. Furthermore, if the Au electrode is not rotated a small additional peak occurs after the Au reduction peak, i.e., at ca.  $0.85 V_{\text{RHE}}$ , which is assigned the oxygen reduction reaction from the oxygen evolved at high potentials. If the electrode is rotated this oxygen in solution is efficiently transported away from the Au surface. This interpretation is in agreement with the concomitant “bending” of the CV after the additional peak in the absence of rotation.

When glucose is introduced to the cell, Fig. 2b, two distinct new

peaks are observed in the forward going scan. The maximum of the first peak is observed at  $0.8 V_{\text{RHE}}$ , whereas the maximum of the second is observed between  $1.3$  and  $1.35 V_{\text{RHE}}$ . The two peaks are followed by the deactivation of the Au surface towards the glucose oxidation reaction (GOR). During the negative going backward scan a rather “abrupt” re-activation towards GOR at  $1.1 V_{\text{RHE}}$  is observed. After the reactivation the currents observed during forward and backward scan are identical. Comparing the CV recorded in the base electrolyte to the CV recorded in the presence of glucose it becomes apparent that the oxidation state of the Au surface drastically influences its activity towards the GOR. The observed surface deactivation in the presence of glucose coincides with the formation of surface oxides in the base electrolyte at  $1.25 V_{\text{RHE}}$ . Similarly, the surface re-activation overlaps with the observed reductive current in the base electrolyte at  $1.1 V_{\text{RHE}}$ . Hence, the reduction of the surface leads to its re-activation and once again the GOR sets in.

Concentrating on the two peaks that indicate glucose oxidation, as shown in Fig. 2b, the magnitude of the peak currents depends on the rotation rate, but no clear-cut current plateau regions are present. This indicates that the oxidation glucose process at this concentration range is at a mixed kinetic-mass transport limited. The dependence of the peak current on the rotation rate strongly suggests that in contrast to most published work, investigating the reaction with forced convection is preferable in order to distinguish between kinetic and mass-transport limited processes. In previous work, the potential of the peak at  $0.8 V_{\text{RHE}}$  was linked to the oxidation of glucose to gluconic acid, whilst the potential of the second peak seems to be related to the gluconic acid oxidation, possibly yielding glucaric acid [19]. To re-assess this hypothesis, we recorded CVs in the presence of gluconic acid instead of glucose, Fig. 2c. The results support the hypothesis in so far that only the peak at  $1.3 V_{\text{RHE}}$  is observed. It can be noticed that the oxidation currents of gluconic acid do not depend on the rotation rate. Instead, they even seem to slightly decrease with increasing rotation rate. These observations lead us to the conclusion that the gluconic acid oxidation process is purely kinetically controlled under the investigated experimental conditions. Additionally, a comparison between the current densities of glucose oxidation in Fig. 2b and gluconic acid oxidation in Fig. 2c implies that if the GOR proceeds via the “gluconic acid pathway”, the second peak in the CV is indeed due a parallel or competitive oxidation process of glucose and gluconic acid, respectively, as well as potential additional reaction intermediates. That is, in this potential region most likely both processes compete for active sites on the catalyst surface.

Next, we investigate the GOR in a lower hydroxide concentration. In Fig. 3 CVs (only the forward scans are shown) recorded at different rotational rates with different glucose concentration in a  $0.02 \text{ M NaOH}$  (Figure S3 depicts rotation series for the individual glucose concentrations) and  $0.1 \text{ M Na}_2\text{SO}_4$  base electrolyte are compared. In Fig. 3a, where  $400 \text{ rpm}$  are applied, an oxidative current is observed, setting in after  $0.4 V_{\text{RHE}}$ . For lower glucose concentrations (black and red line) a distinct second peak is observed after  $1.2 V_{\text{RHE}}$ . For higher glucose concentrations ( $30 - 50 \text{ mM}$ ) a current plateau is observed after reaching the respective maximum current at  $0.7 V_{\text{RHE}}$ , which indicates that the predominant process is mass transport limited. At  $30 \text{ mM}$  glucose concentration (blue line) a small indentation (local minimum) can be seen at  $0.9 V_{\text{RHE}}$ . Then, depending on the glucose concentration, a deactivation of the surface towards GOR occurs between  $1.3$  and  $1.5 V_{\text{RHE}}$ . Interestingly, the maximum current density is inversely correlated to the reactant concentration as the highest and lowest maximum current density are recorded at  $10 \text{ mM}$  and  $50 \text{ mM}$  glucose, respectively.

Increasing the rotation rate to  $900 \text{ rpm}$  in Fig. 3b increased current densities are measured, while the general shapes of the CVs closely resemble the CVs in Fig. 3a. These observations match the ones from Fig. 2. The indentation in the CVs recorded with  $30 \text{ mM}$  glucose concentration (blue line) has become more pronounced, also a small indentation can be observed at  $40 \text{ mM}$  glucose (green line). However,

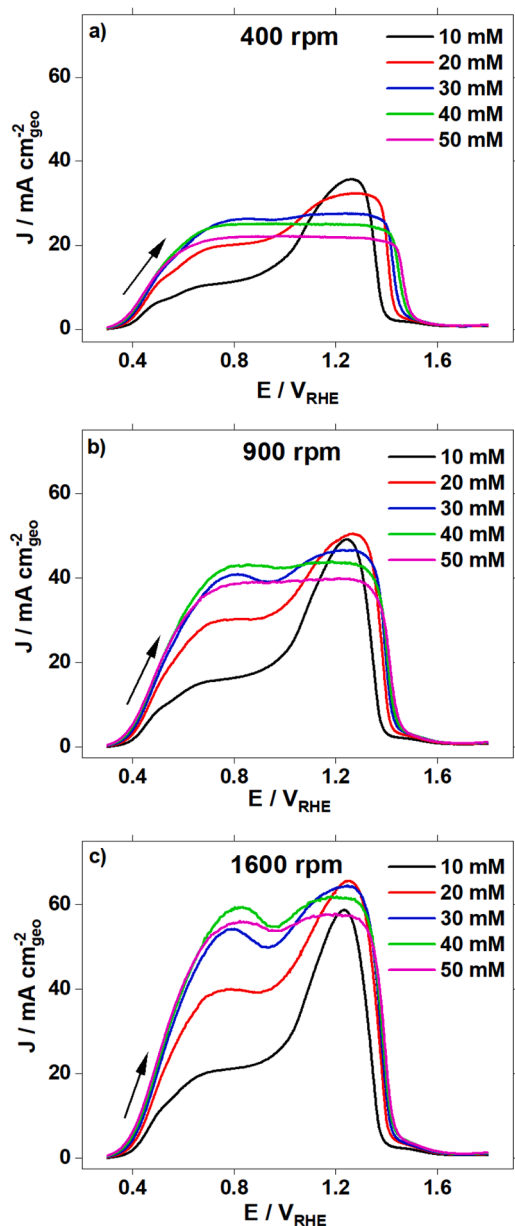


Fig. 3. Cyclic voltammograms recorded with a scan rate of  $50 \text{ mV s}^{-1}$  on a polycrystalline Au-RDE (only forward scans are shown) in  $0.02 \text{ M NaOH}$  and  $0.1 \text{ M Na}_2\text{SO}_4$  with  $10 \text{ mM}$  -  $50 \text{ mM}$  glucose added. a)  $400 \text{ rpm}$ ; b)  $900 \text{ rpm}$ ; c)  $1600 \text{ rpm}$ . All measurements were recorded at room temperature. The arrows indicate the scan direction.

the maximum current density is notably different and is now observed at a glucose concentration of  $20 \text{ mM}$  (red line). At  $1600 \text{ rpm}$  (Fig. 3c) no current plateaus are visible anymore, even the current density at  $50 \text{ mM}$  glucose concentration (magenta line) is slightly indent which means that no mass transport limitations are reached. The shapes of the CVs recorded with  $10$  to  $30 \text{ mM}$  glucose concentration do not change significantly as compared to Fig. 2b and two distinct peaks attributed to the GOR are recorded.

We suggest that the observed CVs can be explained by a “three-way interaction” between  $\text{OH}^-$ , glucose and reaction intermediates (e.g. gluconic acid) at the surface. Because of the low hydroxide concentration of only  $0.02 \text{ M}$  in the electrolyte,  $\text{OH}^-$  at the solid-liquid interface is quickly depleted by the ongoing GOR. This hypothesis would explain the current plateaus observed for higher glucose concentration at lower rotational speed (Fig. 3a) as the rate of mass transport to the surface is

smaller than the rate of  $\text{OH}^-$  consumption thereat. Meanwhile, higher glucose availability at the interface, through higher starting concentrations, leads to higher rates of formation of reaction intermediates, presumably gluconic acid. The formed intermediates then compete with glucose for active sites on the gold surface. It was suggested that the peak at  $1.2 \text{ V}_{\text{RHE}}$  is an overlap of glucose and gluconic acid oxidation. However, our data show that these processes are controlled differently. Glucose oxidation is mixed kinetic-mass transport limited whereas the oxidation of gluconic acid is shown to be kinetically controlled. The ratio between glucose and gluconic acid at the interface therefore influences the overall observed current. A comparison of the CVs recorded with  $10 \text{ mM}$  glucose concentration (black line) and with  $50 \text{ mM}$  glucose concentration (magenta line) from Fig. 3a illustrates this point. The lower observed current density at  $10 \text{ mM}$  glucose concentration between  $0.4$  and  $0.9 \text{ V}_{\text{RHE}}$  indicates a lower rate of reaction intermediate (e.g. gluconic acid) formation than at  $50 \text{ mM}$  glucose concentration. Therefore, there is less competition for active sites at higher potentials which manifests itself in the higher current density at  $10 \text{ mM}$  glucose concentration. Shifting the mass transport limitations by increasing the rotation rate allows for higher maximum current densities at higher glucose concentrations (red CVs in Fig. 3b, c).

Working with an RDE setup opens the possibility of deconvoluting kinetic and mass-transport processes. Using the Koutecký-Levich analysis [35] (Figure S4), we analysed the data at every  $5 \text{ mV}$  from the recorded voltammograms by first plotting the data in a Koutecký-Levich plot at each specific potential as previously done by Zana et al. [36]. From the slope and y-axis-intersect we determined the so called Levich constant as well as the kinetically limiting current in the limit of infinite mass transport. Here we assume that the measured current is limited by the diffusion of glucose. From the Levich constant we calculated the numbers of transferred electrons using  $6.7 \times 10^{-10} \text{ m}^2/\text{s}$  as the diffusion coefficient for glucose and  $1.203 \times 10^{-6} \text{ m}^2/\text{s}^{1/2}$  as the viscosity of the electrolyte solution. The results are shown in Fig. 4. Alternatively, the number of transferred electrons can be determined by potential-controlled coulometry (see Figure S5 in the supporting information). However, a clear advantage of employing the RDE-technique over coulometry is the substantially lower time required for the experiment. One exhaustive coulometry measurement at a certain potential requires more than  $20 \text{ h}$  during which processes like fouling might take place. Also, the obtained data must be fitted, which in turn is a possible source of error. On the other hand, a single RDE-measurement delivers the number of transferred electrons as a function of potential for the entire scan range within one hour.

For GOR the analysis shows that the number of transferred electrons depends on the applied voltage for both  $0.1 \text{ M}$  and  $0.02 \text{ M NaOH}$  concentration (Fig. 4a and c). At glucose concentrations of  $0.5 \text{ mM}$ ,  $5 \text{ mM}$ ,  $10 \text{ mM}$ , and  $50 \text{ mM}$  in  $0.1 \text{ M NaOH}$  (Fig. 4a), as well as  $10 \text{ mM}$  and  $20 \text{ mM}$  in  $0.02 \text{ M NaOH}$  (Fig. 4c), the number of transferred electrons is close to two at potentials between  $0.4 \text{ V}_{\text{RHE}}$  and  $0.6 \text{ V}_{\text{RHE}}$ . Then an increase in transferred electrons is observed reaching its maximum at  $1.2 \text{ V}_{\text{RHE}}$ . At higher glucose concentration, specifically  $500 \text{ mM}$  in  $0.1 \text{ M NaOH}$  as well as  $40 \text{ mM}$  and  $50 \text{ mM}$  in  $0.02 \text{ M NaOH}$  the number of transferred electrons stays constant as a function of potential. Crucially, less than one electron is transferred per molecule of glucose.

To oxidize glucose to gluconic acid two electrons are required, to react gluconic to glucaric acid an additional four electrons must be transferred. Hence, to oxidize glucose to glucaric acid requires six electrons in total. It follows that glucaric acid is not the final oxidation product whenever more than six electrons are transferred. This can occur via the breaking of the carbon chain [15] and oxidising glucose fully to  $\text{CO}_2$  requires  $24$  electrons [28]. As previously mentioned, the obtained data shows the number of transferred electrons changes as a function of potential (Fig. 4a and c), which indicates the occurrence of different oxidation processes at the gold surface: At small applied potentials, when only two electrons are transferred, gluconic acid is a likely product. When the applied overpotential is increased the number of

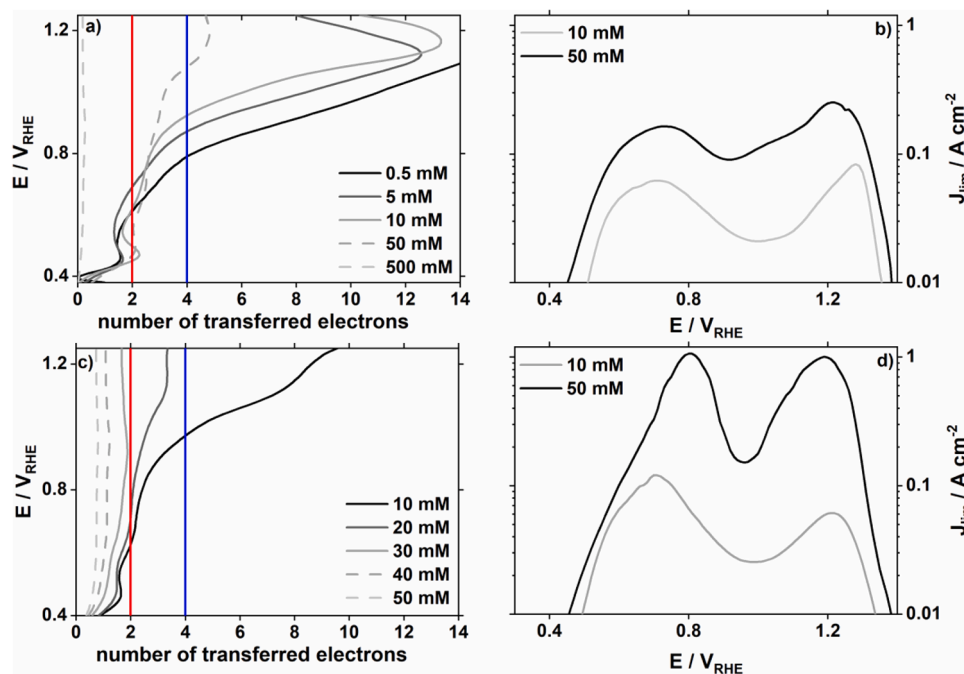


Fig. 4. Koutecký-Levich analysis of RDE-measurement on an Au-disc in 0.1 M Na<sub>2</sub>SO<sub>4</sub> and in different concentrations of glucose: a) numbers of transferred electrons in 0.1 M NaOH; b) kinetically limited current in 0.1 M NaOH; c) numbers of transferred electrons in 0.02 M NaOH; d) kinetically limited current in 0.02 M NaOH.

transferred electrons drastically changes. In the case of 50 mM glucose concentration in 0.1 M NaOH (Fig. 4a) approximately four electrons are transferred between 1.0  $V_{RHE}$  and 1.2  $V_{RHE}$ . Possible products include glucuronic acid, or glucaric acid from gluconic acid. At lower glucose concentrations (0.5 mM to 10 mM) in 0.1 M NaOH (Fig. 4a) more than ten electrons are transferred. Possible products in these cases probably include small organic acids and CO<sub>2</sub>. At 0.02 M NaOH a similar trend is observed: At 10 mM glucose concentration the transfer of more than ten electrons signifies the oxidation past glucaric acid. 20 mM and 30 mM glucose concentrations lead to the partial oxidation to a desired product. In case of higher glucose concentrations, the number of transferred electrons is smaller than one. These observations can be explained by OH<sup>-</sup> scarcity at the catalyst surface which results in a fraction of glucose molecules arriving at the surface and leaving it again unreacted. The same is the case for a glucose concentration of 500 mM in 0.1 M NaOH. The ratio of glucose concentration and hydroxide concentration is therefore an important measure for the glucose oxidation process as a delicate balance between OH<sup>-</sup> and glucose concentration must be reached for the oxidation process to yield desired products: Sufficient OH<sup>-</sup> has to be present at the surface for every reactant to react but OH<sup>-</sup> must not be over-abundant for the reactant to become oxidized past glucaric acid.

In Fig. 4b and d the apparent kinetically limited currents are shown for 10 mM and 50 mM concentration of glucose in 0.1 M NaOH and 0.02 M NaOH respectively. In both cases local maxima for the kinetically limited currents can be found. The first at approximately 0.7  $V_{RHE}$  in the case of 0.1 M NaOH (Fig. 4b) and at 0.8  $V_{RHE}$  in the case of 0.02 M NaOH concentration. The second maximum is observed 1.2  $V_{RHE}$ . In both cases, the obtainable current density correlates with the concentration of glucose: Higher glucose concentration leads to larger kinetically limited current densities. Interestingly, we calculated larger limiting current densities for 0.02 M NaOH concentration (1 A/cm<sup>2</sup>) than at 0.1 M NaOH concentration (250 mA/cm<sup>2</sup>). One would intuitively assume that higher OH<sup>-</sup> availability would increase the achievable maximum current densities, however that does not seem to be the case.

Comparing the experimentally recorded current densities (Figs. 2 and 3) to the maximum current densities calculated by means of the Koutecký-Levich analysis, the data indicate that under all experimental

conditions the reaction is governed by mass transport limitations, even at high rotation speeds. This observation further supports the need for reaction application that make use of force convection. Also, if one wants to gather a deepened understanding of the underlying reaction mechanisms the effect of mass transport has to be considered and accounted for.

The importance of OH<sup>-</sup> availability at the catalyst surface is further illustrated by RDE-experiments on the Au-disc at glucose concentrations of 10 mM to 60 mM (Fig. 5a). With increasing glucose concentration, the peak potential shifts from 1.23  $V_{RHE}$  towards 1.5  $V_{RHE}$ . Accordingly, the deactivation of the gold surface is also shifted towards larger overpotentials. Similar observations have been made by Larew and Johnson [12]. They suggested that this phenomenon is caused by surface blockage of adsorbed glucose. If this was the case, the current would not increase as a function of rotation but would be independent from it. However, as shown in Fig. 2b, a clear dependence of the current on the rotation speed is observed. We suggest therefore, that the observed shift is caused by continuous consumption of adsorbed OH<sup>-</sup><sub>ads</sub> which is a crucial species for the ongoing GOR. When increasing the glucose concentration, more reactant is transported to the catalyst surface leading to increased consumption of already formed hydroxide species, thereby delaying the oxidation of gold. Upon further increase of the overpotential the driving force for the surface oxidation increases until the rate of oxide formation surpasses the rate of consumption. Finally, gold is oxidized and the surface becomes inactive. One concern with testing this hypothesis is the compensation of internal resistance in the electrochemical setup (iR drop). Insufficient or wrong compensation would lead to same observed shift in peak maximum. However, Fig. 3a shows that the shift does not follow the current density but rather the glucose concentration. The highest maximum current density is recorded at a glucose concentration of 10 mM added to the base electrolyte, but the largest deactivation potential is observed at glucose concentration of 50 mM. Thus, the internal cell resistance can be ruled out as the primary cause for the shift in oxidation potential. The experiments performed at glucose concentrations of 20 to 40 mM confirm this trend: Higher glucose concentrations in the base electrolyte lead to larger deactivation potentials but smaller peak maxima.

Discussions of reaction mechanisms based on CVs are always limited.

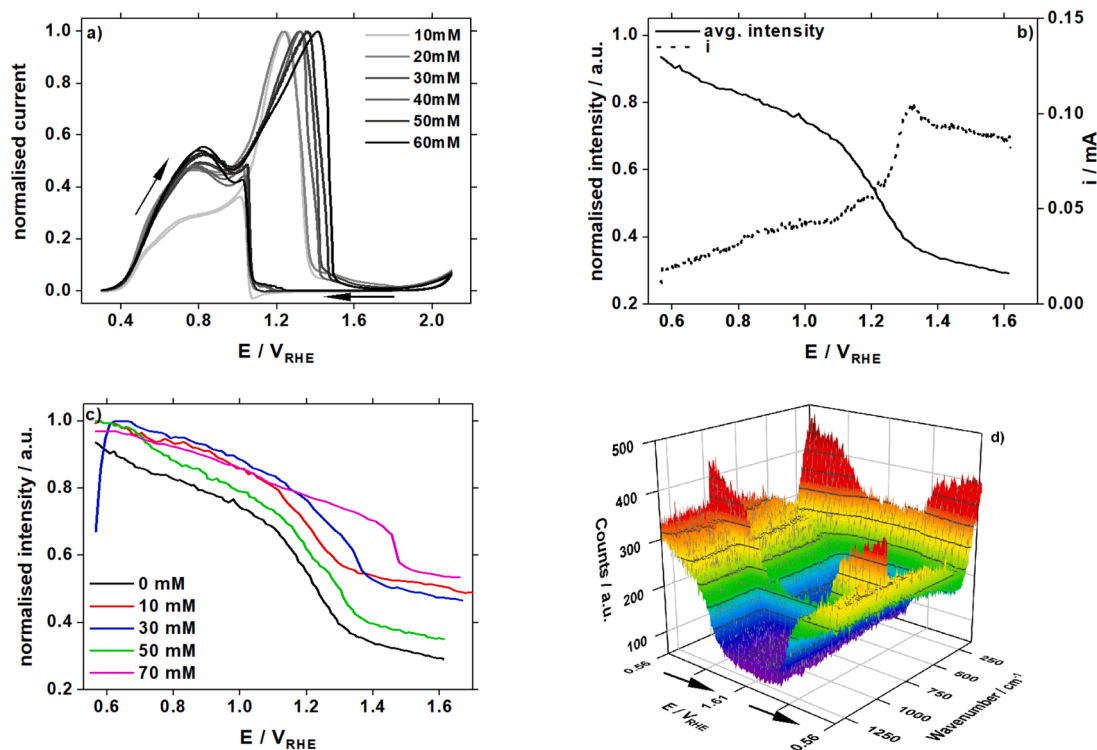


**Fig. 5.** a) 10–60 mM glucose concentration in 0.1 M NaOH and 0.1 M Na<sub>2</sub>SO<sub>4</sub> at 2500 rpm with normalized currents [ $J/J_{\max}$ ], arrows indicate the scan direction; b) averaged recorded intensities (400 cm<sup>-1</sup> to 890 cm<sup>-1</sup>) as a function of potential (left y-axis) and corresponding CV recorded on Au-bead (right y-axis); c) comparison of averaged intensities at different glucose concentrations, 0 mM to 70 mM. d) colour map of Raman spectra continuously recorded during cyclic voltammetry (7 mV s<sup>-1</sup>) in the absence of glucose. All measurements were recorded at room temperature.

Therefore, Raman spectroscopy was used to follow the catalyst surface under reaction conditions and thus gaining spectroscopic insight about the surface state. In-situ measurements during cyclic voltammetry were conducted. Glucose at the interface proved to be difficult to detect due to its low normal Raman scattering (NRS) cross section [37], however, it was noticed that the oxidation state of the gold surface can be tracked, similar to what Pérez-Martínez et al. have reported for glycerol oxidation on gold using visible reflectance and ATR-SEIRAS [38]. Raman spectra were continuously recorded in the range of 200 cm<sup>-1</sup> to 1300 cm<sup>-1</sup> while cycling a gold bead electrode between 0.57 and 1.67 V at 7 mV s<sup>-1</sup>. At 981 cm<sup>-1</sup> a characteristic sulphate peak (symmetric stretching) [39] stemming from the base electrolyte can be observed during the entire CVs, i.e., in the whole covered potential region. The surface reflectance, which we consider to be the background of the spectra, changes as the CVs progress. Fig. 5d shows a colour map of the continuously recorded spectra during a CV. The reflectance dips into a well (blue part of the colour map) and returns to the initial intensity during the backwards scan. In the range of 400 cm<sup>-1</sup> and 890 cm<sup>-1</sup>, where no peaks are detected, the intensities were averaged to minimize the influence of spike signals. Then the averaged intensity was plotted against the recorded CV, see Fig. 5b, where an Au-bead electrode was cycled in the base electrolyte in the absence of glucose. In a first approximation the surface can be considered oxidized at the peak maximum at 1.35 V<sub>RHE</sub><sup>34</sup>. Accordingly, the averaged background reflectance has decreased. We therefore conclude that the observed change in reflectance is connected to the oxidation state of the gold surface: gold hydroxide exhibits a significantly lower reflectance than metallic gold. It follows that the reflectance can be used to observe the oxidation state of the gold electrode.

The experiment was repeated in the presence of different glucose concentrations (Fig. 5c). The trend of delayed oxidation is observed through the reflectance in comparison to glucose free electrolyte (black line). A gradual shift towards higher oxidation potentials is visible from

10 mM (red), 30 mM (blue) to 70 mM (magenta) glucose. The spectra recorded in 50 mM (green) glucose do not match this trend (yet they are reproducible) with the reason being unclear to us. Nonetheless, the observed overall trend spectroscopically supports the electrochemical observation of delayed gold oxidation as a function of glucose concentration as the reactant temporarily hinders the formation of gold oxide

The complex nature of the glucose oxidation mechanism is showcased by Fig. 6 and Fig. 7. Galvanostatic electrolysis RDE-experiments on Au-discs were conducted where we observed three distinct potential regions at which the electrolysis takes place. This is depicted exemplarily in Fig. 6a. Three potential plateaus can be discerned labelled as (1–3): (1) 0.75 V<sub>RHE</sub> – 0.88 V<sub>RHE</sub>, (2) 1.1 V<sub>RHE</sub> – 1.3 V<sub>RHE</sub> and (3) >2.45 V<sub>RHE</sub>. When the electrolysis takes place within the potential range of one of the observed plateaus, a very slow but steady increase in potential is observed. Upon reaching a potential threshold the electrolysis potential “jumps” abruptly to the next potential plateau with the progression in potential always going from the potential region (1) to (2) and finally plateau (3). The potential gradient ramping towards a threshold changes as a function of glucose concentration, applied current densities and rotation rates. Potential region 3 can be ruled out as a GOR-active potential because the gold surface is oxidized and therefore inactive towards glucose oxidation, as observed in Figs. 2 and 3. Therefore it can be assumed that the recorded current is mainly due to the OER proceeding on the gold oxide surface. The potential ranges of (1) and (2) match the potentials of the peaks observed in the CVs as visualized in Fig. 6b where the recorded electrolysis potential (black line) is plotted against a CV recorded with 2500 rpm (red line, right y-axis). It is clearly seen that the transition between potential plateaus coincides with the changes in the oxidation state of the gold surface. Thus, the electrolysis potential will never change back to a lower potential region because no “reducing potential” is applied to the catalyst surface. The introduction of rotation to the galvanostatic electrolysis increases the time before the catalyst becomes inactive towards the GOR



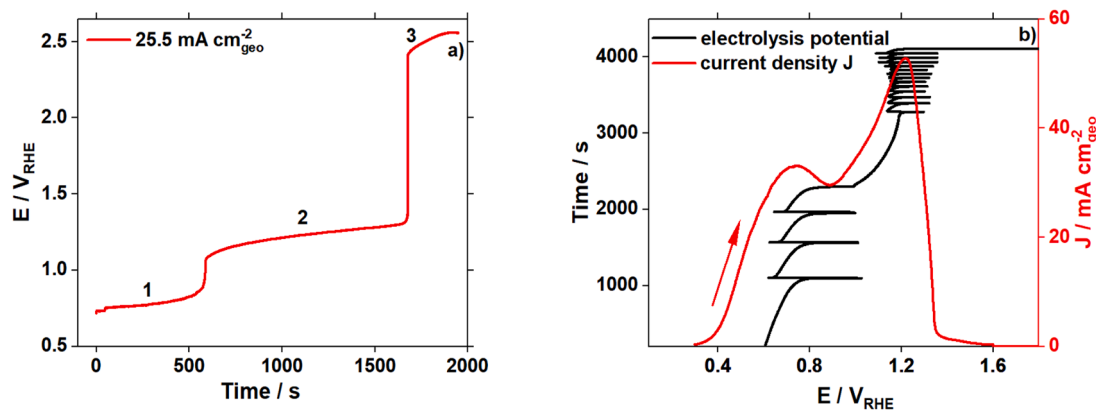


Fig. 6. a) galvanostatic electrolysis measurement: 50 mM glucose, 0.1 M NaOH 25.5 mA  $\text{cm}_{\text{geo}}^{-2}$  applied, rotating at 2500 rpm. b) galvanostatic electrolysis measurement: 50 mM glucose, 0.1 M NaOH 12.76 mA  $\text{cm}_{\text{geo}}^{-2}$  applied, rotating at 2500 rpm. (left y-axis, black line). Forward scan of a steady-state CV recorded in 50 mM glucose at 2500 rpm (right y-axis, red line), arrow indicates the scan direction.

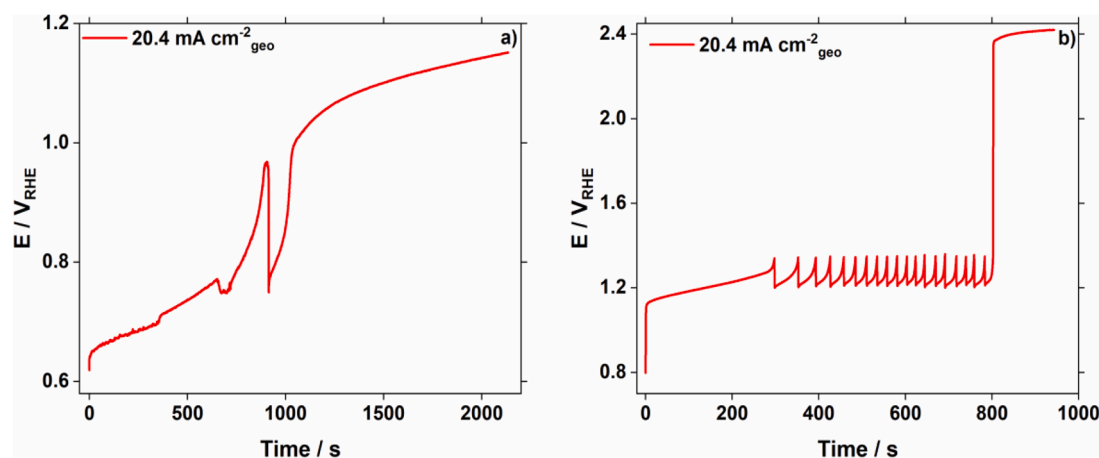


Fig. 7. a) and b): Two separate galvanostatic measurements at identical conditions: 50 mM glucose, 0.1 M NaOH, 20.4 mA  $\text{cm}_{\text{geo}}^{-2}$  applied, 2500 rpm.

and allows for significant current densities (25 mA  $\text{cm}_{\text{geo}}^{-2}$ ) to be applied, whereas without rotation the surface oxidizes almost immediately due to mass transport limitations. Based on these observations and the previously shown RDE experiments (Fig. 2 and 3) electrolysis systems that enhance mass transport seem to be the most suitable candidates for the product-orientated oxidation of glucose.

Under galvanostatic conditions potential oscillations (Figs. 6b, 7a, 7b) have been observed, in both potential regimes (1) and (2). The potential oscillations indicate temporary poisoning/blocking of the catalyst surface, followed by surface cleaning [26,28]. From Fig. 6b it becomes clear that these oscillations fluctuate around the peak potentials of the depicted CV, which coincide with glucose oxidation events as shown in Fig. 1. Similar to Fig. 6a, upon reaching a potential threshold, a transition to the next potential regime occurs.

Fig. 6 and 7 show a selection of galvanostatic measurements conducted under different conditions. From the measurements we found the potential oscillations to be reproducible but not precisely controllable on the polycrystalline gold surface, indicating their structure sensitive nature. Frequency and amplitude are subject of change, also their manifestation in general underlined by the different conditions they occurred at in Fig. 6. Fig. 7 further serves to further illustrate this point: Figs. 7a and 7b show individual experiments conducted under identical conditions. Yet, in Fig. 7a the electrolysis takes place in the regime (1) for more than 1000s, recording one major potential oscillation before transitioning to regime (2). In Fig. 7b, regime (1) is “skipped entirely” reaching (2) after a mere 4 s. The potential gradually increases for 270 s

before the potential starts to oscillate. For the next 500 s these oscillations continue, their amplitude being constant but their frequency increasing. After 800 s of electrolysis, the system transfers to regime (3) when a sudden increase in potential leads to the oxidation of the surface, thereby becoming inactive towards the GOR. In contrast to the GOR, no oscillations have been observed when electrolyzing gluconic acid. It follows that the glucose itself is an important part of these oscillations. However, since two oscillatory regimes were identified, one can also conclude that there exists more than one feedback mechanism and that these mechanisms are either dependant on potential or that the feedback loop in (2) depends also on the surface oxidation state. Furthermore, albeit no systematic study of the oscillations’ dependence on the rotation rate has been conducted, it has been observed that mass transport is crucial for the occurrence of oscillations at different applied currents. In other words, if the mass transport is insufficient, i.e., limited by diffusion, oxide species form on the gold surface, making it inactive towards glucose oxidation and hence no oscillations are observed.

Last but not least, a potentiodynamic electrolysis approach for a technical, product-orientated GOR-process could be an interesting alternative to the often used three-step potential programs first introduced by Belgsir et al. [32]. Like the stepped potential programs, where the applied potential influences the product selectivity, the application of different current densities or rotation rates could be used to achieve similar effects. Allowing the potential to fluctuate during electrolysis could prove useful as the oscillations present a possible self-regenerating

step for the catalyst surface, thereby increasing the catalyst's efficiency.

#### 4. Conclusion

We can derive from our studies several key aspects for future glucose oxidation catalysts and electrolysis setups. From RDE studies, supported by Koutecký-Levich analysis, it becomes apparent that the oxidation of glucose is partially limited by mass transport, hence electrolysis setups with increased mass transport, such as flow-cells, need to be employed in future applications. Moreover, the RDE studies revealed that the second oxidation step, correlating to the oxidation of gluconic acid, is kinetically limited on gold surfaces. Consequently, if gluconic acid is a key intermediate in the glucose oxidation reaction, catalyst design for the reaction needs to focus also on gluconic acid oxidation. To be efficient, catalysts need to shift the gluconic acid oxidation potential towards lower overpotentials. This could be achieved by incorporating different materials to the gold catalyst. Platinum is a reasonable candidate material in that regard as it is active towards gluconic acid oxidation several hundred millivolts earlier than gold [8,40]. Alloying [41–44] or preparing nanocomposites [45] of different metals, such as the already widely used gold and platinum, promises a combination of desirable material properties also in regards to product selectivity and distribution. The experimental evidence that the presence of glucose at the interface shifts the gold oxidation towards higher potentials by competing for available OH<sup>-</sup> with the gold surface might be key to improve the catalyst. Shifting the formation of adsorbed OH-species on the catalyst to lower potentials might help creating highly efficient catalysts for the GOR. On the other hand, both gold and platinum are precious metals and therefore expensive. While Pt is considered a critical raw material by the European Union, this is not the case for Au [46]. To account for the precious metal price, high mass activities are crucial if one is to use these metals. Alternatively, the development of non-precious metal catalysts circumvents the issue elegantly. An example for this, is the work Liu et al. where nickel-iron catalysts were used to produce gluconic acid [47].

Finally, using operando Raman spectroscopy to follow the oxidation state of the catalyst surface, we show a dependence of glucose concentration on the gold oxidation potential. This spectroscopic insight supports the hypothesis that glucose consumes adsorbed OH-species. Hence, increased glucose supply at the interface leads to increased consumption of these species, resulting in the observed oxidation potential shift.

#### Credit author statement

**Nicolas Schlegel:** Performing all electrochemical measurements and Raman spectroscopy, Writing the first draft; **Gustav K. H. Wiberg:** Conceptualization, Software for Raman spectra processing, Reviewing; **Matthias Arenz:** Supervision, Conceptualization, Methodology, Reviewing, Editing.

#### Declaration of Competing Interest

The authors declare that they have no known competing financial interests or personal relationships that could have appeared to influence the work reported in this paper.

#### Acknowledgment

This work was supported by the Swiss National Science Foundation (SNSF) via the project No. 200021\_184742.

#### Supplementary materials

Supplementary material associated with this article can be found, in the online version, at doi:10.1016/j.electacta.2022.140023.

#### References

- [1] T. Werpy, G. Petersen, Top Value Added Chemicals from Biomass Volume I, US Nrel, 2004, <https://doi.org/10.2172/15008859>.
- [2] S. Ramachandran, P. Fontanille, A. Pandey, C. Larroche, Gluconic Acid: properties, Applications and Microbial Production, Food Technol. Biotechnol. 44 (2000) 185–195.
- [3] S. Van De Vyver, Y. Román-Leshkov, Emerging catalytic processes for the production of adipic acid, Catal. Sci. Technol. 3 (2013) 1465–1479.
- [4] M. Ibert, F. Marsais, N. Merboub, C. Brückner, Determination of the side-products formed during the nitroxide-mediated bleach oxidation of glucose to gluconic acid, Carbohydr. Res. 337 (2002) 1059–1063.
- [5] M. Ibert, et al., Improved preparative electrochemical oxidation of D-glucose to D-gluconic acid, Electrochim. Acta 55 (2010) 3589–3594.
- [6] P. Tonda-Mikiela, et al., Synthesis of Gold-Platinum Nanomaterials Using Bromide Anion Exchange-Synergistic Electroactivity toward CO and Glucose Oxidation, J. Electrochem. Soc. 159 (2012) H828–H833.
- [7] S. Hebié, T.W. Napporn, C. Morais, K.B. Kokoh, Size-Dependent Electrocatalytic Activity of Free Gold Nanoparticles for the Glucose Oxidation Reaction, ChemPhysChem 17 (2016) 1454–1462.
- [8] G. Moggia, T. Kenis, N. Daems, T. Breugelmanns, Electrochemical Oxidation of d-Glucose in Alkaline Medium : impact of Oxidation Potential and Chemical Side Reactions on the Selectivity to d-Gluconic and d-Gluconic Acid, ChemElectroChem 7 (2019) 1–11.
- [9] P. Parpot, V.P. Muiuane, V. Defontaine, A.P. Bettencourt, Electrocatalytic oxidation of readily available disaccharides in alkaline medium at gold electrode, Electrochim. Acta 55 (2010) 3157–3163.
- [10] R.A. Escalona-Villalpando, et al., Electrodeposition of gold on oxidized and reduced graphite surfaces and its influence on glucose oxidation, J. Electroanal. Chem. 816 (2018) 92–98.
- [11] S. Cho, H. Shin, C. Kang, Catalytic glucose oxidation on a polycrystalline gold electrode with an amalgamation treatment (TM 05092), Electrochim. Acta 51 (2006) 3781–3786.
- [12] L. A. Larew, D.C. Johnson, Concentration dependence of the mechanism of glucose oxidation at gold electrodes in alkaline media J. Electroanal. Chem. 262 (1989) 167–182.
- [13] S. Biella, L. Prati, M. Rossi, Selective oxidation of D-glucose on gold catalyst, J. Catal. 206 (2002) 242–247.
- [14] C.Y. Li, et al., In Situ Monitoring of Electrooxidation Processes at Gold Single Crystal Surfaces Using Shell-Isolated Nanoparticle-Enhanced Raman Spectroscopy, J. Am. Chem. Soc. 137 (2015) 7648–7651.
- [15] K.B. Kokoh, J.M. Leger, B. Beden, H. Huser, C. Lamy, On line' chromatographic analysis of the products resulting from the electrocatalytic oxidation of D-glucose on pure and adatoms modified Pt and Au electrodes - Par II Alkaline medium, Electrochim. Acta 37 (1992) 1909–1918.
- [16] K.B. Kokoh, J.M. Léger, B. Beden, C. Lamy, On line' chromatographic analysis of the products resulting from the electrocatalytic oxidation of d-glucose on Pt, Au and adatoms modified Pt electrodes-Part I. Acid and neutral media, Electrochim. Acta 37 (1992) 1333–1342.
- [17] Y.B. Vassilyev, O.A. Khazova, N.N. Nikolaeva, Kinetics and mechanism of glucose electrooxidation on different electrode-catalysts. Part I. Adsorption and oxidation on platinum, J. Electroanal. Chem. 196 (1985) 105–125.
- [18] M.F.L. de Mele, H.A. Videla, A.J. Arvia, Potentiodynamic Study of Glucose Electro-Oxidation at Bright Platinum Electrodes, J. Electrochem. Soc. 129 (1982) 2207–2213.
- [19] G. Moggia, J. Schalck, N. Daems, T. Breugelmanns, Two-steps synthesis of D-gluconic acid via D-gluconic acid by electrocatalytic oxidation of D-glucose on gold electrode: influence of operational parameters, Electrochim. Acta 374 (2021), 137852.
- [20] Y.B. Vassilyev, O.A. Khazova, N.N. Nikolaeva, Kinetics and mechanism of glucose electrooxidation on different electrode-catalysts. Part II. Effect of the nature of the electrode and the electrooxidation mechanism, J. Electroanal. Chem. 196 (1985) 127–144.
- [21] A.H.B. Dourado, et al., In situ FTIR insights into the electrooxidation mechanism of glucose as a function of the surface facets of Cu2O-based electrocatalytic sensors, J. Catal. 375 (2019) 95–103.
- [22] T. Ishimoto, Y. Hamatake, H. Kazuno, T. Kishida, M. Koyama, Theoretical study of support effect of Au catalyst for glucose oxidation of alkaline fuel cell anode, Appl. Surf. Sci. 324 (2015) 76–81.
- [23] W. A.B. Mello, G. Cheuquepán, J.M. Feliu, Investigation of reactivity of Pt basal planes towards glucose electro-oxidation in neutral solution (pH 7): structure-sensitivity dependence and mechanistic study J. Electroanal. Chem. 878 (2020), 114549.
- [24] B. Beden, F. Largeaud, K.B. Kokoh, C. Lamy, Fourier transform infrared reflectance spectroscopic investigation of the electrocatalytic oxidation of D-glucose: identification of reactive intermediates and reaction products, Electrochim. Acta 41 (1996) 701–709.
- [25] R.R. Adzic, M.W. Hsiao, E.B. Yeager, Electrochemical oxidation of glucose on single crystal gold surfaces, J. Electroanal. Chem. 260 (1989) 475–485.
- [26] G.C.A. Ferreira, T.W. Napporn, K.B. Kokoh, H. Varela, Complex Oscillatory Kinetics in the Electro-Oxidation of Glucose on Gold, J. Electrochem. Soc. 164 (2017) H603–H607.
- [27] M.V.F. Delmonde, et al., Electrocatalytic efficiency of the oxidation of small organic molecules under oscillatory regime, J. Phys. Chem. C 120 (2016) 22365–22374.

- [28] Gabriel G.B. Melle, T. Altair, Rafael R.L. Romano, H. Varela, Electrocatalytic Efficiency of the Oxidation of Ethylene glycol, Glycerol, and Glucose under Oscillatory Regime, *ChemRxiv. Prepr.* 1 (2020) 1–18.
- [29] R. Nagao, D.A. Cantane, F.H.B. Lima, H. Varela, The dual pathway in action: decoupling parallel routes for CO<sub>2</sub> production during the oscillatory electro-oxidation of methanol, *Phys. Chem. Chem. Phys.* 14 (2012) 8294–8298.
- [30] E. Sitta, M.A. Nascimento, H. Varela, Complex kinetics, high frequency oscillations and temperature compensation in the electro-oxidation of ethylene glycol on platinum, *Phys. Chem. Chem. Phys.* 12 (2010) 15195–15206.
- [31] N. Perini, B.C. Batista, A.C.D. Angelo, I.R. Epstein, H. Varela, Long-lasting oscillations in the electro-oxidation of formic acid on PtSn intermetallic surfaces, *ChemPhysChem* 15 (2014) 1753–1760.
- [32] E.M. Belgsir, et al., Electrosynthesis in aqueous medium: a kinetic study of the electrocatalytic oxidation of oxygenated organic molecules, *Electrochim. Acta* 36 (1991) 1157–1164.
- [33] Y. Fu, A.V. Rudnev, G.K.H. Wiberg, M. Arenz, Single Graphene Layer on Pt(111) Creates Confined Electrochemical Environment via Selective Ion Transport, *Angew. Chemie - Int. Ed.* 56 (2017).
- [34] L.D. Burke, P.F. Nugent, The electrochemistry of gold: I. The redox behaviour of the metal in aqueous media, *Gold Bull* 30 (1997) 43–53.
- [35] A.J. Bard, L.R. Faulker, *ELECTROCHEMICAL METHODS: Fundamentals and Applications*, 2, John Wiley & Sons, Inc, 2001.
- [36] A. Zana, et al., Accessing the Inaccessible: analyzing the Oxygen Reduction Reaction in the Diffusion Limit, *ACS Appl. Mater. Interfaces* 9 (2017) 38176–38180.
- [37] C.R. Yonzon, C.L. Haynes, X. Zhang, J.T. Walsh, R.P. Van Duyne, A Glucose Biosensor Based on Surface-Enhanced Raman Scattering: improved Partition Layer, Temporal Stability, Reversibility, and Resistance to Serum Protein Interference, *Anal. Chem.* 76 (2004) 78–85.
- [38] L. Pérez-Martínez, L. Balke, A. Cuesta, Reactive and inhibiting species in the electrocatalytic oxidation of glycerol on gold. A study combining in-situ visible reflectance and ATR-SEIRAS, *J. Catal.* 394 (2021) 1–7.
- [39] M.D. Fontana, K.Ben B. Mabrouk, T.H. Kauffmann, Raman spectroscopic sensors for inorganic salts, *Spectrosc. Prop. Inorg. Organomet. Compd.* 44 (2013) 40–67.
- [40] K.B. Kokoh, et al., Selective oxidation of D-gluconic acid on platinum and lead adatoms modified platinum electrodes in alkaline medium, *Electrochim. Acta* 38 (1993) 1359–1365.
- [41] M. Tominaga, et al., Electrocatalytic oxidation of glucose at gold-silver alloy, silver and gold nanoparticles in an alkaline solution, *J. Electroanal. Chem.* 590 (2006) 37–46.
- [42] A. Habrioux, et al., Activity of platinum-gold alloys for glucose electrooxidation in biofuel cells, *J. Phys. Chem. B* 111 (2007) 10329–10333.
- [43] J. Zhao, F. Wang, J. Yu, S. Hu, Electro-oxidation of glucose at self-assembled monolayers incorporated by copper particles, *Talanta* 70 (2006) 449–454.
- [44] C. Jin, Z. Chen, Electrocatalytic oxidation of glucose on gold-platinum nanocomposite electrodes and platinum-modified gold electrodes, *Synth. Met.* 157 (2007) 592–596.
- [45] J. Du, et al., Bifunctional Pt-IrO<sub>2</sub>Catalysts for the Oxygen Evolution and Oxygen Reduction Reactions: alloy Nanoparticles versus Nanocomposite Catalysts, *ACS Catal.* 11 (2021) 820–828.
- [46] **Critical raw materials.** Available at: [https://ec.europa.eu/growth/sectors/raw-materials/areas-specific-interest/critical-raw-materials\\_en](https://ec.europa.eu/growth/sectors/raw-materials/areas-specific-interest/critical-raw-materials_en). (Accessed: 1st December 2021).
- [47] W.J. Liu, et al., Efficient electrochemical production of glucaric acid and H<sub>2</sub> via glucose electrolysis, *Nat. Commun.* 11 (2020) 265.

## Supporting Information

### On the electrooxidation of glucose on gold: towards an electrochemical glucaric acid

#### production as value-added chemical

Nicolas Schlegel, Gustav K. H. Wiberg, Matthias Arenz \*

University of Bern, Department of Chemistry, Biochemistry and Pharmaceutical Sciences,  
Freiestrasse 3, 3012 Bern, Switzerland

\*Corresponding Author

E-mail: matthias.arenz@unibe.ch

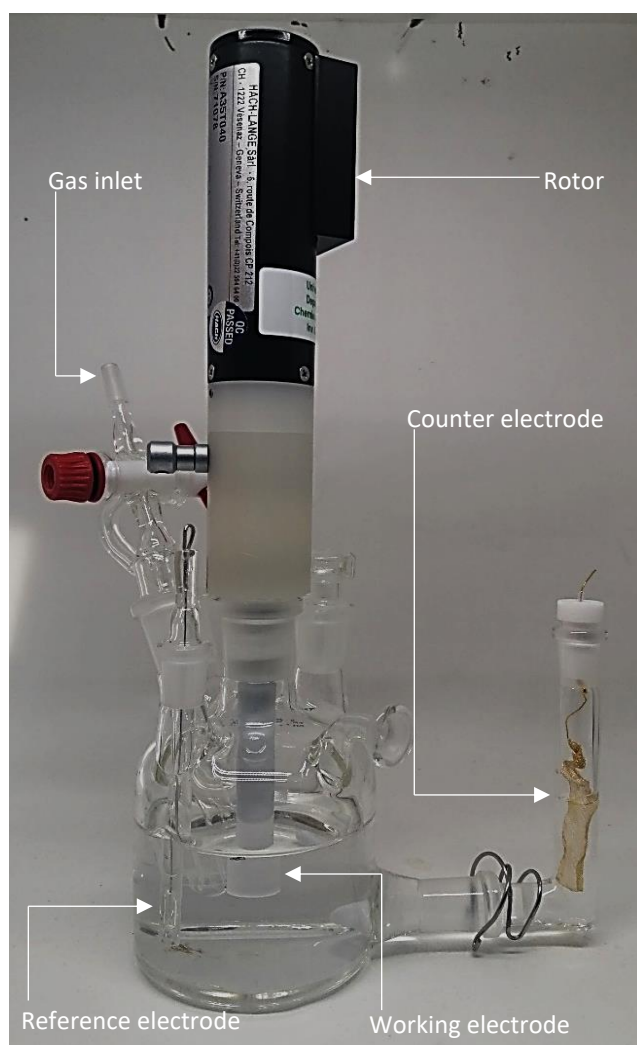
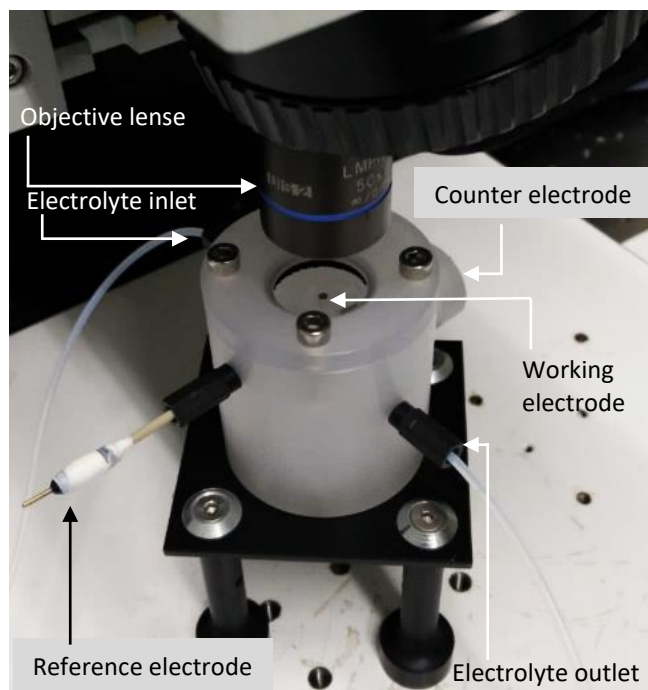


Figure S1: Electrochemical setup consisting of the custom-built glass cell, the prepared trapped H<sub>2</sub>-bubble (reference electrode), the gold mesh (counter electrode), and the gold disc (working electrode) mounted onto the rotor head.



*Figure S2: Kel-F cell designed for in-situ Raman studies. Depicted are the individual cell parts, which are the leakless Ag/AgCl electrode (reference electrode), the contact for the Pt-coil (counter electrode), the gold bead (working electrode), and the quartz glass window. The window is located beneath the objective lens which is used to focus the laser.*

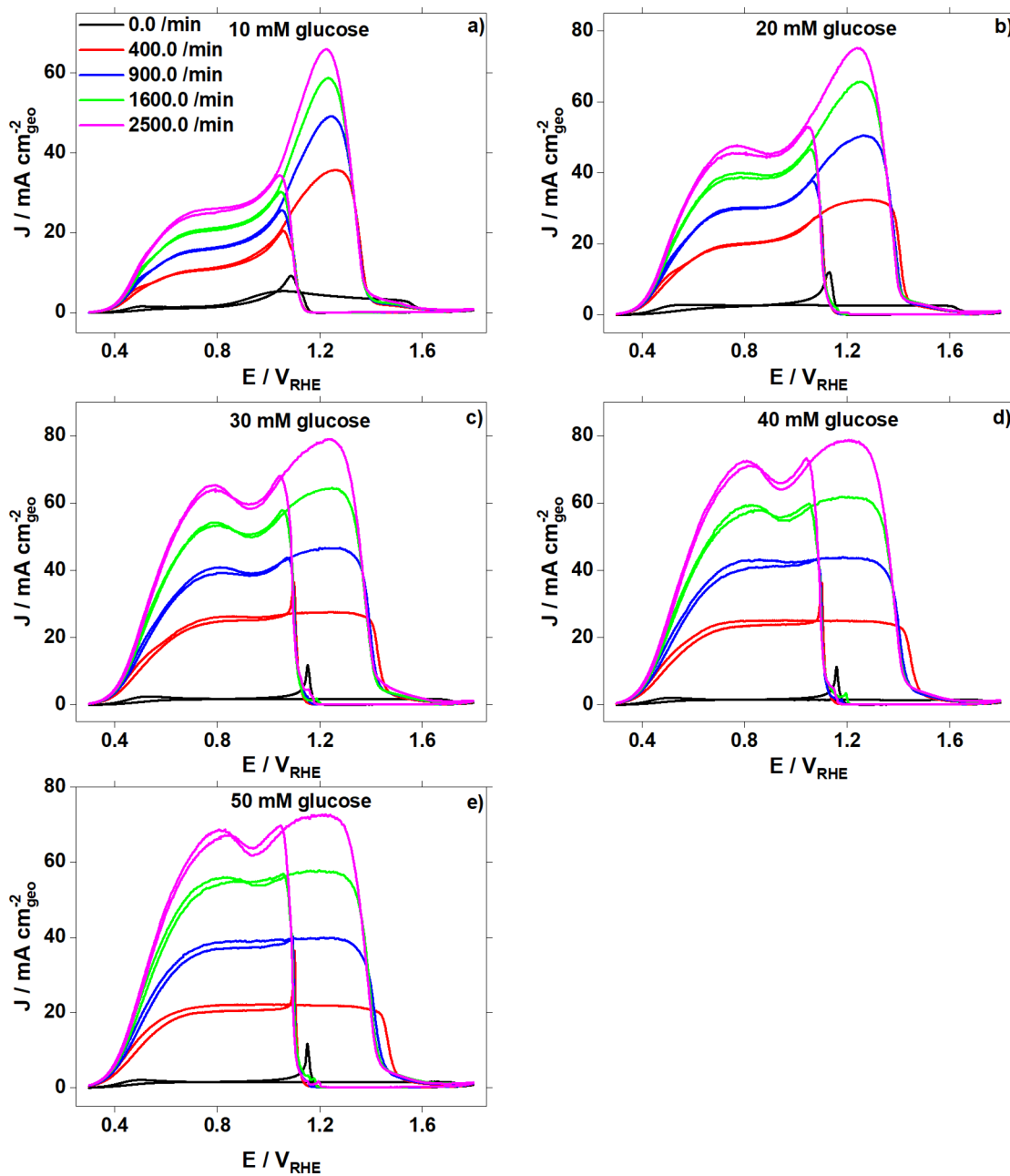


Figure S3: Cyclic voltammograms of an Au-disc in an RDE-setup in 0.02 M NaOH and different glucose concentrations: a) 10 mM; b) 20 mM; c) 30 mM, d) 40 mM and e) 50 mM glucose, respectively.

a) Levich equation  $I_L = 0.201 * n * F * A * D^{2/3} * \omega^{1/2} * \nu^{-1/6} * C$

With the number of transferred electrons  $n$ , Faraday constant  $F$  [C/mol], electrode area  $A$  [cm<sup>2</sup>], diffusion coefficient  $D$  [cm<sup>2</sup>/s], electrode's angular rotation rate  $\omega$  [rpm], kinematic viscosity  $\nu$  [cm<sup>2</sup>/s], and the reactant concentration  $C$  [mol/cm<sup>3</sup>]

The Levich equation models flow conditions at an RDE correlates them to measured currents. In the equation the Levich constant  $B$  is commonly defined as  $I_L = B * \omega^{1/2}$

b) Koutecký-Levich equation:  $\frac{1}{i} = \frac{1}{i_K} + \frac{1}{i_{L,c}} = \frac{1}{i_K} + \frac{1}{0.62 * n * F * A * D^{2/3} * \omega^{1/2} * \nu^{-1/6} * C}$

Where  $i_K$  represents the kinetically limited current, the current in the absence of any mass-transport effect.  $i_K$  can be determined from a Koutecký-Levich where it is equivalent to the inverse of the y-intersect. An exemplary plot is shown here:

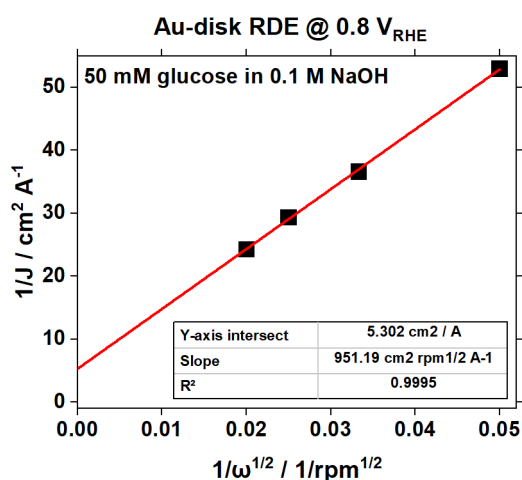


Figure S4: Short explanation of a) Levich-equation and b) Koutecký-Levich analysis.

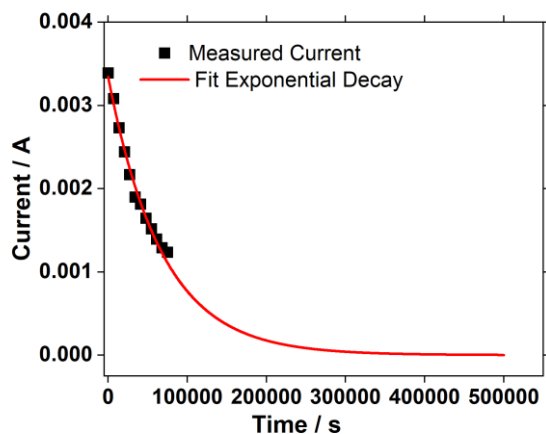


Figure S5: Tri-hold electrolysis measurement conducted at a glucose concentration of 20 mM in 100 ml 0.1 M NaOH and 0.1 M NaClO<sub>4</sub> at a rotation speed of 2500 rpm. Measurement time was set to 20 hours. Additional data points were extrapolated by fitting an exponential decay function.

100 ml of a 20 mM glucose solution was subjected to fixed potential coulometry on a Au-disk in a RDE configuration at 2500 rpm rotation speed. Similar to Belgsir et al.<sup>1</sup> a tri-hold potential program was applied during electrolysis: 30 s 0.8 V<sub>RHE</sub>, 2 s 1.5 V<sub>RHE</sub>, and last 2 s at 0.05 V<sub>RHE</sub>. The measurement was conducted for 20 h. The current decays exponentially, assuming a reaction of first order. To determine the absolute charge required to exhaust the reactant an exponential decay function was employed to extrapolate data points. As a necessary condition the fit's y-offset was set to 0 and the cut-off current was set to be 0.1 % of the initial current. The current boundary was reached after 469986 s. Integrating the area under the curve yields the total charge transferred during the experiment, amounting to 228 C. Using Faraday's constant, the charge can be translated to moles of electrons transferred. Which in this case is 0.0023 mol (2.3 mmol). As 2 mmol of glucose were present when the experiment commenced, 1.15 electrons were transferred per glucose molecule. This value deviates from the values obtained from the Koutecký-Levich analysis at 0.8 V<sub>RDE</sub>, see Figure 4. However, the results are not definitive, as 1.15 electrons do not indicate clearly what process, or processes, take place. In addition, the method has clear limitations with regards to the fitting as a reaction order needs to be assumed and the decay in concentration takes very long. Most likely different processes overlap which however cannot be deconvoluted by coulometry.

## Reference

1. Belgsir, E. M. *et al.* Electrosynthesis in aqueous medium: a kinetic study of the electrocatalytic oxidation of oxygenated organic molecules. *Electrochim. Acta* **36**, 1157–1164 (1991).



**Manuscript II**

Nicolas Schlegel, Alexander Bagger, Jan Rossmeisl, Matthias Arenz

**Elucidating the reaction pathway of glucose electrooxidation to its valuable products:  
the influence of mass transport and electrode potential on the product distribution**

*Submitted*

ChemRxiv: <https://doi.org/10.26434/chemrxiv-2023-5ml1l>

# **Elucidating the reaction pathway of glucose electrooxidation to its valuable products: the Influence of mass transport and electrode potential on the product distribution**

Nicolas Schlegel<sup>a</sup>, Alexander Bagger<sup>b</sup>, Jan Rossmeisl<sup>c</sup>, Matthias Arenz<sup>a, \*</sup>

<sup>a</sup>) Department of Chemistry, Biochemistry and Pharmaceutical Sciences, University of Bern,  
Freiestrasse 3, 3012 Bern, Switzerland

<sup>b</sup>) Department of Chemical Engineering, Imperial College London, London, UK

<sup>c</sup>) Department of Chemistry, University of Copenhagen, Universitetsparken 5, 2100 København Ø

\* Corresponding author: Matthias.arenz@unibe.ch

## **Abstract**

Converting glucose electrochemically to its valuable derivatives, gluconic and glucaric acid, is a promising process for the utilization of renewable carbon sources. Understanding the reaction pathway to form glucaric acid from glucose is key in performing the process efficiently. In this study we investigate the influence of mass transport as well as electrode potential on the product distribution in glucose, gluconic acid and glucuronic acid oxidation on a gold disk in an RDE-setup. We find glucose and glucuronic acid to be easily oxidized, while the oxidation of gluconic acid is kinetically limited. Combining DFT calculations and the experimental results, we show that on gold, the oxidation of aldehyde groups proceeds readily while the oxidation of hydroxyl groups is challenging and occurs indiscriminately on C-atoms in glucose and its derivatives. Additionally, the DFT calculation present a reaction pathway which can explain the absence of glucuronic acid in the conducted experiments.

## **Keywords**

Glucose oxidation reaction; Gold electrode; glucaric acid; gluconic acid; value-added chemical production

## Introduction

Glucose derivatives, namely gluconic and glucaric acid, have been labelled building block chemicals by the U.S. department of energy in 2004<sup>1</sup>, which led to an increased interest in the conversion of glucose. Gluconic acid finds its main applications in the food and pharmaceutical industries and is also found in hygiene products<sup>2</sup>. Glucaric acid is a possible precursor of adipic acid, which itself is a building block of Nylon<sup>3</sup>. Therefore, these glucose derivatives serve as alternative carbon sources for the chemical industry which presently relies on fossil carbon sources. Carbon sourced from the biosphere by this means helps in closing the anthropogenic carbon cycle and de-fossilising the chemical industry.

Among glucose conversion methods, an electrochemical approach offers milder conditions than historically employed approaches which rely on strong oxidants (NaOCl and NaBr<sup>4,5</sup>). Additionally, an electrochemical approach can directly use electricity from renewable sources which helps with and benefits from a de-fossilised economy. When pursuing an electrochemical approach, it has been shown that the applied overpotential can be used to tune product selectivity<sup>6</sup>. Other important parameters that can be used to achieve similar effects is the nature of the electrode, the abundance of hydroxide ions<sup>7</sup>, and ad-atoms on the catalytic electrode<sup>8</sup>. When it comes to electrode materials, gold<sup>9-14</sup> and platinum<sup>15-17</sup> have been found to be the most promising. Recently, composite materials of different noble metals<sup>18-24</sup> as well as non-precious metal catalyst<sup>25-29</sup> have been reported for the electrooxidation of glucose. The latter also alleviating the need for precious, rare materials. This is interesting as abundance will not be a limiting factor during potential future scale-up.

In terms of product distribution, glucose can be oxidised to different degrees resulting in a wide variety of decomposition products. The application of glucose oxidation then dictates the conditions and extent of the oxidation. Full oxidation to CO<sub>2</sub> requires the removal of 24 proton-electron-pairs and follows the reaction  $C_6H_{12}O_6 + 6 H_2O \rightarrow 6 CO_2 + 24 (H^+ + e^-)$ . This process is interesting for a glucose fuel cell approach as the maximum amount of stored energy becomes available. Other products include a whole range of small organic acids which have been reported by Kokoh et al.<sup>30</sup> by oxidising

glucose over a Pt surface in alkaline electrolyte. However, similar to the full oxidation, their formation still presupposes cleaving the C-chain in glucose. For purposes of converting glucose into its saccharic acid derivatives, the valuable gluconic and glucaric acid, glucose must only be oxidised on its C<sub>1</sub> and C<sub>6</sub> (see D-Glucose molecule in **Figure 1**) positions. Mild conditions must therefore be chosen to avoid further oxidation and dissociation of the carbon chain. Gold has been found to readily oxidise glucose to gluconic acid and the reaction mechanism has been explored to a wide extent<sup>17,31–37</sup>. Moggia et al.<sup>38</sup> reported further oxidation to glucaric acid. First the aldehyde group at the C<sub>1</sub>-position is oxidized by removing two proton-electron pairs (**Equation 1**). Then, supposedly, the formed gluconic acid's C<sub>6</sub>-position is oxidised by removing four additional proton-electron pairs to form the second carboxylic group (**Equation 4**).

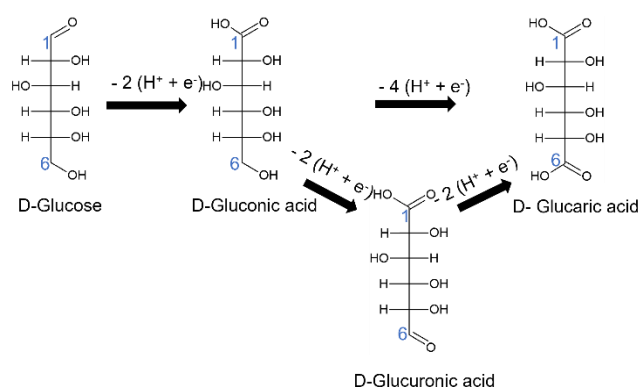


**Figure 1:** Sketch of proposed pathway to form glucaric acid from glucose on an Au-disc in either a two-step process or with glucuronic acid as a second reaction intermediate. The blue labels in the glucose molecule indicate the C<sub>1</sub>- and C<sub>6</sub>- positions respectively.

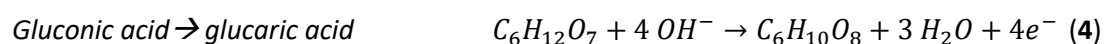
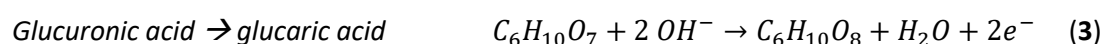
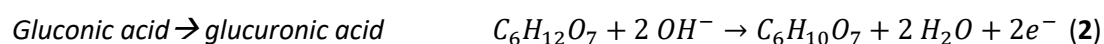
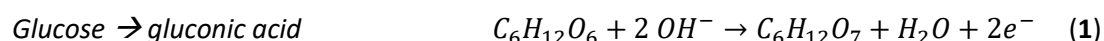


**Figure 1** can also be expressed as individual reaction **Equations 1-4**. Notably, **Equation 4** is the sum of **Equations 2** and **3**. This accounts for the two-step oxidation from glucose to glucaric acid only via gluconic acid.

On Pt-surfaces<sup>39</sup> and NiFe-oxides<sup>26</sup> glucuronic acid has been reported as an oxidation product and an intermediate towards glucaric acid, respectively. A pathway including glucuronic acid divides the oxidation of glucose to glucaric acid into three 2 proton-electron pair steps. On gold-based caesium-promoted catalysts<sup>40</sup>, glucuronic acid has been observed as the final reaction product. However, this study did not pursue an electrochemical approach but rather a conventional heterogenous one. To the best of our knowledge, on gold using an electrocatalytic approach, glucuronic acid has not been reported as a significant intermediate or reaction product. Therefore, the question of how glucaric acid is formed from gluconic acid remains still unanswered.

The electrochemical studies show that the product distribution depend on the operational parameters. Moggia et al.<sup>6</sup> reported gluconic acid to be the main reaction product of glucose oxidation on a gold electrode at 0.55 V<sub>RHE</sub>, while glucaric acid is only observed at oxidation potentials as larger as 1.34 V<sub>RHE</sub>. On platinum, Kokoh et al. have found glucuronic acid to form instead of glucaric acid<sup>39</sup>. To commercialise glucose oxidation, another limiting factor is the rate of oxidation itself. For example, in the aforementioned study of Moggia et al.<sup>6</sup>, the conversion took 65 h. In our previous work conducted in an RDE-setup<sup>41</sup>, we showed that glucose oxidation on a gold disk is mixed kinetic-mass transport controlled. Hence, forced convection immensely increases the current response and therefore the reaction rate. Also, the number of transferred electrons per glucose molecule changes with the applied oxidation potential. This observation agrees with the product distribution changing as a function of potential. On the other hand, we also showed the oxidation of gluconic acid to be mainly kinetically controlled. The current response is therefore unaffected by the applied rotation speed. When publishing these results, we lacked a method to reliably identify and quantify the produced products. Therefore, we could not study the influence convection has on the product distribution. In the

meantime, we were able to develop a high-performance ion chromatography (HPIC) method which satisfies our demand in terms of reproducibility and unambiguity in product separation.

In the presented work, we investigate the rotation speed's effect on product distribution at different oxidation potentials and compare these results to computational simulations. As glucaric acid is the most desired product, we studied glucose oxidation and the intermediate oxidation along the path to glucaric acid: gluconic acid and glucuronic acid oxidation. We seek to determine optimised oxidation parameters to increase the efficiency of glucaric acid production. Employing density functional theory simulations, we try to improve the understanding of the formation mechanism of glucaric acid on gold in an electrochemical setup.

## Experimental

### Chemicals and reagents

All electrolytes used for electrochemical measurements were made using ultra-pure water (MiliQ-systems, 2.7 ppb TOC, 18.2 MΩ). Therein, sodium hydroxide monohydrate (≥99.99 %, suprapur, Merck) and sodium perchlorate (anhydrous, ACS grade, 98 % -102 %, Alfa Aesar) were dissolved to reach a final concentration of 0.1 M each. Sodium perchlorate was added to improve electrolyte conductivity. Also, the perchlorate anion does not interfere with the product analysis. D-glucose (>99.5 %, Sigma-Aldrich), D-gluconic acid sodium salt (>99 %, Sigma-Aldrich), and D-glucuronic acid (>98 %, Sigma Aldrich) were used to prepare the starting electrolytes and Ar-gas (>99.99 %, PanGas) was used to purge the electrolytes. Additionally, drying of electrode tips and cell parts was done with Ar-gas.

The eluent for the PAD detection was produced from sodium acetate (anhydrous, >99%, Sigma-Aldrich) and sodium hydroxide solution (49-51% in water, Supelco, Merck). Sodium carbonate (99%, Merck) was used to prepare the eluent for the product analysis done by the conductivity detector. The standard compounds, glycolic acid (99 %), formic acid (98 %), and tartaric acid (99 %) were all purchased from Sigma-Aldrich.

## Electrochemical setup and measurements

The electrochemical measurements were conducted in a custom-build two-compartment glass cell (**Figure S1**). Before measurements, the cell was disassembled, and the parts were boiled in 25 %  $\text{HNO}_3$  followed by boiling in ultra-pure water. The cell was reassembled after rinsing with ultra-pure water and cooling down. Between single experiments the cell was boiled in and rinsed with ultra-pure water. After cleaning, the cell was filled with 100 ml of supporting electrolyte which was then purged with Ar-gas for 25 min while stirring using a magnetic stirrer and an external stirring plate. The stirring bar was cleaned identically to the cell itself.

A polycrystalline gold-disk (diameter of 5 mm) embedded in a PTFE-RDE-tip was used as a working electrode. Before experiments, the disk was polished using an alumina slurry (0.3  $\mu\text{m}$ , MicroPolish Suspension, Buehler) on a polishing cloth (MicroCloth, Buehler) for 2 min. The polished disk was then rinsed for 30 s, sonicated in water for 5 min, and rinsed again for 30 s before being dried using an Ar-jet. The tip was mounted on a EDI101 rotating disk electrode assembly (Radiometer analytical). Rotation was achieved through a CVT101 speed control unit (Radiometer analytical) controlled by the ECi-210 potentiostat, using EC4 DAQ 4.2 software (both Nordic Electrochemistry ApS), through a software plug-in. A gold mesh served as the counter electrode and a Pt-wire in a glass tube as the reference electrode. The trapped hydrogen electrode was prepared in-situ by applying -9.00 mA between the Pt-wire and the gold mesh in the purged supporting electrolyte. Then, the reactants were introduced into the cell and the electrolyte was purged for another 10 min in Ar.

To minimise the error in potential due to the  $iR$ -drop, the solution resistance was determined by electrochemical impedance spectroscopy (EIS). Therefore, the working electrode was held at 0.3  $V_{\text{RHE}}$  in the double layer region of gold. Using a 5 kHz AC perturbation and an amplitude of 10 mV the effective solution resistance was determined. Applying an analogue feedback scheme of the potentiostat, the feedback was increased until the signal was almost unstable. Signal stability was determined through frequency analysis of the measured signal. Finally, EIS was performed again in the

range of 1 kHz to 50 kHz and an amplitude of 10 mV. From these measurements, the solution resistance was determined to be  $< 1.5 \Omega$ .

## Product analysis

After an experiment, 1 ml of electrolyte was transferred into a 15 ml falcon tube where it was diluted with 9 ml of ultra-pure water. The tube was stored in a fridge at 4 °C. Both the dilution and the cooling served to slow down aging processes. Samples were stored maximally for 24 h before product analysis.

Product analysis was conducted on a 940 Professional IC Vario I (Metrohm). Samples were automatically injected from a cooled 889 IC Sample Center (Metrohm). Two detectors were used: a pulsed amperometric detector (PAD) (wall-jet cell and Au-working electrode) and a suppressed conductivity detector (CD). Each detector was set up on a separate line. The PAD line was fit with a Metrosep Carb 2 (250/4.0, Metrohm) column and a 0.1 M sodium acetate and 0.11 M sodium hydroxide containing mobile phase (0.5 ml/min) was used, while the CD line was fit with a Metrosep A Supp 7 – (250/4.0, Metrohm) column using a 3 mM sodium carbonate eluent (0.7 ml/min). The PAD line was used to quantify gluconic and glucuronic acid. Conductivity detection was used to quantify glucaric acid. Additionally, it was used to check for the presence of the potential side products formic acid, tartaric acid, and glycolic acid. Calibration curves for all components and exemplary chromatograms are shown in the supporting information (**Figures S2 and S3**).

## Density functional theory simulations

The molecule, Au(111) metal slab structure, and the reaction intermediate on Au(111) structures were created in ASE<sup>42</sup>. For the structures, the electronic calculations were carried out with the projector augmented wave method together with the BEEF-vdW functional<sup>43</sup> in the GPAW software<sup>44</sup>. We apply a grid-spacing of 0.18, a vacuum of minimum 10 Ang and all the structures are relaxed to a force below 0.05 eV/Ang. The Au(111) metal structures were created by a 111 surface slab of FCC  $3 \times 3 \times 3$  unit cell, where the two bottom layers were fixed and a  $(3 \times 3 \times 1)$  k-point sampling was used.



As glucose can exist in 3 different types, we calculated the energies of these three configurations in **Figure S4**. Using D-glucose as reference (set to zero) in this analysis it is observed that b-glucose is the most stable configuration. Hence for calculating the energetics of key reaction intermediates b-glucose, water (H<sub>2</sub>O) and hydrogen (H<sub>2</sub>) is used as energetic reference following the equation:

$$\Delta E = E_{ads^*} - E_* - E_{b-glucose} + nE_{H_2} - mE_{H_2O}$$

Where  $E_{ads^*}$  is Au(111) with the intermediate,  $E_*$  is Au(111),  $E_{b-glucose}$  is the glucose reference and n and m have different values depending on the key reaction intermediate  $E_{ads^*}$ . Directly comparing energetics of key reaction intermediates is sufficient, and Gibbs free energy corrections are not calculated as this is cumbersome for large compounds.

## Results and Discussion

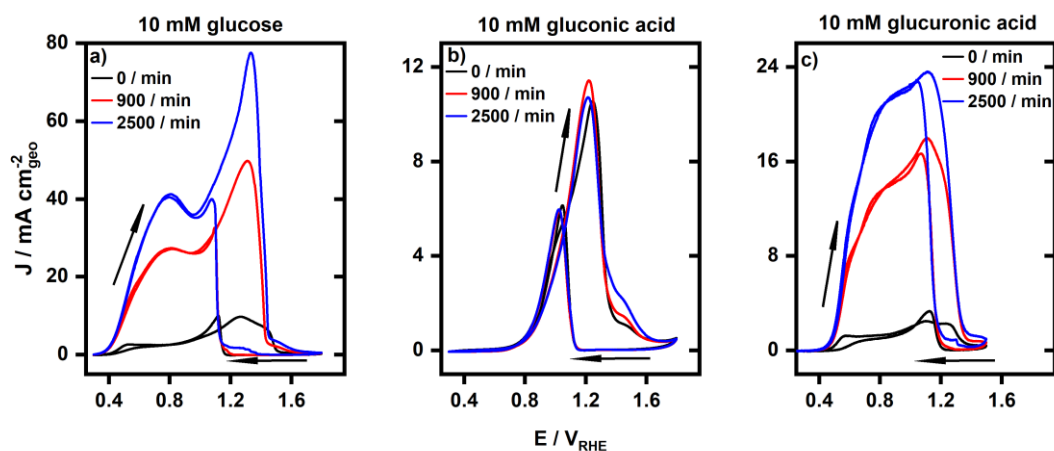


**Figure 2:** Steady-state cyclic voltammograms of glucose (a), gluconic acid (b), and glucuronic acid (c) on an Au-disk: 0.05 M analyte concentration in 0.1 M NaOH and 0.1 M NaClO<sub>4</sub> electrolyte. Data of a) and b) taken from Schlegel et al.<sup>41</sup>

To determine suitable oxidation potentials as well as to demonstrate the influence of convection, cyclic voltammograms of solutions containing glucose (**Figure 2a**), gluconic acid (**Figure 2b**), and glucuronic acid (**Figure 2c**) were recorded in an RDE-configuration using an Au-disk as the working electrode. An in-depth discussion of **Figure 2a & 2b** can be found in our previous work<sup>41</sup>. Comparing the CVs of an Au-disk recorded in a glucose containing and a glucuronic acid containing electrolyte without rotation

(black lines in **Figure 2a & c**) similarities are observed. In the positive going scan, an anodic current response is observed starting at around  $0.4 V_{RHE}$ , with a current maximum at around  $0.55 V_{RHE}$ , and followed by a current plateau up to  $1.0 V_{RHE}$ . An increase in oxidative current is then observed at  $1.25 V_{RHE}$  with a subsequent deactivation of the catalytic surface towards glucose and glucuronic acid oxidation, respectively. The latter can be ascribed to the oxidation of the Au electrode surface. During the negative going scan, a sudden reactivation of the surface occurs at  $1.2 V_{RHE}$  – where Au-oxide reduction occurs<sup>45</sup> - and thereafter forward and backward scan are identical until  $0.6 V_{RHE}$ , where the previously mentioned peak current does not occur in the negative scan direction. With the application of rotation in the case of a glucuronic acid containing electrolyte (red and blue lines in **Figure 2c**) the current response at  $0.4 V_{RHE}$  is significantly increased. The slope of the current response becomes flatter as the positive scan progresses. The current response again culminates at  $1.25 V_{RHE}$  which is then followed by an abrupt decrease in current response. During the negative scan, a reactivation of the surface is observed, identical to the CV without rotation. Then, for the rest of the CV, forward and backward scan are identical. Therefore, in the case of a glucuronic acid containing electrolyte, similar to a glucose containing electrolyte (**Figure 2a**), we conclude that glucuronic acid oxidation is mixed mass transport-kinetically controlled as well.

In contrast, the current response and CV shape when cycling in a gluconic acid containing electrolyte is independent of the applied rotation. The oxidation of gluconic acid seems to be purely kinetically controlled on the Au-disk. Also, there is no oxidative current recorded before  $0.8 V_{RHE}$ . To gain an understanding of the possible reaction pathways in glucose oxidation reaction, we investigated the different steps as well as the different reaction intermediates with the help of DFT calculations. As glucose is large complex molecule, we keep the analysis as simple as possible only focusing on the energetics of key intermediates. The oxidation reaction from glucose to glucaric acid requires 6 proton-electron pairs, which includes both oxidation of glucose but also the addition of oxygen from oxidation of water. To gain insights into the multiple proton-electron transfer process through intermediate species we investigated the energetic aspects of the reactions by constructing an energy diagram of

the reactions as shown in **Figure 3**. The figure shows reaction compounds (black), compound oxidation steps i.e., removal of hydrogen to form intermediates (red) and water oxidation step (blue).

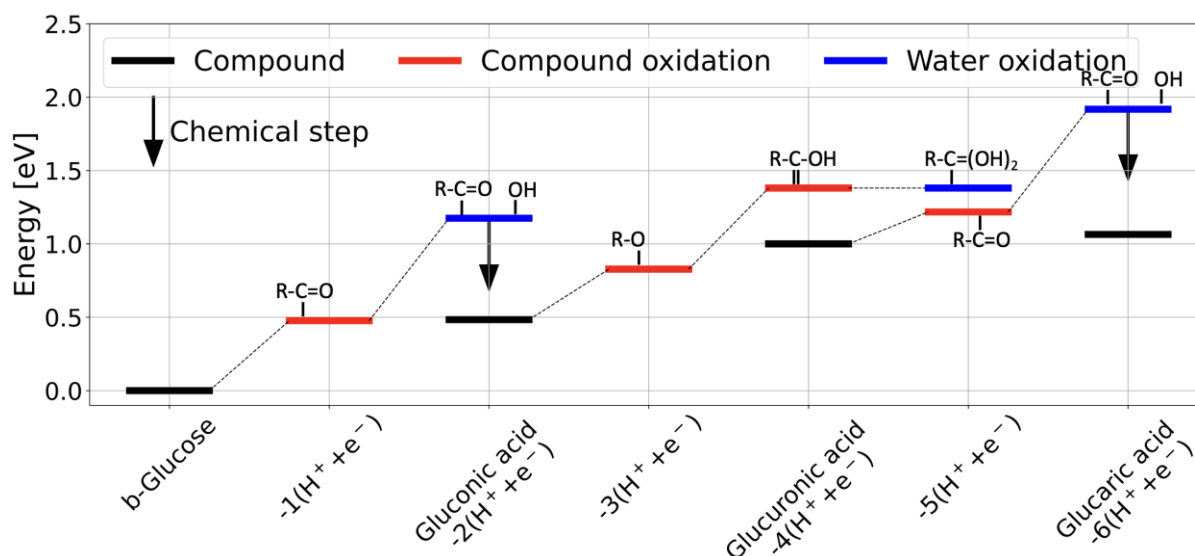


**Figure 3:** Energy diagram of the suggested reaction path from glucose to glucaric acid on Au(111), including the intermediate species Gluconic acid and Glucuronic acid and suggested key reaction intermediates.

**Figure 3** shows that oxidation of an aldehyde group (R-CH=O) to carboxylic acid (R-COOH) requires first an initiation by the first proton removal to (R-\*C=O, where \* indicate a bound intermediate to the Au surface) followed by the addition of \*OH by a water oxidation step to (R-\*C=O + \*OH). From here we believe a chemical step occurs to combine the two species. This process is identical from glucose to gluconic acid and from glucuronic acid to glucaric acid, which corresponds well with the observed similarities in the current responses in experiments shown in **Figure 2a and c**. Interestingly, when oxidizing water (adsorbing \*OH) in the presence of an activated glucose or glucuronic acid molecule \*OH is stabilized significantly compared to direct water oxidation (see **Figure S7**). We investigate this, as it seems that the OH groups from the glucose compounds help with stabilizing OH<sup>-</sup> allowing for this oxidation to happen at low potentials.

The oxidation of gluconic acid to glucaric acid, which requires the oxidation on the terminal alcohol group, is fundamentally more challenging to understand from such analysis. The challenge on Au is that the carbon and oxygen bonded key intermediates are energetically close<sup>46</sup>. Here it is found that hydrogen removal is slightly favoured from the oxygen atom of the OH-group. However, such an oxidation creates an R-CH<sub>2</sub>-\*O compound on the surface (see **Figure S5**). Notable, oxidation could in principle happen everywhere on the glucose derived intermediate compounds, both on the -OH groups but also on the carbon atoms. The question whether the oxygen or the carbon atom of an alcohol group are bound to the metal surface has also been investigated for glycerol dehydrogenation<sup>47</sup>. A process which we expect to behave similarly to glucose and gluconic acid oxidation. To investigate this, a randomly chosen hydrogen atom, located in the middle of the C<sub>6</sub>-chain, was also tested for oxidation, which is found to be energetically favourable (see **Figure S5**). This challenges how gluconic acid is oxidized and particularly how the preferential oxidation of the terminal group can be optimised. Noticeable, this matches the experimental observations of gluconic acid oxidation being challenging. Highest in energy is the oxidation of the carbon hydrogen (R-\*CH-OH) on the end group. Beyond the first proton-electro oxidation there are again multiple possibilities which is shown in **Figure S6**. Here, glucuronic acid is most stable on Au(111) while double oxidation on the end group to (R-\*C-OH) is second most stable. Carrying out the oxidation on a carbon atom, other than C<sub>1</sub>, seems more energetically challenging, possibly due to steric effects of the intermediate now bound to two sites on the surface. From this DFT energetic viewpoint one can learn that preferential oxidation of gluconic acid on the terminal OH-group is significantly challenging. This potentially explains why reaction turnover to gluconic acid is observed but further gluconic acid oxidation does not happen at a large rate (**Figure 2b**). One can speculate that none-preferential oxidations at larger overpotentials eventually leads to dissociative oxidation of the gluconic acid compounds which block the surface.

To combine and discuss the theoretical calculations and the experimental data, it is paramount to identify the reaction products formed during the oxidation experiments. The identification and quantification of these products helps to verify or dismiss the mechanistic interpretation of the glucose

oxidation pathway. Based on the obtained CVs in **Figure 2**, three different oxidation potentials were chosen to be investigated by the product analysis using HPIC: i)  $0.55 V_{RHE}$  because of the observed current peak without rotation in **Figure 2a&c**; ii)  $0.8 V_{RHE}$  because of the observed current peak in **Figure 2a** when rotation is applied; iii)  $1.1 V_{RHE}$  because it is close to the second peak current but still distant from the surface deactivation. However, one-step potentiostatic protocols fail due to a rapid deactivation of the catalytic surface. Therefore, based on previous studies<sup>38,48</sup>, in the measurements a potential sequence including three distinct potential steps was chosen (**Figure 4**). The upper ( $1.5 V_{RHE}$ ) and lower ( $0.05 V_{RHE}$ ) potentials serve to completely oxidize and reduce the Au electrode. Thereby the electrode surface is regenerated. The “middle potential” is considered the oxidation potential for the product analysis.

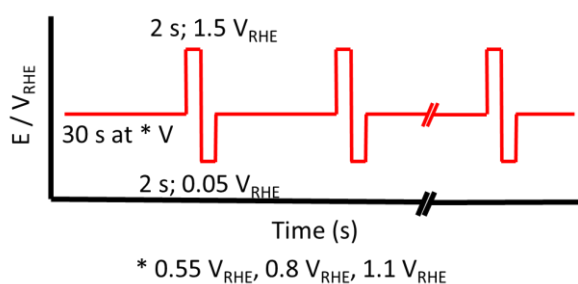


**Figure 4:** Potential program for the electrochemical oxidation of glucose, gluconic acid, and glucuronic acid. After two hours samples of the electrolyte were taken and analysed by HPIC for product analysis.

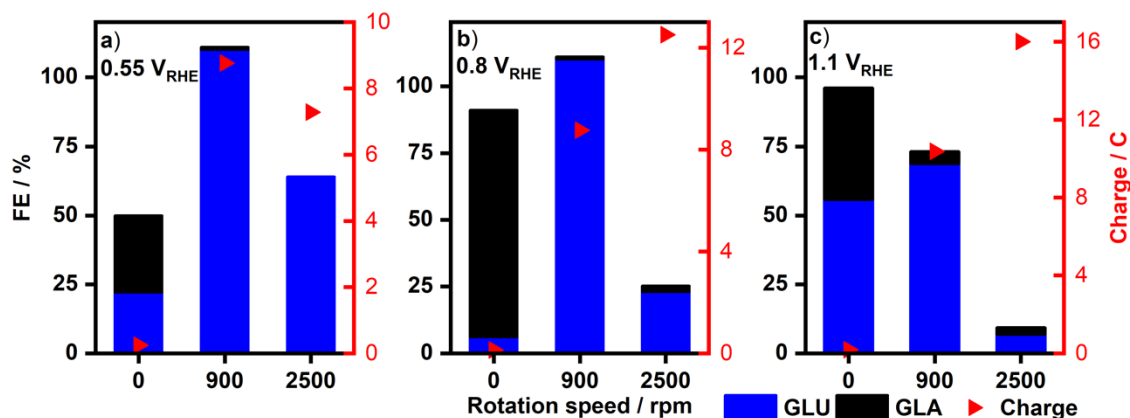


**Figure 5:** Product distribution in glucose oxidation at different oxidation potentials in 0.1 M NaOH and 0.1 M NaClO<sub>4</sub> with 10 mM glucose after 2h at: a) 0.55 V, b) 0.8 V, and c) 1.1 V. Faradaic efficiencies towards gluconic acid (GLU) and glucaric acid (GLA) depicted in blue and black, respectively. The transferred charge is displayed on the right-hand y-axis of each graph.

The thus defined three-step potential program was consecutively run for two hours at each of the oxidation potentials determined from the recorded CVs (**Figure 2**), i.e., 0.55 V, 0.8 V<sub>RHE</sub>, and 1.1 V<sub>RHE</sub>. In **Figure 5**, the Faradaic efficiencies (FE) towards gluconic acid (GLU) and glucaric acid (GLA) are depicted in the left-hand y-axis, while the transferred charge is depicted in the right-hand y-axis. The transferred charge is used to compare the reaction rates at different oxidation potentials and/or rotation speeds. Note, that without rotation, the transferred charges and thus the reaction rates for all reactions were very small, inflicting a high uncertainty on the related FEs. Thus, these values have to be treated with caution in the discussion and serve more for the observation of trends. Furthermore, the low reaction rates mean, that at 0 rpm seemingly high FEs cannot be exploited in a technical process. To determine the transferred charge, the measured currents were integrated. Since all capacitive currents from stepping through the potential program cancel each other out, the integration determines only the charge transferred at the applied oxidation potential of 0.55, 0.8 or 1.1 V<sub>RHE</sub> (**Figure S8** shows exemplary the current response in an experiment). The product analysis concentrates on gluconic, glucuronic and glucaric acid as they are the main interest in this study. Cleavage products

are checked for and shown in the supporting information (**Table ST1**). They appear in multiple measurements but for the most part at miniscule concentrations and are discussed in the relevant cases.

In **Figure 5a** the product distributions of measurements conducted in a 10 mM glucose containing electrolyte at 0.55 V<sub>RHE</sub> at different rotation speeds are shown. Independent of rotation speed, of the desired products only gluconic and glucaric acid are detected during product analysis. Glucuronic acid was not detected. Without rotation, the FEs of gluconic and glucaric acid add up to 50 %, see above discussion concerning the low reaction rates at 0 rpm. Gluconic acid accounts for 22 %, while glucaric acid accounts for 28 %. With the application of 900 rpm of rotation the reaction rates increase substantially (transferred charge increases by a factor of 35) and a shift in product distribution is observed. GLU and GLA account for all the transferred charge. However, after 2h FE<sub>GLA</sub> is just 1 % while FE<sub>GLU</sub> is 110%. If the rotation is further increased to 2500 rpm no GLA is detected anymore and FE<sub>GLU</sub> drops to 64 %. Obviously, a Faradaic efficiency above 100 % is unusual and theoretically impossible if only electrochemically produced products are considered. Nevertheless, we report the “as determined” FEs. Their value is attributed to the error in calibration and uncertainties in the product analysis. Other, non-electrochemical pathways could also lead to nominal FEs above 100 %. For example, there is the possibility of aging in the sample where the oxidation of glucose takes place between the measurement and the product analysis. To investigate the effect of aging, two-month-old blank glucose, gluconic acid and glucuronic acid solutions in 0.1 M NaOH electrolyte were tested and analysed for oxidation products. In short, gluconic acid and glucaric acid were found in very small amounts (**Figure ST3**). However, cleavage products have been found in larger quantities. Specifically glycolic acid and tartaric acid were identified in the blank, aged samples. Therefore, to minimise the influence of aging processes, product analysis was run as soon as possible after finishing an experiment. Other, charge-free processes might occur in the presence of the biased Au surface; however, these were not investigated further.

As mentioned above, when 900 rpm of rotation is applied, the amount of charge transferred increases by a factor of 35 compared to the experiments at 0 rpm. Based on the current response in the CV in **Fig 2a**, this is expected. However, at 2500 rpm the transferred charge is slightly decreased. This observation is in contradiction with the cyclic voltammogram where the current scales with the applied rotation. A key difference between the measurements, however, is that the oxidation experiments are much less dynamic than the cyclic voltammograms. The current response can therefore differ. Also, the increase in rotation speed not only means an increased flux of glucose at the electrode but also a decrease in the time the glucose molecules reside at the surface. Therefore, the glucose molecules might not have ample time to be oxidised at the catalytic interface. This can also explain the lowered FE towards the two detected products. Instead, glucose might be transformed into keto-species, such as 2- or 5-keto-glucose, or glucose dialdehyde<sup>40</sup> which we did not quantify in the product analysis. Other reaction products include cleavage products like tartaric or glycolic acid<sup>39</sup>. Indeed, both acids are detected by product analysis at 2500 rpm indicating higher concentrations of cleavage products than at 900 and 0 rpm. However, it is not possible to determine the Faradaic efficiency towards glycolic acid because the other corresponding cleavage products are unknown. Hence, only the quantities of detected glycolic acid at different experimental conditions can be compared. Quantified concentrations can be found in the supporting information (**Figure ST1**).

A similar picture arises when 0.8 V<sub>RHE</sub> is chosen as the oxidation potential (**Figure 5b**). In the absence of rotation, FE<sub>GLA</sub> of 85 % is reached and accordingly an FE<sub>GLU</sub> of 6 % is observed. At 900 rpm, gluconic acid is the main oxidation product being formed at an FE of 110 % and glucaric acid at an FE of 1 %, again. At the high rotation speed of 2500 rpm, the total FE towards detected products plummets to 25 % (FE<sub>GLU</sub>: 23 %, FE<sub>GLA</sub>: 2 %). The transferred charge is increased with increased rotation speed, as is expected from the cyclic voltammogram. The decline in FE towards the saccharic acids indicates increased rates of formation of side and cleavage products which is confirmed by the detection of larger quantities of cleavage products (**Figure ST1 and ST2**).



Finally, in a 10 mM glucose containing solution at an oxidation potential of 1.1 V (**Figure 5c**), at 0 rpm glucaric acid is formed at a Faradaic efficiency of 40 %, while gluconic acid is the main product at 56 % FE. Applying 900 rpm rotation leads to an increase in  $FE_{\text{GLU}}$  to 69 % while  $FE_{\text{GLA}}$  decreases to 6 %. Therefore, the sum of detected products is lowered compared to the measurement at 0 rpm. This decrease in combined FE is more pronounced at 2500 rpm, where gluconic and glucaric acid account for less than 20 % of the transferred charge. The absolute amount of charge is once again increasing with the applied rotation speed and is also higher than at 0.8  $V_{\text{RHE}}$ . Therefore, more undesired side products are formed. Accordingly, more glycolic acid is detected in the product analysis.

Concluding the observation from the 10 mM glucose containing starting electrolyte, the Faradaic efficiency towards glucaric acid is the highest in the absence of rotation at all oxidation potentials. However, the reaction rate is very low. Gluconic acid is the main product if a rotation of 900 rpm is applied, reaching almost fully selective formation at 0.55  $V_{\text{RHE}}$  and 0.8  $V_{\text{RHE}}$ . If one considers the competition of different species at the interface, this observation can be rationalized. When no rotation is applied, reaction intermediates, such as gluconic acid, stay in proximity of the catalytic interface. Hence, the probability of the intermediates being oxidised further is high. Additionally, only through diffusion can intermediates be removed from the interface and glucose molecules arrive thereat. This explains the higher selectivity towards glucaric acid in the absence of rotation. On the other hand, when rotation is applied, the residing time of the intermediate molecules is shortened as they are removed from the interface through forced convection. On top of that, the flux of glucose molecules, and thereby also the competition for active sites on the catalyst, is increased when rotation is applied. These two effects can explain why gluconic acid is formed at increased rates and with increased selectivity with the application of rotation. While the oxidation currents are highest at 1.1  $V_{\text{RHE}}$ , the FEs towards the gluconic and glucaric acid are decreased. This trend is amplified when rotation is applied, making the combination of 1.1  $V_{\text{RHE}}$  and 2500 rpm an unfavourable condition for the selective glucose oxidation towards GLU and GLA in the series (**Figure 5c**). It appears that side products are formed preferably under these conditions. The more oxidative potential seems to enable

the oxidation not only on the C<sub>1</sub> and C<sub>6</sub> positions but also elsewhere. Breaking the C-C chain can yield small organic acids as has been reported on Pt<sup>30</sup>. Indeed, the small organic acid glycolic acid has been detected in the analytes of the experiments at 2500 rpm. The Faradaic efficiency towards glycolic acid can however not be determined as previously mentioned. Therefore, the number of transferred electrons is also unknown. However, the glycolic acid contents can be compared quantitatively. And indeed, the amount of glycolic and tartaric acid detected in the analyte increases as a function of rotation speed and oxidation potential (**Figure ST1 and ST2**). Thereby confirming the hypothesis that glucose cleavage is increased under strong rotation and high oxidation potential.

For glucose oxidation, the transferred charge is heavily dependent on the applied rotation. Comparing 0 rpm and 900 rpm at the three potentials, 30 times more charge is transferred when rotation is applied. As mentioned above, this means that the high FE<sub>GLA</sub> in the absence of rotation cannot be fully exploited as the rate of formation is very low rendering it uninteresting for potential upscaling. Finally, the conditions leading to the most efficient and selective oxidation of glucose are found to be at moderate rotation of 900 rpm and lower overpotentials of 0.55 V<sub>RHE</sub> and 0.8 V<sub>RHE</sub> (**Figure 5b&c**).

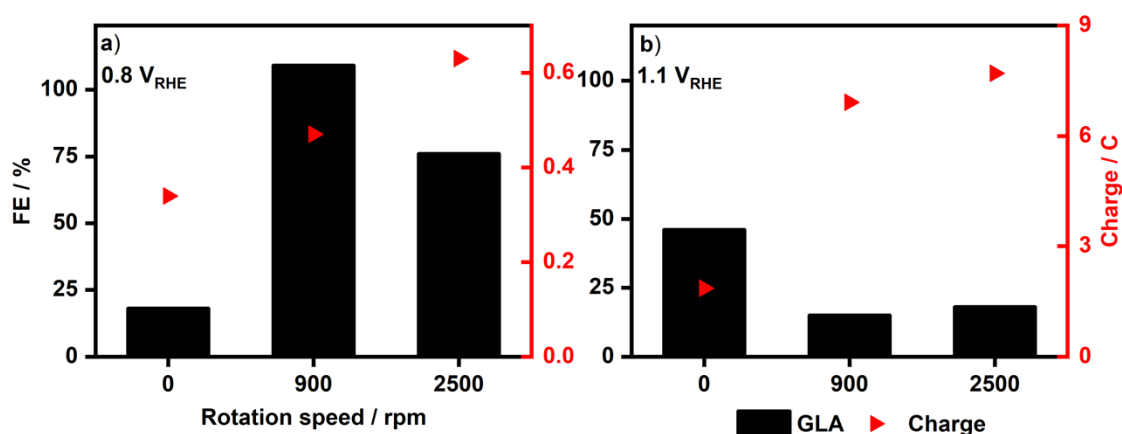


**Figure 6:** Product distribution in gluconic acid oxidation experiments at different oxidation potentials in 0.1 M NaOH and 0.1 M NaClO<sub>4</sub> with 10 mM gluconic acid after 2h: a) 0.8 V<sub>RHE</sub> and b) 1.1 V<sub>RHE</sub>. The transferred charge is displayed on the right-hand y-axis of each graph.

In Figure 6, gluconic acid oxidation has been investigated by running the same experiments replacing the glucose in the electrolyte with gluconic acid at a concentration of 10 mM. Due to the low current response at  $0.55 V_{RHE}$ , also seen in the respective cyclic voltammograms in **Figure 2b**, no product analysis could be reliably conducted for these experiments. Again, no glucuronic acid has been detected in any of the experiments.

At an oxidation potential of  $0.8 V_{RHE}$  (**Figure 6a**) the selectivity towards glucaric acid changes with the applied rotation speed. Without rotation,  $FE_{GLA}$  is 18 %. When rotation is applied an increase in  $FE_{GLA}$  is observed: 107 % and 73 % at 900 rpm and 2500 rpm, respectively. While an increase in the transferred charge is observed, rotation does not have the same effect on the reaction rates as observed in glucose oxidation (**Figure 4**). The transferred charge is increased from 0.34 C at 0 rpm to 0.63 C at 2500 rpm which is an increase of only 85 %, however, it is important to note that the current is 10x lower than for glucose oxidation at similar potential and rotation conditions. Kinetic limitations in gluconic acid oxidation are therefore also present under a less dynamic regime. In comparison, when applying an oxidation potential of  $1.1 V_{RHE}$ , the oxidation rate does depend more on the applied rotation speed and comparable currents to glucose oxidation are measured. However, the product distribution and the  $FE_{GLA}$  are negatively affected by the more oxidative potential. Without rotation a Faradaic efficiency towards glucaric acid of 46 % is reached. When rotation is applied, either 900 rpm or 2500 rpm, the FE decreases to 15 % and 18 %, respectively. Comparing **Figures 6a** and **6b** it is clearly visible that the  $FE_{GLA}$  and the transferred charge are controlled more by the applied potential rather than the rotation. Specifically, in the absence of rotation the application of the larger overpotential of  $1.1 V_{RHE}$  increases the efficiency towards glucaric acid but a decrease in efficiency towards glucaric acid is observed when rotation is applied. The transferred charge depends mainly on the applied potential as it is significantly higher for all the measurements conducted at  $1.1 V_{RHE}$ . The charge which is not accounted for in the  $FE_{GLA}$  likely ends up in side products. Considerable amounts of glycolic and tartaric acid have been detected when oxidising gluconic acid at  $1.1 V_{RHE}$  (**Figure ST1 and ST2**). Mechanistically, this shows that an alcohol group is more difficult to oxidise than the aldehyde group. Noticeably, once the alcohol

group can be oxidized, more dissociation products are formed showing that there seems no preferentially selective oxidation of the -OH groups on the glucose. In principle all OH-groups can be oxidized similarly when high potential is present. This hypothesis is also supported by the DFT calculations presented in this study, from which it was predicted that the terminal OH-group is energetically favoured only slightly, probably by steric effects, over non-terminal groups.

The categoric absence of glucuronic acid poses the question whether it is formed at all. It is possible that on a gold catalyst a pathway from gluconic acid to glucaric acid exists where no glucuronic acid is formed. Based on the energy diagram (**Figure 3**) of the intermediates on gold, glucuronic acid would be a valid intermediate at the chosen potentials. However, the removal of the proton-electron pairs of the O and the C is energetically close on Au. If the removal of the O-proton is kinetically hindered, it is possible to deprotonate C<sub>6</sub> and thereby circumventing glucuronic acid as an intermediate. Another indication for the circumvention of glucuronic acid is the increased formation of tartaric and glycolic acid at larger overpotentials at 1.1 V<sub>RHE</sub>. This indicates that the carbon atoms in the C<sub>6</sub>-chain might be oxidised more easily under these reaction conditions. Alternatively, the formed glucuronic acid might be immediately converted to glucaric acid under the chosen reaction parameters. Supporting this hypothesis is the nature of glucuronic acid oxidation. It is very similar to the oxidation of glucose to gluconic acid: It requires the oxidation of an aldehyde group to a carboxyl group. **Figure 5** (glucose oxidation to gluconic acid) shows that this step readily happens at 0.8 V<sub>RHE</sub>.

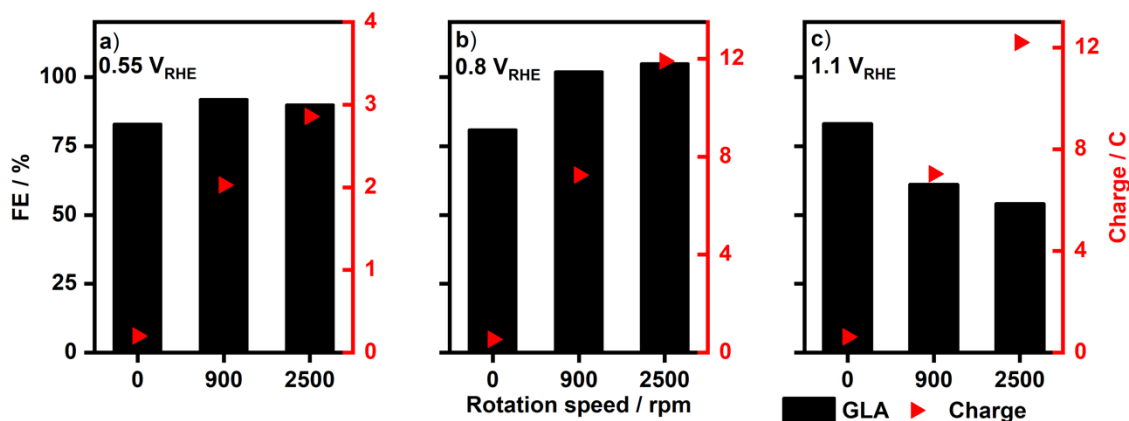


**Figure 7:** Product distribution in glucuronic acid oxidation at different oxidation potentials in 0.1 M NaOH and 0.1 M NaClO<sub>4</sub> with 10 mM glucuronic acid after 2h: a) 0.55 V, b) 0.8 V and c) 1.1 V. The transferred charge is displayed on the right-hand y-axis of each graph.

Glucuronic acid oxidation, as a potential reaction intermediate, has been investigated in **Figure 7** by running the three-step potential program in electrolytes containing 10 mM of glucuronic acid. At 0.55 V<sub>RHE</sub> glucuronic acid is formed with a FE of 83 % at 0 rpm rotation, 92 % at 900 rpm, and 90% at 2500 rpm. Increasing the oxidation potential to 0.8 V<sub>RHE</sub>, FE<sub>GLA</sub> remains high at 81 % without rotation, and 102 % and 105 % at 900 rpm and 2500 rpm respectively. At 1.1 V<sub>RHE</sub>, the Faradaic efficiency towards glucuronic acid decreases with the speed of the applied rotation. In the absence of rotation, a FE<sub>GLA</sub> of 83 % is observed. At 900 rpm the selectivity drops to 61 % and is decreased to 54 % at 2500 rpm. The transferred charge depends on the rotation speed at all oxidation potential. Faster rotation speeds lead to more charge transferred. However, there is no significant difference in the amount of transferred charge comparing the measurements at 0.8 V<sub>RHE</sub> and 1.1 V<sub>RHE</sub>. Analysing **Figures 7a - c**, it becomes apparent that the Faradaic efficiency towards glucuronic acid is independent of the applied potential at 0 rpm. The charge transferred and thus the reaction rate, is however much lower in the absence of rotation compared to the measurements conducted at 900 or 2500 rpm rotation. With applied rotation, the selectivity towards glucuronic acid is superior at 0.8 V<sub>RHE</sub> compared to 0.55 V<sub>RHE</sub> and 1.1 V<sub>RHE</sub>. Glucuronic acid is formed seemingly exclusively. Increasing the oxidation potential to 1.1 V<sub>RHE</sub>

has no beneficial effect. In contrary,  $FE_{\text{GLA}}$  drops while the transferred charge remains identical. The rate of glucaric acid formation is therefore higher at  $0.8 V_{\text{RHE}}$ . Overall, glucuronic acid oxidation is similar to glucose oxidation reaction, which fits our mechanistic understanding from the DFT simulations, where oxidizing an aldehyde group is similar in glucuronic acid and glucose at  $0.8 V_{\text{RHE}}$ . Furthermore, at potentials as high as  $1.1 V_{\text{RHE}}$  both glucose, glucuronic acid and possibly glucaric acid become susceptible to oxidation and cleavage. Supporting this hypothesis is the higher abundance of tartaric and glycolic acid in the electrolyte of experiments at  $1.1 V_{\text{RHE}}$  than at  $0.8 V_{\text{RHE}}$ . These observations imply, that when starting in a glucose containing electrolyte, once glucuronic acid would be formed at  $0.8 V_{\text{RHE}}$ , it likely will be converted to glucaric acid.

## Conclusion

The interplay of mass transport and oxidation potential in the oxidation of glucose, gluconic and glucuronic acid have been investigated. The applied rotation influences the rate of formation, product distribution and overall faradaic efficiency towards the desired products gluconic and glucaric acid. We find the introduction of moderate rotation, 900 rpm in this series of measurements, to be beneficial for the rate and selectivity towards gluconic and glucaric acid. The application of a higher rotation speed, i.e., 2500 rpm, however, decreases the selectivity towards desired products in all cases. We propose that at higher rotation speed the reactants do not reside long enough at the interface for the desired oxidation steps to take place. Rather, side products are preferably formed under these conditions. Furthermore, we find the application of a moderate oxidation potential of  $0.8 V_{RHE}$  to lead to better catalytic performance in terms of product selectivity towards gluconic acid and minor FE towards glucaric acid. At the larger overpotential of  $1.1 V_{RHE}$ , the increased charge transfer is accompanied by a loss of selectivity towards gluconic or glucaric acid, respectively. The detection of glycolic acid, as well as tartaric acid in the case of gluconic acid oxidation, supports this hypothesis. The amount of cleavage products increases with increasing applied oxidation potential. Additionally, in the case of gluconic acid oxidation, the application of 2500 rpm rotation increases the abundance of cleavage products in the analyte.

Applying rotation in experiments, where glucose or glucuronic acid are used as reactants, we found the reaction rates to be greatly increased compared to experiments without applied rotation. Simultaneously, in glucose containing electrolytes the  $FE_{GLU}$  was increased while  $FE_{GLA}$  was decreased under applied rotation. At  $0.8 V_{RHE}$  and 900 rpm gluconic acid is almost selectively formed. At  $0.8 V_{RHE}$  and 0 rpm the main reaction product is glucaric acid which is produced with a FE of 70 %. Due to the very low charge transferred under these conditions, it is however much more interesting to first transform glucose into gluconic acid and then transform it to glucaric acid.

The rate of gluconic acid oxidation has been found to be less influenced by the rotation rate. The product distribution, however, is influenced. We found gluconic acid to be seemingly selectively oxidised to glucaric acid at moderate rotation of 900 rpm but at very low rates. The low reaction rates indicate that oxidation of an alcohol group is difficult on gold. When oxidising glucuronic acid, the best performing parameters have also been found to be at  $0.8 V_{\text{RHE}}$  and 900 rpm. The application of forced convection also increases the transferred charge tremendously, similar to what is observed in glucose oxidation. It appears that the oxidation of an aldehyde group to a carboxylic group is easily achieved on gold. Hence, other studies have already reported the selective formation of gluconic acid from glucose oxidation on gold. Also, this observation suggests that upon formation of glucuronic acid as a reaction intermediate, the transfer of the last two electrons to form glucaric acid might occur easily. From our set of experiments, we however cannot definitively conclude if glucuronic acid is an intermediate in the pathway from glucose to glucaric acid as it was not detected in the product analysis. Based on the DFT calculations, a pathway circumventing glucuronic acid is energetically feasible and supported by the increased abundance of cleavage products in gluconic acid oxidation. In this alternative pathway the carbon instead of the oxygen becomes deprotonated resulting in a pathway where no glucuronic acid is formed.

Independent of glucuronic acid formation, the oxidation of gluconic acid is a clear bottle neck in the conversion of glucose to glucaric acid. Improving the reaction kinetics of this step is the key towards efficient, fast, and selective conversion of glucose to glucaric acid. One possibility is to modify the Au-electrode. For further investigations, it might be interesting to combine the approach of Wojcieszak et al.<sup>40</sup>, which reported the selective oxidation of glucose to glucuronic acid on a caesium-doped Au catalyst, with an electrochemical approach. From there, the final oxidation step to form glucaric acid should be straight forward.



## Acknowledgement

We acknowledge support from the Swiss National Science Foundation (SNSF) project No. 200021\_184742 and the Danish National Research Foundation Center for High Entropy Alloy Catalysis (DNRF 149). A.B. acknowledges support from the Carlsberg Foundation (CF21-0144).

## Author contributions

**Nicolas Schlegel:** Performing electrochemical measurements and product analysis; paper writing.

**Alexander Bagger:** DFT calculations, paper writing; **Jan Rossmeisl:** Supervision; Reviewing; **Matthias**

**Arenz:** Supervision, conceptualization, Reviewing, Editing.

## References

1. Werpy, T. & Petersen, G. Top Value Added Chemicals from Biomass Volume I. *Us Nrel* (2004) doi:10.2172/15008859.
2. Ramachandran, S., Fontanille, P., Pandey, A. & Larroche, C. Gluconic Acid: Properties, Applications and Microbial Production. *Food Technol. Biotechnol.* **44**, 185–195 (2000).
3. Van De Vyver, S. & Román-Leshkov, Y. Emerging catalytic processes for the production of adipic acid. *Catal. Sci. Technol.* **3**, 1465–1479 (2013).
4. Ibert, M., Marsais, F., Merbouh, N. & Brückner, C. Determination of the side-products formed during the nitroxide-mediated bleach oxidation of glucose to glucaric acid. *Carbohydr. Res.* **337**, 1059–1063 (2002).
5. Ibert, M. *et al.* Improved preparative electrochemical oxidation of d-glucose to d-glucaric acid. *Electrochim. Acta* **55**, 3589–3594 (2010).
6. Moggia, G., Kenis, T., Daems, N. & Breugelmanns, T. Electrochemical Oxidation of d -Glucose in

- Alkaline Medium : Impact of Oxidation Potential and Chemical Side Reactions on the Selectivity to d -Gluconic and d -Glucaric Acid. *ChemElectroChem* **7**, 1–11 (2019).
7. Adzic, R. R., Hsiao, M. W. & Yeager, E. B. Electrochemical oxidation of glucose on single crystal gold surfaces. *J. Electroanal. Chem.* **260**, 475–485 (1989).
  8. Aoun, S. Ben *et al.* Effect of metal ad-layers on Au(1 1 1) electrodes on electrocatalytic oxidation of glucose in an alkaline solution. *J. Electroanal. Chem.* **567**, 175–183 (2004).
  9. Cho, S., Shin, H. & Kang, C. Catalytic glucose oxidation on a polycrystalline gold electrode with an amalgamation treatment (TM 05092). *Electrochim. Acta* **51**, 3781–3786 (2006).
  10. A. Larew, L. & Johnson, D. C. Concentration dependence of the mechanism of glucose oxidation at gold electrodes in alkaline media. *J. Electroanal. Chem.* **262**, 167–182 (1989).
  11. Escalona-Villalpando, R. A. *et al.* Electrodeposition of gold on oxidized and reduced graphite surfaces and its influence on glucose oxidation. *J. Electroanal. Chem.* **816**, 92–98 (2018).
  12. Parpot, P., Muiuane, V. P., Defontaine, V. & Bettencourt, A. P. Electrocatalytic oxidation of readily available disaccharides in alkaline medium at gold electrode. *Electrochim. Acta* **55**, 3157–3163 (2010).
  13. Biella, S., Prati, L. & Rossi, M. Selective oxidation of D-glucose on gold catalyst. *J. Catal.* **206**, 242–247 (2002).
  14. Li, C. Y. *et al.* In Situ Monitoring of Electrooxidation Processes at Gold Single Crystal Surfaces Using Shell-Isolated Nanoparticle-Enhanced Raman Spectroscopy. *J. Am. Chem. Soc.* **137**, 7648–7651 (2015).
  15. de Mele, M. F. L., Videla, H. A. & Arvía, A. J. Potentiodynamic Study of Glucose Electro-Oxidation at Bright Platinum Electrodes. *J. Electrochem. Soc.* **129**, 2207–2213 (1982).
  16. Kokoh, K. B., Léger, J. M., Beden, B. & Lamy, C. 'On line' chromatographic analysis of the

- products resulting from the electrocatalytic oxidation of d-glucose on Pt, Au and adatoms modified Pt electrodes-Part I. Acid and neutral media. *Electrochim. Acta* **37**, 1333–1342 (1992).
17. Vassilyev, Y. B., Khazova, O. A. & Nikolaeva, N. N. Kinetics and mechanism of glucose electrooxidation on different electrode-catalysts. Part II. Effect of the nature of the electrode and the electrooxidation mechanism. *J. Electroanal. Chem.* **196**, 127–144 (1985).
  18. Wang, W. *et al.* Combining Bimetallic-Alloy with Selenium Functionalized Carbon to Enhance Electrocatalytic Activity towards Glucose Oxidation. *Electrochim. Acta* **244**, 16–25 (2017).
  19. Tominaga, M. *et al.* Electrocatalytic oxidation of glucose at gold-silver alloy, silver and gold nanoparticles in an alkaline solution. *J. Electroanal. Chem.* **590**, 37–46 (2006).
  20. Habrioux, A. *et al.* Activity of platinum-gold alloys for glucose electrooxidation in biofuel cells. *J. Phys. Chem. B* **111**, 10329–10333 (2007).
  21. Dey, S., Mandal, M. K., Pramanik, S., Atta, S. & Basu, S. Bi<sub>2</sub>O<sub>3</sub>-incorporated carbon-supported bismuth-silver (Bi@Ag/C) nanoparticle as an efficient and stable electrocatalyst for glucose electro-oxidation. *Ionics (Kiel)*. (2022) doi:10.1007/s11581-022-04863-2.
  22. Yan, L. *et al.* Efficient and poison-tolerant PdxAu<sub>y</sub>/C binary electrocatalysts for glucose electrooxidation in alkaline medium. *Appl. Catal. B Environ.* **150–151**, 268–274 (2014).
  23. Yan, X., Ge, X. & Cui, S. Pt-decorated nanoporous gold for glucose electrooxidation in neutral and alkaline solutions. *Nanoscale Res. Lett.* **6**, 6–11 (2011).
  24. Neha, N., Kouamé, B. S. R., Rafaideen, T., Baranton, S. & Coutanceau, C. Remarkably Efficient Carbon-Supported Nanostructured Platinum-Bismuth Catalysts for the Selective Electrooxidation of Glucose and Methyl-Glucoside. *Electrocatalysis* (2020) doi:10.1007/s12678-020-00586-y.
  25. Eshghi, A. & kheirmand, M. Graphene/Ni–Fe layered double hydroxide nano composites as

- advanced electrode materials for glucose electro oxidation. *Int. J. Hydrogen Energy* **42**, 15064–15072 (2017).
26. Liu, W. J. *et al.* Efficient electrochemical production of glucaric acid and H<sub>2</sub> via glucose electrolysis. *Nat. Commun.* **11**, 265 (2020).
  27. Yi, Q., Huang, W., Yu, W., Li, L. & Liu, X. Hydrothermal synthesis of titanium-supported nickel nanoflakes for electrochemical oxidation of glucose. *Electroanalysis* **20**, 2016–2022 (2008).
  28. Cao, M. *et al.* Nickel-copper oxide nanoflowers for highly efficient glucose electrooxidation. *Int. J. Hydrogen Energy* **46**, 28527–28536 (2021).
  29. Zheng, W. *et al.* Cull-Mediated Ultra-efficient Electrooxidation of Glucose. *ChemElectroChem* **4**, 2788–2792 (2017).
  30. Kokoh, K. B., Leger, J. M., Beden, B., Huser, H. & Lamy, C. 'On line' chromatographic analysis of the products resulting from the electrocatalytic oxidation of D-glucose on pure and adatoms modified Pt and Au electrodes - Par II Alkaline medium. *Electrochim. Acta* **37**, 1909–1918 (1992).
  31. Pasta, M., Ruffo, R., Falletta, E., Mari, C. M. & Della Pina, C. Alkaline glucose oxidation on nanostructured gold electrodes. *Gold Bull.* **43**, 60–67 (2010).
  32. Mello, G. A. B., Cheuquepán, W., Briega-Martos, V. & Feliu, J. M. Glucose electro-oxidation on Pt(100) in phosphate buffer solution (pH 7): A mechanistic study. *Electrochim. Acta* **354**, (2020).
  33. Beden, B., Largeaud, F., Kokoh, K. B. & Lamy, C. Fourier transform infrared reflectance spectroscopic investigation of the electrocatalytic oxidation of D-glucose: Identification of reactive intermediates and reaction products. *Electrochim. Acta* **41**, 701–709 (1996).
  34. Ishimoto, T., Hamatake, Y., Kazuno, H., Kishida, T. & Koyama, M. Theoretical study of support effect of Au catalyst for glucose oxidation of alkaline fuel cell anode. *Appl. Surf. Sci.* **324**, 76–

- 81 (2015).
35. Dourado, A. H. B. *et al.* In situ FTIR insights into the electrooxidation mechanism of glucose as a function of the surface facets of Cu<sub>2</sub>O-based electrocatalytic sensors. *J. Catal.* **375**, 95–103 (2019).
  36. Neha, N. *et al.* Revisited Mechanisms for Glucose Electrooxidation at Platinum and Gold Nanoparticles. *Electrocatalysis* **14**, 121–130 (2023).
  37. Faverge, T. *et al.* In Situ Investigation of d-Glucose Oxidation into Value-Added Products on Au, Pt, and Pd under Alkaline Conditions: A Comparative Study. *ACS Catal.* 2657–2669 (2023) doi:10.1021/acscatal.2c05871.
  38. Moggia, G., Schalck, J., Daems, N. & Breugelmans, T. Two-steps synthesis of D-glucaric acid via D-gluconic acid by electrocatalytic oxidation of D-glucose on gold electrode: Influence of operational parameters. *Electrochim. Acta* **374**, 137852 (2021).
  39. Kokoh, K. B. *et al.* Selective oxidation of D-gluconic acid on platinum and lead adatoms modified platinum electrodes in alkaline medium. *Electrochim. Acta* **38**, 1359–1365 (1993).
  40. Wojcieszak, R., Cuccovia, I. M., Silva, M. A. & Rossi, L. M. Selective oxidation of glucose to glucuronic acid by cesium-promoted gold nanoparticle catalyst. *J. Mol. Catal. A Chem.* **422**, 35–42 (2016).
  41. Schlegel, N., Wiberg, G. K. H. & Arenz, M. On the electrooxidation of glucose on gold: Towards an electrochemical glucaric acid production as value-added chemical. *Electrochim. Acta* **410**, 140023 (2022).
  42. Hjorth Larsen, A. *et al.* The atomic simulation environment - A Python library for working with atoms. *J. Phys. Condens. Matter* **29**, (2017).
  43. Wellendorff, J. *et al.* Density functionals for surface science: Exchange-correlation model development with Bayesian error estimation. *Phys. Rev. B - Condens. Matter Mater. Phys.* **85**,

- 32–34 (2012).
44. Enkovaara, J. *et al.* Electronic structure calculations with GPAW: A real-space implementation of the projector augmented-wave method. *J. Phys. Condens. Matter* **22**, (2010).
  45. Burke, L. D. & Nugent, P. F. The electrochemistry of gold: I. The redox behaviour of the metal in aqueous media. *Gold Bull.* **30**, 43–53 (1997).
  46. Bagger, A., Ju, W., Varela, A. S., Strasser, P. & Rossmeisl, J. Electrochemical CO<sub>2</sub> Reduction: A Classification Problem. *ChemPhysChem* **18**, 3266–3273 (2017).
  47. Valter, M., Dos Santos, E. C., Pettersson, L. G. M. & Hellman, A. Selectivity of the first two glycerol dehydrogenation steps determined using scaling relationships. *ACS Catal.* **11**, 3487–3497 (2021).
  48. Belgsir, E. M. *et al.* Electrosynthesis in aqueous medium: a kinetic study of the electrocatalytic oxidation of oxygenated organic molecules. *Electrochim. Acta* **36**, 1157–1164 (1991).

## Supporting Information

### **Electrooxidation of glucose, gluconic acid and glucuronic acid: Influence of rotation speed and potential on product distribution**

Nicolas Schlegel<sup>a</sup>, Alexander Bagger<sup>b</sup>, Jan Rossmeisl<sup>c</sup>, Matthias Arenz<sup>a, \*</sup>

<sup>a</sup>) Department of Chemistry, Biochemistry and Pharmaceutical Sciences, University of Bern, Freiestrasse 3, 3012 Bern, Switzerland

<sup>b</sup>) Department of Chemical Engineering, Imperial College London, London, UK

<sup>c</sup>) Department of Chemistry, University of Copenhagen, Universitetsparken 5, 2100 København Ø

\* Corresponding author: [Matthias.arenz@unibe.ch](mailto:Matthias.arenz@unibe.ch)

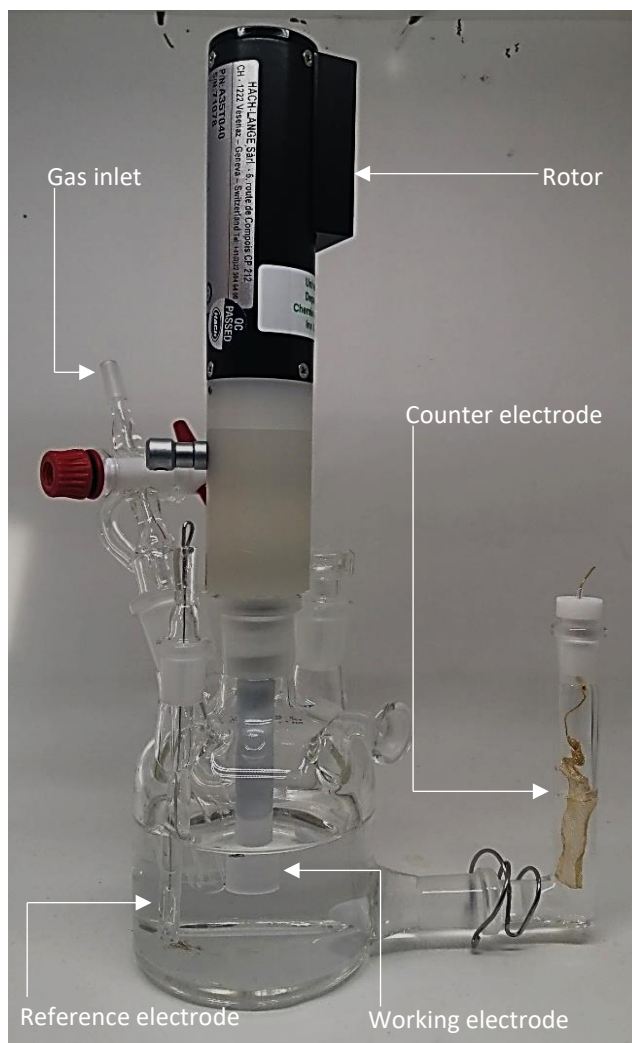


**Figure S1:** Electrochemical setup used for all experiments. It contains the gold mesh (counter electrode), the in-situ prepared trapped hydrogen electrode (reference electrode) and the PTFE-embedded Au-disk (working electrode). Picture taken from ref<sup>1</sup> with permission from the authors.



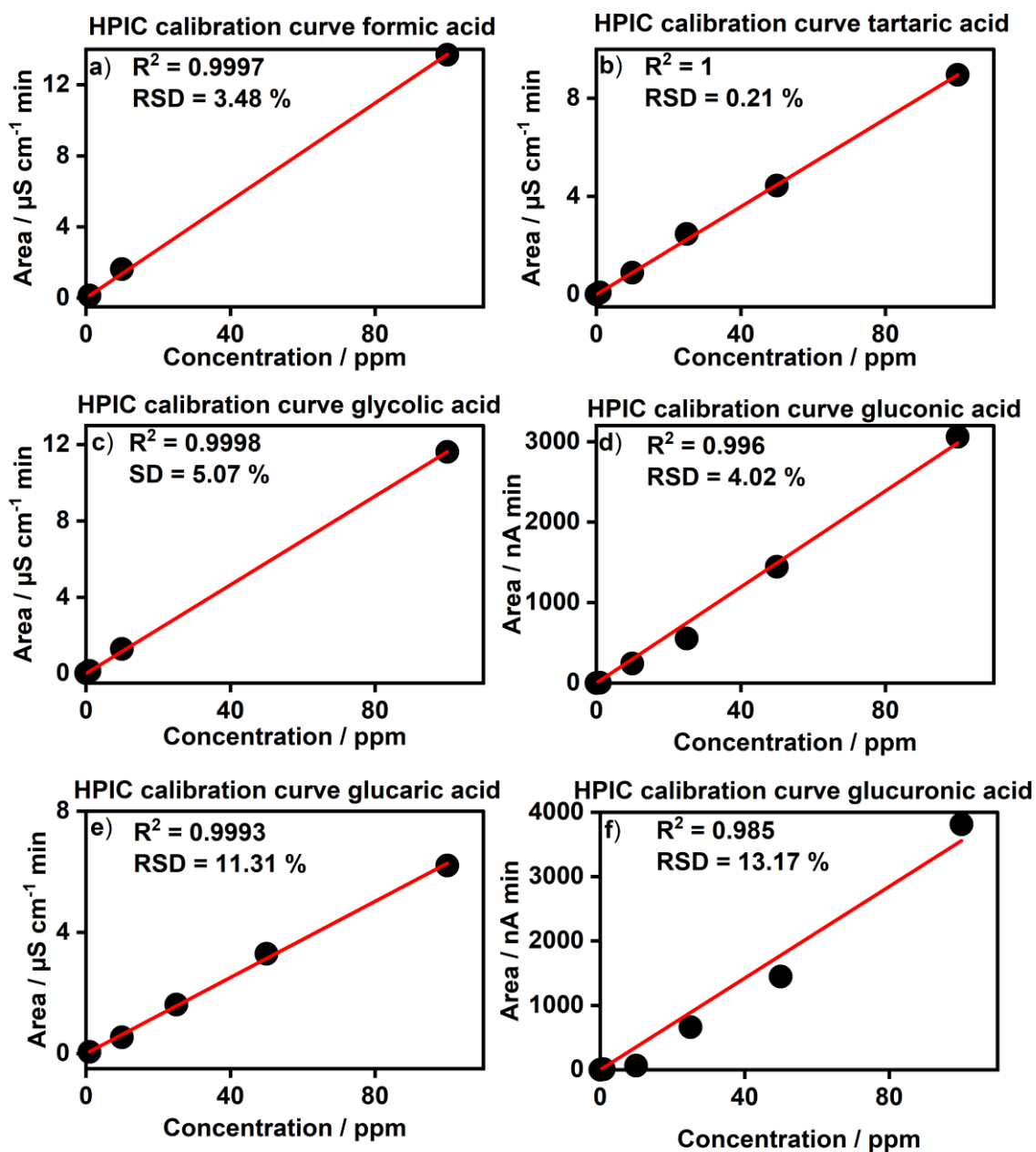


**Figure S2:** Calibration curves for the dissociation products: a) formic acid, b) tartaric acid, c) glycolic acid. Calibration curves for the saccharic acids: d) gluconic acid, e) glucaric acid, f) glucuronic acid. The calibration window ranges from 0.1 ppm and 100 ppm for tartaric acid, gluconic acid, glucuronic acid, and glucaric acid. The calibration windows of glycolic acid and formic acid range from 1 to 100 ppm.  $R^2$  values and relative standard deviation values are shown in the respective graphs.

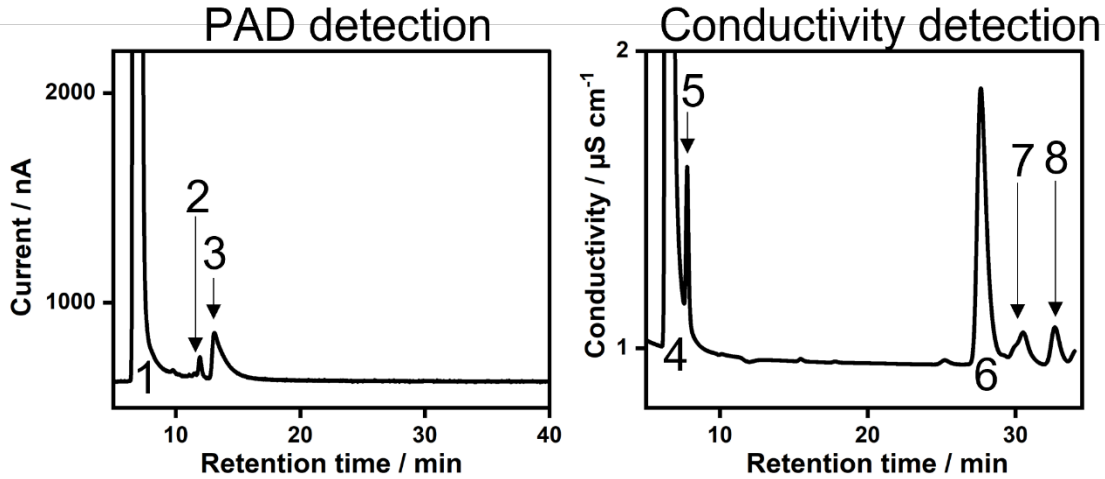


**Figure S3:** Exemplary chromatograms recorded through the PAD line (a) and the conductivity line (b). Experimental conditions for the chromatograms: a) 10 mM glucose, 1.1  $V_{RHE}$ , 2500 rpm; b) 10 mM glucuronic acid, 0.8  $V_{RHE}$ , 2500 rpm. The indices label glucose (1), fructose (2), gluconic acid (3), glucuronic acid (4), formic acid (5), glucaric acid (6), tartaric acid (7), glycolic acid (8).

The presence of fructose (2) in experiments containing glucose as the starting compound is explained by both the purity of the glucose precursor and the isomerization of glucose to fructose occurring in aqueous, alkaline media<sup>2</sup>. Not that, using the PAD detector, glucuronic acid would also be detectable (RT= 32 min) but none was formed in the experiments, seemingly. Conductivity detection was not used to quantify glucuronic acid because there was peak overlap with gluconic acid. Quantifying only a selection of C-C dissociation products serves to validate the product analysis method and to confirm that the missing charge is used to cleave the reactant molecules.

The faradaic efficiencies towards compound  $i$  is calculated using the following equation:

$$FE_i = \frac{Q_i}{Q_{tot}} * 100 = \frac{ppm_i * Z * V * F}{Q_{tot} * 10^3 * M_i}$$

Where  $Q_i$  is the partial charge of the compound,  $Q_{tot}$  the total charge transferred during the experiment,  $ppm_i$  the concentration of compound  $i$  determined by HPIC,  $Z$  the number of electrons involved in the electrode reaction,  $V$  the volume of the electrolyte,  $F$  Faraday's constant, and  $M_i$  the molar mass of compound  $i$ .

## DFT calculations

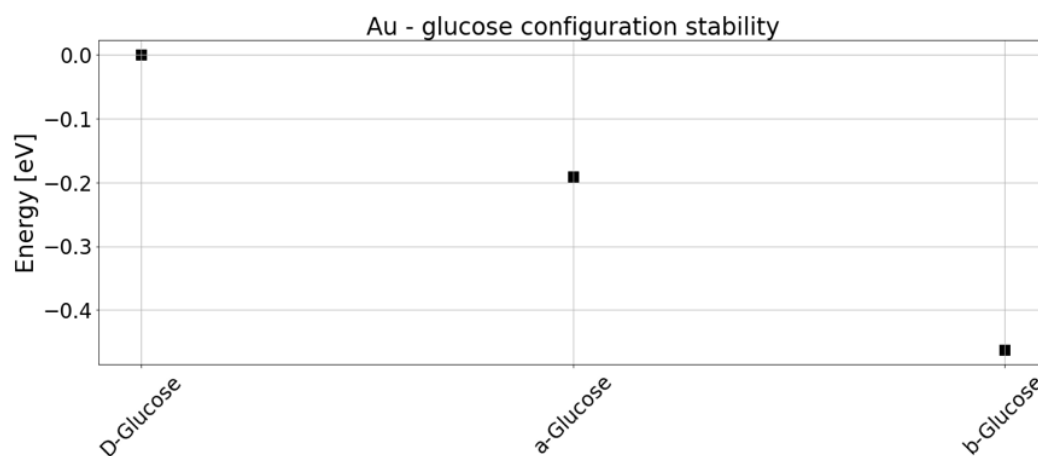


**Figure S4:** DFT investigations of the energetics of the different glucose configurations with reference to D-glucose.

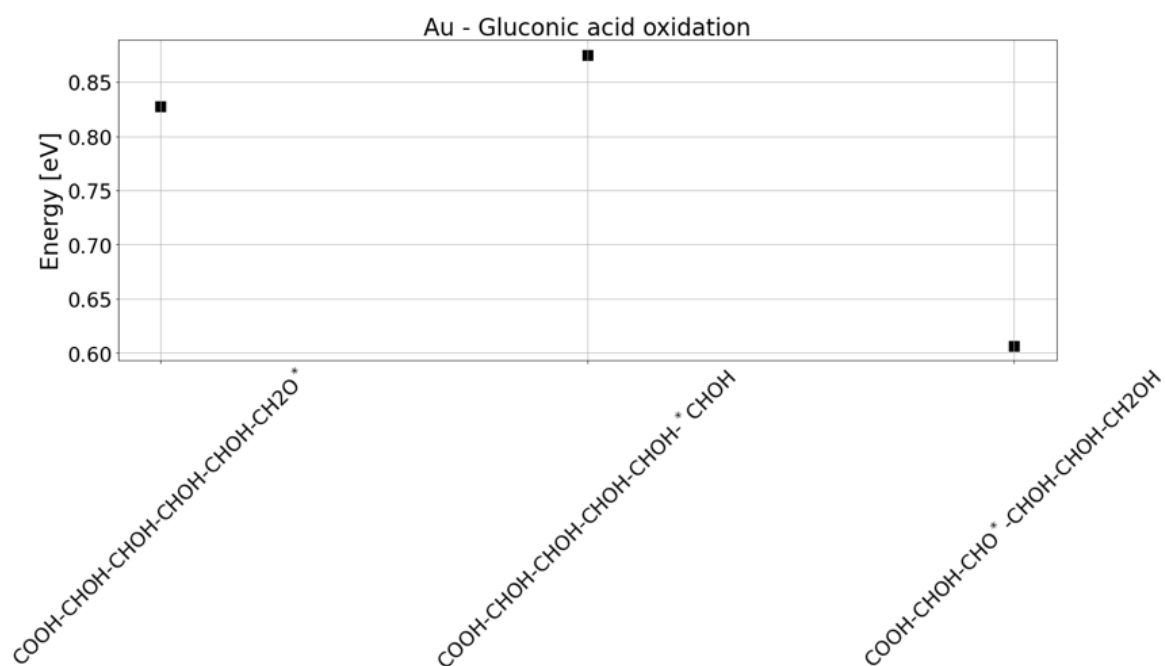


**Figure S5:** DFT investigations of oxidizing the first proton-electron from gluconic acid.

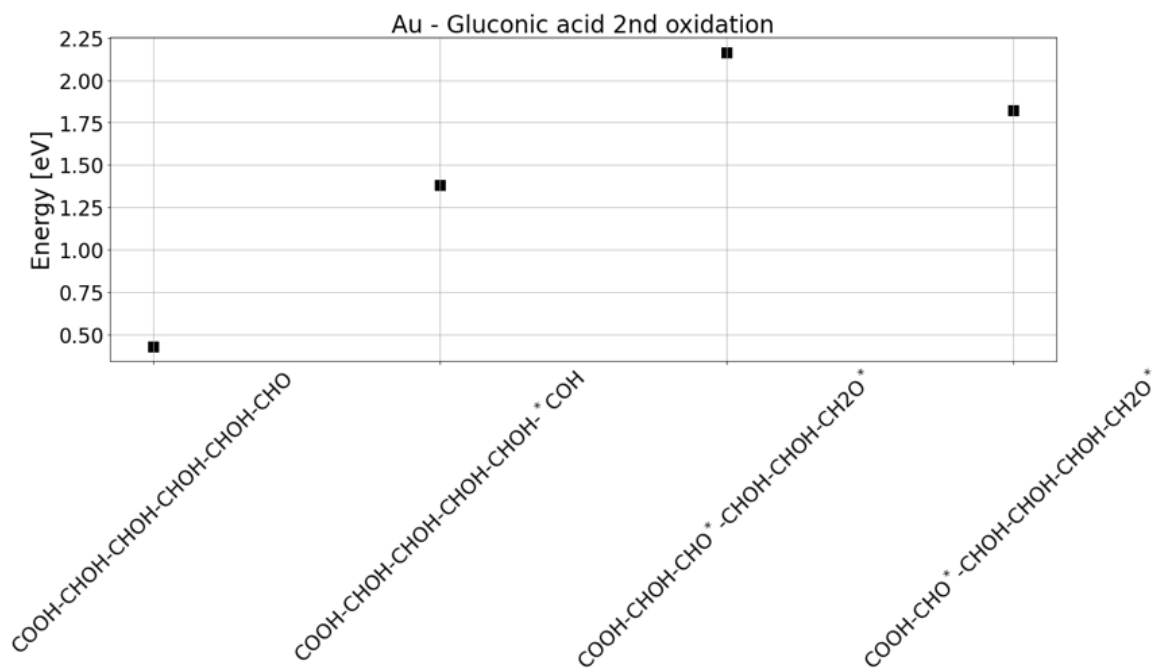


**Figure S6:** DFT investigations of oxidizing the second proton-electron from gluconic acid.

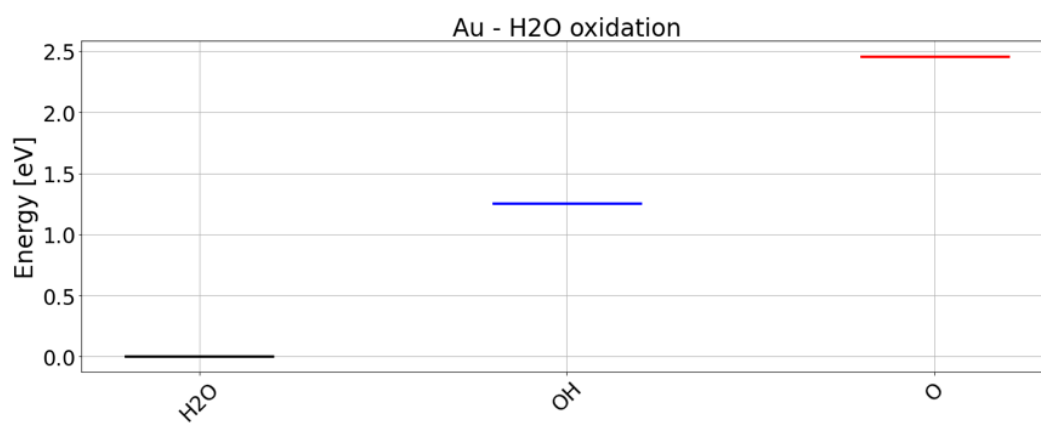


**Figure S7:** DFT investigations of water oxidation on Au(111).

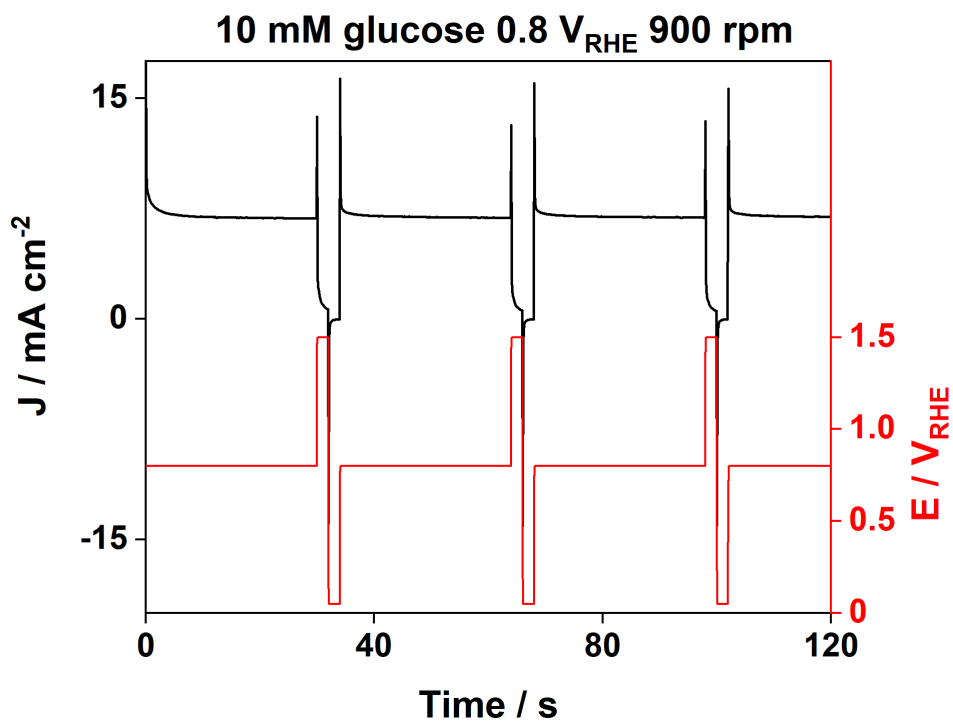


**Figure S8:** Excerpt of the current response of a 2 h potential step program: 10 mM glucose starting concentration at an oxidation potential of 0.8 V<sub>RHE</sub> at 900 rpm in 0.1 M NaOH and 0.1 M NaClO<sub>4</sub> supporting electrolyte (left y-axis). Applied potential steps depicted in red (right hand y-axis).

<b>10 mM glucose concentration</b>			
<b>glycolic acid in ppm</b>	<b>0.55 V<sub>RHE</sub></b>	<b>0.8 V<sub>RHE</sub></b>	<b>1.1 V<sub>RHE</sub></b>
0 rpm	0.8	ND	ND
900 rpm	ND	0.1	0.5
2500 rpm	0.87	ND	4
<b>10 mM gluconic acid concentration</b>			
<b>glycolic acid in ppm</b>		<b>0.8 V<sub>RHE</sub></b>	<b>1.1 V<sub>RHE</sub></b>
0 rpm		ND	0.32
900 rpm		0.08	0.161
2500 rpm		0.34	1.36
<b>10 mM glucuronic acid concentration</b>			
<b>glycolic acid in ppm</b>	<b>0.55 V<sub>RHE</sub></b>	<b>0.8 V<sub>RHE</sub></b>	<b>1.1 V<sub>RHE</sub></b>
0 rpm	0.31	0.206	0.429
900 rpm	0.44	0.36	3.6
2500 rpm	ND	0.67	0.87

**Table ST1:** Concentrations of glycolic acid in electrolytes after 2h of oxidation time. ND indicating “not detected”. Note that glycolic acid might still be present in these electrolytes but at a concentration below the limit of detection.

<b>10 mM glucose concentration</b>			
<b>tartaric acid in ppm</b>	<b>0.55 V<sub>RHE</sub></b>	<b>0.8 V<sub>RHE</sub></b>	<b>1.1 V<sub>RHE</sub></b>
0 rpm	3.2	0.01	0.66
900 rpm	ND	ND	0.5
2500 rpm	3.57	2.99	4
<b>10 mM gluconic acid concentration</b>			
<b>tartaric acid in ppm</b>		<b>0.8 V<sub>RHE</sub></b>	<b>1.1 V<sub>RHE</sub></b>
0 rpm		ND	1.17
900 rpm		0.08	0.15
2500 rpm		0.41	11.1
<b>10 mM glucuronic acid concentration</b>			
<b>tartaric acid in ppm</b>	<b>0.55 V<sub>RHE</sub></b>	<b>0.8 V<sub>RHE</sub></b>	<b>1.1 V<sub>RHE</sub></b>
0 rpm	ND	ND	ND
900 rpm	0.236	0.16	0.8
2500 rpm	0.59	0.51	0.93

**Table ST2:** Concentrations of tartaric acid in electrolytes after 2h of oxidation time. ND indicating “not detected”. Nota that tartaric acid might still be in these electrolytes but at a concentration below the limit of detection.

Since the number of electrons involved in the formation of glycolic and tartaric acid is not known only their absolute concentrations can be compared. Two rough trends for the concentrations are observed: with increasing potential and/or rotation also the concentration of these two dissociation products increases. It is worth mentioning that the list of dissociation products we tracked is not exhaustive. There are other small organic acids and different oxidation products that might be formed. The focus of this work lies on gluconic, glucuronic, and glucaric acid. The detection of the chosen dissociation products suggests, however, that cleavage of the C-C chains occurs.

### Product analysis in blank samples

2 months blank in 0.1 M NaOH	10 mM glucose	10 mM gluconic acid	10 mM glucuronic acid
gluconic acid [ppm]	3.3	-	-
glucuronic acid [ppm]	ND	ND	-
glucaric acid [ppm]	ND	ND	33
glycolic acid [ppm]	ND	ND	142.6
tartaric acid [ppm]	ND	ND	475.2
formic acid [ppm]	ND	ND	ND

**Table ST3:** Concentrations of saccharic acids and cleavage products in 2-month-old 0.1 M NaOH and 0.1 M NaClO<sub>4</sub> solution with the starting concentrations of 10 mM glucose, 10 mM gluconic acid or 10 mM glucuronic acid, respectively.

The concentrations of tartaric and glycolic acid detected in the aged electrolyte containing glucuronic acid are outside their respective calibration windows. In this case, the accuracy of the quantification is not paramount. The results still show well enough that considerable degradation takes place, especially in the case of glucuronic acid oxidation.

### References

1. Schlegel, N., Wiberg, G. K. H. & Arenz, M. On the electrooxidation of glucose on gold: Towards an electrochemical glucaric acid production as value-added chemical. *Electrochim. Acta* **410**, 140023 (2022).
2. Kooyman, C., Vellenga, K. & De Wilt, H. G. J. The isomerization of d-glucose into d-fructose in aqueous alkaline solutions. *Carbohydr. Res.* **54**, 33–44 (1977).



### **Manuscript III**

Nicolas Schlegel, Stefanie Punke, Rebecca Pittkowski, Divyansh Gautam, Ulrik Friis-Jensen, Etienne Berner, Nicola Ramseyer, Kirsten M. Ø. Jensen, Matthias Arenz

**On the electrooxidation of glucose on gold: Towards an electrochemical glucaric acid production as value-added chemical**

*In preparation*

## Characterization of multimetallic PtFeCoNiPd samples during synthesis by combined *in-situ* PXRD and XANES (*In preparation*)

Nicolas Schlegel<sup>a</sup>, Stefanie Punke<sup>b</sup>, Rebecca Pittkowski<sup>b</sup>, Divyansh Gautam<sup>a</sup>, Ulrik Friis-Jensen<sup>b</sup>, Etienne Berner<sup>a</sup>, Nicola Ramseyer<sup>a</sup>, Kirsten M. Ø. Jensen<sup>b</sup>, Matthias Arenz<sup>a</sup>

<sup>a</sup> Department of Chemistry, Biochemistry and Pharmaceutical Sciences, University of Bern, Freiestrasse 3, 3012 Bern, Switzerland

<sup>b</sup> Department of Chemistry, University of Copenhagen, Universitetsparken 5, 2100 Copenhagen Ø

### Introduction

- Synthesis of high-entropy alloy nanoparticles (HEA-NP) via various synthesis routes has become more prevalent in the last years due to increased application of HEA-NP in catalysis.
- Formation mechanism to obtain single-phase HEA-NP at lower temperature (< 750°C) is not yet fully understood.
- In the presented study, we investigate precursor samples containing different combinations of elements including both precious and non-precious metals (PtFe, PtFeCo, PtFeCoNi, and PtFeCoNiPd)

We follow the reduction of the metals (via XANES) and the formation of crystal phases (via PXRD) to investigate the impact of the number of elements on the formation of and transition between metal phases.

### Experimental

#### *Synthesis/preparation of multimetallic samples for synchrotron measurements*

- The PtFe, PtFeCo, PtFeCoNi & PtFeCoNiPd samples were synthesized by an incipient wetness impregnation approach on Ketjen Black EC-300J carbon with target loadings of 60 and 70 wt%.
- The synthesis was interrupted before the reduction step. Therefore, it resulted in precursor salts dried onto the carbon support which were then reduced at ESRF.

#### *In situ sample characterization by tandem X-ray absorption (XAS) and powder X-ray diffraction (PXRD)*

- At BM31 at ESRF in Grenoble, the samples were filled into quartz capillaries and placed in the experimental setup that consists of a blow furnace and provides a reducing H<sub>2</sub>/Ar-atmosphere (see **Image 1**).
- Temperature program: 100 °C h<sup>-1</sup> to 400 °C, followed by 350 °C h<sup>-1</sup> to 750 °C and cooling to ambient temperatures.

- Up to 400 °C, the analysis included recording first the absorption edge (XAS) of each metal in increasing X-ray absorption edge energy followed by the PXRD measurements. This protocol led to a temperature resolution of 25 °C between the individual spectra and diffractograms. Then, up to 750°C and during cooling only PXRD was recorded.

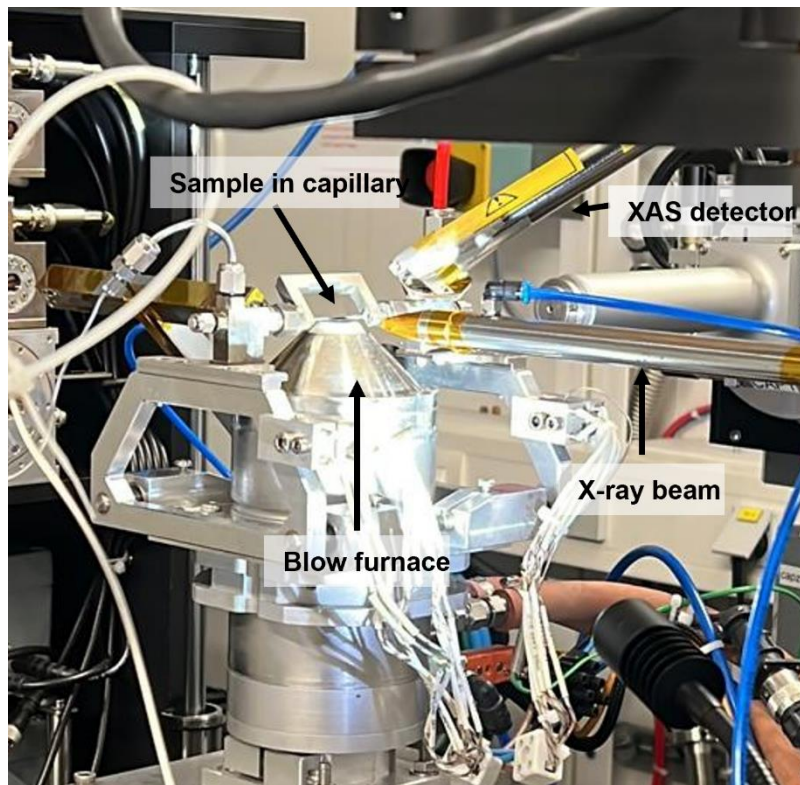


**Image 1:** Filled capillary mounted over blow furnace before the reduction starts.

## Results & Discussion

Heating to 400 °C

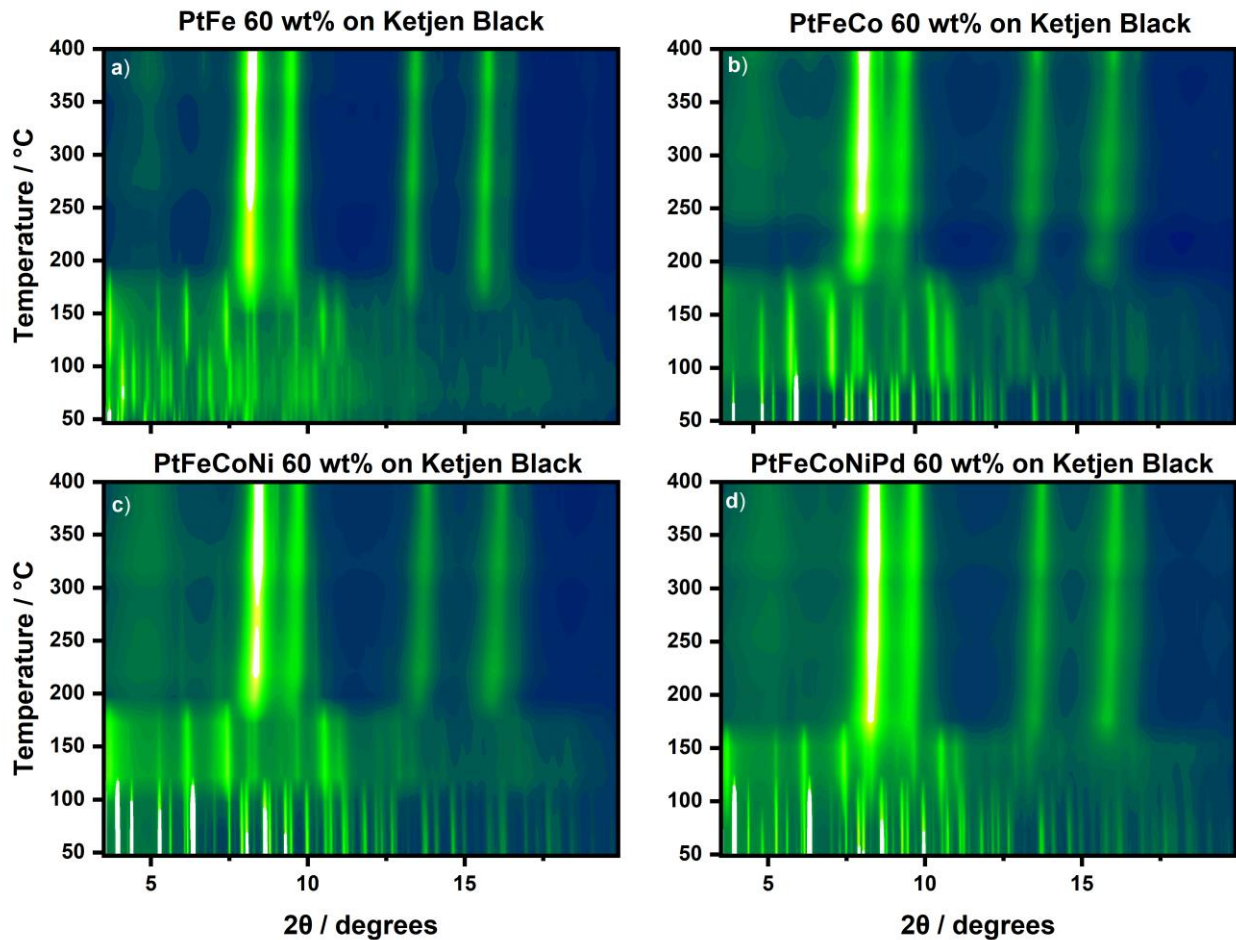


**Figure 1:** Contour plots of PXR diffractograms of a) a PtFe, b) a PtFeCo, c) PtFeCoNi, and d) PtFeCoNiPd sample on Ketjen Black EC300-J with a metal loading of 60 wt% recorded during heating to 400 °C. The green regions indicate high intensities while the blue regions indicate low intensities in the diffractograms.

- The formation of a face-centered cubic (fcc) phase from metal precursor phases is observed in all samples. Based on this analysis the PtFeCoNiPd can be considered a HEA.
- In all samples, the phase formation occurs rapidly which is indicated by the drastic changes in the contour plots, **Figure 1 a)-d)**, at 200 °C.
- The temperature of fcc formation is found to be approximately 200 °C for the PtFe, PtFeCo, and PtFeCoNi samples (**Figure 1 a)-c)**) and 175 °C in the PtFeCoNiPd sample (**Figure 1d)**). The HEA sample seemingly reduces earlier.
- The tilt of the interferences towards larger 2 θ angles with increasing reduction temperature indicates shrinking of the unit cell.

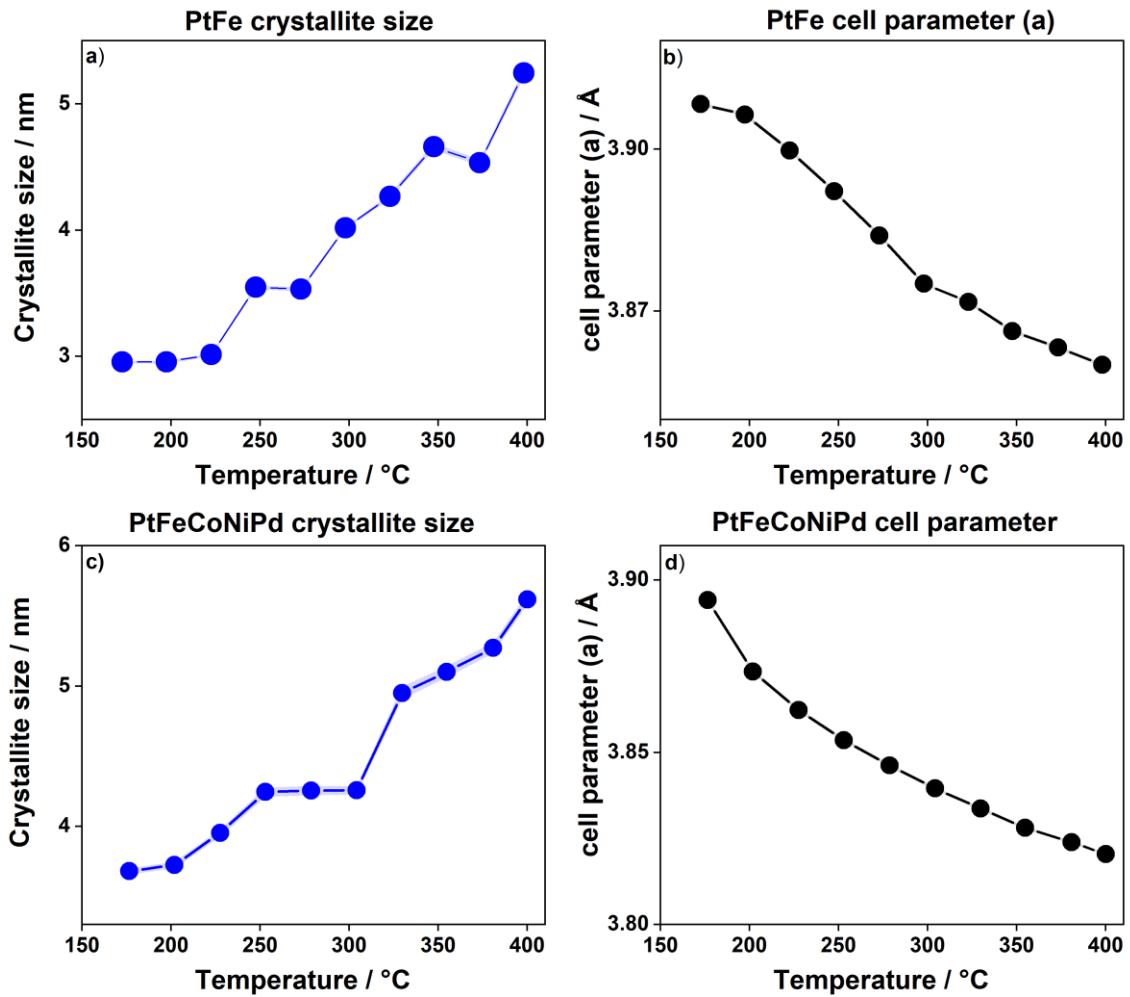


**Figure 2:** Crystallite size and cell parameter of the formed fcc phases obtained from sequential Rietveld refinements using GSAS-II<sup>1</sup> of PtFe 60 wt%, a) and b), and PtFeCoNiPd 60 wt%, c) and d). Microstrain was kept constant during the sequential refinement.

- Crystallite growth is observed in both samples with increasing temperature. In PtFe 60 wt%, the crystallites grow from 3 nm to 5.3 nm (**Figure 2a**), while the crystallites in PtFeCoNiPd 60 wt% grow from 3.6 nm to 6.7 nm (**Figure 2c**) during the heating process. This indicates that the formed NP, therefore, grow as well.
- The growth of the phase is accompanied with a shrinking of the unit cell. In PtFe 60 wt%, the fcc cell parameter “a” decreases from 3.91 Å to 3.86 Å (**Figure 2b**). In the HEA sample PtFeCoNiPd, the cell parameter “a” shrinks from 3.89 Å to 3.82 Å (**Figure 2d**). The shrinking unit cell parameters concur with the shift of the peaks observed in the contour plots (**Figure 1a** and **d**)

- The difference in unit cell size can be rationalized by the fact that PtFe, as compared to PtFeCoNiPd, contains more Pt, which is the constituent element with the largest unit cell. Therefore, the resulting unit cell is larger in the two-elemental sample.

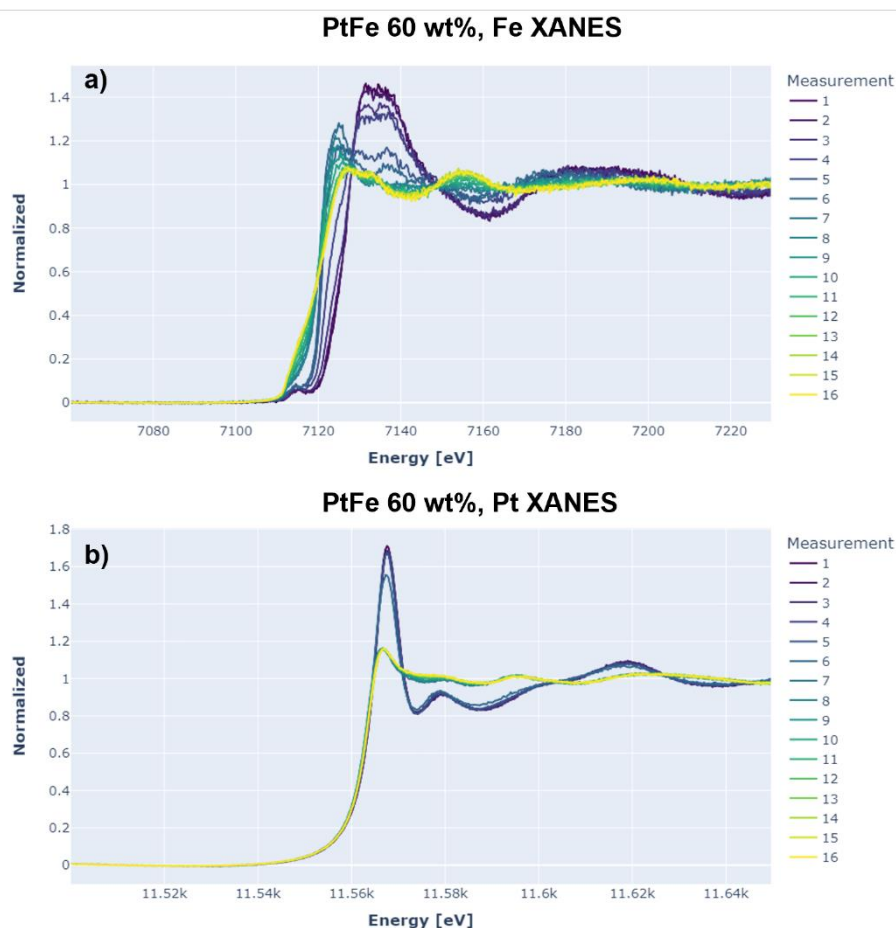


**Figure 3:** XANES spectra of Fe (a) and Pt (b) in the PtFe 60wt%. The measurement numbers in the legend indicate the increasing temperature during the synthesis. Measurement 1 was recorded at 45 °C and measurement 16 at 400 °C.

- The absorption spectra in **Figure 3** show the different reduction behaviors of Fe (**3a**) and Pt (**3b**). Pt reduces from its precursor form ( $\text{Pt}^{4+}$ ) to the final state ( $\text{Pt}^0$ ) within the temperature range of approximately 50 °C without an obvious intermediate state. However, the absence of an intermediate state cannot be concluded on as it might be present only for very brief periods of time and therefore be missed by the individual scans. Fe reduces from its precursor form ( $\text{Fe}^{3+}$ ) via an intermediate step ( $\text{Fe}^{2+}$ ) before reaching its final state ( $\text{Fe}^0$ ). The process of reduction occurs over a larger temperature window.
- The spectra are used to perform linear combination analysis (LCA) (**Figure 4**). LCA give insight into the ratio of precursor to final state of a metal. It also can show intermediate states.

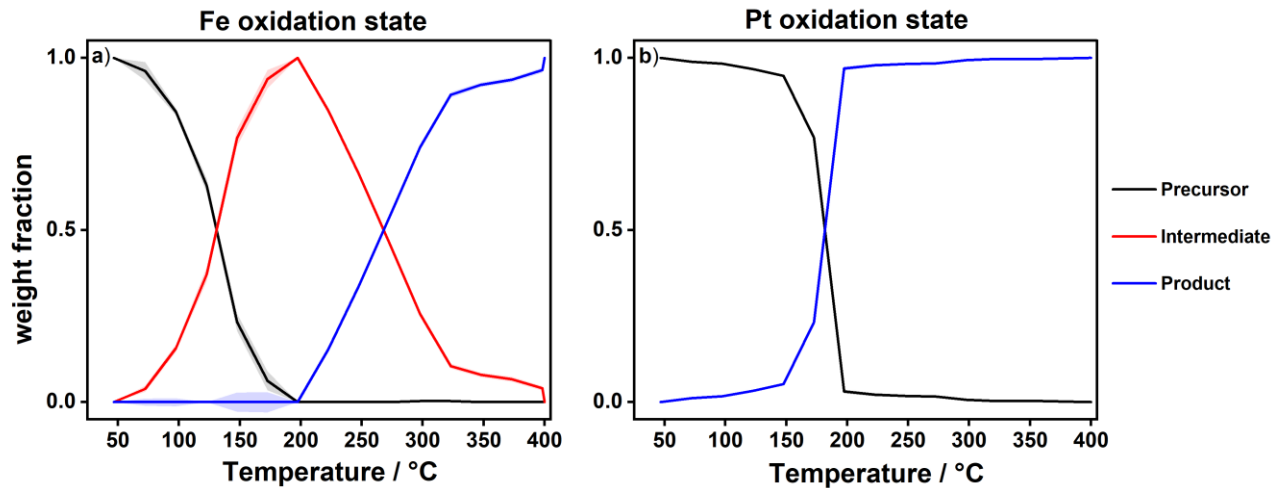


**Figure 4:** Linear combination analysis (LCA) of XANES spectra recorded during the reduction of a PtFe 60 wt% sample for Fe (a) and Pt (b). Precursors are indicated in black, intermediates in red, and products in blue. The weight fractions determined by the LCA are normalized to the main absorption edge. Note that Pt does not reduce via an apparent intermediate. *T*

- LCA of the XANES spectra depicted in **Figure 4** indicate that Fe starts to reduce to from an intermediate state already at 100 °C. The intermediate is reached at 200 °C which concurs with the reduction of the Pt.
- The majority of Fe is only reduced upon reaching 300 °C. Therefore, the temperature window of Fe reduction spans from 100 °C to 300 °C. The reduction window of Pt is much narrower and is found between 150 °C and 200 °C.
- Combining the information from **Figure 1 a)** and **Figure 4** confirms that the formation of the initial fcc phase coincides with the reduction of Pt. Interestingly, even though the metals exhibit different reduction temperatures only one apparent crystal phase is formed.
- Possibly, the Fe gets continuously reduced and also continuously incorporated into the existing fcc phase.

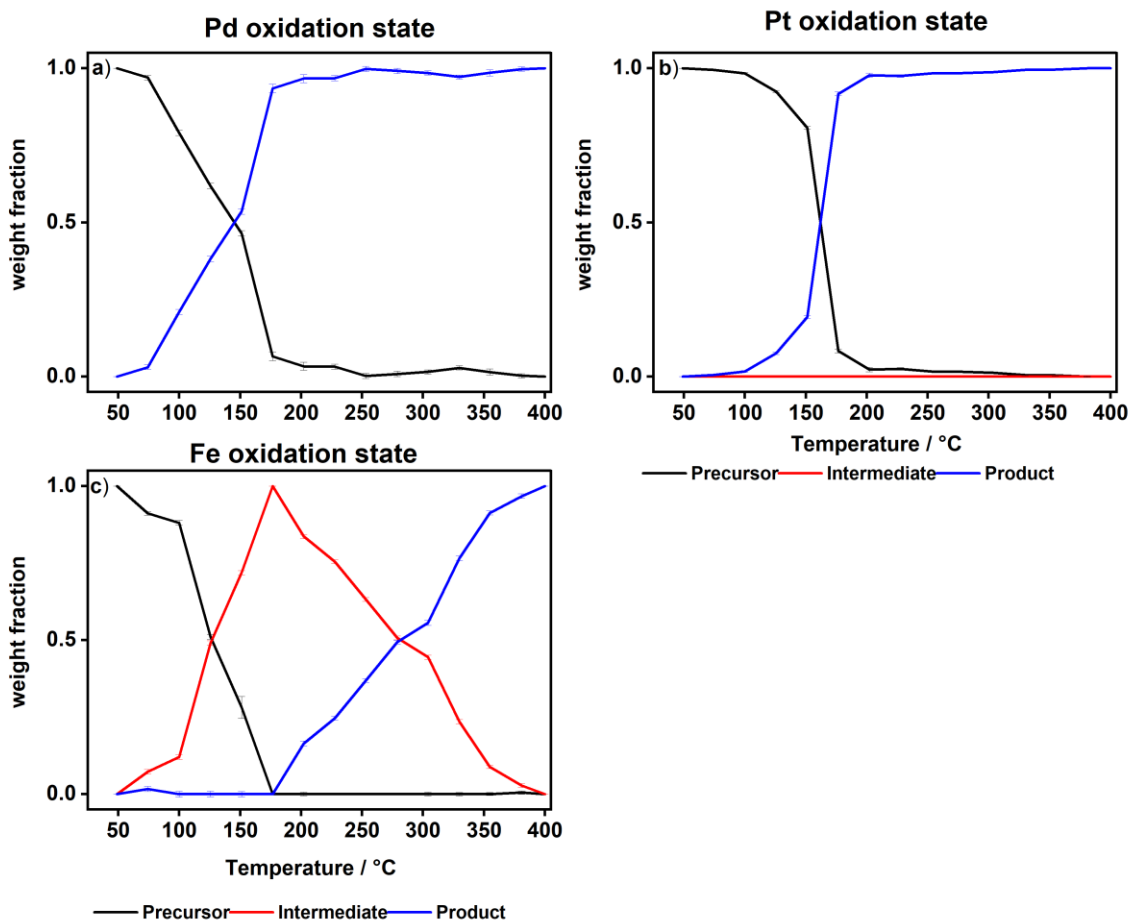


**Figure 5:** Linear combination analysis (LCA) of XANES spectra recorded during the reduction of a PtFeCoNiPd 60 wt% sample for Pd (a), Pt (b), and Fe (c). Precursors are indicated in black, intermediates in red, and products in blue. The weight fractions determined by the LCA are normalized to the main absorption edge. Note that Pt and Pd do not reduce via an apparent intermediate. The LCA for Co and Ni is missing due to on-going complications with the autoXAS script.

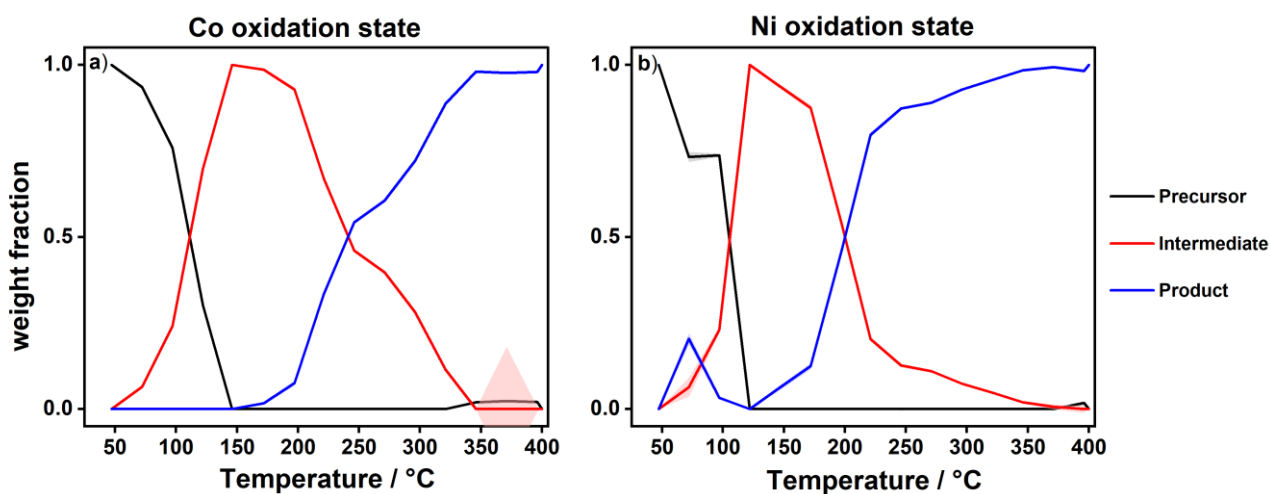


**Figure 6:** Linear combination analysis (LCA) of XANES spectra recorded during the reduction of a PtFeCoNi 60 wt% sample for Co (a) and Ni (b). Precursors are indicated in black, intermediates in red, and products in blue. The weight fractions determined by the LCA are normalized to the main



absorption edge. We assume the reduction behaviour of these elements to be similar in the PtFeCoNiPd sample.

- The LCAs in **Figures 5 & 6** depict the reduction behaviors of the individual elements in PtFeCoNiPd 60 wt%. Note, that the LCA of Co and Ni (**Figure 6**) are taken from the sample PtFeNiCo and serve as placeholders until technical complication with autoXAS are resolved. The addition of Pd to the analysis, for some unknown reason, disrupts the analysis of Co and Ni. Until then, we assume the reduction behavior of Ni Co to be similar in PtFeCoNi and PtFeCoNiPd.
- The noble metals, Pd ( $\text{Pd}^{2+} \rightarrow \text{Pd}^0$ ) and Pt ( $\text{Pt}^{4+} \rightarrow \text{Pt}^0$ ), reduce without forming an apparent intermediate. Both are nearly fully reduced at 175 °C. The non-precious metals, Fe ( $\text{Fe}^{3+} \rightarrow \text{Fe}^{2+} \rightarrow \text{Fe}^0$ ), Co, and Ni, all reduce via an intermediate step. Similar to Fe in the sample PtFe 60 wt% (**Figure 4a**). However, for Co and Ni no clear oxidation can be assigned to the intermediate state. Comparing the XANES spectra to literature indicates that the precursor and final states correspond to oxidation states 2+ and 0, respectively.
- Independent of the differences in reduction temperatures, only one fcc phase seems to form at first.

Heating to 780 °C

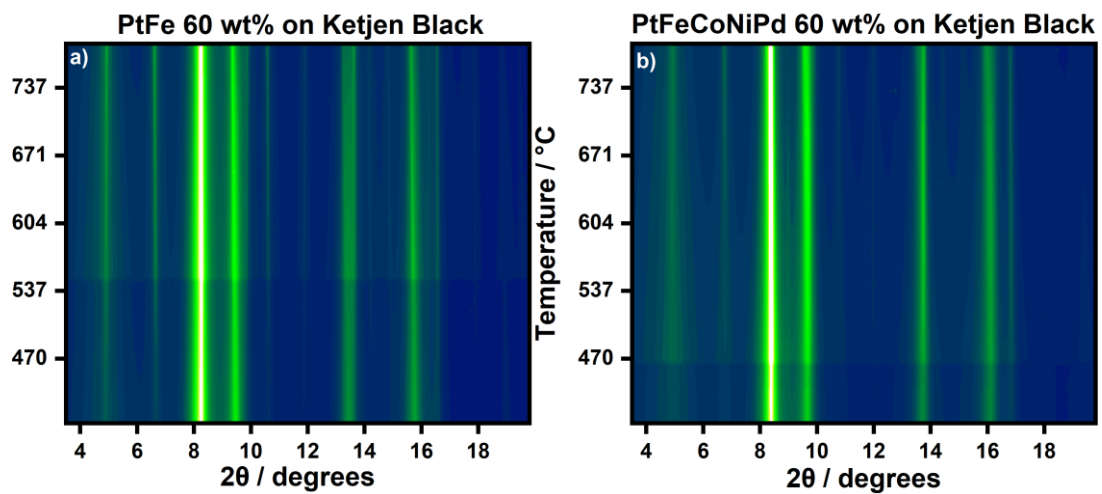


**Figure 7:** Contour plots of PXRD diffractograms of a) PtFe and a) PtFeCoNiPd samples on Ketjen Black EC300-J with a metal loading of 60 wt% recorded during heating to 750 °C. The green regions indicate high intensities while the blue regions indicate low intensities in the diffractograms.

- In addition to the characteristic fcc diffraction pattern observed in the contour plots in **Figure 1a) & d)**, further peaks are observed in the contour plots depicted in **Figure 7**. For both investigated samples, peaks appear at 5  $2\theta$  and 7  $2\theta$ . The additional peaks already faintly appear before 400 °C in the case of PtFe (**Figure 1a) & 7a)** and also start to form in the PtFeCoNiPd sample after reaching 400 °C (**Figure 7b)**). Therefore, the phase transformation apparently commences at lower temperatures in the bimetallic sample.
- The individual interferences of the diffraction patterns match well with a tetragonal phase (space group P4/mmm). Overlapping the diffraction patterns of PtFe (**Figure 8a)**) and PtFeCoNiPd (**Figure 8b)**) recorded at 780 °C with the reference phases supports this hypothesis.
- The peaks become more intense as the heating commences, likely indicating growth of this newly formed phase as well as the continuous phase transformation from fcc to tetragonal P4/mmm.

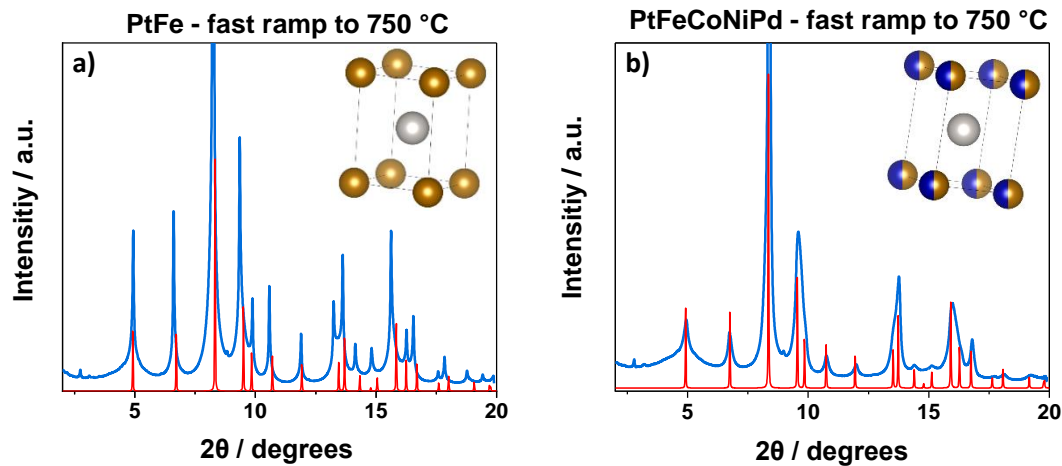


**Figure 8:** Diffractograms of a PtFe (a) sample and a PtFeCoNiPd (b) sample, each with a loading of 60 wt%. The diffractograms were recorded after heating to 750 °C. The blue trace depicts the recorded diffractogram while the red trace depicts two references. The reference in a) corresponds to a PtFe phase<sup>2</sup> of space group  $P4/mmm$  and the reference in b) corresponds to a PtFe<sub>0.5</sub>Co<sub>0.5</sub> phase<sup>3</sup> of space group  $P4/mmm$ . The unit cells of both references shown in the graphs were drawn using VESTA<sup>4</sup>.

- The reference diffractograms match well with the recorded diffractograms. However, Rietveld refinement is necessary to determine if a full transformation from fcc to  $P4/mmm$  has taken place or if both phases coexist.
- The diffractogram of the PtFe sample (**Figure 8a**) exhibits much sharper peaks than the PtFeCoNiPd sample (**Figure 8b**). Two parameters are mainly responsible for peak width. First, crystallite size and, second, strain within the particle. Likely, a combination of the two responsible for the observed differences. Hence, PtFe grows to form larger particle with less strain.

## Conclusion

- From XANES it became apparent that the precious metals, Pt and Pd, and non-precious metals, Fe, Co, and Ni, show distinctly different reduction behaviors. The precious metals reduce in a narrower temperature window than the non-precious metals. No intermediate reduction state can be resolved, whereas a clear intermediate state is seen during the reduction of the non-precious metals.
- In all investigated sample, at first, an fcc phase is formed. Refining the acquired diffractograms reveals a crystallite growth and unit cell shrinking during heating to 400 °C.
- Upon heating to 750 °C, an at least partial phase transformation from the fcc to a tetragonal P4/mmm is observed. Based on the diffractograms, the transformation commences at a lower temperature in the PtFe sample than in the HEA PtFeCoNiPd sample.

## References

1. Toby, B. H. & Von Dreele, R. B. GSAS-II: The genesis of a modern open-source all purpose crystallography software package. *J. Appl. Crystallogr.* **46**, 544–549 (2013).
2. Yuasa, S., Miyajima, H. & Otani, Y. Magneto-Volume and Tetragonal Elongation Effects on Magnetic Phase Transitions of Body-Centered Tetragonal FeRh<sub>1-x</sub>Ptx. *J. Phys. Soc. Japan* **63**, 3129–3144 (1994).
3. Woolley, J. C. & Bates, B. ORDERING IN CoPt-FePt. *J. Less Common Met.* **1**, 382–389 (1959).
4. Momma, K. & Izumi, F. VESTA: A three-dimensional visualization system for electronic and structural analysis. *J. Appl. Crystallogr.* **41**, 653–658 (2008).

**Manuscript IV**

Baiyu Wang<sup>†</sup>, Nicolas Schlegel<sup>†</sup>, Olivia Aalling-Frederiksen, Etienne Berner, Damin Zhang, Kirsten M. Ø. Jensen & Matthias Arenz

<sup>†</sup>These authors contributed equally

**On the electrooxidation of glucose on gold: Towards an electrochemical glucaric acid production as value-added chemical**

*Accessible on ChemRxiv, to be submitted*

# Elucidating the Steady-State OER Activity of $(\text{Ni}_{1-x}\text{Fe}_x)\text{OOH}$ Binary Nanoparticles in As-prepared and Purified KOH Electrolyte Solutions

Baiyu Wang<sup>+,a</sup>, Nicolas Schlegel<sup>+,b</sup>, Olivia Aalling-Frederiksen<sup>a</sup>, Etienne Berner<sup>b</sup>, Damin Zhang<sup>b</sup>, Rebecca K. Pittkowski<sup>a</sup>, Kirsten M. Ø. Jensen<sup>a,\*</sup> & Matthias Arenz<sup>b,\*</sup>

<sup>+</sup>) Authors contributed in equal parts

a) Department of Chemistry, University of Copenhagen, Universitetsparken 5, 2100 Copenhagen Ø

b) Department of Chemistry, Biochemistry and Pharmaceutical Sciences, University of Bern, Freiestrasse 3, 3012 Bern, Switzerland

\* Corresponding authors: [matthias.arenz@unibe.ch](mailto:matthias.arenz@unibe.ch), [kirsten@chem.ku.dk](mailto:kirsten@chem.ku.dk)

## Abstract

Replacing critical raw materials employed in water electrolysis applications as electrocatalysts with earth-abundant materials is paramount for the future upscaling to industrial dimensions. In that regard, Ni and Ni-based multimetallic hydroxides, above all NiFe-hydroxides, have shown promising performance towards the oxygen evolution reaction (OER) in alkaline conditions. However, it has been shown that the extraordinary performance of these materials is owed largely to Fe impurities found in commercial KOH from which electrolyte solutions are prepared. The mechanism of action of these impurities is still not fully understood, and therefore, at the heart of ongoing discussions. In this study, we investigate the OER activity of different nanostructured  $(\text{Ni}_{1-x}\text{Fe}_x)\text{OOH}$  samples and find their activities to be influenced differently by the presence of Fe impurities in the electrolyte. From the gathered data, we conclude that the presence of Fe impurities impacts gravely the structure sensitivity of the OER. In purified electrolyte solutions the OER appears to be a structure-sensitive reaction while this seems not to be the case in the presence of said impurities.

## Keywords

## 1. Introduction

To reduce society's dependence on fossil resources, renewable primary energy sources must be expanded. Furthermore, new methods of storing energy must be explored and developed. Electrochemical water splitting to form hydrogen and oxygen is among the most promising and well-established approaches to achieve this goal.<sup>1-3</sup> In water electrolyzers the two half-cell reactions involved are the hydrogen evolution reaction (HER) and the oxygen evolution reaction (OER).<sup>4</sup> In practice, water electrolyzers can be operated in acidic or alkaline conditions.<sup>5</sup> In both, alkaline and acidic conditions, the anodic oxygen evolution reaction requires large overpotentials to achieve the high current densities demanded in commercial applications.<sup>6</sup> Additionally, in acidic media, the state-of-the-art OER catalyst materials are IrO<sub>2</sub>, RuO<sub>2</sub>, and composite Ir-Ru-oxides.<sup>4, 7-9</sup> Both metals are labelled critical raw materials by the European Union<sup>10</sup> and, therefore, suboptimal choices concerning upscaling. In alkaline media, Ni-based hydroxides (NiOOH), more specifically layered double hydroxides (LDH), have proven to be viable catalysts that also circumvent the problem of scarcity previously mentioned.<sup>6, 11-13</sup> Combinations of Ni with other transition metals are amongst the most active OER catalysts in alkaline media.<sup>6, 14, 15</sup> While Ni-M-LDH (M =Ce, Al, Co) have shown interesting behavior, NiFe-LDHs have been found to be the most promising earth abundant catalysts for the OER.<sup>16</sup>

Although the OER performance of (Ni<sub>1-x</sub>Fe<sub>x</sub>)OOH-materials is studied extensively, the activity-promoting effect of Fe on the Ni-structures is still at the heart of ongoing debates. Corrigan et al.<sup>17</sup> first reported that incorporating metal ions in NiOOH thin films increases substantially the OER activities of the films. They put forth that the inclusion of Fe in the NiOOH-structure during synthesis and aging increases their conductivity which in turn increases their OER activity. Trotochaud et al.<sup>18</sup> were able to show that NiOOH is a poor OER catalyst after the removal of the Fe-impurities from the commercially available KOH electrolyte. They also showed that the increase of conductivity proposed by Corrigan et al.<sup>17</sup> does not account for the observed increase in OER activity in the presence of Fe-impurities. Since then, several studies have confirmed these observations.<sup>19-21</sup> However, there is no common agreement on the mechanism of action of the Fe-impurities to improve the OER. Klaus et al.<sup>19</sup> and Trotochaud et al.<sup>18</sup> argued that the incorporation and absorption of Fe from the electrolyte, and not from the synthesis, into NiOOH structures

is the reason for the activation towards OER. They proposed that the Fe-sites formed on the Ni-surface become the active sites for OER. Spanos et al.<sup>20</sup> showed that the concentration of Fe in the electrolyte decreased during polarization of the Ni-surface. Hence, they concluded that the Fe adsorbs on or incorporates into the catalyst structure upon application of a potential. Other studies<sup>22-24</sup> argue that incorporation of Fe-impurities leads to the formation of active Fe edge-sites and clusters, rather than single sites, that are the active component of the catalysts.

Independent of the specific mechanism of action of the Fe-impurities, structure-activity relationships can be established to maximize the enhancement effect of the Fe. In this work, we investigate the steady-state OER activities of structurally distinct (Ni<sub>1-x</sub>Fe<sub>x</sub>)OOH catalysts in both as-prepared – iron-containing- and purified – “iron-free” – electrolytes to investigate and potentially identify these relationships.

## **2. Experimental Details**

### **2.1 Synthesis of (Ni<sub>1-x</sub>Fe<sub>x</sub>)OOH and NiCoOOH samples**

For the (Ni<sub>0.5</sub>Fe<sub>0.5</sub>)OOH and (Ni<sub>0.8</sub>Fe<sub>0.2</sub>)OOH samples, Fe(NO<sub>3</sub>)<sub>3</sub>·9H<sub>2</sub>O (Sigma-Aldrich, ACS reagent, ≥98 %) and Ni(NO<sub>3</sub>)<sub>2</sub>·6H<sub>2</sub>O (Sigma-Aldrich, purum p.a., crystallized, ≥97.0 %) were used as precursors. The total concentration of the two precursors was 0.028 M. The precursors were dissolved in water, and urea (CO(NH<sub>2</sub>)<sub>2</sub>) (Alfa Aesar, ACS, 99.0 - 100.5 %) was added (0.16 M). The solutions were added to autoclaves and heated at 140 °C for 2-24 hours. The reaction mixtures were cooled down, and the precipitates were washed and centrifuged in ethanol three times at 4500 rpm to obtain the final products.

For the NiCoOOH sample, Ni(NO<sub>3</sub>)<sub>2</sub>·6H<sub>2</sub>O and Co(NO<sub>3</sub>)<sub>2</sub>·6H<sub>2</sub>O (Sigma-Aldrich, reagent grade, 98 %) were used as the precursors. The total concentration of the two precursors was 0.5 M. The precursors were dissolved in absolute ethanol (VWR), and urea (CO(NH<sub>2</sub>)<sub>2</sub>) was added (3.35 M). The reaction mixtures were transferred to autoclaves and heated at 120 °C for 3 hours. The reaction mixtures were cooled down, and the precipitates were washed and centrifuged in ethanol three times at 4500 rpm to obtain the final products.

### **2.2 Powder X-ray diffraction**

Synchrotron powder diffraction patterns were collected at the P02.1 beamline at DESY in Hamburg. The samples were loaded into Kapton capillaries with an inner diameter of



1.00 mm and data were measured with a wavelength of 0.207 Å and a VAREX 4343CT detector. The sample-to-detector distance was 1700 mm.

### **2.3 Data acquisition for total scattering experiments and pair function distribution analysis**

Total scattering data were collected at the P02.1 beamline at DESY in Hamburg. The samples were loaded into borosilicate glass capillaries with an inner diameter of 1.00 mm and data were measured using the rapid acquisitions PDF setup<sup>25</sup> with a wavelength of 0.207 Å and a VAREX 4343CT detector. The sample-to-detector distance was 290 mm.

The 2D patterns were integrated using the Dioptas 5.0 software<sup>26</sup> and the 1D patterns Fourier transformed with xPDFsuite<sup>27</sup> to obtain the PDFs with the following parameters being used:  $Q_{\min} = 0.6 \text{ \AA}^{-1}$ ,  $Q_{\max} = 18 \text{ \AA}^{-1}$ ,  $r_{\text{poly}} = 1.0 \text{ \AA}$ . The PDFs were modeled using PDFgui.<sup>28</sup>

### **2.4 Transmission electron microscopy and scanning electron microscopy-energy dispersive X-ray spectroscopy**

Transmission electron microscopy (TEM) images were collected on a Tecnai T20 G2 200kV TEM. The TEM samples were prepared by drop-casting an ethanol suspension of the prepared catalyst powders on lacey carbon TEM grids. The images were processed with the FIJI software.<sup>29</sup>

Scanning electron microscopy-energy dispersive X-ray spectroscopy (SEM-EDS) measurements were performed with a Zeiss GeminiSEM 450 operated by SmartSEM 6.05 software, and an EDS Photodetector Ultim max 65 from Oxford Instruments. Data analysis was derived by AZTec 5.0 software. EDS maps were recorded at a working distance (WD) of 8.5 mm, and the acceleration voltage was set to 15 kV. The probe current applied was 500 pA. For the mapping, the resolution was set to 1024 x 768 pixels. A pixel dwell time of 15 μs leads to a measuring time of ~ 12 s per frame and ~ 5 cps / eV of the measured Kα peaks of Ni and Fe, respectively, for 50:50 distributions. For the elemental distribution, only K-series peaks were evaluated. For the measurement area, two spots at two magnifications each were evaluated per sample - a total of 4 spots per sample (100 x and 500 x magnifications;  $1.1 \times 0.85 \text{ mm}^2 = 0.94 \text{ mm}^2$  and  $228 \times 171 \text{ μm}^2 = 0.039 \text{ mm}^2$ ).

### **2.5 Inductively coupled plasma mass spectrometry**

Quantification of the Fe amount in the electrolyte was evaluated by ICP-MS (PerkinElmer, NexION 2000 ICP-Mass). The ICP-MS was equipped with a cyclonic spray chamber and a

PFA-nebulizer. The RF power for the plasma was held at 1300 W with a gas flow of 15 L/min. Due to the interference of  $^{56}\text{Fe}$  and  $^{40}\text{Ar}^{16}\text{O}^+$ ,  $^{57}\text{Fe}$  was used to calibrate the Fe contents of samples and standards. Calibration standards were employed to prepare diluted calibration solutions with four points (5 ppb, 10 ppb, 20 ppb, and 50 ppb). A 50 ppb concentration of Yttrium was used as an internal standard. 0.1M KOH (both as-prepared and purified) was neutralized and diluted by 0.2 M nitric acid ( $\text{HNO}_3$ ) for the measurements.

## 2.6 KOH electrolyte purification

The purification approach used in this work was taken from ref<sup>18</sup>. KOH pellets (EMSURE, Merck) were purchased from Sigma-Aldrich. For “iron-free” measurements, the 0.1 M KOH electrolyte was purified by the following procedures: To a 50 mL polypropylene centrifuge tube, cleaned by  $\text{H}_2\text{SO}_4$  in advance, 2 g of  $\text{Ni}(\text{NO}_3)_2 \cdot 6\text{H}_2\text{O}$  (98.5 %, Sigma-Aldrich) were dissolved in 4 mL ultrapure water (MiliQ-systems,  $18.2 \text{ M}\Omega \cdot \text{cm}$ , 2.7 ppb TOC). To precipitate high-purity  $\text{Ni}(\text{OH})_2$ , 20mL of 0.1 M KOH was added. The mixture was then shaken and centrifuged at 4000 rpm. Afterward, the supernatant was removed. The precipitated  $\text{Ni}(\text{OH})_2$  was washed three times by the same procedure: 20 mL of ultrapure  $\text{H}_2\text{O}$  and 2 mL of 0.1 M KOH were added to the tube to redisperse the solid, the suspension was centrifuged at 4000 rpm, and the supernatant was removed. Finally, 50 mL of 0.1 M KOH was added to the tube for purification. The solid was redispersed and sonicated for at least 10 min, followed by overnight resting. The next day, the mixture was centrifuged, and the purified KOH supernatant was transferred into an  $\text{H}_2\text{SO}_4$ -cleaned polypropylene bottle for future use. ICP-MS measurements were carried out to investigate the Fe content in both as-prepared and purified KOH solutions, presented in Table 1. The Ni content was investigated as well since the purification method relies on precipitating bulk  $\text{Ni}(\text{OH})_2$  to adsorb the Fe impurities and, thereby, introduces excess Ni to the KOH electrolyte. As seen in Table 2, the Fe content decreased from 28 ppb to 14 ppb after purification. However, it is necessary to point out that the Ni content increased significantly after the purification, from 496 ppb to 907 ppb showing the limitations of the purification process. However, since the calibration window was between 5 and 50 ppb, these determinations are not extremely accurate. Nonetheless, we note that the Ni contents increase upon the purification from Fe. As the purification method relies on precipitating bulk  $\text{Ni}(\text{OH})_2$  to remove the Fe impurities from the electrolyte, it can lead to

an increase in the  $\text{Ni}^{2+}$  concentration in the electrolyte. The effect of excess  $\text{Ni}^{2+}$  ions on the reaction system remains unclear. Possibly, the  $\text{Ni}^{2+}$  ions have a negative or zero influence on the activity as well.

**Table 1:** Fe and Ni content in as-prepared and purified KOH measured by ICP-MS.

	Fe content (ppb)	Ni content (ppb)
As-prepared KOH	28	496
Purified KOH	14	907

## 2.7 Catalyst ink and film preparation

The catalyst inks for the RDE measurements were prepared by dispersing the respective dried catalyst powder in ethanol absolute (VWR, 99.8%). The ink solution was homogenized by using a sonication bath (VWR) and a horn sonicator (Qaonica sonicator, Q500) until a homogeneous ink was obtained. The inks were cooled in ice baths during sonication to prevent solvent evaporation. The resulting homogeneous catalyst ink had a total  $(\text{Ni}_{1-x}\text{Fe}_x)\text{OOH}$  or  $(\text{Ni}_{0.5}\text{Co}_{0.5})\text{OOH}$  concentration of  $0.5 \text{ mg}_{\text{sample}}/\text{L}$ .

The glassy carbon disk electrodes were mechanically polished with an alumina slurry (0.3  $\mu\text{m}$  MicroPolish, Buehler) on a polishing cloth (MicroCloth, Buehler) for 2 minutes. Then, the electrode tips were rinsed with ultrapure water, sonicated in a bath sonicator for 3 minutes, and finally rinsed again with ultrapure water.

Thin catalyst films were prepared by pipetting  $19.6 \mu\text{L}$  ( $0.5 \text{ mg}_{\text{sample}}/\text{L}$ ) of each catalyst ink onto a freshly polished glassy carbon (GC) disk of 5 mm diameter. The disk was then dried in an Ar gas stream humidified with IPA and  $\text{H}_2\text{O}$ . The disk was kept stationary in the drying step. The resulting films had a catalyst loading of  $50 \mu\text{g}/\text{cm}^2$  and were stored in an ambient atmosphere before the electrochemical measurements.

## 2.8 Rotating disk electrode (RDE) measurements

A custom-built, three-compartment Teflon cell<sup>30</sup> was used to conduct all electrochemical measurements. The cell was cleaned by first boiling in 25 %  $\text{HNO}_3$ , followed by boiling in ultrapure (MilliQ-systems, 2.7 ppb TOC, 18.2 M $\Omega$ )  $\text{H}_2\text{O}$ . Finally, the cell was thoroughly rinsed using ultrapure water. All RDE electrochemical measurements were performed at room temperature with a computer-controlled potentiostat (ECi 200, Nordic Electrochemistry ApS). The prepared sample tips (glassy carbon disks, 5 mm diameter)

were mounted onto an EDI101 rotating disk electrode assembly (Radiometer analytical) and served as working electrodes (WE). Rotation was controlled by a CTV101 speed control unit (Radiometer analytical) during the experiments. An Au wire served as the counter electrode (CE) and a saturated calomel electrode (SCE) in a glass sleeve fit with a ceramic frit, connected to the WE compartment by a Luggin capillary, served as the reference electrode (RE). An aqueous 0.1 M KOH electrolyte was used, which was saturated with Ar for 20 minutes before the measurements, if not mentioned otherwise. The solution resistance was determined with a superimposed AC signal (5 mV amplitude and 5 kHz frequency) and was compensated down to  $< 2 \Omega$  using an active feedback scheme.<sup>31</sup>

To determine the RE's shift versus the reversible hydrogen electrode (RHE), before measuring each sample, a Pt-disk electrode (treated identically to the GC-tips described above) served as a WE and the shift versus RHE was determined following Inaba et al.'s protocol.<sup>32</sup> In short, the KOH electrolyte was first saturated with H<sub>2</sub>. Then, two consecutive cyclic voltammograms (CV) from  $-1.075V_{SCE}$  to  $0.05V_{SCE}$ , were recorded with a scan rate of 0.050 V/s. From the measurement, the onsets of the hydrogen evolution and hydrogen oxidation currents (HER/HOR) were determined. Thereby, 0 V<sub>RHE</sub> versus the SCE RE was established as the potential where the HER/HOR currents canceled each other out.

To establish the electrocatalytic performance of the different (Ni<sub>1-x</sub>Fe<sub>x</sub>)OOH and (Ni<sub>0.5</sub>Co<sub>0.5</sub>)OOH thin catalyst films with respect to the OER (oxygen evolution reaction), three catalyst films were tested for each catalyst. The schematical illustration of the measurement protocol is shown in Figure S1. The electrocatalytic testing included the following steps: Ar saturation of the electrolyte, recording of cyclic voltammograms (CVs), determining the OER activity under steady-state conditions, and recording a final CV. The CV scans were conducted between 1.2 V<sub>RHE</sub> and 1.8 V<sub>RHE</sub> (2 cycles in total) with a scan rate of 5 mV/s. Afterwards, the electrode potential was stepwise increased between 1.55 V<sub>RHE</sub> and 1.8 V<sub>RHE</sub> with a step interval of 0.025 V and a hold time of 60 s per step. The steady-state OER activity was established by averaging the current of the last 10 s of the respective potential step. These steady-state measurements were conducted at two rotation speeds, i.e., 2500 rpm and 4900 rpm. Furthermore, CVs were recorded that indicate a (qualitative) value for the electrochemical surface area (ECSA) of the individual

samples, see SI. For this, the capacitive current at 1.40 V<sub>RHE</sub> was determined for each sample. Using capacitive currents for determining the ECSA of (Ni<sub>1-x</sub>Fe<sub>x</sub>)OOH materials has been used previously<sup>13, 33</sup>, however, it should be noted that the ECSA determined by this method can only be used to compare the individual samples to one another. A more quantitative determination of the ECSA is not possible through this approach.

### 3. Results and Discussion

#### 3.1 Characterization of (Ni<sub>0.5</sub>Fe<sub>0.5</sub>)OOH samples

To obtain structural information on the prepared samples, powder x-ray diffraction (PXRD) was performed. Figure 1a shows the PXRD patterns of the two different (Ni<sub>0.5</sub>Fe<sub>0.5</sub>)OOH samples. We show data collected with synchrotron radiation (wavelength 0.207 Å). Transmission electron microscopy (TEM) images are shown in Figure 1b-c. Here, samples were named by the metal precursor ratio used in the synthesis and the synthesis time, i.e., Ni<sub>x</sub>:Fe<sub>y</sub>-*t*h means the sample was synthesized with a metal precursor ratio Ni:Fe *x*:*y* for *t* hours. The two samples for which PXRD patterns are shown below were synthesized with a Ni:Fe ratio of 1:1 for 2 h and 6 h.

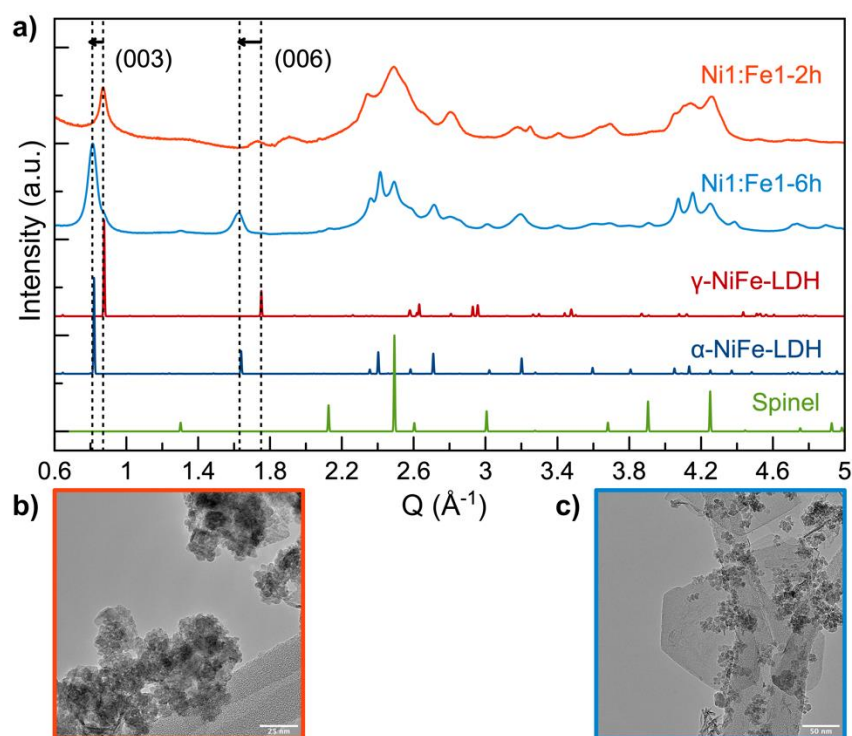


**Figure 1:** a) PXRD patterns of the same two as-synthesized (Ni<sub>0.5</sub>Fe<sub>0.5</sub>)OOH samples collected at synchrotron DESY, P02.1, with a wavelength of 0.21 Å. Samples were named by the metal precursor ratio used in synthesis and the synthesis time. CIF files for α-NiFe-LDH

and  $\gamma$ -NiFe-LDH are from ref<sup>34</sup>. b-c) Exemplary TEM images of the two  $(\text{Ni}_{0.5}\text{Fe}_{0.5})\text{OOH}$  samples: (b) Ni1:Fe1-2h and (c) Ni1:Fe1-6h.

As seen in Figure 1a, both samples show broad, weak diffraction peaks, indicating nanostructured samples. The two first peaks at low Q-values can be assigned to the (003) and (006) reflections of the LDH structure respectively. Comparing Ni1:Fe1-2h with Ni1:Fe1-6h, we observe a shift of these two peaks to lower Q-values when changing the heating time from 2 to 6 hours. The interlayer distance of the LDH structure thus increases from 7.2 Å to 7.8 Å, i.e., about 8 % (see discussion below), when the heating time is increased. The interlayer distance in LDHs relates to the nature of ions intercalated into the structure as well as structural disorder, such as faults in the stacking of layers and layer tilting.

Several different LDHs have been reported, and calculated patterns of the  $\gamma$ - and the  $\alpha$ -NiFe-LDH<sup>34</sup> are shown in Figure 1a. A structure with an interlayer structure similar to the  $\gamma$ -NiFe-LDH is thus initially obtained in the synthesis. With prolonged synthesis time, a structure closer to the  $\alpha$ -NiFe-LDH polymorph forms. However, the broad diffraction peaks indicate both small nanoparticles, as well as disordered samples, and assigning a single structural model from the PXRD data is challenging.

To estimate the crystallite size of the LDH particles, we conducted single peak fitting of the (003) reflection at 0.87 Å<sup>-1</sup> for Ni1:Fe1-2h, and 0.81 Å<sup>-1</sup> for Ni1:Fe1-6h. The fits are shown in Figure S2-3. The (003) peak originates from distances in the stacking direction. Using the Scherrer equation<sup>35</sup> the crystallite size in the stacking direction of the two samples is estimated to be ca. 49 nm and 37 nm. We note, however, that crystallite size estimation for the highly disordered samples contains very large uncertainties, e.g., stacking disorder and the presence of additional layer distances within the samples are not considered.

The data furthermore show diffraction peaks indicating the formation of an additional phase, a spinel structure (space group Fd-3m), in the both samples, assigned in Figure 1a. The reflections of the spinel structure in the Ni1:Fe1-2h sample are very broad cannot be assigned unambiguously

As observed in the TEM image of sample Ni1:Fe1-6h, Figure 1c (Figure S4), two morphologies are dominating the particles formed: large sheets and small, close-to-

spherical particles. For sample Ni1:Fe1-2h, TEM in Figure 1b, it is challenging to assign the morphology of the very agglomerating nanoparticles. We suggest that the sheet-like structure observed can be attributed to the LDH-phase while the smaller more spherical particles likely represent the spinel phase<sup>36,37</sup>. The larger sheets observed in the Ni1:Fe1-6h sample suggest that with the increased synthesis time, as the layer distance increases, the LDH structure grows in size as well. However, the broad size distribution and a high degree of agglomeration make it challenging to give a more accurate size estimate.

Scanning electron microscopy - energy dispersive spectroscopy (SEM-EDS) was used to determine the atomic metal ratios in the sample, see Table 2. For the two (Ni<sub>0.5</sub>Fe<sub>0.5</sub>)OOH samples the determined Ni:Fe ratio matches with the metal ratio used in the synthesis (within the error range of EDS as an analysis technique).

**Table 2:** Metal ratio (at. %) of the two (Ni<sub>0.5</sub>Fe<sub>0.5</sub>)OOH samples from SEM-EDS.

Sample	Ni (at. %)	Error (at. %)	Fe (at. %)	Error (at. %)
Ni1:Fe1-2h	46	1.4	54	1.4
Ni1:Fe1-6h	47	1.3	53	1.3

Further structural characterization was done using X-ray total scattering with Pair Distribution Function (PDF) analysis, which is well suited for the structural analysis of nanomaterials.<sup>38</sup> The PDFs from the two samples are shown in Figure 2. To extract quantitative structural information, we performed PDF modelling, where a structural model is fitted to the experimental data. We used the Ni(OH)<sub>2</sub>-LDH<sup>39</sup> (space group R-3m) structure as the starting model for the LDH-phase. The calculated PDFs from Ni(OH)<sub>2</sub>-LDH,  $\alpha$ -NiFe-LDH, and  $\gamma$ -NiFe-LDH are shown in Figure S5, from which it is observed that the PDFs are quite similar locally. We, therefore, used the simplest structure, Ni(OH)<sub>2</sub>-LDH, for the modelling. As shown from the refinements presented in Figure S6 and Table S2, the LDH model alone does not give a complete description of the data. On the other hand, the calculated PDF from the spinel structure, which was also identified from diffraction data, shows high similarity with the difference curves in the fits. We, therefore,

use the Ni(OH)<sub>2</sub>-LDH and spinel structure in a two-phase refinement, shown in Figure 2. The refined parameters can be found in Table S3. The model gives a relatively good description of the local structure (low *r*-range). However, the features at high *r* are not fitted. The misfit likely arises from the anisotropic nature of the LDH particles. For simplicity, we use a spherical particle model for both phases. While this is likely a good approximation for the spinel phase, it is not a good description of the LDH morphology. This misfit limits the amount of information that can be extracted from the refinements, and the fit results should therefore be seen more as trends than absolute values.

The PDF refinement reveals that after 2 hours of synthesis, the sample consists of approximately 70 wt.% LDH and 30 wt.% spinel. After 6 hours of synthesis, the phase fraction of LDH has increased to 80 wt.%. The PDF refinements furthermore confirm that the interlayer distance increases with synthesis time. The refined unit cell parameter, *c*, for the Ni(OH)<sub>2</sub>-LDH structure in the stacking direction is refined to 21.79 Å and 22.74 Å for Ni1:Fe1-2h and Ni1:Fe1-6h, respectively.

The refinements also show a high degree of structural disorder in the layering. In the PDF fit shown in Figure 2, we have refined anisotropic atomic displacement (ADP) values for Ni in the Ni(OH)<sub>2</sub>-LDH structure. The ADP in the stacking direction (*c*) is significantly larger than in the *a* and *b* directions (Table S3). This anisotropic ADP value indicates a high degree of stacking disorder in the LDH structure.<sup>40</sup> For comparison, the refinement using isotropic ADP values is shown in Figure S7 and Table S4.

In the PDF analysis, we also refine a crystallite domain size. The refined spherical diameter of the Ni(OH)<sub>2</sub>-LDH structure refine to 51 Å and 19 Å for the Ni1:Fe1-6h with Ni1: Fe1-2h respectively. The misfit at high *r*-values in the PDF refinement means that these numbers should not be considered absolute. However, they indicate that either the particle size or the order in the crystal structure increases with synthesis time. In the TEM micrographs, an increase in particle size is qualitatively confirmed.

Two other (Ni<sub>1-x</sub>Fe<sub>x</sub>)OOH samples with different Fe content and one (Ni<sub>1-x</sub>Co<sub>x</sub>)OOH sample were characterized as well, see SI (Figure S8-9, Table S5). These samples mainly serve for the discussion of the influence of iron (in the samples as well as in the electrolyte) on the electrocatalytic performance of the samples.



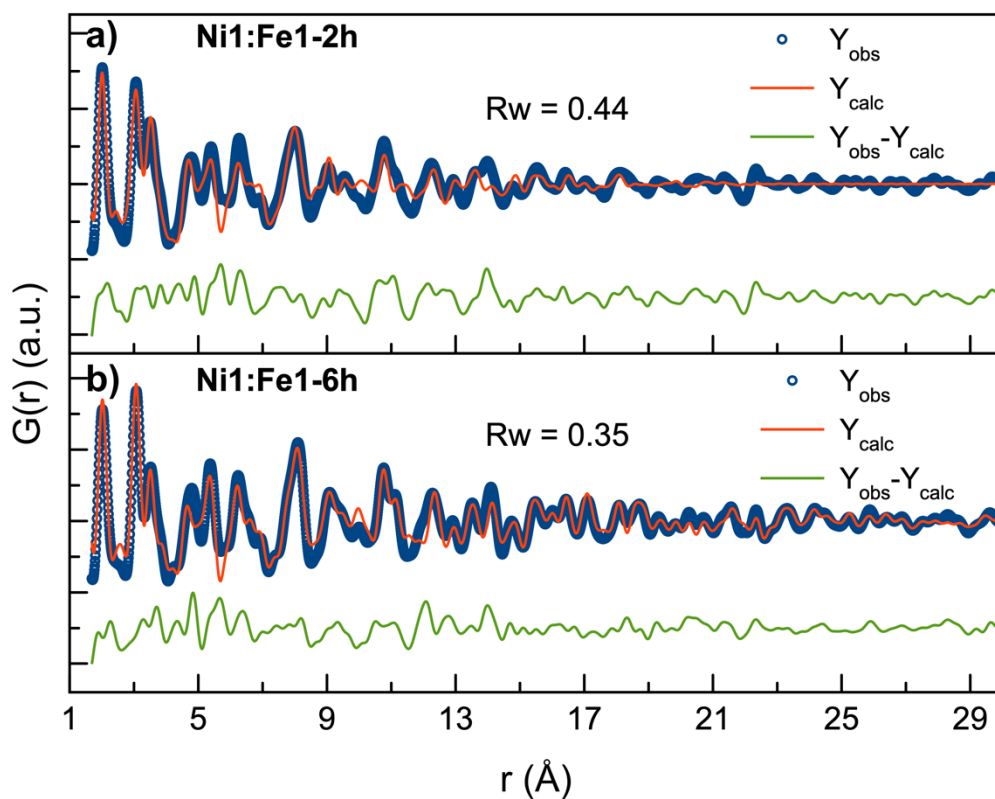


**Figure 2:** PDF refinements of products synthesized with Ni:Fe 1:1 ratio for a) 2h and b) 6h. The fits were based on a two-phase model using  $\text{Ni}(\text{OH})_2\text{-LDH}^{39}$  and spinel<sup>41</sup> structures. The blue circles show the experimental PDFs, the red lines are simulated PDFs, and the green lines are the difference curves of the two. Refined parameters are given in Table S3.

### 3.2 Electrochemical measurements

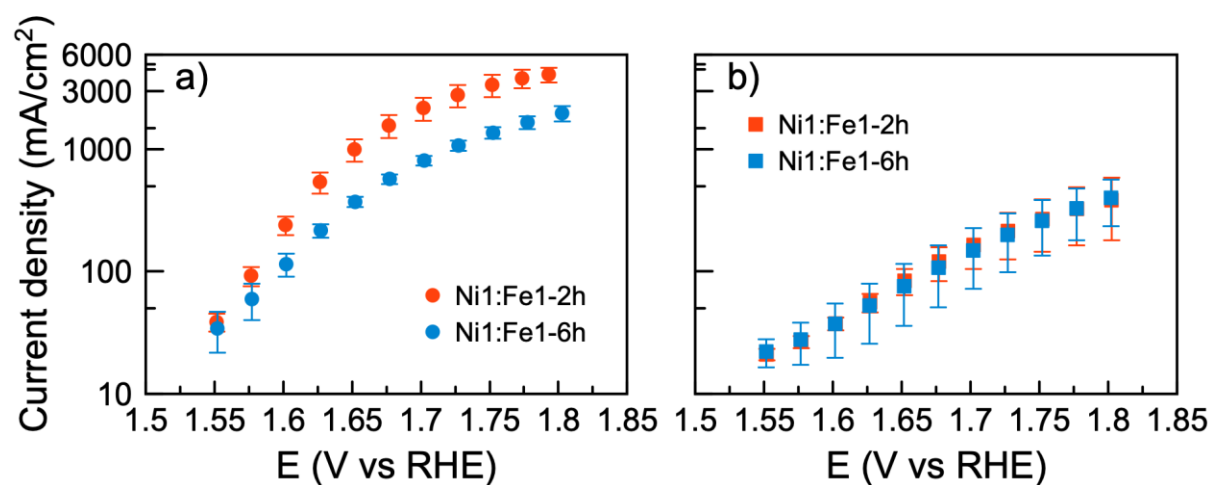


**Figure 3:** Steady-state OER activities of the two  $(\text{Ni}_{0.5}\text{Fe}_{0.5})\text{OOH}$  samples in a) as-prepared and b) purified 0.1 M KOH electrolyte measured at 2500 rpm. The activities shown are normalized to the geometric surface area of the RDE tip. The error bars indicate the standard deviation from measuring three different RDE tips.

To compare the OER performance of the two different  $(\text{Ni}_{0.5}\text{Fe}_{0.5})\text{OOH}$  samples, as well as to investigate the effect of iron impurities on the measurements, their activities were determined in as-prepared and purified 0.1 M KOH electrolyte. Figure 3 shows the first steady-state measurements (at 2500 rpm) of the two samples in (a) as-prepared and (b) purified KOH electrolyte. The activities are normalized to the geometric surface area of the working electrode. As the catalyst loading on the GC tips of the RDE was fixed, these activity values directly translate to the mass activity of the samples. In the as-prepared electrolyte (Figure 3a) the activity trends of the  $(\text{Ni}_{0.5}\text{Fe}_{0.5})\text{OOH}$  samples can be separated into two potential ranges with different behavior. In the first potential range, a linear Tafel behavior is observed (between  $1.55 V_{\text{RHE}}$  and  $1.68 V_{\text{RHE}}$ ), while it deviates from the linear behavior above  $1.68 V_{\text{RHE}}$ . The “bending” of the Tafel slope in the second potential range ( $1.68 V_{\text{RHE}}$  and  $1.8 V_{\text{RHE}}$ ) indicates mass transport limitations. This is a typical observation for OER measurements recorded with an RDE and indicates that at higher currents, parts of the catalyst surface are covered by bubbles of evolved oxygen that are not removed quickly enough from the catalyst surface. Ni1:Fe1-2h exhibits this slope “bending” behavior clearly, while in the other  $(\text{Ni}_{0.5}\text{Fe}_{0.5})\text{OOH}$ -sample the change in slope

is more subtle. Note that Ni1:Fe1-2h is also the more active sample, as will be discussed further below. Hence, this observation supports the hypothesis of mass transport limitations: as more oxygen is evolved at the more active sample, the surface blocking is subsequently enhanced resulting in the strongest “bending” of the slope.

Figure 3b depicts the determined activities of the samples in purified KOH electrolyte. Substantial differences between the two sets of determinations are observed. In the purified KOH electrolyte, the measured current densities of both samples are substantially lower (up to a factor of ten times lower OER currents) than the ones determined in as-prepared KOH at the corresponding potentials. However, the different (Ni<sub>0.5</sub>Fe<sub>0.5</sub>)OOH samples are affected by the Fe-impurities to different extents. A dedicated graph depicting the difference in current densities can be found in Figure S10. The lower activities are expected and consistent with previous studies. It is well known that Fe-impurities in the electrolyte have an enhancing effect on the catalytic performance and this effect has been discussed intensely.<sup>18-20, 42-45</sup> However, it is noteworthy that the reported purification process by no means was able to remove Fe completely from the electrolyte.<sup>18</sup> Furthermore, it is observed that the reported purification process leads to an increase in the Ni concentration in the electrolyte, see ICP-MS results of the electrolyte in the experimental section.

**Table 3:** Activities at 1.6  $V_{RHE}$  and calculated Tafel slopes of synthesized samples during the first set of potential steps (2500 rpm).

Sample	As-prepared KOH		Purified KOH	
	Current density @1.6 $V_{RHE}$ (mA/cm <sup>2</sup> )	Tafel slope (mV/dec)	Current density @1.6 $V_{RHE}$ (mA/cm <sup>2</sup> )	Tafel slope (mV/dec)
Ni1:Fe1-2h	241 ± 41.07	63	37 ± 4.58	160
Ni1:Fe1-6h	115 ± 24.69	83	37 ± 17.55	100

Table 3 quantifies the general observations about the impact of Fe-impurities on the samples. The table shows the activities at 1.6  $V_{RHE}$  and Tafel slopes of both samples from the first measurement at 2500 rpm in as-prepared and purified KOH.

### 3.2.1 OER activities in as-prepared electrolyte

We first compare the performance of the two samples in as-prepared KOH. Here, Ni1:Fe1-2h performs substantially better than Ni1:Fe1-6h, exhibiting a steady-state current density of 241 mA/cm<sup>2</sup> at 1.6 V<sub>RHE</sub> with a Tafel slope of 63 mV/dec, see Table 3. This performance is comparable to those of other (Ni<sub>1-x</sub>Fe<sub>x</sub>)OOH-based catalysts reported in other studies recorded under transient conditions (potential scans).<sup>46-50</sup> Its steady-state current density is roughly twice as high as the determined steady-state current density of Ni1:Fe1-6h. Additionally, Ni1:Fe1-2h exhibits a less steep Tafel slope. Therefore, in terms of mass activity, the sample with a shorter synthesis time outperforms the sample with a longer synthesis time. Based on the structural characterization discussed above, the prolonged synthesis time results in several changes in the sample, including increased basal spacing and crystallite size. Furthermore, a slightly higher phase fraction of LDH was seen with increased synthesis time. Especially the smaller crystallite size likely affects the absolute performance towards the OER positively because smaller structures exhibit a larger surface-to-volume ratio. It could be assumed that part of the decreased performance of Ni1:Fe1-6h (as compared to Ni1:Fe1-2h) is due to a decrease in active surface area. Interestingly, Dionigi et al. observed in *in situ* PXRD measurements of NiFe-LDH, a contraction of the lattice spacing by ca. 8 % upon the onset of the OER.<sup>34</sup> This contraction is in the same value as the observed expansion of the lattice spacing upon increased heating time, see discussion of PXRD results. Therefore, in addition to the loss in active surface area, the observed increase in lattice spacing during heating might be in part responsible for the decreased performance of Ni1:Fe1-6h.

### 3.2.2 OER activities in purified electrolyte

However, the *in situ* measurements of Dionigi et al. were performed in purified KOH electrolyte. When comparing our samples in the purified electrolyte, they both exhibit identical activities of 37 mA/cm<sup>2</sup> at 1.6 V<sub>RHE</sub> within the accuracy of the measurements. This means that the OER activities and accompanying Tafel slopes recorded in purified electrolyte have severely deteriorated as compared to the activities in as-prepared electrolytes, see Table 3. The activity deterioration in purified electrolyte is well known,<sup>18</sup> and, our results show that the differences in structural parameters, i.e., lattice spacing, particle size, and slightly higher phase fraction of LDH only seem to have a strong influence on the OER mass activity in as-prepared electrolyte.

### 3.2.3 Investigating the structure sensitivity of the OER on NiFe-LDHs

In catalysis, one distinguishes between structure-sensitive and structure-insensitive reactions. This distinction has been regarded as “one of the most successful classifications of catalytic reactions”<sup>51</sup> and is used for more than 50 years<sup>52</sup> in catalysis and surface science. To unravel structure sensitivity, typically the specific activity (or turnover frequency) needs to be determined.<sup>53</sup> Structure-insensitive reactions exhibit a specific activity independent of the particle size/active surface area. Or in other words, for structure-insensitive reactions, the mass activity scales with the active surface area.

Determining the specific activity requires a method for measuring the active surface area of the catalysts. To that end, several strategies can be employed. Structural characterization relies on knowing the particle size distribution and applying geometric models to calculate the surface area. Alternatively, the Brunauer-Emmett-Teller (BET) theory can be employed to determine the surface through gas adsorption. Importantly, these structural and physical methods do not determine the density or number of active sites in the sample which can be a major issue. On the other hand, electrochemical methods can determine the number of electrochemically available sites and thereby generally give a good estimate of the electrochemically active surface area (ECSA). In the absence of techniques that rely on the adsorption of molecules or atoms,<sup>54</sup> the ECSA can be determined through capacitance measurements.<sup>55</sup> Determining the ECSA of (Ni<sub>1-x</sub>Fe<sub>x</sub>)OOH materials using capacitive currents has been reported previously<sup>13,33</sup>, however, for LDHs, these determinations are complicated due to the material’s response to the application of a potential. A main concern is the dependence of the electrical conductivity on the applied potential.<sup>56</sup> Also, LDH materials exhibit limited potential windows of purely capacitive currents. A determination approach based on capacitance, already controversial for LDH structures<sup>34</sup>, becomes even more complicated when the samples do not have smooth surfaces,<sup>57</sup> as is the case in the presented study. Recently, the capacitance of adsorbed OER intermediates calculated through electrochemical impedance spectroscopy (EIS) has been used to compare the ECSA of different LDH structures.<sup>16,58</sup> This approach, while presumably more accurate and circumventing parts of the problems capacitance measurements exhibit on LDHs surfaces, does not solve the problem of the required smooth electrode surface. The EIS analysis and fitting might also not be straightforward. Hence, as of now, there exists no simple and reliable way of determining the ECSA of transition metal LDH structures.

In the case of the presented samples, it appears that structure sensitivity is better discussed by data acquired through structural characterization. The combination of insights gained from PDF, PXRD, and TEM suggests that Ni1:Fe1-2h contains smaller crystallites and particles than Ni1:Fe1-6h. From this, it follows that Ni1:Fe1-2h exhibits a larger surface area than Ni1:Fe1-6h. Interestingly, the larger surface area does not lead to a higher OER mass activity in purified electrolyte. This means that the OER is a structure-sensitive reaction. The larger surface area does not lead to more active sites. However, in as-prepared electrolyte the reactivity becomes mainly governed by the Fe-impurities in the electrolyte. The larger surface area of Ni1:Fe1-2h leads to a higher mass activity. In other words, the larger the surface area exposed at the interface between catalyst and electrolyte, the stronger the enhancing effect of the Fe-impurities on samples that perform similarly in purified electrolyte. Due to the lack of an of absolute values of the electrochemically accessible surface areas, we cannot determine if there is a linear relationship between mass activity and surface area (i.e., that the OER becomes a structure-insensitive reaction). However, our results suggest that the structure sensitivity observed in purified electrolyte is strongly reduced in as-prepared electrolyte. To assure that the observed behavior originates from the Fe-impurities and not from different factors, another pair of  $(\text{Ni}_{1-x}\text{Fe}_x)\text{OOH}$  samples with different Fe content and a  $(\text{Ni}_{0.5}\text{Co}_{0.5})\text{OOH}$  sample were investigated well. The determined mass activities and corresponding Tafel slopes can be found in Figure S11. The additional  $(\text{Ni}_{1-x}\text{Fe}_x)\text{OOH}$  samples have a Ni: Fe ratio of 4:1 with different synthesis times to investigate the effect of Fe-content in the sample. The  $(\text{Ni}_{0.5}\text{Co}_{0.5})\text{OOH}$  sample contains no Fe, hence it can be suggested that the Fe impurities originate from the electrolyte and not the electrode itself. Both reference systems affirm the observed trends for the Ni1:Fe1 samples: Of the Ni4:Fe1-samples, the sample with shorter synthesis time, and smaller crystallites, performs better in as-prepared electrolyte. After purification, the samples' activities are substantially reduced and the sample with longer synthesis time even performs slightly better. In the case of the  $(\text{Ni}_{0.5}\text{Co}_{0.5})\text{OOH}$  sample, a decreased steady-state OER activity is observed in purified electrolyte as compared to the activity determined in as-prepared KOH electrolyte. This confirms that the Fe-impurities in the electrolyte are causing the activation.

In this context, it should be mentioned that structure sensitivity is mostly discussed for precious metal-based catalysts. The  $(\text{Ni}_{1-x}(\text{M})_x)\text{OOH}$  materials employed in alkaline

electrolysis are non-precious and as a result comparatively cheap. Therefore, the utilization of the material - the density of active sites - is less important than in platinum group or other precious metal catalysts. A more important factor to optimize in alkaline OER is the volumetric power density. This means that high geometric current densities are desirable as are achieved here.

### **3.2.4 The influence of electrolysis time on the OER activity**

In addition to the discussed effects, it was observed that the measured OER activities change with measurement time. Figure 4 displays the steady-state activities of the two (Ni<sub>0.5</sub>Fe<sub>0.5</sub>)OOH samples recorded in chronological order. The electrolysis protocol involves four consecutive sets of potential steps starting at 2500 rpm, followed by 4900 rpm, 2500 rpm-2<sup>nd</sup>, and 4900 rpm-2<sup>nd</sup> to investigate the effect of electrolysis time on OER activity. For the measurements conducted in purified KOH, the order of the measurement was kept the same except there is no repetition for 4900 rpm. The different rotation speeds were applied to remove evolved oxygen from the working electrode while simultaneously investigating possible mass-transport effects. In as-prepared KOH, both samples (Figures 4a and c) exhibit a substantial increase in activity after the first steady-state measurements (2500 rpm, blue points in Figures 4a and c). The OER activity of sample Ni1:Fe1-2h remains constant for the subsequent potential steps. Meanwhile, the activity of Ni1:Fe1-6h continuously increases even after the second set of potential steps - albeit at a lower rate. In addition, the determined OER activities are not influenced systematically by the different rotation speeds. Apparently, the activities are influenced mainly by electrolysis time while rotation speed has no obvious influence. For both samples (Figures 4b and d), an increase in activity with progressing electrolysis time is also observed in purified electrolyte. However, for both Ni1:Fe1-2h and Ni1:Fe1-6h, the initial increase is less substantial than in the as-prepared electrolyte. On the other hand, the continuous increase with ongoing electrolysis, before only observed in Ni1:Fe1-6h, is now observed for both samples. The reference system of the Ni4:Fe1 samples reveals the same trend of activity enhancement with prolonged synthesis time. A further discussion of the measurements is found in the supporting information at Figure S1.

Two possible explanations for the enhanced OER activities as a function of electrolysis time come to mind. i) by stepping through the potential range, the continuing potential steps cause a roughening of the sample surface thereby leading to an increase in activity<sup>59</sup>; ii) the LDH structure of the sample might be subject to change. Specifically, a

rearrangement of the LDH sheets according to Bode et al.<sup>60</sup> seems likely. Since the activity enhancement differs in the presence, or absence, of Fe-impurities, it seems that the mechanism of activation is directly influenced by the impurities. The impurities seem to at least facilitate and accelerate the changes in the sample. Because of residual Fe in the purified electrolyte (Table 1), the same phenomenon as in the as-prepared electrolyte may be observed. Since the iron content is decreased the effects might take longer to manifest. The presence of residual Fe-impurities could also indicate that the Fe in the electrolyte is necessary for the activation to take place at all. From the present data, it is not possible to support or dismiss any particular supposition. To that end, *operando* PXRD characterization is necessary. This would allow the structure to be followed as a function of potential and electrolysis time. Through such an investigation light could be shed on the structural influences the Fe-impurities exert on the  $(\text{Ni}_{0.5}\text{Fe}_{0.5})\text{OOH}$  samples.

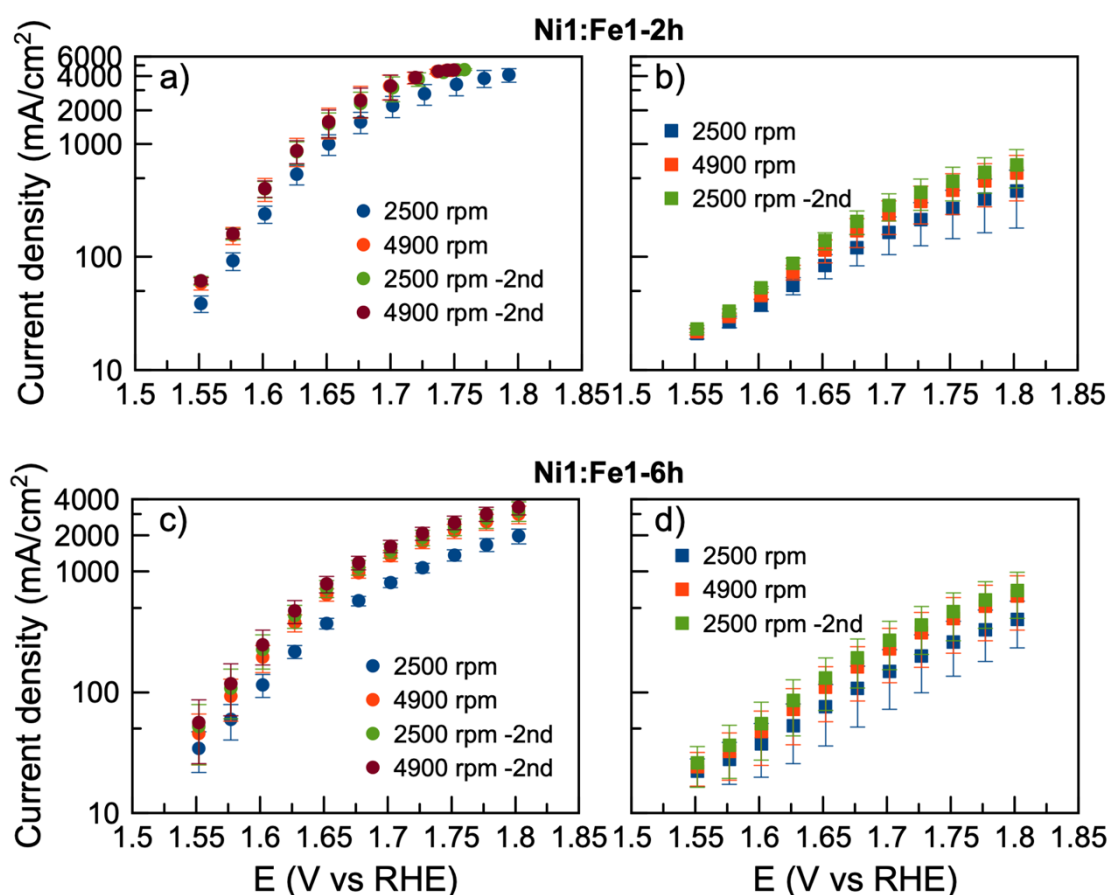


**Figure 4:** Steady-state OER activities of two  $(\text{Ni}_{0.5}\text{Fe}_{0.5})\text{OOH}$  samples: (a-b) Ni1:Fe1-2h, (c-d) Ni1:Fe1-6h in as-prepared (a, c) and purified (b, d) 0.1 M KOH electrolyte. The



*measurements were conducted in the order of 2500 rpm, 4900 rpm, 2500 rpm-2nd, and 4900 rpm-2nd. Note that for the measurements carried out in purified KOH, there were no 4900 rpm-2nd. And the activities shown here were normalized to the geometric surface area.*

#### **4 Conclusion and Outlook**

In this study, we have investigated the structure of  $(\text{Ni}_{1-x}\text{Fe}_x)\text{OOH}$  NPs and their resulting catalytic properties towards the OER in alkaline environment. First, the synthesis and structure relations were studied. It was illustrated that the size, structure, and morphology of  $(\text{Ni}_{1-x}\text{Fe}_x)\text{OOH}$  can be tuned by varying the synthesis time and the metal precursor ratio. PDF and PXRD analysis suggest that increased synthesis times lead to the transformation of the spinel to the LDH structure accompanied by the simultaneous growth of the crystallites and their basal spacing.

The catalytic performance of the synthesized  $(\text{Ni}_{1-x}\text{Fe}_x)\text{OOH}$  NPs towards the OER was investigated in as-prepared and purified KOH electrolyte. In the as-prepared KOH electrolyte, Ni1:Fe1-2h exhibits a steady-state OER activity of 241 mA/cm<sup>2</sup> at 1.6 V<sub>RHE</sub> with an accompanying Tafel slope of 63 mV/dec, which is similar to  $(\text{Ni}_{1-x}\text{Fe}_x)\text{OOH}$  catalysts reported in literature.<sup>46-50</sup> In comparison, Ni1:Fe1-6h performs worse (115 mA/cm<sup>2</sup> at 1.6 V<sub>RHE</sub>, 83 mV/dec) in the as-prepared electrolyte. From physical characterization (PXRD and PDF) we conclude that prolonged synthesis time leads to larger crystallite sizes and larger basal spacing. In accordance, Ni1:Fe1-2h exhibits smaller structural features than Ni1:Fe1-6h. In purified electrolyte, the determined OER activities of all investigated sample decreases substantially, and the observed structural differences do not have a large influence on the OER activity. Based on the different crystallite sizes, a structure-sensitive reaction can be concluded. The difference in activity observed in the as-prepared electrolyte can be explained by Ni1:Fe1-2h displaying an improved interaction with the Fe species in the electrolyte as compared to Ni1:Fe1-6h. Similar behavior was also observed for the reference  $(\text{Ni}_{0.8}\text{Fe}_{0.2})\text{OOH}$  samples introduced in the SI. So much so that other structural features seem to have no significant effect on the catalytic performance anymore. This suggests that the OER activity is governed by the interaction of the catalysts with the Fe-impurities and the concurrent enhancement effect is mainly related to the exposed surface area and not the structure of the catalysts.

The OER activity of the  $(\text{Ni}_{0.5}\text{Fe}_{0.5})\text{OOH}$  samples was also investigated as a function of electrolysis time. It was found that in both our purified and as-prepared electrolyte the catalytic performance of the samples increases with prolonged measurement time. There are, however, differences between measurements in the two electrolytes: In the as-prepared electrolyte a substantial increase in activity is observed after the first set of potential steps. Afterward, the activities are constant for Ni1:Fe1-2h and increase only slowly for Ni1:Fe1-6h. However, in purified electrolytes, both samples exhibit activities which are steadily increasing over the time of the measurement. Here, we can only hypothesize that the Fe-impurities are influencing the structural changes but cannot determine how these alterations occur exactly. For that, *ex situ* characterizations are insufficient and *operando* studies on the catalyst structure are necessary, e.g. *operando* PXRD and/or PDF analysis, as the interaction between Fe-impurities and catalyst is dependent on electrode polarization.<sup>20</sup>

## 5 Acknowledgement

We acknowledge support from the Swiss National Science Foundation (SNSF) project No. 200021\_184742 and the Danish National Research Foundation Center for High Entropy Alloy Catalysis (DNRF 149). We are grateful to the Villum Foundation for financial support through a Villum Young Investigator grant. We furthermore thank DANSCATT (supported by the Danish Agency for Science and Higher Education) for support. Funding from the Danish Ministry of Higher Education and Science through the SMART Lighthouse is gratefully acknowledged. We acknowledge DESY (Hamburg, Germany), a member of the Helmholtz Association HGF, for the provision of experimental facilities. Parts of this research were carried out at PETRA III and we would like to thank Henrik Jeppesen for assistance in using the beamline P02.1. Beamtime was allocated by an In-House contingent.

## 6 Author contributions

**Baiyu Wang:** Electrochemical measurements, sample characterization, data analysis, paper writing. **Nicolas Schlegel:** Experimental supervision, data analysis, paper writing. **Olivia Aalling-Frederiksen:** Sample synthesis, sample characterization, TEM imaging. **Etienne Berner:** SEM-EDS measurements and analysis. **Damin Zhang:** ICP-MS

measurements. **Rebecca Pittkowski:** Data analysis and discussion, reviewing. **Kirsten M. Ø. Jensen:** Supervision, reviewing. **Matthias Arenz:** Supervision, conceptualization, reviewing, editing.

## 7 References

1. Chu, S.; Majumdar, A., Opportunities and challenges for a sustainable energy future. *nature* **2012**, *488* (7411), 294-303.
2. You, B.; Sun, Y., Innovative strategies for electrocatalytic water splitting. *Accounts of chemical research* **2018**, *51* (7), 1571-1580.
3. Kibsgaard, J.; Chorkendorff, I., Considerations for the scaling-up of water splitting catalysts. *Nature Energy* **2019**, *4* (6), 430-433.
4. Montoya, J. H.; Seitz, L. C.; Chakthranont, P.; Vojvodic, A.; Jaramillo, T. F.; Nørskov, J. K., Materials for solar fuels and chemicals. *Nature materials* **2017**, *16* (1), 70-81.
5. Liang, Q.; Brocks, G.; Bieberle-Hütter, A., Oxygen evolution reaction (OER) mechanism under alkaline and acidic conditions. *Journal of Physics: Energy* **2021**, *3* (2), 026001.
6. Mohammed-Ibrahim, J., A review on NiFe-based electrocatalysts for efficient alkaline oxygen evolution reaction. *Journal of Power Sources* **2020**, *448*, 227375.
7. Wei, C.; Rao, R. R.; Peng, J.; Huang, B.; Stephens, I. E.; Risch, M.; Xu, Z. J.; Shao-Horn, Y., Recommended practices and benchmark activity for hydrogen and oxygen electrocatalysis in water splitting and fuel cells. *Advanced Materials* **2019**, *31* (31), 1806296.
8. McCrory, C. C.; Jung, S.; Peters, J. C.; Jaramillo, T. F., Benchmarking heterogeneous electrocatalysts for the oxygen evolution reaction. *Journal of the American Chemical Society* **2013**, *135* (45), 16977-16987.
9. Lee, Y.; Suntivich, J.; May, K. J.; Perry, E. E.; Shao-Horn, Y., Synthesis and activities of rutile IrO<sub>2</sub> and RuO<sub>2</sub> nanoparticles for oxygen evolution in acid and alkaline solutions. *The journal of physical chemistry letters* **2012**, *3* (3), 399-404.
10. Commission, E. Critical raw material. [https://ec.europa.eu/growth/sectors/raw-materials/areas-specific-interest/critical-raw-materials\\_en](https://ec.europa.eu/growth/sectors/raw-materials/areas-specific-interest/critical-raw-materials_en) (accessed January 20, 2023).
11. Qian, L.; Lu, Z.; Xu, T.; Wu, X.; Tian, Y.; Li, Y.; Huo, Z.; Sun, X.; Duan, X., Ternary layered double hydroxides as high-performance bifunctional materials for oxygen electrocatalysis. *Advanced energy materials* **2015**, *5* (13), 1500245.
12. Shao, M.; Zhang, R.; Li, Z.; Wei, M.; Evans, D. G.; Duan, X., Layered double hydroxides toward electrochemical energy storage and conversion: design, synthesis and applications. *Chemical communications* **2015**, *51* (88), 15880-15893.

13. Asnavandi, M.; Yin, Y.; Li, Y.; Sun, C.; Zhao, C., Promoting oxygen evolution reactions through introduction of oxygen vacancies to benchmark NiFe–OOH catalysts. *ACS Energy Letters* **2018**, *3* (7), 1515-1520.
14. Zhu, W.; Chen, W.; Yu, H.; Zeng, Y.; Ming, F.; Liang, H.; Wang, Z., NiCo/NiCo–OH and NiFe/NiFe–OH core shell nanostructures for water splitting electrocatalysis at large currents. *Applied Catalysis B: Environmental* **2020**, *278*, 119326.
15. Enman, L. J.; Stevens, M. B.; Dahan, M. H.; Nellist, M. R.; Toroker, M. C.; Boettcher, S. W., Operando x-ray absorption spectroscopy shows iron oxidation is concurrent with oxygen evolution in cobalt–iron (oxy) hydroxide electrocatalysts. *Angewandte Chemie* **2018**, *130* (39), 13022-13026.
16. Dionigi, F.; Zhu, J.; Zeng, Z.; Merzdorf, T.; Sarodnik, H.; Gliech, M.; Pan, L.; Li, W. X.; Greeley, J.; Strasser, P., Intrinsic electrocatalytic activity for oxygen evolution of crystalline 3D-transition metal layered double hydroxides. *Angewandte Chemie* **2021**, *133* (26), 14567-14578.
17. Corrigan, D. A., The catalysis of the oxygen evolution reaction by iron impurities in thin film nickel oxide electrodes. *Journal of The Electrochemical Society* **1987**, *134* (2), 377.
18. Trotochaud, L.; Young, S. L.; Ranney, J. K.; Boettcher, S. W., Nickel–iron oxyhydroxide oxygen-evolution electrocatalysts: the role of intentional and incidental iron incorporation. *Journal of the American Chemical Society* **2014**, *136* (18), 6744-6753.
19. Klaus, S.; Cai, Y.; Louie, M. W.; Trotochaud, L.; Bell, A. T., Effects of Fe electrolyte impurities on Ni (OH) <sub>2</sub>/NiOOH structure and oxygen evolution activity. *The Journal of Physical Chemistry C* **2015**, *119* (13), 7243-7254.
20. Spanos, I.; Masa, J.; Zeradjanin, A.; Schlögl, R., The effect of iron impurities on transition metal catalysts for the oxygen evolution reaction in alkaline environment: activity mediators or active sites? *Catalysis Letters* **2021**, *151* (7), 1843-1856.
21. Anantharaj, S.; Kundu, S.; Noda, S., “The Fe Effect”: A review unveiling the critical roles of Fe in enhancing OER activity of Ni and Co based catalysts. *Nano Energy* **2021**, *80*, 105514.
22. Farhat, R.; Dhainy, J.; Halaoui, L. I., Oer catalysis at activated and codeposited nife-oxo/hydroxide thin films is due to postdeposition surface-fe and is not sustainable without fe in solution. *ACS Catalysis* **2019**, *10* (1), 20-35.

23. Zhang, T.; Nellist, M. R.; Enman, L. J.; Xiang, J.; Boettcher, S. W., Modes of Fe incorporation in Co–Fe (Oxy) hydroxide oxygen evolution electrocatalysts. *ChemSusChem* **2019**, *12* (9), 2015-2021.
24. Stevens, M. B.; Trang, C. D.; Enman, L. J.; Deng, J.; Boettcher, S. W., Reactive Fe-sites in Ni/Fe (oxy) hydroxide are responsible for exceptional oxygen electrocatalysis activity. *Journal of the American Chemical Society* **2017**, *139* (33), 11361-11364.
25. Chupas, P. J.; Qiu, X.; Hanson, J. C.; Lee, P. L.; Grey, C. P.; Billinge, S. J., Rapid-acquisition pair distribution function (RA-PDF) analysis. *Journal of Applied Crystallography* **2003**, *36* (6), 1342-1347.
26. Prescher, C.; Prakapenka, V. B., DIOPTAS: a program for reduction of two-dimensional X-ray diffraction data and data exploration. *High Pressure Research* **2015**, *35* (3), 223-230.
27. Yang, X.; Juhas, P.; Farrow, C. L.; Billinge, S. J., xPDFsuite: an end-to-end software solution for high throughput pair distribution function transformation, visualization and analysis. *arXiv preprint arXiv:1402.3163* **2014**.
28. Farrow, C. L.; Juhas, P.; Liu, J. W.; Bryndin, D.; Bozin, E. S.; Bloch, J.; Proffen, T.; Billinge, S. J., PDFfit2 and PDFgui: computer programs for studying nanostructure in crystals. *J Phys Condens Matter* **2007**, *19* (33), 335219.
29. Schindelin, J.; Arganda-Carreras, I.; Frise, E.; Kaynig, V.; Longair, M.; Pietzsch, T.; Preibisch, S.; Rueden, C.; Saalfeld, S.; Schmid, B., Fiji: an open-source platform for biological-image analysis. *Nature methods* **2012**, *9* (7), 676-682.
30. Mayrhofer, K.; Wiberg, G.; Arenz, M., Impact of glass corrosion on the electrocatalysis on Pt electrodes in alkaline electrolyte. *Journal of the Electrochemical Society* **2007**, *155* (1), P1.
31. Wiberg, G. K. H. The development of a state-of-the-art experimental setup demonstrated by the investigation of fuel cell reactions in alkaline electrolyte. Technische Universität München, 2010.
32. Inaba, M.; Quinson, J.; Bucher, J. R.; Arenz, M., On the preparation and testing of fuel cell catalysts using the thin film rotating disk electrode method. *Journal of Visualized Experiments: JoVE* **2018**, (133).
33. Wu, Y.; Wang, H.; Ji, S.; Tian, X.; Li, G.; Wang, X.; Wang, R., Ultrastable NiFeOOH/NiFe/Ni electrocatalysts prepared by in-situ electro-oxidation for oxygen evolution reaction at large current density. *Applied Surface Science* **2021**, *564*, 150440.

34. Dionigi, F.; Zeng, Z.; Sinev, I.; Merzdorf, T.; Deshpande, S.; Lopez, M. B.; Kunze, S.; Zegkinoglou, I.; Sarodnik, H.; Fan, D., In-situ structure and catalytic mechanism of NiFe and CoFe layered double hydroxides during oxygen evolution. *Nature communications* **2020**, *11* (1), 1-10.
35. Scherrer, P., Bestimmung der Grösse und der inneren Struktur von Kolloidteilchen mittels Röntgenstrahlen. *Nachrichten von der Gesellschaft der Wissenschaften zu Göttingen, mathematisch-physikalische Klasse* **1918**, *1918*, 98-100.
36. Song, F.; Hu, X., Exfoliation of layered double hydroxides for enhanced oxygen evolution catalysis. *Nature communications* **2014**, *5* (1), 1-9.
37. Cook, D. S.; Kashtiban, R. J.; Krambrock, K.; de Lima, G. M.; Stumpf, H. O.; Lara, L. R.; Ardisson, J. D.; Walton, R. I., Nanocrystalline Transition-Metal Gallium Oxide Spinel from Acetylacetonate Precursors via Solvothermal Synthesis. *Materials* **2019**, *12* (5), 838.
38. Christiansen, T. L.; Cooper, S. R.; Jensen, K. M. O., There's no place like real-space: elucidating size-dependent atomic structure of nanomaterials using pair distribution function analysis. *Nanoscale Adv.* **2020**, *2* (6), 2234-2254.
39. Glemser, O.; Einerhand, J., Die struktur höherer nickelhydroxyde. *Zeitschrift für anorganische Chemie* **1950**, *261* (1-2), 43-51.
40. Yang, X.; Masadeh, A. S.; McBride, J. R.; Božin, E. S.; Rosenthal, S. J.; Billinge, S. J., Confirmation of disordered structure of ultrasmall CdSe nanoparticles from X-ray atomic pair distribution function analysis. *Physical Chemistry Chemical Physics* **2013**, *15* (22), 8480-8486.
41. Tsukimura, K.; Sasaki, S.; Kimizuka, N., Cation distributions in nickel ferrites. *Japanese journal of applied physics* **1997**, *36* (6R), 3609.
42. Tichenor, R. L., Nickel oxides-relation between electrochemical and foreign ion content. *Industrial & Engineering Chemistry* **1952**, *44* (5), 973-977.
43. Anantharaj, S.; Nagamatsu, T.; Yamaoka, S.; Li, M.; Noda, S., Efficient Methanol Electrooxidation Catalyzed by Potentiostatically Grown Cu-O/OH (Ni) Nanowires: Role of Inherent Ni Impurity. *ACS Applied Energy Materials* **2021**, *5* (1), 419-429.
44. Spanos, I.; Tesch, M. F.; Yu, M.; Tüysüz, H.; Zhang, J.; Feng, X.; Müllen, K.; Schlögl, R.; Mechler, A. K., Facile protocol for alkaline electrolyte purification and its influence on a Ni-Co oxide catalyst for the oxygen evolution reaction. *ACS Catalysis* **2019**, *9* (9), 8165-8170.

45. Subbaraman, R.; Danilovic, N.; Lopes, P.; Tripkovic, D.; Strmcnik, D.; Stamenkovic, V.; Markovic, N., Origin of anomalous activities for electrocatalysts in alkaline electrolytes. *The Journal of Physical Chemistry C* **2012**, *116* (42), 22231-22237.
46. Gao, R.; Yan, D., Fast formation of single-unit-cell-thick and defect-rich layered double hydroxide nanosheets with highly enhanced oxygen evolution reaction for water splitting. *Nano Research* **2018**, *11* (4), 1883-1894.
47. Zhong, H.; Liu, T.; Zhang, S.; Li, D.; Tang, P.; Alonso-Vante, N.; Feng, Y., Template-free synthesis of three-dimensional NiFe-LDH hollow microsphere with enhanced OER performance in alkaline media. *Journal of energy chemistry* **2019**, *33*, 130-137.
48. Yang, X.; Pan, J.; Nie, Y.; Sun, Y.; Wan, P., A facile and scalable complexation-precipitation method of iron doped nickel hydroxide nanosheets as a superior oxygen evolution catalyst. *International Journal of Hydrogen Energy* **2017**, *42* (43), 26575-26585.
49. Xie, J.; Qu, H.; Lei, F.; Peng, X.; Liu, W.; Gao, L.; Hao, P.; Cui, G.; Tang, B., Partially amorphous nickel-iron layered double hydroxide nanosheet arrays for robust bifunctional electrocatalysis. *Journal of Materials Chemistry A* **2018**, *6* (33), 16121-16129.
50. Zeng, L.; Yang, L.; Lu, J.; Jia, J.; Yu, J.; Deng, Y.; Shao, M.; Zhou, W., One-step synthesis of Fe-Ni hydroxide nanosheets derived from bimetallic foam for efficient electrocatalytic oxygen evolution and overall water splitting. *Chinese Chemical Letters* **2018**, *29* (12), 1875-1878.
51. Somorjai, G., The structure sensitivity and insensitivity of catalytic reactions in light of the adsorbate induced dynamic restructuring of surfaces. *Catalysis Letters* **1990**, *7*, 169-182.
52. Boudart, M., Catalysis by supported metals. *Advances in catalysis* **1969**, *20*, 153-166.
53. Shinozaki, K.; Zack, J. W.; Pylypenko, S.; Richards, R. M.; Pivovar, B. S.; Kocha, S. S., Benchmarking the oxygen reduction reaction activity of Pt-based catalysts using standardized rotating disk electrode methods. *International Journal of Hydrogen Energy* **2015**, *40* (46), 16820-16830.
54. Binniger, T.; Fabbri, E.; Kötzt, R.; Schmidt, T. J., Determination of the electrochemically active surface area of metal-oxide supported platinum catalyst. *Journal of The Electrochemical Society* **2013**, *161* (3), H121.
55. Ashton, S. J.; Arenz, M., Comparative DEMS study on the electrochemical oxidation of carbon blacks. *Journal of Power Sources* **2012**, *217*, 392-399.



56. Batchellor, A. S.; Boettcher, S. W., Pulse-electrodeposited Ni–Fe (oxy) hydroxide oxygen evolution electrocatalysts with high geometric and intrinsic activities at large mass loadings. *ACS Catalysis* **2015**, *5* (11), 6680-6689.
57. Cossar, E.; Houache, M. S.; Zhang, Z.; Baranova, E. A., Comparison of electrochemical active surface area methods for various nickel nanostructures. *Journal of Electroanalytical Chemistry* **2020**, *870*, 114246.
58. Watzele, S.; Hauenstein, P.; Liang, Y.; Xue, S.; Fichtner, J.; Garlyyev, B.; Scieszka, D.; Claudel, F.; Maillard, F.; Bandarenka, A. S., Determination of electroactive surface area of Ni-, Co-, Fe-, and Ir-based oxide electrocatalysts. *ACS Catalysis* **2019**, *9* (10), 9222-9230.
59. Seenivasan, S.; Jung, H.; Han, J. W.; Kim, D. H., Surface roughening strategy for highly efficient bifunctional electrocatalyst: combination of atomic layer deposition and anion exchange reaction. *Small Methods* **2022**, *6* (2), 2101308.
60. Bode, H.; Dehmelt, K.; Witte, J., Zur kenntnis der nickelhydroxidelektrode—I. Über das nickel (II)-hydroxidhydrat. *Electrochimica Acta* **1966**, *11* (8), 1079-1087.

## Supporting Information

### **Elucidating the Steady-State OER Activity of (Ni<sub>1-x</sub>Fe<sub>x</sub>)OOH Binary Nanoparticles in As-prepared and Purified KOH Electrolyte Solutions**

Baiyu Wang<sup>+,a</sup>, Nicolas Schlegel<sup>+,b</sup>, , Olivia Aalling-Frederiksen<sup>a</sup>, Etienne Berner<sup>b</sup>, Damin Zhang<sup>b</sup>, Rebecca K. Pittkowski<sup>a</sup>, Kirsten M. Ø. Jensen<sup>a,\*</sup> & Matthias Arenz<sup>b,\*</sup>

+ ) These authors contributed in equal parts.

a) Department of Chemistry, University of Copenhagen, Universitetsparken 5, 2100 Copenhagen Ø

b) Department of Chemistry, Biochemistry and Pharmaceutical Sciences, University of Bern, Freiestrasse 3, 3012 Bern, Switzerland

\* Corresponding authors: [matthias.arenz@unibe.ch](mailto:matthias.arenz@unibe.ch), [kirsten@chem.ku.dk](mailto:kirsten@chem.ku.dk)

## Measurement protocol

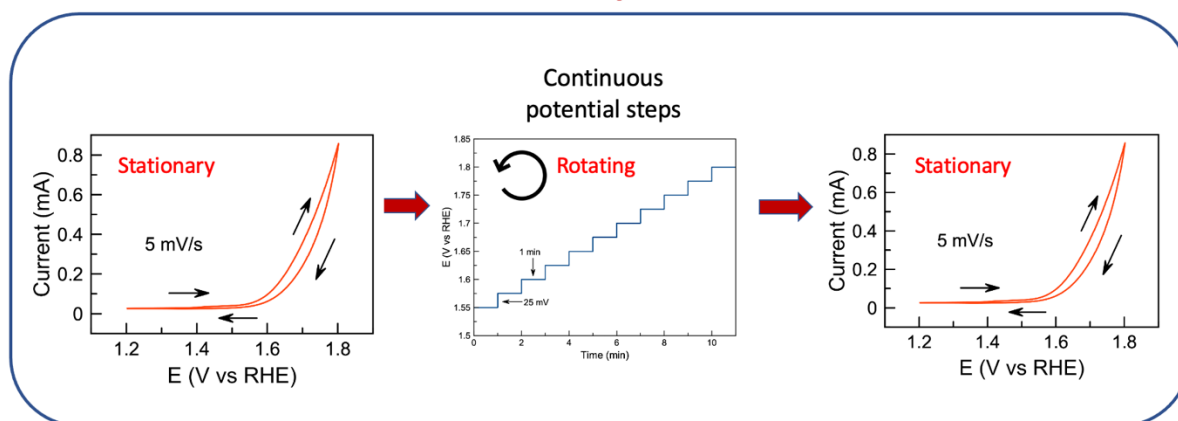


**Figure S1:** Schematic illustration of the measurement protocol. The continuous potential steps figure was plotted in time vs  $E$  (V vs RHE). Potential steps start from  $1.55 V_{RHE}$  to  $1.8 V_{RHE}$ , with a step size of  $25 \text{ mV}$  and  $60 \text{ s}$  holding at each potential. The potential steps were measured with two rotation speeds:  $2500 \text{ rpm}$  and  $4900 \text{ rpm}$ , in the order of  $2500 \text{ rpm} \rightarrow 4900 \text{ rpm} \rightarrow 2500 \text{ rpm-2nd} \rightarrow 4900 \text{ rpm-2nd}$ .

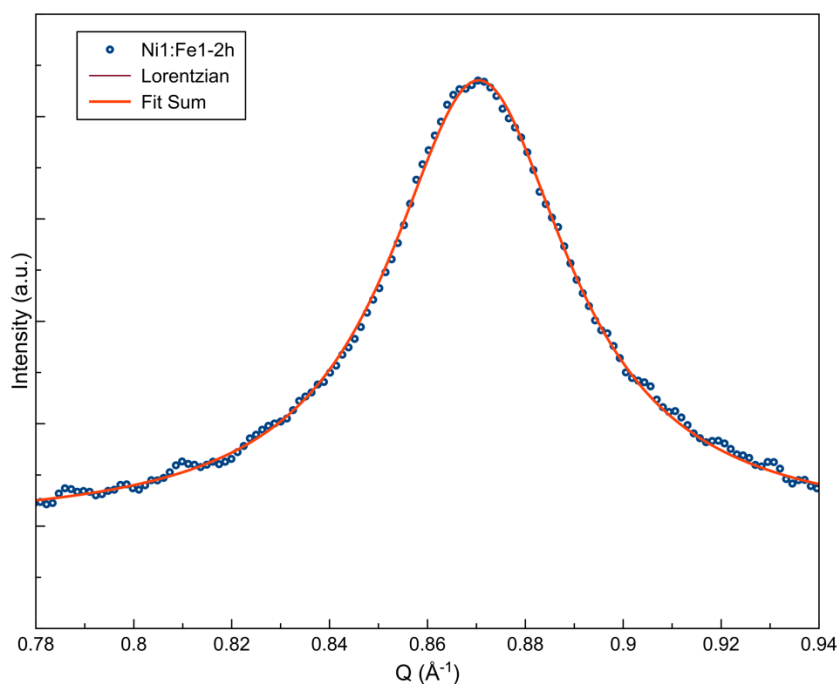


**Figure S2:** Peak fitting of the (003) peak from diffraction pattern of sample 'Ni1:Fe1-2h' using Lorentzian function.

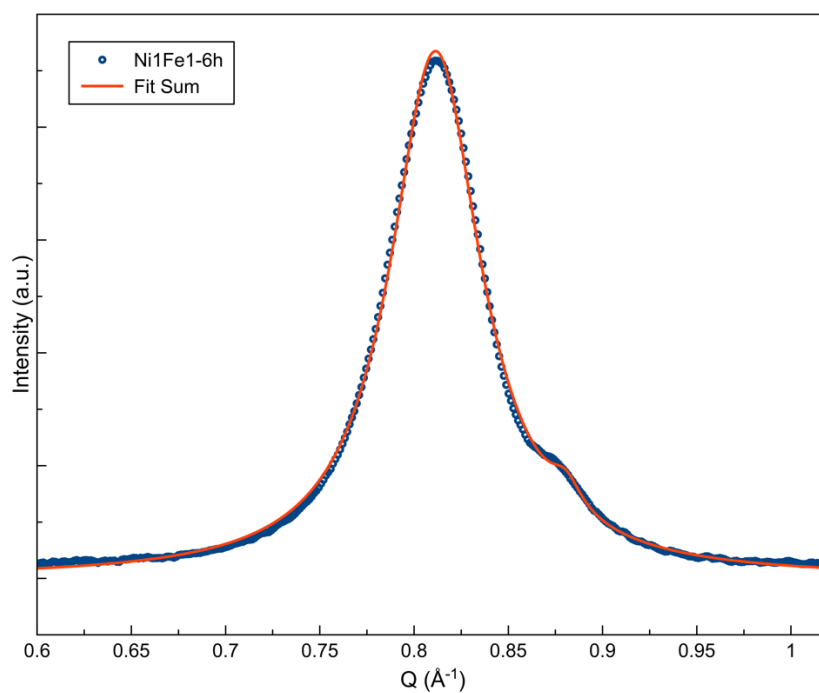


**Figure S3:** Peak fitting of the (001) peak from diffraction pattern of sample 'Ni1:Fe1-6h' using Lorentzian function.

**Table S1:** Fitting parameters from the two single peak fitting of diffraction patterns from sample 'Ni1:Fe1-2h' and 'Ni1:Fe1-6h'.

Sample	Ni1:Fe1-2h	Ni1:Fe1-6h
Amplitude	0.435 ( $\pm 0.15 \cdot 10^{-2}$ )	0.934 ( $\pm 0.20 \cdot 10^{-2}$ )
X Position	0.871 ( $\pm 0.77 \cdot 10^{-4}$ )	0.811 ( $\pm 0.65 \cdot 10^{-4}$ )
HWHM	0.022 ( $\pm 0.16 \cdot 10^{-3}$ )	0.030 ( $\pm 0.12 \cdot 10^{-3}$ )

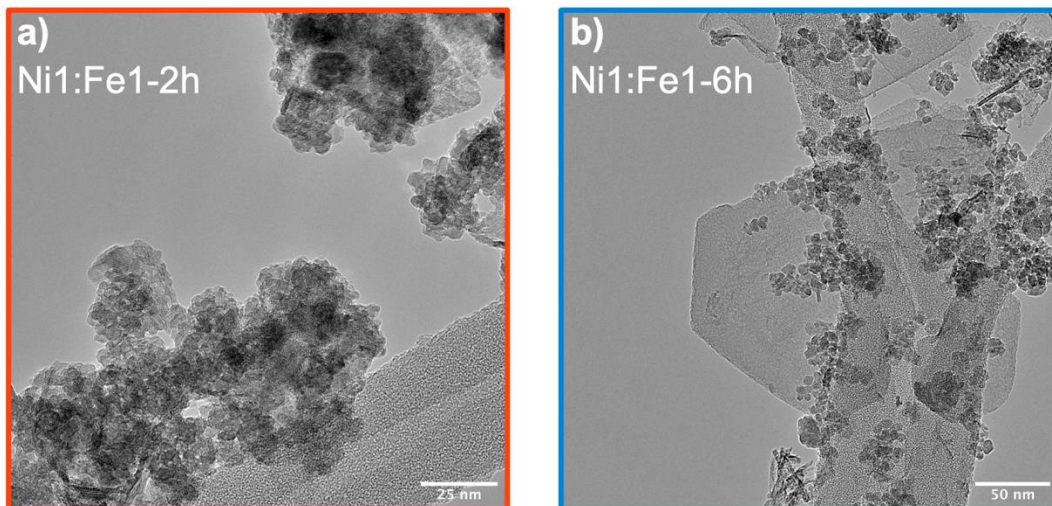


**Figure S4:** Exemplary TEM images of the two  $(\text{Ni}_{0.5}\text{Fe}_{0.5})\text{OOH}$  samples: (a) Ni1:Fe1-2h and (b) Ni1:Fe1-6h. Amplification TEM images of Figure 1b-c.

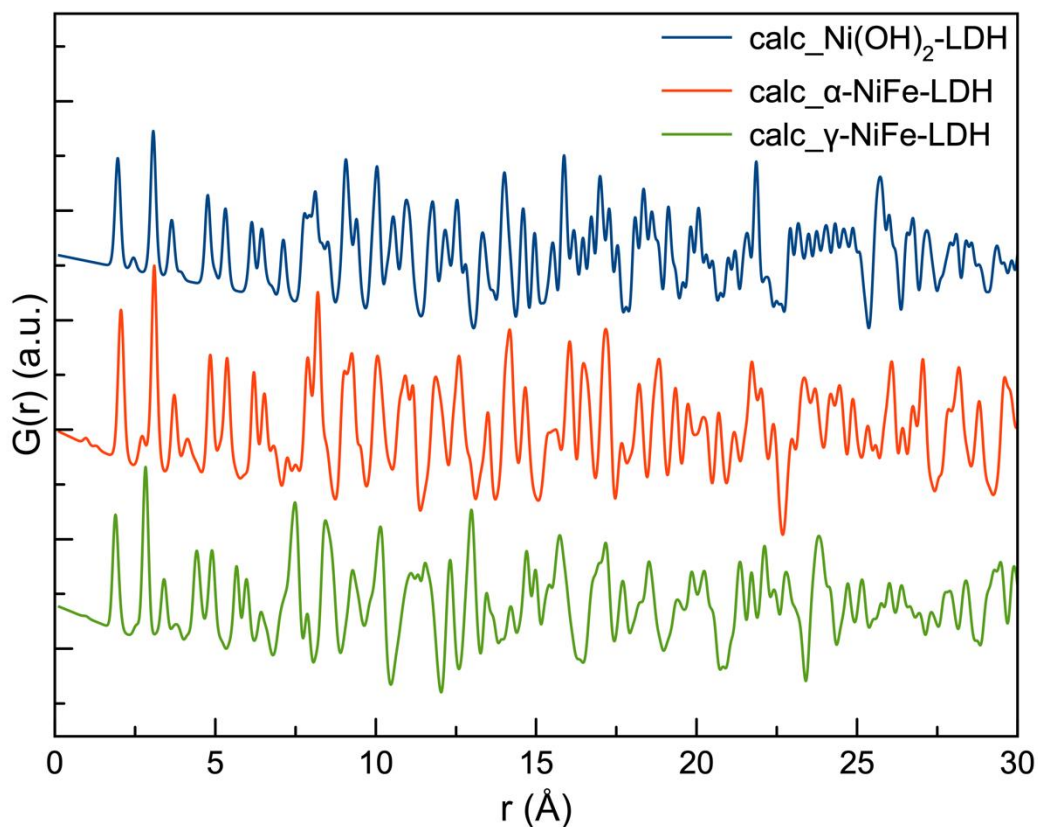


**Figure S5:** Calculated PDFs from  $\text{Ni}(\text{OH})_2\text{-LDH}$ ,  $\alpha\text{-NiFe-LDH}$ , and  $\gamma\text{-NiFe-LDH}$  structures.

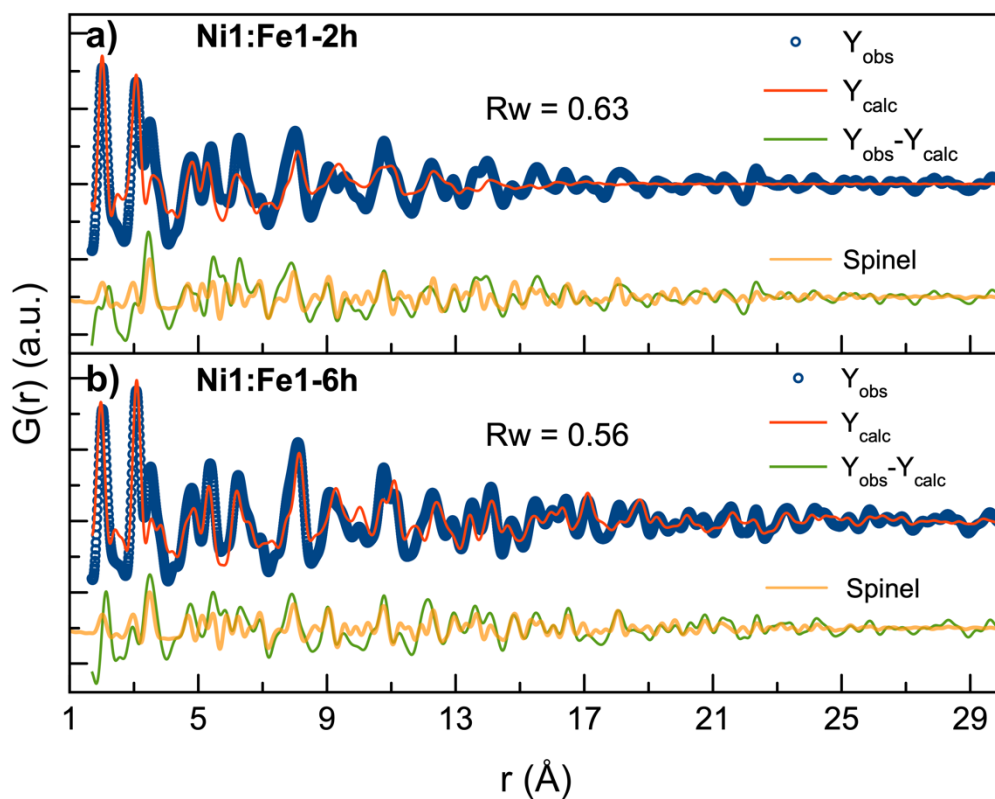


**Figure S6:** PDF refinements of products synthesized with Ni: Fe 1: 1 ratio for a) 2h and b) 6h. The fits were based on a single phase model using NiO<sub>2</sub>-LDH<sup>1</sup> structures. The blue circles show the experimental PDFs, the red lines are simulated PDFs, the green lines are the difference curves of the two, and the orange lines are the calculated PDFs from spinel structure. Refined parameters are given in Table S4.

**Table S2:** Refined values obtained from PDF refinement of PDFs from sample 'Ni1:Fe1-2h' and sample 'Ni1: Fe1-6h' using a single phase model includes Ni(OH)<sub>2</sub>-LDH<sup>1</sup> structures.

	Ni1:Fe1-2h	Ni1: Fe1-6h
<b>R<sub>w</sub></b>	0.629	0.565
<b>Scale factor</b>	0.540	0.529
<b>SPdiameter / Å</b>	21	42
<b>LDH cell / Å</b>	3.07 /	3.09/
<b>(a / c)</b>	24.52	23.44
<b>δ<sub>2</sub> / Å<sup>2</sup></b>	3.4	3.7

$U_{\text{ani}}(\text{Ni}) / \text{\AA}^2$	0.009 /	0.009 /
$(U_{11} / U_{33})$	0.078	0.078
$U_{\text{aniso}}(\text{O}) / \text{\AA}^2$	0.014	0.014
$O_{\text{pos}} / \text{\AA}$	0.627	0.626

For both samples, the parameters refined include scale factors, unit cell (a, c), atomic displacement parameters (ADPs), SP diameter and  $\delta_2$ , which accounts for the correlated local atomic motion in the structure.

**Table S3:** Refined values obtained from PDF refinement of PDFs from sample 'Ni1:Fe1-2h' and sample 'Ni1: Fe1-6h' shown in Figure 2.

	Ni1:Fe1-2h	Ni1: Fe1-6h
$R_w$	0.439	0.351
<b>Phase fraction / %</b>	67 / 33	77 / 23
<b>(LDH / Spinel)</b>		
<b>Scale factor</b>	0.446/ 0.340	0.488/ 0.152
<b>(LDH / Spinel)</b>		
<b>SPdiameter / \AA</b>	19/	51 /
<b>(LDH/Spinel)</b>	25	34
<b>LDH cell / \AA</b>	3.10 /	3.09/
<b>(a / c)</b>	21.79	22.74
<b>Spinel cell / \AA</b>	8.38	8.37
$\delta_2 / \text{\AA}^2$	3.6	3.9
$U_{\text{aniso}}(\text{Ni}) / \text{\AA}^2$	0.010 /	0.006 /
<b>LDH (<math>U_{11} / U_{33}</math>)</b>	0.199	0.980
$U_{\text{ani}}(\text{Fe}) / \text{\AA}^2$	0.010	0.006
<b>Spinel</b>		
$U_{\text{ani}}(\text{O}) / \text{\AA}^2$	0.007	0.011
$O_{\text{pos}} / \text{\AA}$	0.627 /	0.626 /
<b>(LDH / Spinel)</b>	-0.758	-0.757

For both samples, the parameters refined include scale factors, unit cell (a, c), atomic displacement parameters (ADPs), spherical diameter (SPdiameter), and oxygen atomic positions and  $\delta_2$ , which accounts for the correlated local atomic motion in the structure.

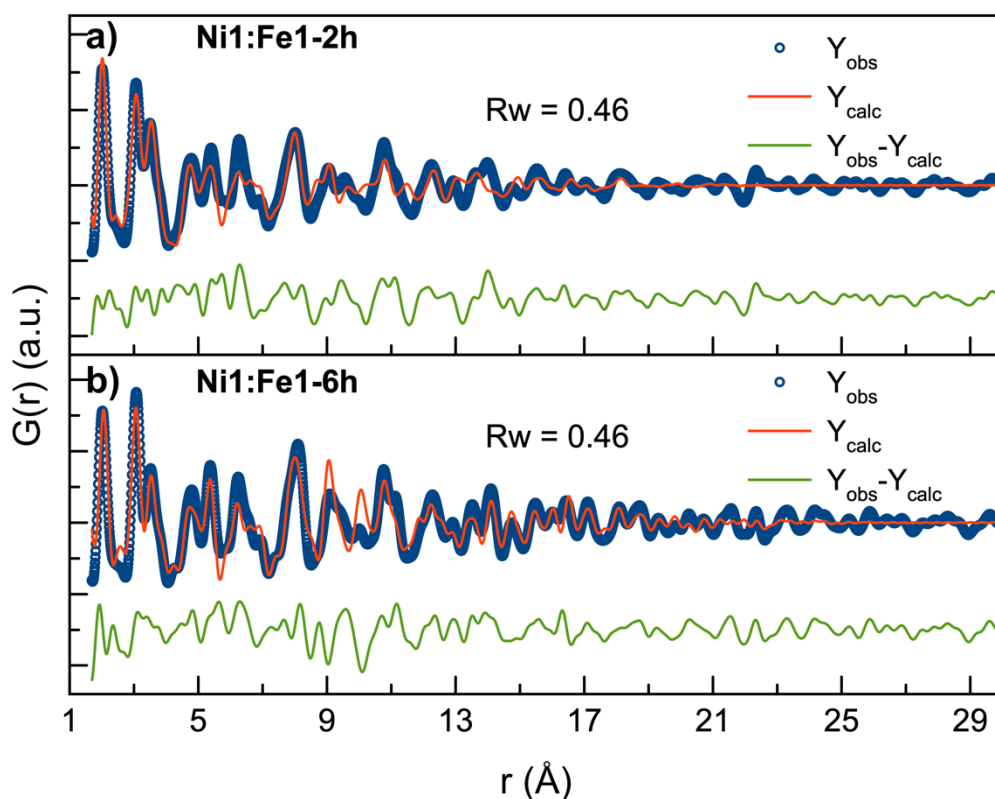


**Figure S7:** PDF refinements of products synthesized with Ni: Fe 1: 1 ratio for a) 2h and b) 6h. The fits were based on a two-phase model using  $\text{NiO}_2\text{-LDH}^{38}$  and  $\text{spinel}^{39}$  structures without refining the ADPs. The blue circles show the experimental PDFs, the red lines are simulated PDFs, and the green lines are the difference curves of the two. Refined parameters are given in Table S5.

**Table S4:** Refined values obtained from PDF refinement of PDFs from sample 'Ni1:Fe1-2h' and sample 'Ni1: Fe1-6h' based on a two-phase model using  $\text{Ni(OH)}_2\text{-LDH}^{38}$  and  $\text{spinel}^{39}$  structures without refining the ADPs.

	Ni1:Fe1-2h	Ni1: Fe1-6h
<b>R<sub>w</sub></b>	0.460	0.455



<b>Phase fraction / %</b>	71 / 29	76 / 24
<b>(LDH / Spinel)</b>		
<b>Scale factor (LDH / Spinel)</b>	0.599/ 0.260	0.465/ 0.151
<b>SPdiameter / Å (LDH/Spinel)</b>	12/ 24	28 / 29
<b>LDH cell / Å (a / c)</b>	3.11 / 21.71	3.09/ 23.06
<b>Spinel cell / Å</b>	8.41	8.36
<b><math>\delta_2 / \text{Å}^2</math></b>	3.1	2.9

For both samples, the parameters refined include scale factors, unit cell (a, c), SP diameter, oxygen atomic positions and  $\delta_2$ , which accounts for the correlated local atomic motion in the structure.

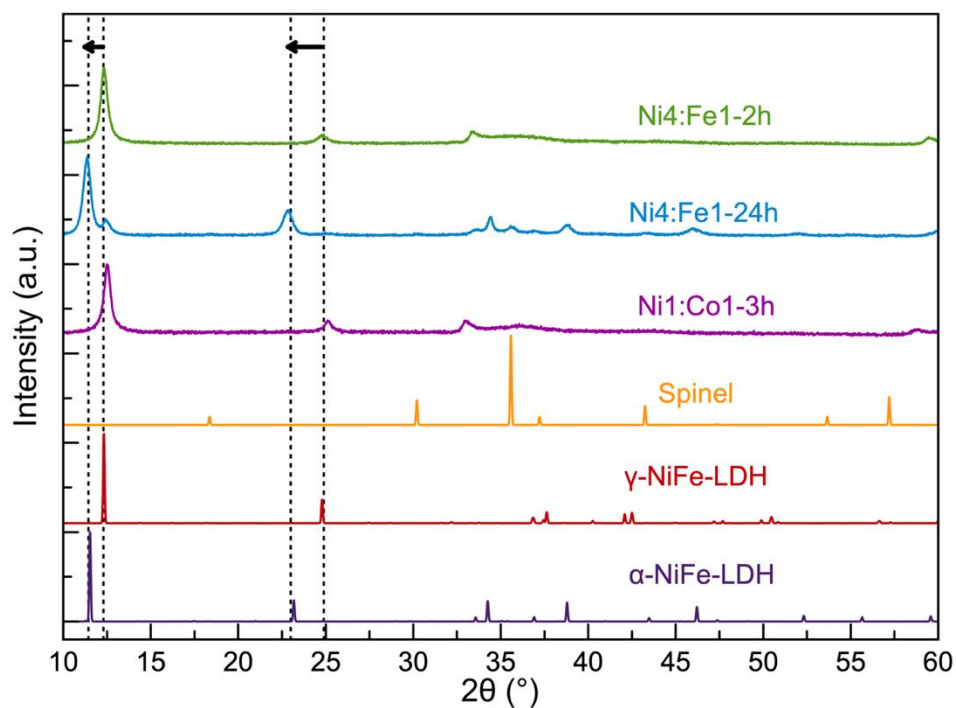


**Figure S8:** PXRD patterns of the two different as-synthesized  $(\text{Ni}_{0.8}\text{Fe}_{0.2})\text{OOH}$  samples and the as-synthesized  $(\text{Ni}_{1-x}\text{Co}_x)\text{OOH}$  sample. Samples were named by the metal precursor ratio used in synthesis and the synthesis time.

Laboratory powder XRD measurements were performed in a Bragg-Brentano configuration on a Bruker D8 instrument equipped with  $\text{Cu K}\alpha$  radiation with an x-ray wavelength of 1.54 Å. To minimize the background levels from fluorescence arising from Fe in the samples, the detector-discriminator voltage range was set to 0.190 V to 0.270 V as recommended by the manufacturer.

**Figure S8** displays the PXRD patterns of the two  $(\text{Ni}_{0.8}\text{Fe}_{0.2})\text{OOH}$  samples and the  $(\text{Ni}_{0.5}\text{Co}_{0.5})\text{OOH}$  sample used as reference materials for the two  $(\text{Ni}_{0.5}\text{Fe}_{0.5})\text{OOH}$ -samples discussed in the main manuscript. Their Ni:Fe ratio is 4:1 and they were synthesized for 2 h and 24 h, respectively. The  $(\text{Ni}_{0.5}\text{Co}_{0.5})\text{OOH}$  sample was synthesized with a Ni:Co ratio of 1:1 for 3 h. The diffraction pattern of sample Ni4:Fe1-2h shows peaks at  $12^\circ 2\theta$  and  $25^\circ 2\theta$  which match with the pattern of the  $\gamma$ -NiFe-LDH reference. While the peaks at  $11^\circ 2\theta$  and  $23^\circ 2\theta$  in the pattern of sample Ni4:Fe1-24h match with the calculated pattern of  $\alpha$ -NiFe-LDH. For sample Ni4:Fe1-24h, there are two separate peaks in the  $2\theta$  region of  $11^\circ - 12^\circ$ , implying the coexistence of both LDH polymorphs. Apart from the peak shift, the formation/growth of a spinel phase is observed with increased synthesis time. After 2h synthesis time, only a broad shoulder is visible between  $35^\circ$  and  $36^\circ 2\theta$ . However, when increasing the synthesis time to 24 h, a sharper peak is observed at  $35.5^\circ 2\theta$ , which is in good agreement with the reference pattern of the spinel structure. The sharpening of the peak as a function of synthesis time suggests that the spinel crystallite size increases as function thereof. For the Ni1:Co1-3h sample, the two peaks at  $12^\circ$  and  $25^\circ 2\theta$  indicate the presence of  $\alpha$ -LDH phase in the structure. A spinel phase might also exist as there is a broad shoulder at  $36^\circ 2\theta$ . The pattern is however non-conclusive in that regard.

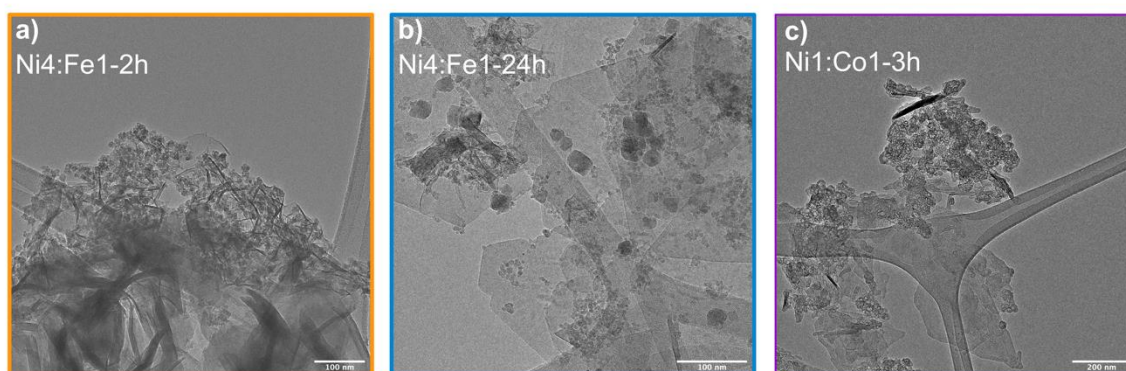


**Figure S9:** Exemplary TEM images of the other two  $(\text{Ni}_{0.8}\text{Fe}_{0.2})\text{OOH}$  samples and the  $(\text{Ni}_{0.5}\text{Co}_{0.5})\text{OOH}$  sample: Ni4:Fe1 - (a) 2h and (b) 24h, (c) Ni1:Co1-3h.

The TEM images of the two  $(\text{Ni}_{0.8}\text{Fe}_{0.2})\text{OOH}$  samples and the  $(\text{Ni}_{0.5}\text{Co}_{0.5})\text{OOH}$  sample are shown in **Figure S9**. Generally, the observations obtained here are similar with the two  $(\text{Ni}_{0.5}\text{Fe}_{0.5})\text{OOH}$  samples. From sample Ni4:Fe1-24h (**Figure S9b**) two types of morphologies can be distinguished clearly: large sheets and small almost spherical particles. While sample Ni4:Fe1-2h (**Figure S9a**) also exhibits both types of structure, the overall size of the sheets and the particles is smaller in comparison. The two types of morphologies are observed in the Ni1:Co1-3h sample in **Figure S9c** as well: sheets and small particles.

**Table S5:** Metal ratio (at. %) of the two  $(\text{Ni}_{0.8}\text{Fe}_{0.2})\text{OOH}$  samples and the  $(\text{Ni}_{0.5}\text{Co}_{0.5})\text{OOH}$  sample from SEM-EDS. The targeted atomic ratio in the NiFe-samples is Ni:Fe 4:1 and in the NiCo-sample it is Ni:Co 1:1.

Sample	Ni (at. %)	Error (at. %)	Fe (at. %)	Error (at. %)
Ni4:Fe1-2h	86	1.0	14	1.0
Ni4:Fe1-24h	80	1.0	20	1.0
Sample	Ni (at. %)	Error (at. %)	Co (at. %)	Error (at. %)
Ni1:Co1-3h	50	1.3	50	1.3

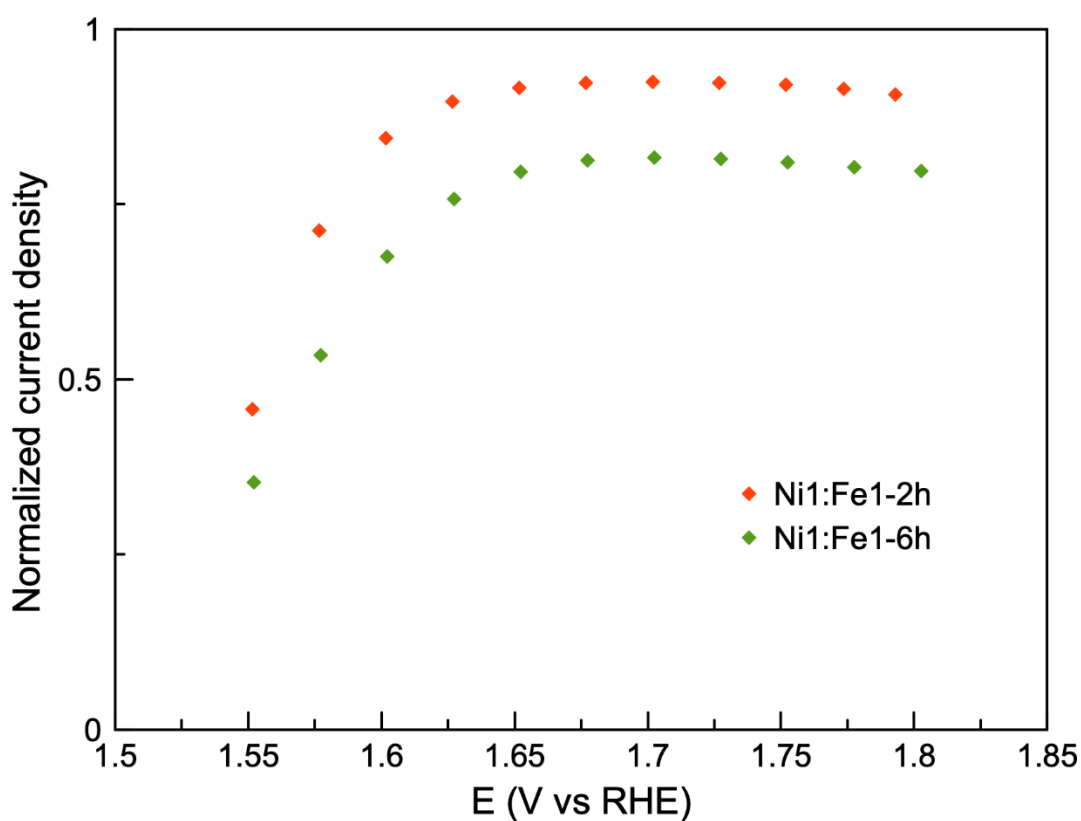


**Figure S10:** Subtraction of steady-state OER activities in purified KOH from in as-prepared KOH of two  $(\text{Ni}_{0.5}\text{Fe}_{0.5})\text{OOH}$  samples. The activities are normalized to the activities determined in as-prepared KOH electrolyte.

The normalized residue after subtracting the OER activity determined in purified KOH from the activity determined in as-prepared shows the impact of the Fe impurities. In both sample at 1.55  $V_{\text{RHE}}$ , the impurities account for approximately 40 % and 30 %, respectively.

respectively, of the measured current while at potentials larger than 1.6 V<sub>RHE</sub> the impurities account for 90 % and 75 % of the respective currents. Hence, the Fe-impurities seem to contribute more to the OER activity at larger overpotentials and seem to be the main contributor to the overall OER activity

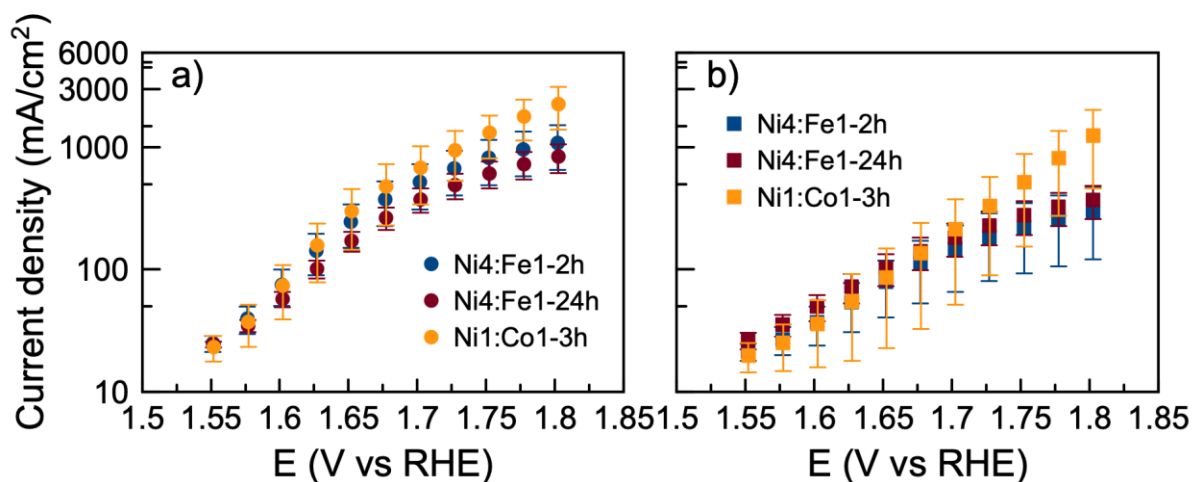


**Figure S11:** Steady-state OER activities of the two  $(\text{Ni}_{0.8}\text{Fe}_{0.2})\text{OOH}$  samples and one  $(\text{Ni}_{0.5}\text{Co}_{0.5})\text{OOH}$  sample in a) as-prepared and b) purified 0.1M KOH electrolyte measured at 2500 rpm. The current densities were taken from the average value of the last 10 seconds out of 60s steady state measurements. The activities shown are normalized to the geometric surface area.

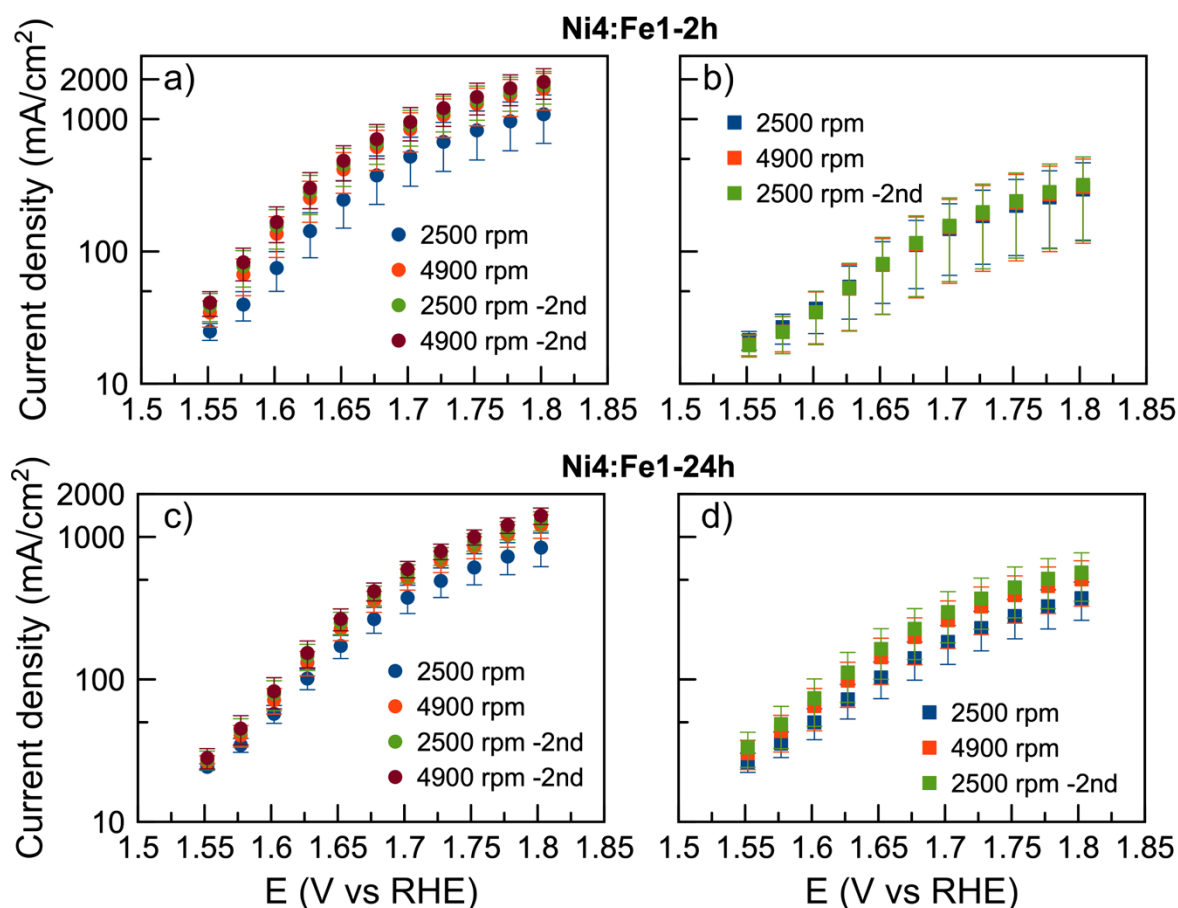


**Figure S12:** Steady-state OER activities of two  $(\text{Ni}_{0.8}\text{Fe}_{0.2})\text{OOH}$  samples: (a-b)  $\text{Ni}_4:\text{Fe}_1\text{-}2\text{h}$ , (c-d)  $\text{Ni}_4:\text{Fe}_1\text{-}24\text{h}$  in as-prepared (a, c) and purified (b, d) 0.1 M KOH electrolyte. The measurements were conducted in the order of 2500 rpm, 4900 rpm, 2500 rpm-2nd, and 4900 rpm-2nd. The activities shown here were normalized to the geometric surface area.

Similar behavior to the  $(\text{Ni}_{0.5}\text{Fe}_{0.5})\text{OOH}$  samples discussed in the main manuscript is observed. An initial, substantial increase in activity is observed for both samples in as-prepared KOH electrolyte. The following activity measurements are similar and only show miniscule changes in activity. In purified KOH electrolyte,  $\text{Ni}_4:\text{Fe}_1\text{-}2\text{h}$  shows constant activity throughout the entire measurement.  $\text{Ni}_4:\text{Fe}_1\text{-}24\text{h}$  exhibits continuously increasing activity as the measurement progresses. The trends observed in the  $\text{Ni}_1:\text{Fe}_1$ -samples is therefore confirmed.

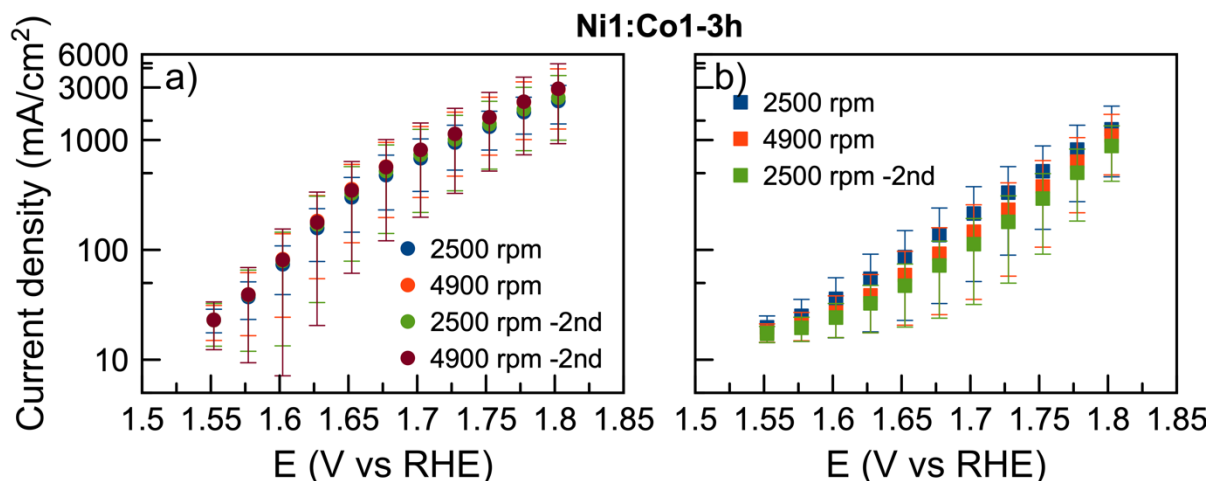


**Figure S13:** Steady-state OER activities of the  $(\text{Ni}_{0.5}\text{Co}_{0.5})\text{OOH}$  sample in a) as-prepared and b) purified 0.1 M KOH electrolyte. The measurements were conducted in the order of 2500 rpm, 4900 rpm, 2500 rpm-2<sup>nd</sup>, and 4900 rpm-2<sup>nd</sup>. The activities shown here were normalized to the geometric surface area.

The determined activity of Ni1:Co1-3h in as-prepared electrolyte does not change substantially with on-going electrolysis. In contrast, in purified electrolyte, a deteriorating trend in activity is observed: with on-going electrolysis, the determined activities decrease. Possibly, the Fe-impurities stabilize the NiCo-sample or their presence masks the degradation of the sample which, in contrast, is observed in the purified electrolyte.

1. Glemser, O.; Einerhand, J., Die struktur höherer nickelhydroxyde. *Zeitschrift für anorganische Chemie* **1950**, 261 (1-2), 43-51.

## Declaration of consent

on the basis of Article 18 of the PromR Phil.-nat. 19

Name/First Name:

Registration Number:

Study program:

Bachelor       Master       Dissertation

Title of the thesis:

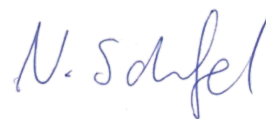
Supervisor:

I declare herewith that this thesis is my own work and that I have not used any sources other than those stated. I have indicated the adoption of quotations as well as thoughts taken from other authors as such in the thesis. I am aware that the Senate pursuant to Article 36 paragraph 1 litera r of the University Act of September 5th, 1996 and Article 69 of the University Statute of June 7th, 2011 is authorized to revoke the doctoral degree awarded on the basis of this thesis.

For the purposes of evaluation and verification of compliance with the declaration of originality and the regulations governing plagiarism, I hereby grant the University of Bern the right to process my personal data and to perform the acts of use this requires, in particular, to reproduce the written thesis and to store it permanently in a database, and to use said database, or to make said database available, to enable comparison with theses submitted by others.

Place/Date

Signature

A handwritten signature in blue ink, appearing to read 'N. Schafel', is written over the printed word 'Signature'.